Array Processing Methods for Calibrating Inverse Synthetic Aperture Radar and Multiple Pass Synthetic Aperture Radar

by

Zhishun She

B.Sc, M.Sc

Thesis submitted for the degree of

Doctor of Philosophy

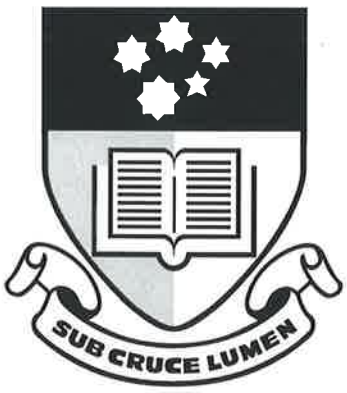

Department of Electrical and Electronic Engineering

School of Engineering

The University of Adelaide

January 2000

Table of Corrections

Page	Line	Error	Correction
21	30	in 1988	in 1989
53	10	They have also used	They have also been used
95	6	is shown Figure 5.4	is shown in Figure 5.4
96	6	three orthogonal axises	three orthogonal axes
96	17	will located in	will be located in
97	7	processing has following	processing has the following
103	13	which corresponds a	which corresponds to a
105	1	two important performances for an imaging systems	two important performance measures for an imaging system
116	20	geometric distortions require to	geometric distortions requiring to
137	7	in previous chapter	in the previous chapter
137	20	signal incident the flight path array	signal incident on the flight path array
140	3	It is pointed that	It is pointed out that
154	7	This statistics	This statistic
180	24	based on the this model	based on this model
189	5	$l(z_0,...,z_{M-1};d)$ respect to	$l(z_0,...,z_{M-1};d)$ with respect to

Table of Contents

Abstract

Synthetic Aperture Radars (SAR) have been widely utilized for military purposes and civilian applications and make use of the relative motion between the radar and an object to create a synthetic aperture to provide a high-resolution radar image. For proper coherent processing of SAR signals, the shape of this synthetic aperture needs to be known to a fraction of radar wavelength. In practice the turbulence and uncertainty of the relative motion make the synthetic aperture different from its nominal shape degrading the SAR high-resolution capability. How to compensate for the imperfection forms the basis of the work conducted in this thesis.

This thesis investigates calibration for errors of a synthetic aperture in Inverse Synthetic Aperture Radar (ISAR) and Multiple Pass Synthetic Aperture Radar (MPSAR). Both are reviewed as the problems of array processing and are solved from the point of array calibration.

A signal model for ISAR autofocus is derived by use of a scatterer model and four new ISAR autofocus methods based on conventional beamforming, optimum beamforming, signal subspace and noise subspace are developed. ISAR autofocus is effected by adjusting the steering vector to maximize the output powers of conventional and optimum beamformers. Alternatively it can be performed by projecting the steering vector into the signal subspace and the noise subspace, respectively. A subaperture processing is described to reduce the computational load. Computer simulations are conducted and real data results of ISAR imaging are presented. Statistical analyses of the four methods are carried out. The signal subspace method is identified to be the maximum likelihood (ML) estimation for ISAR autofocus. The Cramer-Rao lower bound (CRLB) of the estimated

complex vector associated with ISAR autofocus and the CRLB of the estimated distance between two scatterers are derived. Further the CRLBs are analysed to obtain useful insight into the developed methods and ISAR autofocus.

A novel processing step for three-dimensional (3D) SAR imaging via MPSAR processing is proposed which includes conventional SAR processing, image registration, phase correction and elevational imaging. For multiple SAR image registration, the complex correlation, the minimum distance and the image model matching approaches are developed. With regard to phase correction, the eigenvector method, the terrain centroid tracking and the strong scatterer reference are described. Frequency domain beamforming is used for elevational imaging and the maximum entropy extrapolation and the subspace methods are adopted to enhance elevational resolution. All developed methods are verified for computer simulated data and first European Remote Sensing satellite (ERS-1) real data of repeat orbits and their statistical performances are analysed.

Declaration

This work contains no material which has been accepted for the award of any other degree or diploma in any university or other tertiary institution and, to the best of my knowledge and belief, contains no material previously published or written by another person, except where due reference has been made in the text.

I give consent to this copy of my thesis, when deposited in the University Library, being available for loan and photocopying.

Signature:

Data: January 20, 2000

Acknowledgments

I would like to thank my joint supervisors, Professor Bob Bogner and Professor Doug Gray. Bob provided steady support and encouragement throughout my candidature and was particularly helpful in improving my technical writing style. Doug introduced multiple pass SAR to me and his expertise in array processing provided me with useful insight into my work. Doug also taught me a lot about presentations, both oral and written.

I also would like to thank Dr. John Homer and Professor Dennis Longstaff, The University of Queensland. I thank them for providing the ERS-1 data. John discussed with me the details of multiple pass SAR, gave me some useful suggestions and looked after me when I collected real data in Lake Frome and studied in Brisbane.

Thanks go to my colleagues in signal processing Laboratory, Carmine Pontecorvo, Ben Raymond, Jamie Sherrah, Habib Hosseini, Steve Wawryk, Hong Gunn Chew, Qiang Fu, Anna Buzescu and Kathryn Burgess. I thank them for all their help and the happy time we spent together.

I gratefully acknowledge the financial support provided by CSSIP, OPRS from Australian Research Council (ARC) and University of Adelaide Scholarships (UAS).

To my wife, child and parents, I thank them for their never ending support during all my years of study.

List of Figures

List of Tables

Glossary

Abbreviations

3D	three dimension
AIC	Akaike information criterion
AR	auto-regressive
ARMA	auto-regressive moving average
CBP	convolution back-propagation algorithm
CRLB	Cramer-Rao low bound
DEM	digital elevation model
DFT	discrete Fourier transform
DBS	Doppler beam sharpening
ESPRIT	estimation of signal parameters via rotational invariance techniques
ECP	extended coherent processing
ERS-1	first European remote sensing satellite
FFT	fast Fourier transform
GPS	global position systems
INS	inertial navigation systems
ISLR	integrated sidelobe ratio
InSAR	interferometric synthetic aperture radar
ISAR	inverse synthetic aperture radar

MP	matrix pencil
ME	maximum entropy
MAG	maximum array gain
ML	maximum likelihood
MMSE	minimum mean-square error
MPWC	minimum power with constraint
MPSAR	multiple pass synthetic aperture radar
MUSIC	multiple signal classification
NRL	naval research laboratory
PGA	phase gradient autofocus
PSF	point spread function
PFP	polar format processing
PRI	pulse repetition interval
RLOS	the radar-line-of-sight
SNR	signal-to-noise ratio
STAP	space-time adaptive processing
SAR	synthetic aperture radar
WSF	weighted subspace fitting

Symbols

$A(x, y)$	amplitude of two-dimensional image
$A(\theta)$	directional matrix
$a(\theta)$	directional vector
B_a	baseline
B_w	bandwidth of transmitted signal
b_i	discrete window function
$b_p(\theta)$	beampattern
$b(t)$	amplitude of sinusoidal wave
$C_r(\Delta x, \Delta y)$	two-dimensional correlation function
C_x	covariance matrix of received signal vector for ISAR
C_{xy}	covariance matrix of pixel vector for MPSAR
c	speed of light propagation
D	complex vector of translational motion
D_m	the m th element of D
$\mathcal{D}$	distance measure
D_e	complex vector corresponding to uncertainty of multiple flight passes
$D(\Delta x, \Delta y)$	sum of two-dimensional amplitude difference
d	distance between two scatterers
d_e	baseline between adjacent two flight paths
d_T	elevational aperture length
det ( )	the determinant of a matrix
E_M	the energy in the mainlobe of beampattern
E_T	the total energy of beampattern
e^f	forward prediction error
e^b	backward prediction error
$G_i(x, y)$	SAR image of i th flight path
$G'(x, y, i)$	SAR image of i th flight path after phase correction
H	platform height

h	terrain height
$h_k(x, y)$	prediction coefficient of pixel (x,y)
I_r	improved ratio of ground-range resolution
J	Fisher's information matrix
j	$\sqrt{-1}$
K	number of scatterers
L	number of stepped frequencies
M	number of pulses
$M(x, y)$	image model
N	number of range cells
N_e	number of extrapolated flight passes
N_p	number of flight passes
N_x	dimension of SAR image in range direction
N_y	dimension of SAR image in azimuthal direction
O	exchange matrix
P_i	ith flight path
P_{rs}	projection matrix onto the signal subspace
P_{rn}	projection matrix onto the noise subspace
$P(\theta)$	output power of beamformer
$p(x;D)$	joint probability density function
Q	AR model order
$\boldsymbol{q} = (q_x, q_y, q_z)$	vector in the data domain
r	range between the radar and the scatterer
R	range between the radar and the object centroid
$S(q_x, q_y)$	two-dimensional Fourier transform of image
$S(f, R_0)$	spectrum of received signal
$S_o(f, R_0)$	output of matched filter
$s_r(t, R_0)$	received signal
s_v	the speed of object

T	pulse repetition interval
Tr ( )	the trace of a matrix
$t_k(x, y)$	reflection coefficient of pixel (x,y)
U	matrix of eigenvectors
U_s	matrix of eigenvectors of the signal subspace
U_n	matrix of eigenvectors of the noise subspace
$U(f)$	spectrum of transmitted signal
$u(t)$	transmitted signal waveform
u_e	maximal unambiguous length in elevation
u_i	eigenvector of covariance matrix
$V(x, y)$	pixel vector before phase correction
$V'(x, y)$	pixel vector after phase correction
Var (x)	estimated variance of variable x
v	steering vector
$\hat{v}$	estimation of steering vector
v^T	transpose of vector v
v^H	conjugate transpose of vector v
$\|\|v\|\|$	Euclidean norm of vector v
$W(t)$	noise vector
w_{nm}	additive noise
X_n	vector of received signal for ISAR
x_{nm}	received signal at n th range cell of m th range profile
$Z(t)$	vector of array output
α	baseline orientation angle
β	incidence angle of radar
γ	slope angle of terrain
$\Delta\theta$	rotating angle of object
δ	Dirac delta function
θ	aspect angle

Λ	diagonal matrix of eigenvalue
λ	wavelength of transmitted signal
λ_i	eigenvalue of covariance matrix
$\rho\,(x, y, z)$	reflectivity of terrain
ρ_k	reflectivity of kth scatterer
σ_w^2	power of noise
τ_a	azimuthal resolution
τ_e	elevational resolution
τ_g	ground-range resolution
τ_r	range resolution
ϕ_m	phase for phase correction
φ	interferometric phase
$\lvert\ \rvert$	module of a complex variable

Publications

This work has resulted in the following publications:

Zhishun She, R.E.Bogner and D.A.Gray, "An eigenvector approach for inverse synthetic aperture radar (ISAR) motion compensation and imaging", *Proceedings of the 1997 IEEE Region 10 Annual Conference on Speech and Image Technologies for Computing and Telecommunications, (TENCON'97),* Brisbane, Australia, December 1997, pp.659-662.

Zhishun She, R.E.Bogner and D.A.Gray, "Autofocus for inverse synthetic aperture radar (ISAR) imaging by beamforming", *Proceedings of the IEEE Radar Conference, (RADARCON'98),* Dallas, U.S.A., May 1998, pp.233-238.

Zhishun She and R.E.Bogner, "Image registration for multiple pass synthetic aperture radar (SAR)", *Proceedings of the Information, Decision and Control Conference (IDC'99),* Adelaide, Australia, February 1999, pp.341-345.

Zhishun She, D.A.Gray, R.E.Bogner and J.Homer, "Three-dimensional synthetic aperture radar (SAR) imaging via multiple pass processing", *Proceedings of 1999 IEEE International Geoscience and Remote Sensing Symposium, (IGARSS'99),* Hamburg, Germany, June 1999, pp.2389-2391.

Zhishun She, D.A.Gray and R.E.Bogner, "Autofocus for inverse synthetic aperture radar (ISAR) imaging", Submitted to *Signal Processing*, pp.1-32.

Zhishun She, D.A.Gray, R.E.Bogner and J.Homer, "Three-dimensional synthetic aperture radar (SAR) imaging via multiple pass processing", Submitted to *IEEE Transactions on Geoscience and Remote Sensing,* pp.1-34.

Chapter 1 Introduction

1.1 Motivation

Since its origins in the 1950s, synthetic aperture radar (SAR) has been extensively developed [1]. Its advantages over other remote sensors of operating in all-weather conditions and its high-resolution imaging have been exploited for civilian applications and surveillance purposes. Many airborne and spaceborne SAR systems have been widely utilized. Unlike other radars for target detection and tracking, SAR systems are used primarily for mapping stationary targets (such as terrain, ocean and glacier) and imaging moving objects (such as aircraft, ships and satellites).

SAR is able to produce two-dimensional high resolution images in the range and azimuthal (cross-range) directions. High range resolution is obtained by transmitting a wideband signal and high azimuthal resolution is achieved by synthesizing a large aperture in azimuth. SAR is typically carried on a moving platform for air-to-ground mapping of stationary terrain where motion of the platform creates the synthetic aperture. Inverse SAR (ISAR), the inverse mode of SAR, is usually deployed on the earth for ground-to-air imaging of moving objects. The synthetic aperture required for high azimuthal resolution is provided by the motion of object.

SAR and ISAR imaging are coherent processes and require that the errors in synthesizing the azimuthal aperture are less than a fraction of radar wavelength. However, in practice, the synthesized aperture usually deviates much more than this from its designed shape due to flight turbulence for SAR and unpredictable flight path for ISAR. In order to meet the strict requirements of coherent processing, the actual shape of synthetic aperture should be

precisely estimated and appropriate correction made prior to image formation. This correction is called motion compensation.

Motion compensation of SAR imaging can be assisted with inertial navigation systems (INS) and global position systems (GPS). However motion compensation for ISAR imaging is more challenging than that of SAR because ISAR targets are often not cooperative. Such compensation is usually conducted in two steps, that is, range realignment (coarse compensation) and autofocus (fine compensation). Although many approaches to ISAR autofocus have been proposed and developed, robust autofocus for ISAR imaging has still remained a fascinating area of research.

Even if SAR or ISAR results in a two-dimensional high resolution image in the range and azimuth, it can not resolve two scatterers locating at the same range-azimuth resolution cell and different elevation. In some applications such as topographic mapping and military reconnaissance, a three-dimensional (3D), i.e., range, azimuthal and elevational high resolution image is required. Then interferometric SAR (InSAR) comes into being.

InSAR is a technique for extracting the 3D target information by using the phase content of two complex SAR images acquired at two different spatial positions which form the baseline of InSAR. Normally InSAR signal processing includes: first two complex images are registered; second the interferogram is formed by multiplying one image with the conjugate of the other; third the principal value phase of the interferogram is unwrapped; and finally the unwrapped phase and the baseline are used to calculate the terrain height.

The application of InSAR is primarily restricted by phase unwrapping and baseline estimation. The phase unwrapping may be appropriate in a low-noise environment in which the progression of wrapped phase is consistent. However in the more realistic high-noise environment such as spaceborne SAR where the wrapped phase usually progresses inconsistently, the phase unwrapping may become ambiguous. On the other hand, the baseline estimation requires the existence of several ground control points which may also be impractical in many situations.

InSAR only estimates the height of the terrain, but the reflectivity of the terrain remains unknown. Multiple pass SAR (MPSAR) processing is a natural extension of conventional InSAR. It makes use of more than two SAR imaging flight passes to synthesise an aperture in elevation, resulting in improved accuracy and resolving power in the elevational

direction. The resulting resolution in elevation, coupled with the resolving capability of single-pass SAR imagery in range and azimuth, constructs a 3D SAR image. This 3D SAR image provides the information about both the elevational variation and the reflectivity of terrain which is important to terrain mapping, analysis and classification. Nevertheless this topic of research is in its infancy and its theory and practice require further investigation.

Based on the above motivations, two issues on SAR signal processing are addressed in this thesis. One is the autofocus problem for ISAR imaging. The other is the 3D SAR imaging via MPSAR processing. They are considered as problems of array processing and are approached from the perspective of array calibration. The aim is twofold. One is to apply the array processing approaches to ISAR and MPSAR which have been treated by use of the intuitive methods. The other is to develop a unifying framework where the intuitive methods for ISAR and MPSAR could be interpreted and evaluated in a new way.

1.2 Thesis Outline and Contributions

In **Chapter 2**, background material on SAR, ISAR, InSAR and array processing is provided. ISAR processing can be divided into two steps: motion compensation and image formation and existing techniques for these are reviewed and examples of simulated ISAR images of Boeing-727 aircraft are demonstrated. Image registration and phase unwrapping are critical issues of InSAR processing and previous methods for image registration and phase unwrapping are outlined and interferograms of simulated data and first European Remote Sensing satellite (ERS-1) real data are presented. Examples of one and two dimensional phase unwrapping are given. Techniques of array processing including beamforming, subspaces methods and array calibration are briefly reviewed.

In **Chapter 3**, some ideas from the calibration of antenna arrays are applied to ISAR autofocus. First a signal model for ISAR autofocus is derived by use of a scatterer model. Then two new approaches to ISAR autofocus are developed by adjusting the steering vector to maximize the output powers of conventional and optimum beamformers respectively. It is verified that the steering vector converges to the complex vector corresponding to the translational motion of object if the covariance matrix is known precisely. Next another two new ISAR autofocus approaches are developed based on the

signal and noise subspaces of the covariance matrix. They make use of the orthogonality between the noise subspace and the steering vector when the steering vector points to the signal vector associated with the translational motion of object and are equivalent if the covariance matrix is known. Subaperture processing is described and its advantage in reducing computational complexity is pointed out. Finally computer simulations are conducted and real data results are presented for both one-dimensional and two-dimensional ISAR imaging. ***The main contributions are: (a) deriving the signal model for ISAR autofocus, (b) developing four new ISAR autofocus methods based on conventional beamforming, optimum beamforming, signal subspace and noise subspace.***

In **Chapter 4**, the approaches developed in previous chapter are considered from an estimation perspective. The schemes for estimating covariance matrices are described. The relations of the signal subspace method to conventional methods of ISAR autofocus are identified. The signal subspace method is shown to be equivalent to the maximum likelihood (ML) estimation of the complex vector corresponding to the translational motion. Theoretical performance bounds (Cramer-Rao lower bounds; CRLB) for ISAR autofocus and location are determined. The CRLB of the estimated complex vector associated with the translational motion of object and the CRLB of the estimated distance between two scatterers are derived. The statistical performances of conventional beamforming, optimum beamforming, signal and noise subspace methods for calibration are analysed and compared with the CRLBs versus signal-to-noise ratio (SNR). ***The main contributions are: (a) the identification of ML estimation of the complex vector for ISAR autofocus, (b) the determination of CRLBs for ISAR autofocus and location and (c) the investigation of statistical performances of developed approaches.***

In **Chapter 5**, novel processing steps for 3D SAR imaging via MPSAR processing are proposed which include conventional SAR processing, image registration, phase correction and elevational imaging based on a mathematical model for 3D SAR imaging using 3D Fourier transform. The advantages of this method over typical InSAR are highlighted. Computer simulations are conducted and ERS-1 data are processed to verify the proposed processing steps. ***The main contribution is the development of new processing steps for 3D SAR imaging via MPSAR processing.***

In **Chapter 6**, after an overview of the concepts of image registration, a model for MPSAR images is derived. A new approach of SAR image registration by use of complex correlation is developed for image pairs. Then a minimal distance approach and an image model matching approach are proposed for multiple image registration. The complex correlation and the image model matching approaches are compared with the conventional amplitude correlation method by processing real data of ERS-1. The results show that they register multiple images more precisely than the amplitude correlation method. ***The main contributions are the developments of the complex correlation, the minimal distance and the image model matching approaches for MPSAR image registration.***

In **Chapter 7**, phased array calibration techniques are utilized for the phase correction of multiple complex SAR images before the formation of focused beams in the elevational direction. Three methods for phase correction are developed; eigenvector approach, terrain centroid tracking and strong scatterer reference. The eigenvector approach is the ML estimation of the phase factor. The terrain centroid tracking is valid for the terrain where multiple strong scatterers exist whilst the strong scatterer reference is suitable for the terrain where a dominant strong scatterer is detected. The proposed methods are verified by processing the ERS-1 data. ***The main contributions are the developments of the eigenvector approach, the terrain centroid tracking and the strong scatterer reference for phase correction of MPSAR processing.***

In **Chapter 8**, the formation and enhancement of elevational beams are studied. Multiple receiving beams are formed for the elevational resolution which is efficiently implemented with a discrete Fourier transform (DFT). A window is applied to control sidelobes and zero-padding prior to DFT is used to increase the number of output beams. The elevational resolution is enhanced by a maximum entropy data extrapolation or by a subspace method. The maximum entropy data extrapolation extends the signal series of each pixel across multiple SAR images forward and backward in the data domain using an auto-regressive prediction filter. Then Fourier processing of extrapolated data produces a 3D superresolution image. The subspace method makes use of the orthogonality between the noise subspace and the signal subspace of covariance matrix of signal series to provide a superresolution capability. The DFT processing, the maximum entropy data extrapolation and the subspace method are compared by processing ERS-1 data. ***The main contributions are (a) to use the DFT to beamform in elevation, (b) to apply the***

maximum entropy data extrapolation and the subspace method to enhance the elevational resolution.

In **Chapter 9**, the thesis is summarised and conclusions are drawn. Topics for further research are suggested.

There are three appendices. The eigendecomposition of a covariance matrix for ISAR autofocus is presented in Appendix A. Appendix B derives the solution for eigenvalues and eigenvectors of a 2×2 covariance matrix. The CRLB of the estimated distance between two scatterers are derived in Appendix C.

Chapter 2 Background Information

This chapter introduces some of the concepts associated with Synthetic Aperture Radar (SAR), Inverse Synthetic Aperture Radar (ISAR), Interferometric Synthetic Aperture Radar (InSAR) and array processing and provides a background for material presented in later chapters. The discussion of SAR is very brief. Some good references on SAR are books by Harger [77], Curlander and McDonough [78] and Wehner [1]. The descriptions of ISAR and InSAR are written from a signal processing perspective. Other material on ISAR and InSAR is available in books [1] [79] and papers [4] [44] [45]. Techniques for array processing including beamforming, subspace methods and array calibration are overviewed briefly. More detailed discussions on array processing theory are available in the literature [2] [85] [117].

2.1 Synthetic Aperture Radar

Radar is an electromagnetic system mainly for the detection and tracking of objects. It operates by transmitting a particular type of waveform and detecting the nature of the echo signal to locate the object. However in many classical treatments, information on structure, shape and size of object is unavailable because the object is considered as a point target due to limited resolving capability of the radar.

In 1950s, a high resolution coherent radar, SAR, appeared where the object is regarded as an extended target rather than a point target, which provides a discrimination in range and

azimuthal directions where a large bandwidth waveform is used to achieve high resolution in range and a synthetic aperture provides high resolution power in azimuth.

SAR is typically carried on a moving platform which is intended to be used in air-to-ground imaging of terrain as shown in Figure 2.1. It operates almost independently of meteorological conditions and sun illumination which makes it most suitable for topographic mapping and large area surveillance tasks. Both airborne and spaceborne SAR systems are now widely used.

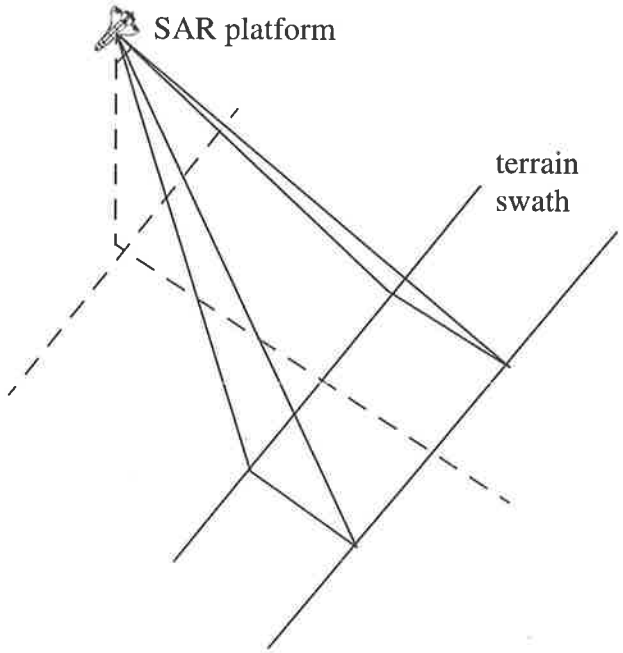

Figure 2.1 SAR strip mapping

A simplified block diagram of SAR is shown in Figure 2.2. A wideband signal is generated by a transmitter and radiated into space by an antenna. A duplexer permits a single antenna to be used for both transmission and reception. Reflecting objects intercept and reradiate a portion of the transmitted signal; a small amount of signal returns back to radar and is collected by the antenna coherently, i.e., the received signal is recorded in amplitude and phase or in in-phase (I) and quadrature (Q) components. Range processing produces the high range resolution profiles and azimuthal processing achieves the high resolution in the azimuth.

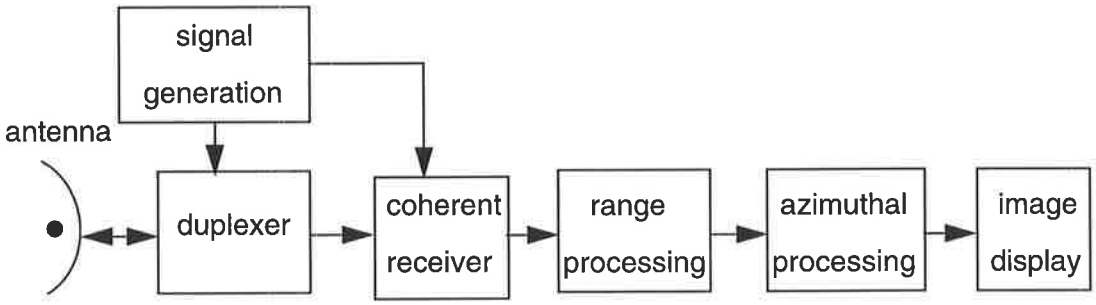

Figure 2.2 SAR block diagram

Besides strip mapping as shown in Figure 2.1, many other modes of SAR such as Doppler Beam Sharpening (DBS)[1], squint mode SAR[1], spotlight SAR[79], scan SAR[1], inverse SAR (ISAR)[1] and interferometric SAR (InSAR)[79] have appeared. ISAR and InSAR will be described below.

2.2 Inverse SAR

ISAR is the inverse mode of SAR [1]. It is usually deployed on the earth which can be used for ground-to-air imaging of non-cooperative moving targets such as missiles, satellites, aircraft, ships and celestial objects at a long distances no matter whether it is rainy or foggy, day or night. ISARs have been applied extensively for radio astronomy and military purposes.

Figure 2.3 shows ISAR imaging an aircraft flying in a straight line. The relative motion between radar and object can be decomposed into translational motion and rotational motion [3]. The translational motion represents the trajectory motion of a reference point of the object. The rotational motion denotes the rotation of the object around the reference point. Only the latter contributes to image formation. The former should be compensated before image formation; this is called motion compensation.

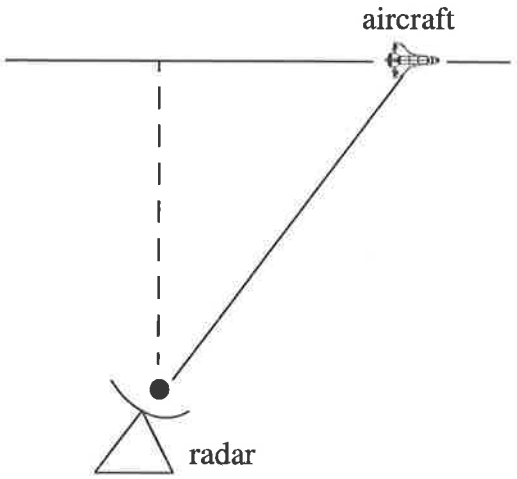

Figure 2.3 ISAR imaging

After the translational motion is removed, ISAR imaging is changed into rotating platform imaging as shown in Figure 2.4 where a ground-fixed radar is used to image object on rotating platform. Radar images are produced using the range-Doppler principle [4].

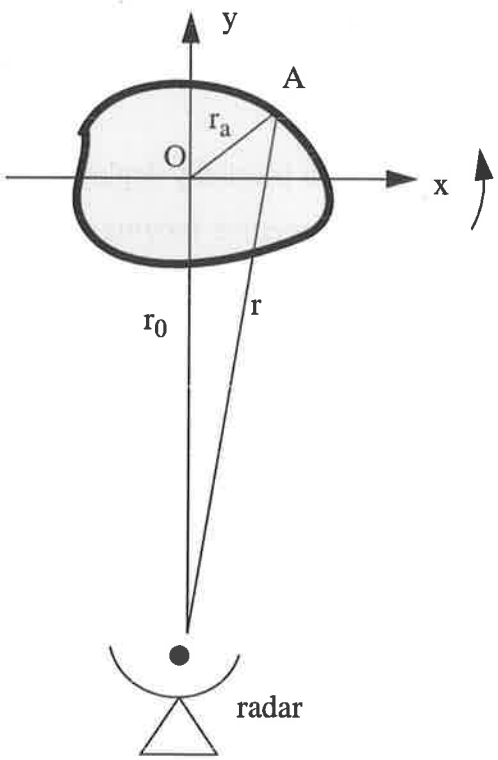

Figure 2.4 Rotating platform imaging

The range resolution τ_r of ISAR is determined by the bandwidth B_w of the transmitted signal according to following relation

$$\tau_r = \frac{c}{2B_w} \tag{2.1}$$

where c is the speed of light. ISAR azimuthal resolution is created by the rotational motion of object relative to the radar-line-of-sight (RLOS). The azimuthal resolution of ISAR τ_a is related to the angle $\Delta\theta$ through which the object rotates relatively to RLOS during the coherent processing time. The relation between τ_a and $\Delta\theta$ is

$$\tau_a = \frac{\lambda}{2\Delta\theta} \tag{2.2}$$

where λ denotes the wavelength of the transmitted signal. (2.1) and (2.2) are valid when the total rotation angle $\Delta\theta$ is so small that there is no point scatterer on the object which may move through a range-Doppler resolution cell[5]. To avoid image degradation caused by motion through a resolution cell while using the simple range-Doppler analysis, we must limit the total rotation angle $\Delta\theta$. For large rotating angle imaging and near field imaging[141], the motion of scatterer through the range-Doppler resolution cells should be compensated [5].

The signal processing used in ISAR imaging can be divided into two steps. The first is motion compensation which removes the translational motion and simplifies ISAR imaging into rotating platform imaging. The second step is image formation which reconstructs the reflectivity distribution of an object. The typical ISAR signal processing procedure is shown in Figure 2.5. Precise motion compensation is realized by a combination of range realignment and phase compensation (autofocus). The image formation includes angular estimation and image reconstruction.

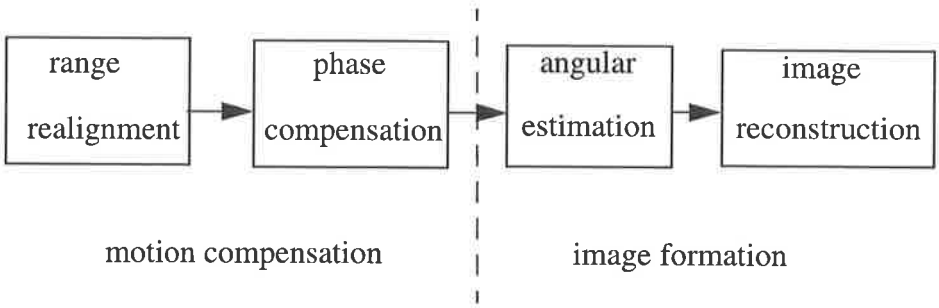

Figure 2.5 ISAR signal processing procedure

2.3 ISAR Image Formation

2.3.1 Angular Estimation

After motion compensation, ISAR imaging is turned into rotating platform imaging and ideally the rotating velocity should be constant, implying that the aspect change between adjacent two pulses is same. However in practical situations, this is usually not the case [22] and therefore, to precisely image, there is a need to compensate by resampling or interpolating the aspect samples. Moreover in the case of large rotating angle imaging, precise knowledge of the rotating angle of the object is required to compensate for the motion of scatterer through range-Doppler resolution cells [5]. Finally the ISAR image needs to be scaled accurately in both the range and azimuthal dimensions in order to provide object information such as length, size and shape. Improper scaling in range and azimuth may result in distortion of the object image, making target classification and identification difficult. Since the bandwidth of the transmitted signal is totally controlled, range scaling is not a problem. However, for non-cooperative objects, the cross-range scaling depends on the unknown aspect angle change and in order to scale the ISAR image in azimuth, the aspect angle change must be accurately estimated.

The problem of ISAR azimuth scaling was first presented by Prickett and Chen in 1980 [3] and Chen and Andrews in 1980 [6] noticed the influence of angular nonuniformity. Werness et al. in 1990 [27] assumed that three prominent scatterers existed in an ISAR image and used the first point to remove the translational motion, the second one to

measure and compensate for the angular nonuniformity and the third point to estimate the azimuthal scale factor. However the selection of multiple strong scatterers and measurement of their phase components were infeasible in practical applications. Bocker et al. in 1991 [15] approximated the translational motion and rotational motion with quadratic polynomials and an iterative procedure was applied to estimate the translational motion and the nonuniform rotational motion. Delisle and Wu in 1994 [28] made use of a two-receiver radar to compute the target angular trajectory although this may rarely be a practical option. We in 1994 [29] developed an approach which was based on the principle of tomographic imaging and the property of coherent processing to estimate the aspect angle change from the wideband echo data and gave an improved approach based on extended-coherent-processing in 1995 [30]. Nash in 1994 [31] employed a polar-format-processing imaging method to determine the aspect angle change.

2.3.2 Image Reconstruction

Image reconstruction is the estimation of the reflectivity distribution of an object by processing the motion compensated echo data. The simple standard method is FFT range-Doppler processing [4]where the two-dimensional processing is decomposed into two one-dimensional processings. Fast Fourier transform (FFT) is utilized in the range and azimuth processing to enhance computational efficiency. The FFT range-Doppler processing assumes that no point scatterers move through the range-Doppler resolution cells during the coherent processing time which is only valid for small rotating angle imaging.

An image reconstruction method for large rotating angle imaging is extended-coherent-processing (ECP) [4][32]. It replaces the total coherent interval with a number of small subintervals in which no point scatterers move through the range-Doppler resolution cells. With subintervals of such size, the ISAR images can be calculated by the range-Doppler processing. Then the subimages obtained in each subinterval are aligned in range and range-rate to account for the relative motion of scatterers occurring between separate subintervals and coherently summed to produce the extended image of the total coherent duration.

Walker in 1980 [33] developed another large rotating angle imaging approach known as polar-format-processing (PFP). After the translational motion is removed, the ISAR image may be reconstructed by an inverse two-dimensional Fourier transform. In order to exploit

FFT, received signals in polar coordinates are required to be interpolated into Cartesian coordinates. The interpolation involves two steps; range and azimuthal interpolations.

Munson et al. in 1984 [34] interpreted spotlight-mode SAR as a tomographic reconstruction problem. By use of the projection-slice theorem of computer-aided tomography, ISAR image can be reconstructed using the convolution back-propagation algorithm (CBP) in the case of large rotating angle imaging.

In conventional range-Doppler processing, range resolution and azimuthal resolution can only be enhanced by increasing the effective bandwidth of the transmitted signal and the total rotation angle of the object relative to RLOS, respectively. This course of action may be undesirable in many practical applications of ISAR imaging. An alterative approach for improving the resolution of ISAR image relies on the use of advanced super-resolution signal processing methods. This technique will be used to enhance the elevational resolution in chapter 8.

The maximum entropy method could be used in ISAR imaging [36]. A modified approach which extrapolated the observed data in the forward and backward directions with an auto-regressive (AR) model and performed the FFT processing over the extended data was shown to be robust to model order and noise [37]. Gupta in 1994 [38] employed a two-dimensional linear prediction to get super-resolution ISAR images. Nash [31] and Odentaal et al. [39] applied multiple signal classification (MUSIC) spectral estimation to ISAR imaging. Hua et al. exploited Matrix Pencil (MP) high resolution spectral estimation techniques to produce super-resolution capability of ISAR [40]. Super-resolution imaging was formulated as a least square problem and solved by use of a Hopfield neural network [41].

As an example, ISAR images of Boeing-727 are demonstrated. They were produced by processing simulated data obtained from Naval Research Laboratory (NRL) of U.S.A. through the internet. For the simulated data, a stepped frequency waveform was used. The parameters of simulated data are listed in Table 2.1. Figure 2.6 (a) shows an impressive image of aircraft by compared with the plan view in Figure 2.6 (b). However if ISAR motion compensation is undone, the resulting image will be out of focus as shown in Figure 2.6 (c). Consequently motion compensation plays a key role in ISAR imaging and is discussed below.

Table 2.1 Parameters of simulated ISAR data

Object	Central frequency	PRF	Bandwidth	No. of pulses	No. of range samples
Boeing-727	9 GHz	20 KHz	150 MHz	32	64

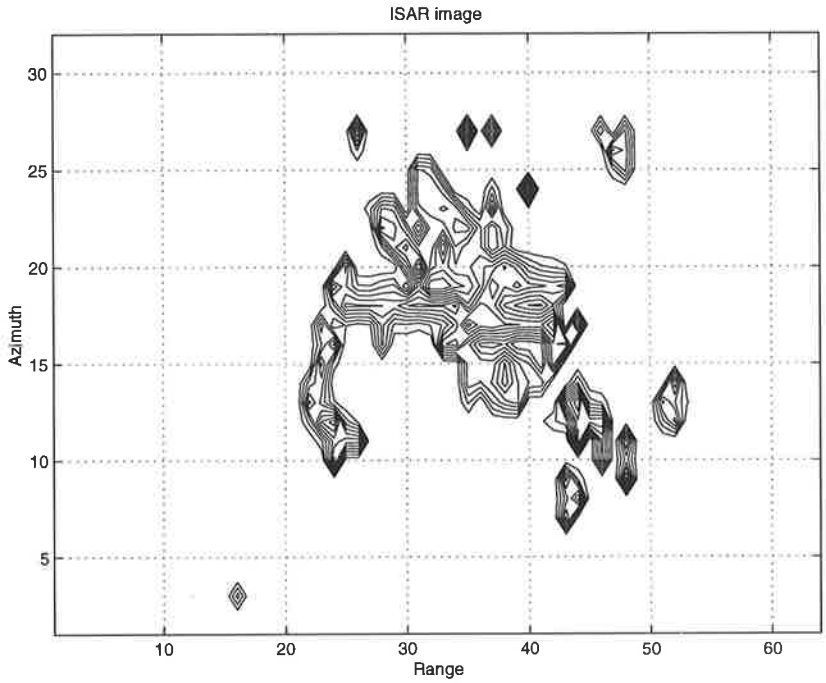

(a) ISAR image of Boeing-727

(b) Plan view of Boeing-727

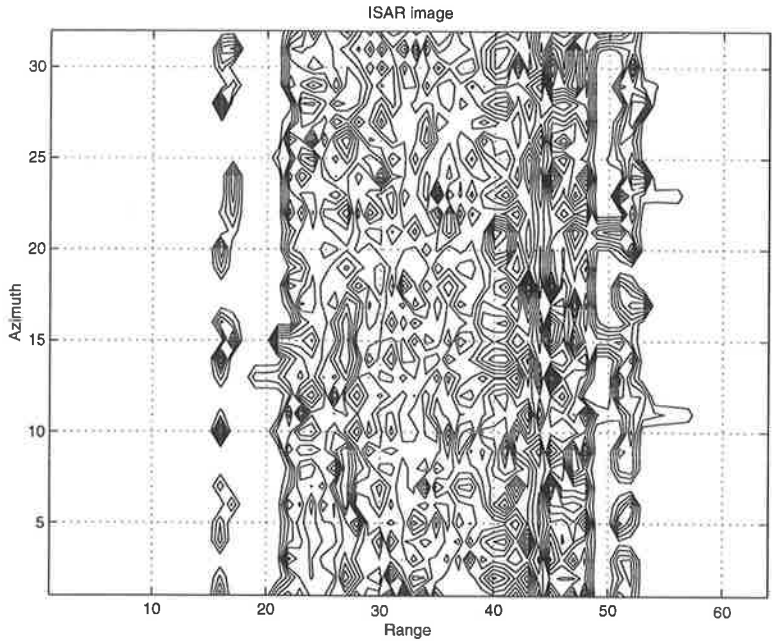

(c) ISAR image of Boeing-727 without motion compensation

Figure 2.6 ISAR images of Boeing-727

2.4 ISAR Motion Compensation

ISAR motion compensation estimates the undesirable translational motion of an object using the echo data and subsequently compensates for it, thus changing ISAR imaging into rotating platform imaging. The accuracy of ISAR motion compensation is usually required to be less than a eighth of wavelength of the transmitted signal. This strict requirement is usually satisfied by carrying out ISAR motion compensation in two steps; range realignment and autofocus (phase compensation).

2.4.1 Range Realignment

After range compression of echo data, a series of high resolution range profiles are obtained. Range walk can occur in these range profiles due to the translational motion of the object between the transmitted pulses. Range realignment aligns the high resolution range profiles in the range direction by placing the returns of different pulses from the same scatterer in the same range cell. It is a coarse compensation of translational motion and can be simply carried out by tracking a strong scatterer of the object in a short interval

[6]. However this approach will be likely to fail when fluctuations of the target return or the level of scintillation noise become too high.

Two automatic algorithms were proposed to realign the echo data[6]. The first, spatial domain realignment, assumes that the amplitudes of adjacent range profiles are similar except for a small range shift due to the tiny change of aspect angle during a pulse repetition interval (PRI). The peak position of cross-correlation between these range profiles is used to estimate this small range shift. The second, frequency domain realignment, supposes that the differences between two adjacent complex range profiles are the shift of range walk and the phase change due to the motion of the target centre. Only the first of these differences needs to be estimated for range alignment and phase correlation in the frequency domain is used to estimate it.

Recently, a Kalman filter has been employed for range realignment [7] [8]. A two or three state Kalman filter was used to provide the filtered estimates of the range shift. The Hough transform was applied to range realignment in clutter environment [9].

2.4.2 Autofocus

After range realignment is accomplished, all range walks in range profiles should be less than half a range resolution cell. The residual error of translational motion is then minimized by phase compensation which is a fine compensation of translational motion. Phase compensation is usually called autofocus with the reference point being termed the focal point. The many ISAR autofocus methods which have appeared are reviewed below.

One simple approach to ISAR autofocus is to choose as the reference point a range cell containing a strong scatterer[10]. The phase exponential function of the reference point in m th range profile can be estimated by

$$\exp\{j\hat{\phi}_m\} = \frac{x_{n_1 m}}{|x_{n_1 m}|} \tag{2.3}$$

where $x_{n_1 m}$ denotes the m th complex range profile resulting from the m th transmitted pulse and n_1 is the reference range cell where the strong scatterer is located. All the range profiles are corrected by the phase factor of the reference point. The reference range cell n_1 can be detected with criteria such as minimal variance [10], maximal average amplitude, minimal entropy or maximal energy [11].

For a complex target that does not have a stable prominent scatterer, an estimate of the pulse-to-pulse phase difference of the reference point can be made by taking the phase differences for each range cell and averaging them weighted by the amplitudes of the content of each range cell[1][3]. An alternative is to average the phase differences of only the range cells which contain a strong scatterer[12][13]. Since both approaches require phase averaging, it is necessary to unwrap the phase.

The other method of autofocus is to estimate the track parameters of translational motion. In a short time interval, the phase due to translational motion can be approximated by

$$\hat{\phi}_m = a_1 (mT)^2 + a_2 (mT) + a_3 \tag{2.4}$$

where T stands for PRI, a_1, a_2 and a_3 are track parameters. The track parameters can be determined by image contrast optimization[14] [15] [16] [17]. Recently the parameters of instantaneous frequency have been estimated via the maximum likelihood principle for ISAR autofocus [18].

Another method based on phase gradient autofocus (PGA) was proposed for SAR phase error correction [19]. It has been used for ISAR autofocus [20] and a two-stage algorithm to find the ML estimator of translational motion has been developed [21].

The range-Doppler principle assumes that object rotates with a constant velocity around a fixed axis. However in practical situations, objects such as aircraft and ships are manoeuvring. Yaw, roll and pitch result in the variations of rotation velocity and rotation axis. The variation of rotation velocity brings about non-uniform rotating ISAR imaging [22] and time-frequency analysis has been used in these situations[23] [24] [25]. The variation of rotation axis will change the image plane of ISAR, consequently blurring the ISAR image[26].

As stated above, many techniques have been proposed for ISAR autofocus. Some of them depend on the existence of strong scatterers. The others need to unwrap the phase to do phase averaging or fitting. Most of them are only verified with simulated data and when applied to real data, some work and some fail.

ISAR autofocus actually eliminates the effect of the undesirable translational motion of object based on the estimated shape of synthesised aperture which is typically a problem of array calibration. Whilst techniques of array calibration have been extensively

developed by the array signal processing community, applying them to ISAR autofocus is a novelty and thus contributes to the theory of ISAR imaging. In this thesis new approaches for ISAR autofocus by use of the calibration techniques of antenna array will be developed and verified with simulated and real data in chapter 3. Their statistical performances will be investigated in chapter 4.

2.5 Interferometric SAR

As discussed above, SAR is a coherent imaging system in which the 2D complex SAR image is an estimate of the complex reflectivity of the terrain. InSAR is a technique for extracting 3D information about target by using the phase content of the 2D complex SAR images as additional information that can be derived from the radar echo data.

Radar interferometry was first used in observation of the surfaces of Venus and the Moon in 1969 [42] and 1972 [43], respectively. Graham in 1974 [44] was the first to introduce InSAR for a topographic mapping and pointed out that two kinds of information were required for the production of topographic map. Firstly, the various objects and features to be mapped must be presented in an image with sufficient resolution to be identified. Secondly, a three-dimensional measurement of position of a sufficient number of points must be made to define the terrain surface. In 1986, Zebker and Goldstein [45] presented the first practical results of observation with a side-looking airborne radar. Goldstein et al. in 1988 [46] extended the research from the airborne images to SEASAT satellite observations. They used data acquired over the Cottonball Basin of Death Valley three days apart and their resulting topographic map agreed very well with the Geological Survey maps.

2.5.1 InSAR Principle

InSAR consists of two antenna receivers P_1 and P_2 as shown in Figure 2.7. The distance between P_1 and P_2 is called the InSAR baseline B_a. P_1 transmits pulse signals. P_1 and P_2 receive the echo data simultaneously for one flight pass. Thus two complex images of the same scene can be obtained by typical SAR signal processing.

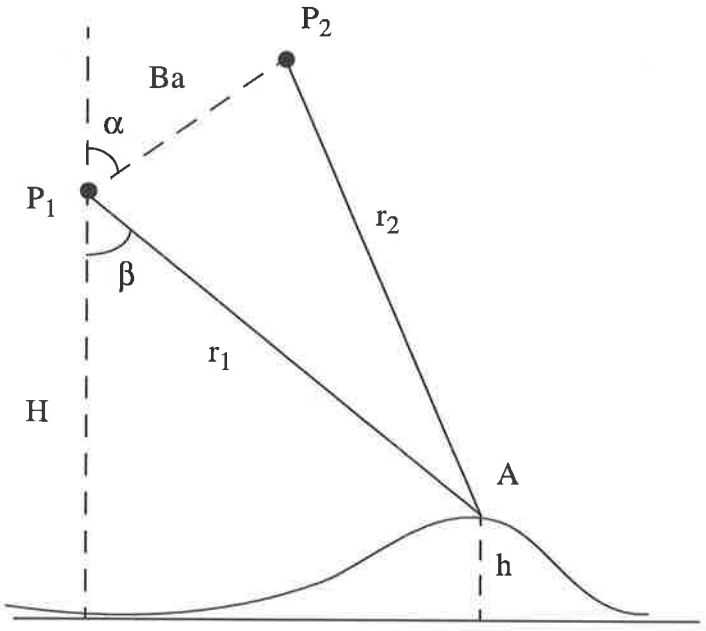

Figure 2.7 InSAR geometry

The phase difference φ of returned signals between P_1 and P_2 corresponding to a given scene scatterer A will be expressed as

$$\varphi = \frac{2\pi}{\lambda}(r_2 - r_1) = \frac{2\pi}{\lambda}\left[\left(r_1^2 + {B_a}^2 + 2r_1 B_a \cos(\beta + \alpha)\right)^{\frac{1}{2}} - r_1\right] \tag{2.5}$$

where r_1 and r_2 are the distances of A with respect to P_1 and P_2, respectively. The parameters that are measured by the radar or are assumed known are r_1, H (platform height), B_a, α (baseline orientation), λ (wavelength) and φ (though it is modulo 2π). Hence r_2, β (incidence angle) and h (terrain height) can be calculated from the relations

$$r_2 = r_1 + \frac{\varphi\lambda}{2\pi}, \tag{2.6}$$

$$\beta = arc\cos\left(\frac{r_2^2 - {B_a}^2 - r_1^2}{2B_a r_1}\right) - \alpha \tag{2.7}$$

and

$$h = H - r_1 \cos\beta. \tag{2.8}$$

Thus the terrain height h, of a given pixel, can be obtained from the measured interferometric phase φ. Doing this over the whole image allows a three-dimensional version of the target scene to be obtained at the same image resolution as the original two-dimensional SAR images.

Use of a two-antenna system is one way to realize an InSAR system[44]. In this system, a single data collection pass provides the necessary two-channel data in a controlled fashion. This single-pass approach provides InSAR data without pass-to-pass alignment problems and without the possibility of temporal changes in terrain inherent in a two-pass system. However the two-antenna system requires a second antenna and must handle twice the data recording rates in order to simultaneously collect the two data streams. Typically, radome and antenna sizes limit the baseline length of a two-antenna system.

Another way to collect InSAR data is to make two sensor collection passes with a single antenna system[48]. This approach is known as two pass InSAR. With two pass InSAR, the φ in (2.5) is doubled due to two-way propagation. An advantage of this two-pass single-antenna system is that an existing single-channel SAR sensor can collect InSAR data without modification. However this technique requires a stable high-performance navigation subsystem. This subsystem ensures that the two data collection passes have accurately known and nearly identical data collection geometries with the necessary baseline separation. A significant disadvantage of this approach is that changes in terrain condition between passes affect the InSAR phase measurements and ultimately contaminate the terrain height measurement.

When the InSAR baseline B_a is perpendicular to the flight direction, it is called across-track InSAR and can be used to measure the terrain height as described above. It will be addressed in this thesis. If the baseline is parallel to flight direction, it is called along-track InSAR which may be used to measure the scene movement such as the mapping of water currents[100], the detection of moving objects[202][203] and the measurement of directional wave spectra [204].

Differential InSAR has been used for the measurement of small-scale movements in vertical direction and provides a relative accuracy of the order of a few centimetres or even less. The theory of differential InSAR was firstly described by Gabriel et al. in 1988 [131]. It has been used to measure distortions of earth crust due to earthquake [132] and volcano eruptions [133] and to detect small changes in ice sheet motion [134].

For topographic mapping, the InSAR signal processing procedure is shown in Figure 2.8. The two SAR images should be processed with the same Doppler parameters to preserve the coherence of two images. After image registration, the interferogram can be formed by multiplying one registrated image with the conjugate of the other. Then the absolute phase is restored by a two-dimensional phase unwrapping procedure. Finally the terrain elevation can be calculated with (2.5) - (2.8). The critical steps of InSAR signal processing are image registration and phase unwrapping which will be discussed in section 2.6 and section 2.7, respectively.

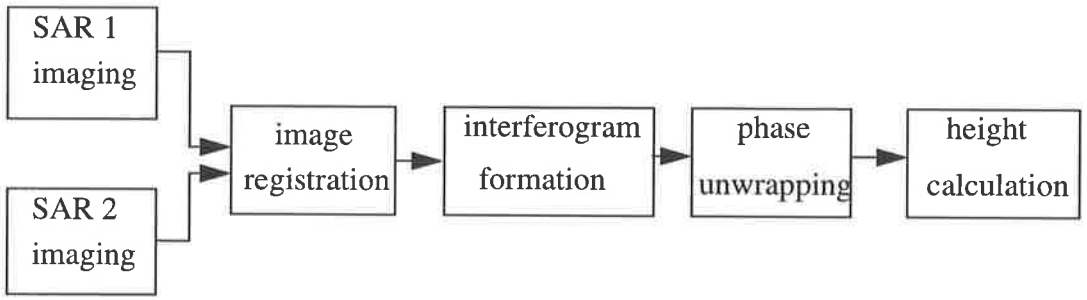

Figure 2.8 InSAR signal processing procedure

Computer simulation of interferograms for flat terrain were conducted. In the simulation, the altitude of satellite was 785 km, baseline 40 m, incidence angle 23^o, and radar wavelength 5.67 cm. Figure 2.9 shows the resulting interferogram. The real data acquired by the first European Remote Sensing satellite (ERS-1) over the area of Bonn, Germany with three-day repeat pass were processed. The interferogram is shown in Figure 2.10 where the radar wavelength is 5.67 cm and the baseline is about 45 m. The fringes in Figure 2.9 are more distinct than those in Figure 2.10. This is due to the limited SNR of real data and the urban terrain of ERS-1 experimental area.

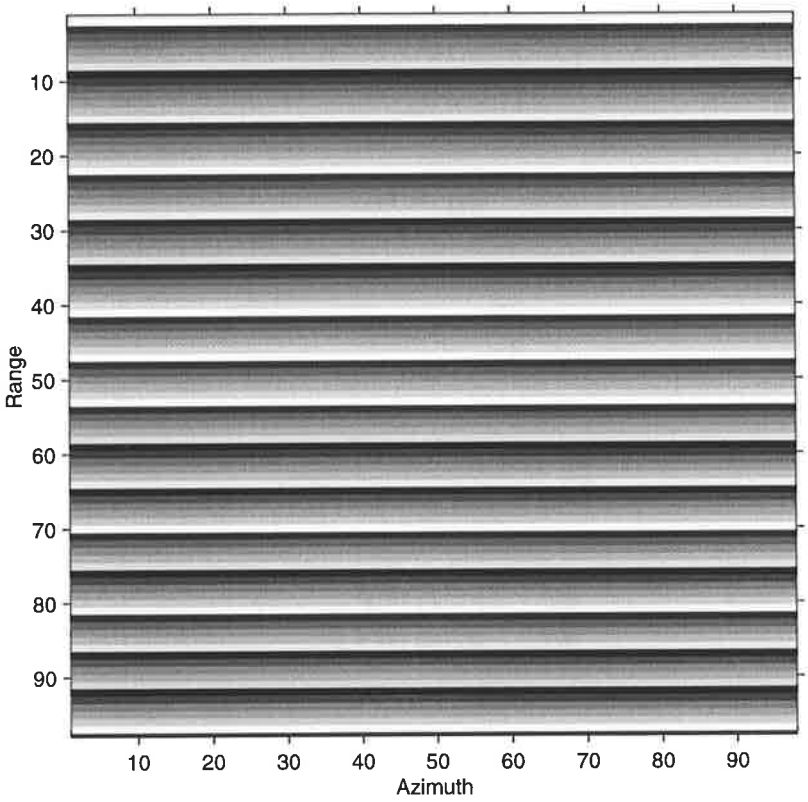

Figure 2.9 Simulated interferogram of flat terrain

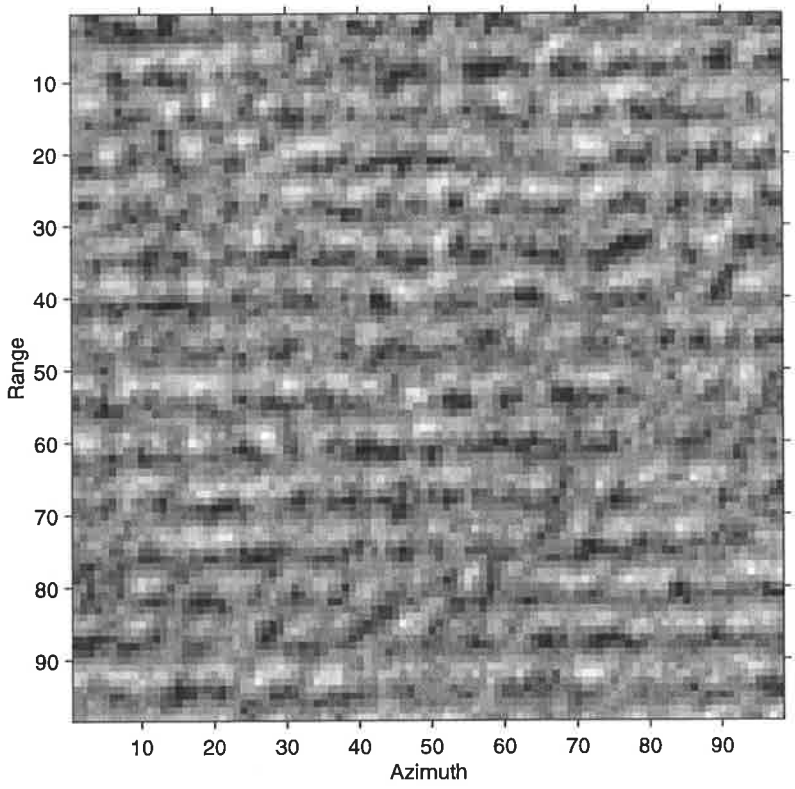

Figure 2.10 Interferogram of ERS-1 data

2.5.2 InSAR Error Analysis

Differentiation of (2.8) with respect to H, r_1, φ, B_a, α and λ then allows the height error to be found as follows

$$\frac{\partial h}{\partial H} = 1, \tag{2.9}$$

$$\frac{\partial h}{\partial r_1} = -\cos\beta, \tag{2.10}$$

$$\frac{\partial h}{\partial \varphi} = -\frac{\lambda r_1 \sin\beta}{2\pi B_a \sin(\alpha+\beta)}, \tag{2.11}$$

$$\frac{\partial h}{\partial B_a} = \frac{r_1 \sin\beta}{B_a \tan(\alpha+\beta)}, \tag{2.12}$$

$$\frac{\partial h}{\partial \alpha} = -r_1 \sin\beta, \tag{2.13}$$

$$\frac{\partial h}{\partial \lambda} = -\frac{r_1 \sin\beta}{\lambda \tan(\alpha+\beta)}. \tag{2.14}$$

(2.11), (2.12) and (2.13) show that the estimated height is a sensitive function of phase difference φ, baseline B_a and baseline orientation α. This means that precise measurements of phase difference and baseline are required for accurate topographic mapping.

The phase differences that form the interferogram may be corrupted by phase noise, firstly due to the finite signal-to-noise ratio in each of the two images, and secondly due to the temporal decorrelation, and finally due to the baseline decorrelation. The temporal decorrelation results from the variation of reflectivity of terrain between the two flight passes[47]. Both nature and humans can significantly alter the terrain through processes such as precipitation from rainfall or irrigation, wind, plant growth, clearing, construction, and vehicle incursions. Similarly, tropospheric propagation changes related to weather change can contribute to temporal decorrelation. The baseline decorrelation is due to the change of looking angle between two passes and increases with baseline increase. The critical baseline is the baseline length when statistical correlation between images of two

flight passes approaches to zero [48] [49]. The baseline decorrelation is explained by the spectral shift of echo data of two flight passes [50] [51].

The interferogram also suffers from shadowing or layover. Shadowing occurs when part of the target scene is invisible to the radar and the corresponding parts of the image consist of noise. Layover happens when there are two targets located in the same slant range cell. The signals from those targets are superimposed.

An effective approach to reduce InSAR error is to make use of multiple flight passes. This will be discussed in chapter 5.

2.6 Image Registration

Image registration is the first step of InSAR processing. It estimates the shifts of two SAR images in range and azimuth so that an image pair is accurately aligned. The existing methods of image registration are classified as spatial processing and frequency processing.

Spatial processing includes correlation [52], sequential similarity detection [53], and matched filtering [54]. Two-dimensional correlation is a basic statistical approach used in image registration. The correlation measure is defined as

$$C_{r1}(\Delta x, \Delta y) = \sum_x \sum_y A_1(x, y) A_2(x + \Delta x, y + \Delta y) \tag{2.15}$$

where $A_1(x, y)$ and $A_2(x, y)$ represent the amplitudes of two SAR images and the normalized correlation measure is expressed as

$$C_{r2}(\Delta x, \Delta y) = \frac{\sum_x \sum_y [A_1(x, y) - \bar{A}_1][A_2(x + \Delta x, y + \Delta y) - \bar{A}_2]}{\sqrt{\sum_x \sum_y [A_1(x, y) - \bar{A}_1]^2} \sqrt{\sum_x \sum_y [A_2(x, y) - \bar{A}_2]^2}} \tag{2.16}$$

where $\bar{A}_1 = \frac{1}{N_x N_y} \sum_x \sum_y A_1(x, y)$, $\bar{A}_2 = \frac{1}{N_x N_y} \sum_x \sum_y A_2(x, y)$ and (x, y) are indices in an $N_x \times N_y$ point window area which is located within an $N_{sx} \times N_{sy}$ point search area. Figure 2.11 illustrates the relationship between the search area and the window area. In general, the correlation need be computed for all $(N_{sx} - N_x + 1)(N_{sy} - N_y + 1)$ possible translations

of the window area within the search area to determine its maximal value and obtain a translational estimate.

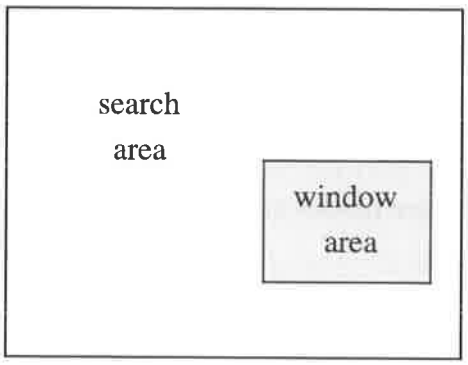

Figure 2.11 Relationship between search and window areas

Rotational and scaling search processes must be carried out in addition to translational search if the angular and scale differences are severe. This costly search procedure can be simplified if some control points are available to determine the scale factor and rotation initially. The scale factor and rotation are then updated from the translational correlation results. The correlation can be calculated efficiently with the FFT [52].

The second method of spatial processing is to compute the sum of the absolute differences between two images at each pixel, i.e.,

$$D_1(\Delta x, \Delta y) = \sum_x \sum_y \left| A_1(x, y) - A_2(x + \Delta x, y + \Delta y) \right| \tag{2.17}$$

or the normalized measure which is defined as

$$D_2(\Delta x, \Delta y) = \sum_x \sum_y \left| A_1(x, y) - \overline{A_1} - A_2(x + \Delta x, y + \Delta y) + \overline{A_2} \right|. \tag{2.18}$$

These measures decrease with the degree of similarity; the difference being smallest when two aligned images are most similar. A far more efficient improvement of this method is a sequential search strategy. For each window of the image, one of the similarity measures defined above is accumulated until the threshold is exceeded. For each window the number of points that are examined before the threshold is exceeded is recorded. The window which examines the most points is assumed to have the lowest measure and is

therefore the best registration. This search strategy is actually a fast implementation of the correlation approach.

The third method of spatial processing is to filter the images prior to correlation. If the image is noisy, the peak of the correlation may not be discernible. In such cases, the images should be prefiltered before correlation. The prefilter can be determined if the noise in the image satisfies certain statistical properties. Techniques which prefilter based on the properties of the noise of the image in order to maximize the peak correlation with respect to this noise are called matched filter techniques. Under certain assumptions, the prefilter is a Laplacian filter or a gradient filter.

Frequency processing searches for the registration parameters in the frequency domain. One method of frequency processing is phase correlation [55]. Given two intensity images A_1 and A_2 with displacement $(\Delta x, \Delta y)$, i.e.,

$$A_2(x, y) = A_1(x - \Delta x, y - \Delta y), \tag{2.19}$$

their corresponding Fourier transforms $S_1(q_x, q_y)$ and $S_2(q_x, q_y)$ are related by

$$S_2(q_x, q_y) = S_1(q_x, q_y) \exp\{-j2\pi(\Delta x q_x + \Delta y q_y)\}. \tag{2.20}$$

The phase of the cross-power spectrum of the two images is

$$\frac{S_2(q_x, q_y) S_1^*(q_x, q_y)}{\left|S_2(q_x, q_y) S_1^*(q_x, q_y)\right|} = \exp\{-j2\pi(\Delta x q_x + \Delta y q_y)\}. \tag{2.21}$$

By taking the inverse Fourier transform of (2.21), we will have a function which is approximately zero everywhere except at the displacement which is needed to optimally register the two images. The other method of frequency processing makes use of the power cepstrum of image. This method is cumbersome to describe and details are available [56].

Spatial and frequency processings are both only applicable for image misregistration with global geometric transformations. In other words, they are suitable to register small images. In order to register large images with local geometric transformation, control point mapping or elastic matching techniques need to be used [57].

Recently a number of studies on SAR image registration have been reported. Gabriel and Goldstein in 1988 [58] removed the effect of small path pitch by resampling the image in

the range direction. Image registration was implemented by finding spectral signal-to-noise ratio of interference fringes and searching for the existence of maximal peak in the power spectrum of the fringe. When the corresponding pixels are matched most closely, the fringes of interferogram are most distinct and strongest. If misalignments exist, the fringe patterns are noiser and the power spectrum is smoother. Li and Goldstein in 1990 [48] used a statistical correlation of two amplitude images to determine the range and azimuth pixel offset of any two images. The relative correlation coefficients between two images at various offsets in range and azimuth were calculated. The offset that produced maximum correlation was obtained by fitting the correlation coefficients over the discrete pixel offsets. Lin et al. in 1992 [59] defined an average fluctuation function of phase difference image on large areas in the interferogram and minimised its values by subpixel shifting in range and azimuth and scaling in range of the two images. In a recent paper[60], Fornaro and Franceschetti developed a new image registration procedure implemented at the raw data processing stage. The two complex SAR images were generated with respect to a common reference output system. The registration was achieved via a scaling and shifting compensation that can be efficiently and easily included in a standard SAR processing code. Homer et al. applied the technique of sign change of subtraction image to SAR image registration[61]. Determination of the optimal parameter associated with image variation was described.

All the methods described above deal with a pair of SAR images. Multiple image registration will be investigated in chapter 6.

2.7 Phase Unwrapping

The difference phase of two registrated images, which is directly related to the topography, is only measured modulo 2π. In order to reconstruct the height unambiguously, it is necessary to add the appropriate number of cycles of phase, which is known as phase unwrapping.

The adaptive integration method of phase derivative for one-dimensional phase unwrapping was proposed by Tribolet[62]. This can be understood by reference to Figure 2.12(a) which shows a one-dimensional sequence of phase values. The cycle is 1. If we make the assumption that adjacent phase values can not differ by more than half a cycle, it

is clear from Figure 2.12(a) that to unwrap the phase, one cycle needs to be added to the last three values as shown in Figure 2.12(b).

0.5 0.6 0.7 0.8 0.9 0.0 0.1 0.2	0.5 0.6 0.7 0.8 0.9 1.0 1.1 1.2
(a) Wrapped phase values	(b) Unwrapped phase values

Figure 2.12 One-dimensional phase unwrapping

One of the most successful approach to two-dimensional phase unwrapping was based on identifying and linking a so-called residue[46]. In the case of two-dimensional phase unwrapping, the consistency of the phase progression around each closed cycle of four phase values is evaluated, under the same assumption that adjacent values can not differ by more than half a cycle. In most cases the phase progression is consistent. But occasionally this is not the case, leading to a positive or negative inconsistency. These inconsistencies are named residues. The steps of one method for two-dimensional phase unwrapping, known as the path-following method, includes residue identification, branch cut determination and phase unwrapping. Figure 2.13 shows an example of two-dimensional phase unwrapping with the cycle equal to 1: (a) the original phase values, (b) the residue value matrix, and (c) the result of phase unwrapping where the adjacent phase is consistent except in the region of branch cut (solid line).

0.6 0.7 0.1 0.3 0.7 0.7 0.8 0.2 0.4 0.8 0.6 0.7 0.3 0.1 0.4 0.5 0.6 0.4 0.7 0.1 0.6 0.7 0.6 0.3 0.7	0 0 0 0 0 +1 0 0 0 0 -1 0 0 0 0 0	0.6 0.7 1.1 1.3 1.7 0.7 0.8 1.2 1.4 1.8 0.6 0.7 0.3 1.1 1.4 0.5 0.6 0.4 0.7 1.1 0.6 0.7 0.6 0.3 0.7
(a) Wrapped phase values	(b) Residue values	(c) Unwrapped phase values

Figure 2.13 Two-dimensional phase unwrapping

Various approaches to two-dimensional phase unwrapping have been developed which are classified as path-following and least-square estimation. Prati et al. in 1990 [63] presented a modified path-following method by exploiting the information of phase and amplitude

of InSAR image. Lin et al. in 1992 [59] developed a phase unwrapping approach by detecting the fringe lines in the phase difference image with edge detection techniques. Gollaro et al. in 1998 [76] introduced a statistical approach to phase unwrapping by searching the phase integration path with a genetic algorithm. Xu and Cumming in 1999 developed an algorithm for determining the phase integration path by use of region-growing technique[135]. The concept of multiresolution for phase unwrapping was introduced by Davidson and Bamler in 1999 [136].

The least-square method of phase unwrapping was firstly described by Hunt in 1979 [64]. Takajo and Takahashi in 1988 [66] gave a new least-squares phase estimation. Fornaro et al. in 1996 [74] employed the Green's first identity to do two-dimensional phase unwrapping. They presented a new algorithm for InSAR phase unwrapping based on the finite element method in 1997 [75]. Network programming was proposed for two-dimensional phase unwrapping in 1998[231]. Other techniques of the least-square method are available [67]-[73].

Although many papers on phase unwrapping have appeared, phase unwrapping is still an area of active research. There remain a host of theoretical as well as practical issues that are not totally resolved by any present phase unwrapping methodology. Even if this thesis does not address phase unwrapping, it is suggested for further research.

2.8 Array Processing Fundamentals[2]

Considering sensor arrays immersed in the far-field of a sinusoidal wave with amplitude $b_k(t)$ and carrier frequency ω impinging the array from direction θ_k, the sensor converts the signals in the medium to electrical signals. If t is time and (x_m, y_m) are the coordinates of m th sensor, then the field at the m th sensor $z_m(t)$ can be represented by [2]

$$z_m(t) = b_k(t) \exp\{j\omega t - j\frac{2\pi}{\lambda}(x_m \cos\theta_k + y_m \sin\theta_k)\}. \quad (2.22)$$

Dropping the carrier term for baseband processing, the output of the m th sensor is modelled by

$$z_m(t) = b_k(t) \exp\{-j\frac{2\pi}{\lambda}(x_m \cos\theta_k + y_m \sin\theta_k)\} = b_k(t)\, a_m(\theta_k). \quad (2.23)$$

For an M element array, the vector of the array output is expressed as

$$Z(t) = b_k(t)\, a(\theta_k) \tag{2.24}$$

where $Z(t) = [z_1(t), \ldots, z_M(t)]^T$ and $a(\theta_k) = [a_1(\theta_k), \ldots, a_M(\theta_k)]^T$. If K signals impinge on the array from directions $\theta_1, \ldots, \theta_K$, the output vector takes the form

$$Z(t) = \sum_{k=1}^{K} b_k(t)\, a(\theta_k) . \tag{2.25}$$

In the presence of an additive (baseband) noise $W(t)$, we get the model commonly used in array processing

$$Z(t) = A(\theta) S(t) + W(t) \tag{2.26}$$

where $A(\theta) = [a(\theta_1), \ldots, a(\theta_K)]$ and $S(t) = [b_1(t), \ldots, b_K(t)]^T$.

Assuming that the incident signals are uncorrelated with the receiver noise, the covariance matrix of $Z(t)$ is

$$C_x = \mathrm{E}\{Z(t) Z^H(t)\} = A C_s A^H + C_w \tag{2.27}$$

where $\mathrm{E}\{\ \}$ denotes ensemble average, $C_s = \mathrm{E}\{S(t) S^H(t)\}$ is the covariance matrix of signal sources, and $C_w = \mathrm{E}\{W(t) W^H(t)\}$ is the covariance matrix of the noise. When the environment consists of K uncorrelated directional sources and uncorrelated white noise, we have

$$C_s = \mathrm{diag}\,[p_1, \ldots, p_K] \tag{2.28}$$

and

$$C_w = \sigma_w^2 I \tag{2.29}$$

where p_i is the power of each source and σ_w^2 is the variance of white noise.

Based on (2.27), C_x is Hermitian symmetrical and positive definite. The eigenvalues of C_x in descending order are always positive numbers, that is,

$$\lambda_1 \geq \lambda_2 \geq \ldots \geq \lambda_M > 0 \tag{2.30}$$

and the corresponding eigenvectors u_i i=1,..., M are orthogonal, that is,

$$u_i^H u_j = \delta_{ij}. \tag{2.31}$$

The eigen space decomposition of C_x can be expressed by

$$C_x = U\Lambda U^H \tag{2.32}$$

where $U = (u_1, \ldots, u_M)$ and $\Lambda = \text{diag}(\lambda_1, \ldots, \lambda_M)$. By virture of the orthogonality of the eigenvectors, the space of receiver outputs can be decomposed into signal subspace and noise subspace.

Assuming that the number of sensors is larger than that of sources signals, that is, $M > K$, the eigenvalues and eigenvectors of C_x can be divided into two sets. The number of eigenvalues in the first set is equal to the number of these sources and their values are larger than the power of the white noise; that is,

$$\lambda_1 \geq \lambda_2 \geq \ldots \geq \lambda_K > \sigma_w^2. \tag{2.33}$$

These eigenvalues are referred to as the signal eigenvalues. The range space of A, which is called the signal subspace, is spanned by the corresponding eigenvectors.

The eigenvalues in the second set are of equal value. They are independent of the directional sources and equal to the power of the white noise. These eigenvalues are referred to as noise eigenvalues. The number of noise eigenvalues is $M - K$; that is,

$$\lambda_{K+1} = \ldots = \lambda_M = \sigma_w^2. \tag{2.34}$$

The corresponding eigenvectors belonging to the second set span the null space of A^H which is called noise subspace.

Hence the space of receiver outputs can be decomposed into the direct sum of the signal subspace $S_s = \text{span}\{a(\theta_1, \phi_1), \ldots, a(\theta_K, \phi_K)\} = \text{span}\{u_1, \ldots, u_K\}$ and the noise subspace $S_n = \text{span}\{u_{K+1}, \ldots, u_M\}$. The covariance matrix is decomposed into

$$C_x = U_s \Lambda_s U_s^H + U_n \Lambda_n U_n^H \tag{2.35}$$

where $\Lambda_s = \text{diag}(\lambda_1, \ldots, \lambda_K)$, $U_s = (u_1, \ldots, u_K)$, $\Lambda_n = \text{diag}(\lambda_{K+1}, \ldots, \lambda_M)$ and $U_n = (u_{K+1}, \ldots, u_M)$. The projection matrices onto the signal and noise subspaces are expressed as

$$P_{rs} = U_s U_s^H = A(A^H A)^{-1} A^H \tag{2.36}$$

$$P_{rn} = U_n U_n^H = I - A(A^H A)^{-1} A^H \tag{2.37}$$

respectively. It can be shown that $P_{rs}^2 = P_{rs}$, $P_{rn}^2 = P_{rn}$, and $P_{rs} + P_{rn} = I$.

Thus far it has been assumed that the exact covariance matrix is known. However in practice the covariance matrix needs to be estimated from a finite number of snapshots N_t, and is usually estimated as

$$\hat{C}_x = \frac{1}{N_t} \sum_{t=1}^{N_t} Z(t) Z^H(t) . \tag{2.38}$$

The eigendecomposition of $\hat{C}_x$ is given by

$$\hat{C}_x = \hat{U}_s \hat{\Lambda}_s \hat{U}_s^H + \hat{U}_n \hat{\Lambda}_n \hat{U}_n^H \tag{2.39}$$

where $\hat{\Lambda}_s$ and $\hat{\Lambda}_n$ are the estimated eigenvalues of signal and noise subspace. $\hat{U}_s$ and $\hat{U}_n$ are the corresponding estimated eigenvectors. It is noted that the number of signal sources K is supposed to be known before localisation of signal sources can be conducted. Techniques for estimating K are available in the literature [103].

2.8.1 Beamforming Methods

Propagating signals in space (wavefronts) contain much information about the sources that produce them and their temporal and spatial characteristics allow us to estimate the source locations. However other sources in addition to the one of interest usually exist in the real world and noise always contaminates measured signals. Thus the required signal processing is to enhance desired signals and attenuate other signals. One means of enhancement is linear spatial filtering. For propagating signals, temporal and spatial filters are employed to separate signals according to their frequency content and their directions of propagation, respectively. Temporal filtering can be accomplished with a single sensor

but spatial filtering requires an array of sensors which spatially samples the propagation field.

The term beamforming [2] [117] refers to a spatial filter designed to constructively reinforce a signal radiating from a specific direction and suppress signals from other directions. Beamforming algorithms use constructive interference to focus the array's spatial filter toward desired directions algorithmically rather than physically. In this thesis, the beamforming by phase shifting narrow-band receiver outputs is considered. The conventional beamforming output of the phase shift beamformer is expressed as

$$y(t,\theta) = \frac{1}{M} v^{H}(\theta) Z(t) \tag{2.40}$$

where $v(\theta) = [v_1(\theta), \ldots, v_M(\theta)]^T$ is the vector of weights (the steering complex vector) for forming a beam in direction θ, $v_i(\theta) = \exp\{j\frac{2\pi(i-1)d_l \sin\theta}{\lambda}\}$, θ the steering direction and d_l the element space of an equispaced linear array. If $Z(t)$ is a vector of random variables, it follows that $y(t,\theta)$ is a random function. The mean output power of the beam steered in direction θ is then given by

$$P_c(\theta) = E\{|y(t,\theta)|^2\} = \frac{1}{M^2} v^H(\theta) C_x v(\theta). \tag{2.41}$$

This conventional beamformer may be viewed as a spatial matched filter when the spatial noise is white.

The optimum beamformer has weights that optimize the signal processing in some way. For example, minimum power with constraint (MPWC) beamformer minimises the output power of the beamformer subject to the constraint that the output due to a signal from a chosen steering θ_0 is held constant. Other optimum processors[2] have been proposed with different criteria for optimization such as maximum array gain (MAG), maximum likelihood (ML) criterion and minimum mean-square error (MMSE). The weights for these optimum beamformers are listed in Table 2.2 where p is a scaling factor and r_{xd} is the correlation coefficient between the desired signal and the array output.

Table 2.2 Weights for optimum beamformers

Type	MAG	ML	MPWC	MMSE
Weights	$pC_w^{-1}v(\theta_0)$	$C_w^{-1}v(\theta_0)/(v^H(\theta_0)C_w^{-1}v(\theta_0))$	$C_x^{-1}v(\theta_0)/(v^H(\theta_0)C_x^{-1}v(\theta_0))$	$C_x^{-1}r_{xd}$

2.8.2 Subspace Methods

Subspace methods have been used successfully in array processing to estimate the directions of arrival (DoA) of plane wave signals incident upon a sensor array [85]. They are a natural extension of beamforming approaches and utilise geometric properties of an assumed plane wave model to provide a formal analytic framework for further theoretical development and a computational framework for the practical applications. The covariance matrix plays a key role in defining the subspaces of interest. Subspace methods have a theoretical resolution that is not limited by the aperture of the array, or the SNR. They originated from Pisarenko's method [129]. The popular multiple signal classification (MUSIC) [104] approach is

$$P_{MUSIC}(\theta) = \frac{1}{a^H(\theta)\,\hat{U}_n\hat{U}_n^H a(\theta)}. \tag{2.42}$$

where $\hat{U}_n$ are the eigenvectors defined in (2.39). MUSIC will be used to enhance the elevational imaging in chapter 8. Other methods such as estimation of signal parameters via rotational invariance techniques (ESPRIT) [118] and weighted subspace fitting (WSF)[119] have been developed.

2.8.3 Array Calibration

The problem of array calibration has been considered in various fields. Examples of array calibration application are in telescopes [122], radio cameras [123], sonar towed arrays [86], synthetic aperture sonar [124], over-the-horizon radar [125], space-time adaptive processing (STAP) [126], ultrasound arrays [127] and magnetic resonance imaging [128]. Many techniques have been developed for array calibration and they may be classified as active or passive methods. The active ones make use of sources in known directions [120]. The most common passive method is to utilize other assisted measurements. However it is subject to the accuracy limitation of measurement devices. Appealing passive methods are

the data-driven techniques which includes sharpness[122], closure phase[142], beamforming[143] and subspace methods[86]. The sharpness and closure phase methods were used successfully in radio astronomy. The beamforming and subspace approaches have been applied to towed sonar array shape estimation. They will be employed for ISAR autofocus and phase correction of MPSAR in later chapters.

2.9 Summary

This chapter introduced many important concepts that are to be used throughout the thesis. We began with a simplified description of the SAR system block diagram. The range resolution is obtained by transmitting wideband signals. The azimuthal resolution is achieved by synthesising the aperture introduced by the motion of the radar.

Then ISAR was introduced. The range resolution relies on the bandwidth of transmitted signals and the azimuthal resolution is determined by the rotation angle of object relative to RLOS. Examples of ISAR images of Boeing-727 were demonstrated by processing simulated data of NRL and illustrated the importance of motion compensation in the image formation steps of ISAR processing. Existing techniques of ISAR image formation and motion compensation methods were discussed in detail and autofocus was identified as the topic to be further researched in later chapters.

Next the principle of InSAR was described. It is based on the coherence of SAR images and calculates the elevation of terrain with the unwrapped phase of interferogram. Examples of interferograms were shown by processing simulated and real data. Image registration and phase unwrapping are the critical issues of InSAR processing. They were reviewed in detail and image registration was identified as an important topic to be studied for MPSAR. Although phase unwrapping is obviated in MPSAR processing as described in chapter 5, it is still not yet solved thoroughly and is recommended for further development.

Finally the techniques for array processing were highlighted. They included beamforming, subspace methods and array calibration. They are employed in this thesis for calibrating ISAR and MPSAR.

Chapter 3 Array Processing Approaches for ISAR Autofocus

3.1 Introduction

The use of an array of sensors allows many advantages over the use of single sensor. Array processing approaches including beamforming and subspace methods have been used for sensor arrays in many fields such as radar [111], sonar [112], seismic exploration [113], biomedical imaging [114], wireless communications [115], radio astronomy [116] and laser [159] to detect weak signals, to resolve closely-spaced targets and to estimate the bearing and other properties of a signal source. Beamforming involves the steering of a beam to obtain a spatial spectrum from which the signal bearings can be estimated and provides gain for the detection of weak signals. Subspace methods make use of the eigenstructure of the covariance matrix of received signals and its properties. They are based on the fact that the signal subspace intersects the array manifold at locations corresponding to the direction of signals. This chapter describes how to apply conventional beamforming, optimum beamforming, signal subspace and noise subspace methods to ISAR autofocus.

Section 3.2 derives a signal model of ISAR autofocus by use of a point scatterer model. Two new approaches for ISAR autofocus are developed in section 3.3 based on maximizing the output powers of conventional and optimum beamformers. Section 3.4 presents two new approaches for ISAR autofocus by use of the signal and noise subspaces. A subaperture processing scheme is described in section 3.5. Simulated data and real data are processed for both one-dimensional and two-dimensional ISAR imaging in section 3.6 and section 3.7, respectively.

3.2 Signal Model of ISAR Autofocus

When an object such as an aircraft is illuminated by a radar, the backscattered radiation may be determined from Maxwell's equations. However the exact solutions of Maxwell's equations are often too sophisticated to use for complex objects and the backscatter from a complex object is determined using the principles of specular, diffractive, multiple or travelling wave scatterings[80]. Travelling wave scattering is significant only when the wavelength of the incident radiation is similar to the object size which is not the case for the microwave frequencies considered here. Multiple scattering is caused by cavity structures of an object and is a weak part of backscatter which is only important in some specific applications such as radar target classification. Normally specular scattering and diffractive scattering account for the majority of backscatter from aircraft, with the former usually being much larger in amplitude than the latter. Therefore it is usually a good approximation to only consider the specular scattering.

For a distributed target, we define $\rho(x, y)\, dx\, dy$ to be the overall reflectivity of the differential area located at (x, y) on the object where, for convenience, $\rho(x, y)$ includes propagation effects and other gains. The received signal due to this differential area is

$$ds_{lm}(x, y) = \rho(x, y) \exp\{-j\frac{4\pi}{c} f_l r(x, y)\}\, dx\, dy \tag{3.1}$$

where $r(x, y)$ is the distance from the radar to (x, y) when lth frequency signal f_l of the mth pulse is sent. By combining the received contribution from all parts of the object, the total received signal becomes

$$s_{lm} = \iint \rho(x, y) \exp\{-j\frac{4\pi}{c} f_l r(x, y)\}\, dx\, dy \tag{3.2}$$

where the integration is taken over the region occupied by the object.

For a complex object, $\rho(x, y)$ is actually a function of aspect angle due to shadowing and other effects and is also dependent on the frequency of the transmitted signal. Nevertheless for ease of analysis, it is assumed that $\rho(x, y)$ in (3.2) is independent of the illuminating frequency and aspect angle. These assumptions are quite accurate for ISAR because the object is viewed over a narrow range of viewing angles and a small relative bandwidth (the ratio of bandwidth to centre frequency) is used.

In principle, an exact representation of (3.2) implies an infinite number of point scatterers. However, since noise and system imperfections prevent making exact measurements, the approximation of an object by a finite and manageable number of point scatterers plus noise may be entirely adequate for microwave frequency [81]. Therefore the discrete version of (3.2) can be written as

$$s_{lm} = \sum_k \rho_k \exp\{-j\frac{4\pi}{c} f_l r_{km}\} + w_{lm} \tag{3.3}$$

where w_{lm} is an additive noise in frequency domain.

Suppose that a moving object is flying in a straight line ox as shown in Figure 3.1. The motion of a rigid object can be decomposed into two parts: translational motion of a certain reference point o on the object and rotational motion of the object about the point o. Let the Cartesian coordinates xoy be fixed on the object with range along the y-axis and cross-range along the x-axis when the object is at its closest point of approach to the radar. The radar transmits M stepped-frequency bursts. The aspect angle of the object relative to the RLOS and the distance from the radar to the point o when the m th burst is sent are represented by θ_m and R_{om}, respectively, where $m = 0, \ldots, M-1$.

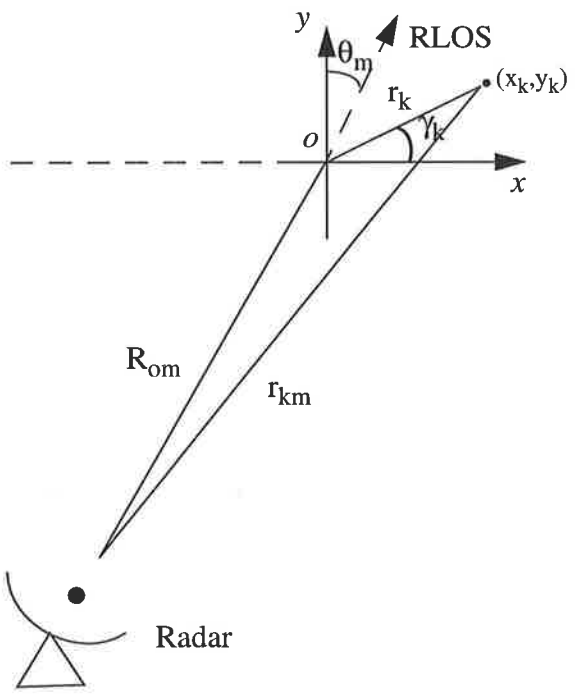

Figure 3.1 ISAR imaging geometry

Assume that the received signals can be approximated by using K scatterers on the object. The k th scatterer is situated at a distance r_{km} from the radar when the m th burst is sent. The range between radar and the k th scatterer with coordinate (r_k, γ_k) or (x_k, y_k) as shown in Figure 3.1 is given by

$$r_{km} = \left[R_{om}^2 + r_k^2 + 2R_{om}r_k \sin(\theta_m + \gamma_k)\right]^{\frac{1}{2}}. \tag{3.4}$$

If the distance to the object is much larger than the size of the object, that is, $R_{om} \gg r_k$, we have the approximation;

$$r_{km} \cong R_{om} + x_k \sin\theta_m + y_k \cos\theta_m. \tag{3.5}$$

Let ρ_k denote the complex reflected signal of the k th scatterer which is assumed to be constant with changes in the illuminating frequency and the aspect angle. For each burst, L stepped frequencies $f_l = f_0 + l\Delta f$, $l = 0, \ldots, L-1$, are used where f_0 and Δf are the initial frequency and the frequency step, respectively. The received signal resulting from the k th scatterer and the l th illuminating frequency during the m th burst can be written as $\rho_k \exp\{-j\frac{4\pi}{c} f_l r_{km}\}$. The total received signal s_{lm} caused by the l th illuminating frequency of the m th burst is

$$s_{lm} = \sum_{k=1}^{K} \rho_k \exp\{-j\frac{4\pi}{c} f_l r_{km}\} + w_{lm} = \sum_{k=1}^{K} \rho_k \exp\{-j\frac{4\pi}{c}(f_0 + l\Delta f) r_{km}\} + w_{lm}. \tag{3.6}$$

After the pulse compression in the range direction using an inverse discrete Fourier transform (IDFT) [1] and substitution of (3.5) and (3.6), the complex envelope in the n th range cell of the m th burst becomes

$$\begin{aligned} x_{nm} &= \sum_{l=0}^{L-1} s_{lm} \exp\{j\frac{2\pi}{L} nl\} \\ &= \sum_{k=1}^{K} \rho_k \exp\{-j\frac{4\pi}{c} f_0 r_{km}\} \sum_{l=0}^{L-1} \exp\{j\left(\frac{2\pi}{L} n - \frac{4\pi}{c}\Delta f\, r_{km}\right) l\} + w'_{nm} \\ &= \exp\{-j\frac{4\pi}{c} f_0 R_{om}\}\, e_{nm} + w'_{nm} \end{aligned} \tag{3.7}$$

where

$$e_{nm} = \sum_{k=1}^{K} \rho_k \exp\{-j\frac{4\pi}{c} f_0 (x_k \sin\theta_m + y_k \cos\theta_m)\} \cdot \frac{\sin\left[L\left(\frac{\pi n}{L} - \frac{2\pi\Delta f}{c} r_{km}\right)\right]}{\sin\left[\left(\frac{\pi n}{L} - \frac{2\pi\Delta f}{c} r_{km}\right)\right]} \exp\{j(L-1)\left(\frac{\pi n}{L} - \frac{2\pi\Delta f}{c} r_{km}\right)\} \quad (3.8)$$

w'_{nm} $m = 0, \ldots, M-1$ $n = 0, \ldots, N-1$ is the complex envelope of the additive noise and N is the total number of range cells. We assume that w'_{nm} is independent identically distributed complex Gaussian noise components with zero mean and variance σ_w^2.

(3.7) indicates that the ISAR received signal consists of two terms. One is $\exp\{-j\frac{4\pi}{c} f_0 R_{om}\}$ induced by the translational motion of object which should be compensated prior to image formation. The other is e_{nm}, corresponding to the rotational motion of object, is used to construct the ISAR image.

Following range compression, range realignment is done to align the high resolution range profiles in the range direction so that the returns of different pulses from the same scatterer lie in the same range cell. After range realignment is accomplished, it holds that $r_{k(m+1)} \cong r_{km}$ $m = 0, \ldots, M-2$. If only the translational motion for ISAR autofocus is considered and the rotational motion for image formation is ignored[6], a good approximation is that two adjacent pulses have approximate equal value of aspect angle, that is, $\theta_{m+1} \cong \theta_m$ $m = 0, \ldots, M-2$. These approximations, discussed below, allow the signal model x_{nm} of ISAR autofocus to be written as

$$x_{nm} \cong \exp\{-j\frac{4\pi}{c} f_0 R_{om}\} e_{n0} + w'_{nm} \quad (3.9)$$

where

$$e_{n0} \cong \sum_{k=1}^{K} \rho_k \exp\{-j\frac{4\pi}{c} f_0 (x_k \sin\theta_0 + y_k \cos\theta_0)\} \cdot \frac{\sin\left[L\left(\frac{\pi n}{L} - \frac{2\pi\Delta f}{c} r_{k0}\right)\right]}{\sin\left[\left(\frac{\pi n}{L} - \frac{2\pi\Delta f}{c} r_{k0}\right)\right]} \exp\{j(L-1)\left(\frac{\pi n}{L} - \frac{2\pi\Delta f}{c} r_{k0}\right)\} \quad (3.10)$$

The complex envelope vector in the nth range cell can be expressed as the desired signal model

$$X_n = e_{n0}D + W_n \tag{3.11}$$

where $X_n = [x_{n0}, \ldots, x_{n(M-1)}]^T$, $W_n = [w'_{n0}, \ldots, w'_{n(M-1)}]^T$, λ is the wavelength corresponding to f_0, and $D = \left[\exp\{-j\frac{4\pi}{\lambda}R_{o0}\}, \ldots, \exp\{-j\frac{4\pi}{\lambda}R_{o(M-1)}\}\right]^T$ which is the complex vector that ISAR autofocus needs to estimate. (3.11) is the vector form of signal model for ISAR autofocus.

Although the above signal model is derived by use of a stepped frequency waveform, it is straightforward to generalize it to other signal waveforms such as the short pulse and chirp pulse-compression waveforms. It is noted that a similar signal model has been used for SAR phase error [82] rather than ISAR autofocus. The above derivation shows that the signal model (3.11) is valid after both the range compression and the range realignment have been accomplished for ISAR autofocus. Finally it is worth noticing that the complex vector D is space invariant and does not correspond to a particular strong scatterer.

In order to satisfy the approximation $\theta_{m+1} \cong \theta_m$, the phase variation induced by the rotational motion should be less than $\pi/2$ corresponding to a range error of $\lambda/8$ [4]. Consider two adjacent mth and $m+1$ th pulses; the exact signal returns from one scatterer are

$$e_{nm} = \rho_1 \exp\{-j\frac{4\pi}{\lambda}(x_1 \sin\theta_m + y_1 \cos\theta_m)\} \frac{\sin\left[L\left(\frac{\pi n}{L} - \frac{2\pi\Delta f}{c}r_{km}\right)\right]}{\sin\left[\left(\frac{\pi n}{L} - \frac{2\pi\Delta f}{c}r_{km}\right)\right]} \exp\{j(L-1)\left(\frac{\pi n}{L} - \frac{2\pi\Delta f}{c}r_{km}\right)\} \tag{3.12}$$

$$e_{n(m+1)} = \rho_1 \exp\{-j\frac{4\pi}{\lambda}(x_1 \sin\theta_{m+1} + y_1 \cos\theta_{m+1})\} \frac{\sin\left[L\left(\frac{\pi n}{L} - \frac{2\pi\Delta f}{c}r_{k(m+1)}\right)\right]}{\sin\left[\left(\frac{\pi n}{L} - \frac{2\pi\Delta f}{c}r_{k(m+1)}\right)\right]} \exp\{j(L-1)\left(\frac{\pi n}{L} - \frac{2\pi\Delta f}{c}r_{k(m+1)}\right)\} \tag{3.13}$$

and the phase variation due to the rotational motion is

$$\Delta\phi_m = \frac{4\pi}{\lambda}[x_1(\sin\theta_{m+1} - \sin\theta_m) + y_1(\cos\theta_{m+1} - \cos\theta_m)]. \tag{3.14}$$

Limiting $\Delta\phi_m$ to be less than $\pi/2$, we have a strict constraint

$$|x_1(\sin\theta_{m+1} - \sin\theta_m)| + |y_1(\cos\theta_{m+1} - \cos\theta_m)| < \frac{\lambda}{8}. \tag{3.15}$$

By use of $\sin(\delta\theta_m/2) \cong \delta\theta_m/2$ for small $\delta\theta_m/2$ where $\delta\theta_m = \theta_{m+1} - \theta_m$, we have

$$\delta\theta_m < \frac{\lambda}{8\{|x_1\cos[(\theta_m + \theta_{m+1})/2]| + |y_1\sin[(\theta_m + \theta_{m+1})/2]|\}}. \tag{3.16}$$

Thus the sample interval l_s of the synthetic aperture must satisfy

$$l_s = R_o\delta\theta_m < \frac{\lambda R_o}{8\{|x_1\cos[(\theta_m + \theta_{m+1})/2]| + |y_1\sin[(\theta_m + \theta_{m+1})/2]|\}} \tag{3.17}$$

where R_o is the distance between the radar and object. Figure 3.2 shows the required sampling interval versus $\theta_m + \theta_{m+1}$ where the parameters are chosen as λ = 3 cm, x_1 = 1 m and y_1 = 1 m. It indicates that the required sampling interval decreases as the aspect angle increases. The minimum sampling intervals are 26.51 m and 79.53 m when the R_o equals to 10 km and 30 km, respectively. This condition can be met by increasing the PRF to satisfy $\text{PRF} > \frac{8s_v\{|x_1\cos[(\theta_m + \theta_{m+1})/2]| + |y_1\sin[(\theta_m + \theta_{m+1})/2]|\}}{\lambda R_o}$ where s_v is the speed of the object.

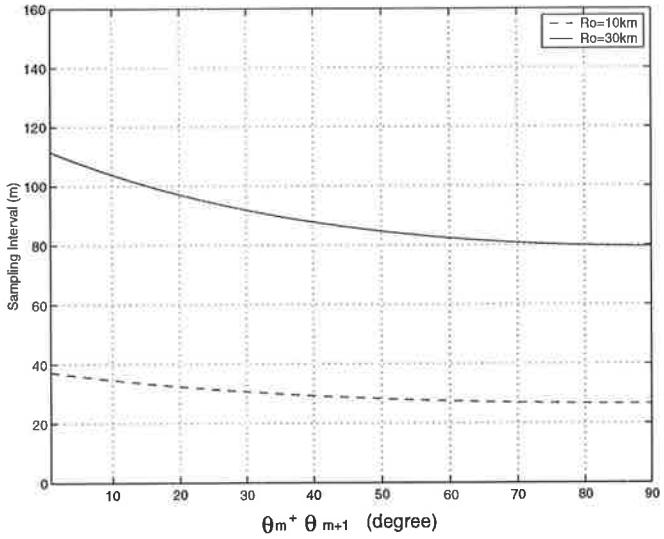

Figure 3.2 Sampling interval versus aspect angle

One requirement for range realignment to satisfy the approximation $r_{k(m+1)} \cong r_{km}$ is that the variation of relative position between scatterers in range profile should be less than one range resolution cell. Consider an example of two scatterers as shown in Figure 3.3, they

are at first located at A and B. During the interval of two adjacent pulses, they rotate to positions A_1 and B_1. The initial and final projections of two scatterers on range direction (y axis) are $d\cos\theta_m$ and $d\cos\theta_{m+1}$, respectively where d is the distance between two scatterers. The variation of relative position between two scatterers in range profiles needs to satisfy $d|\cos\theta_{m+1} - \cos\theta_m| < \tau_r$ where τ_r is the range resolution. By use of $\sin(\delta\theta_m) \approx \delta\theta_m$, this relation becomes

$$\delta\theta_m < \frac{\tau_r}{d\sin[(\theta_m + \theta_{m+1})/2]}. \tag{3.18}$$

This is a weak requirement as compared with (3.16) if $\lambda < \tau_r$.

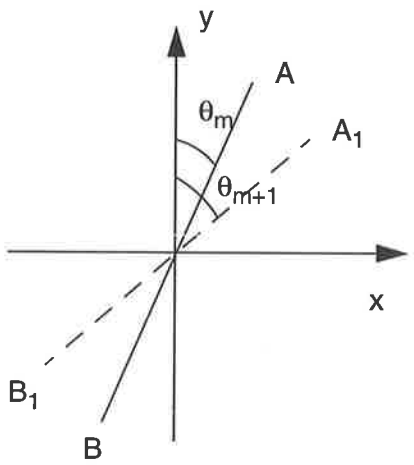

Figure 3.3 Position variation of two scatterers

In standard ISAR autofocusing algorithms, R_{om} is estimated and the range aligned signals are corrected with the phase term $\exp\{-j\frac{4\pi}{\lambda}R_{om}\}$. However, from (3.11) it can be seen that for the above signal model, we only need to work with the $x'_{nm} = x_{nm}\exp\{j\frac{4\pi}{\lambda}R_{om}\}$. Thus it is unnecessary to estimate R_{om} and all that is required is an estimate of $\exp\{j\frac{4\pi}{\lambda}R_{om}\}$, obviating the need for phase unwrapping. In this thesis, we will develop new approaches for estimating the $\exp\{-j\frac{4\pi}{\lambda}R_{om}\}$ $m = 0, \ldots, M-1$, that is the complex vector D rather than R_{om}. The block diagram of ISAR processing without phase unwrapping is shown in Figure 3.4.

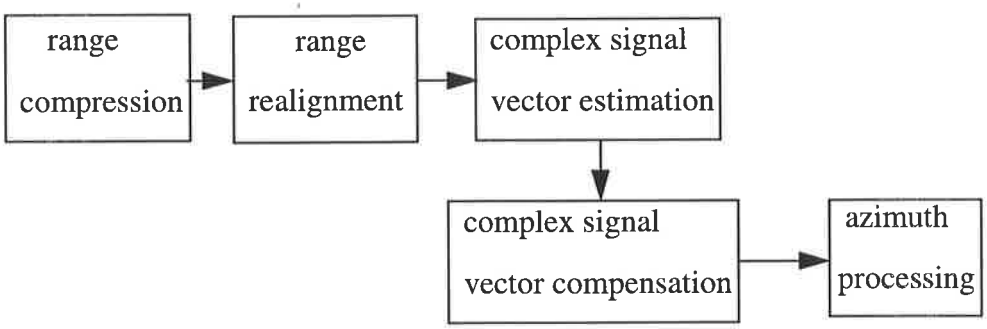

Figure 3.4 ISAR processing without phase unwrapping

3.3 Beamforming Methods for ISAR Autofocus

It is assumed that the conventional beamformer with uniform shading across the array sets the weights to be equal to the steering vector [2]. In conventional beamforming the steering vector is parameterized by the steering angle; however for the present application it is parameterized by the R_{om}, namely, the range between the radar and the object when the m th burst is transmitted. Loosely, this may be thought of as beamforming in range. Thus the beamforming weight vector v is defined as

$$v = [v_0, v_1, \ldots, v_{(M-1)}]^T \tag{3.19}$$

where $v_m = \exp\{-j\frac{4\pi}{\lambda}\hat{R}_{om}\}$, $m = 0, 1, \ldots, M-1$. As discussed above it is not necessary to determine the R_{om} only the v_m to carry out autofocus. We consider a number of methods for doing so when the covariance matrix C_x is known in this and next sections.

3.3.1 Conventional Beamforming Approach

The output of the conventional beamformer is given by

$$P_c = \frac{1}{M^2} v^H C_x v \tag{3.20}$$

where H denotes the Hermitian transpose and C_x is the covariance matrix of the signal vector in the n th range cell. Based on (3.11), we have

$$C_x = p_n DD^H + \sigma_w^2 I_M \tag{3.21}$$

where I_M is an $M \times M$ identity matrix and $p_n = |e_{n0}|^2$. Then P_c becomes

$$P_c = \frac{p_n}{M^2} v^H DD^H v + \frac{\sigma_w^2}{M}. \tag{3.22}$$

which, apart from an arbitrary scaling parameter, is maximized with the constraint $v^H v = M$ when

$$v_{opt1} = D. \tag{3.23}$$

(3.23) means that when the unknown translational motion phase matches the actual translational motion phase, P_c attains its maximum

$$P_{cmax} = p_n + \frac{\sigma_w^2}{M}. \tag{3.24}$$

If the steering vector v does not point to the direction of signal vector D, the output power of the conventional beamformer will decrease.

As an example, computer simulations were conducted to calculate the output power of conventional beamformer. In the simulation, we assumed a point scatterer flying in a straight line at a constant speed $s_v = 200$ m/s. The initial range R_{o0} and initial aspect angle θ_0 were 30 km and 0^o respectively, as shown in Figure 3.1. A coherent radar transmitted a narrowband waveform with central frequency 10 GHz and pulse-repetition-interval (PRI) $T = 1/400$ s. The number of the transmitted waveforms M was 1024. In order to display the variation of beamformer output the range from the object to the radar, R_{om}, when mth pulse is transmitted is approximated by $\hat{R}_{om} = R_{o0} + (s_v mT)^2 / (2R_{o0})$. The steering vector is thus a function of R_{o0} and s_v. Figure 3.5 shows the output power of the conventional beamformer versus speed. It indicates that although the output power has many local maxima, the output power achieves its global maximum when the search speed is equal to the true value. The output power is asymmetrical with respect to the search speed.

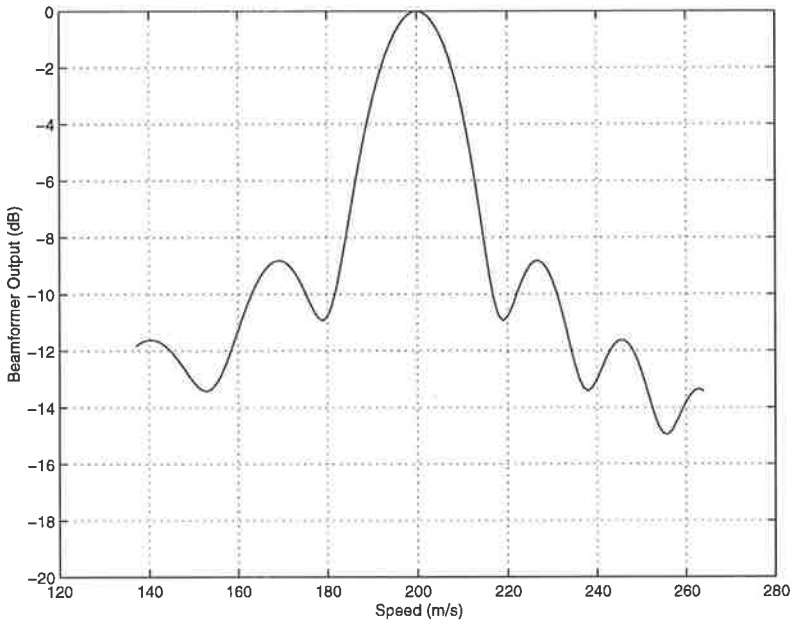

Figure 3.5 Output power P_c of conventional beamformer

The conventional beamforming method for ISAR autofocus can be expressed as maximization of the conventional beamformer output, that is,

$$\max\{\frac{1}{M^2}v^H C_x v\} \tag{3.25}$$

subject to the constraint $v^H v = M$. The above optimization can be combined in a single equation

$$\varepsilon = \frac{1}{2}v^H C_x v - \mu[v^H v - M] \tag{3.26}$$

where μ is a Lagrange multipler. By taking the gradient with respect to v and setting it to zero, we have

$$C_x v - \mu v = 0. \tag{3.27}$$

Thus μ and v are found to be the eigenvalue and eigenvector of C_x, respectively. Substituting (3.27) into (3.25), we get

$$\max\{\frac{1}{M^2}v^H C_x v\} = \max\{\frac{\lambda_i}{M}\} = \frac{\lambda_1}{M} \tag{3.28}$$

where λ_i is the eigenvalue of C_x and λ_1 is the maximum eigenvalue of C_x and the maximizing phases are given by the components of the eigenvector corresponding to the maximum eigenvalue.

3.3.2 Optimum Beamforming Approach

Four optimum beamformers, maximum array gain, maximum likelihood, minimum power with constraint and minimum mean-square error, are described in section 2.8.1. If a scaling parameter is selected properly, the maximum array gain beamformer is equivalent to the maximum likelihood beamformer and the minimum mean-square error beamformer is equivalent to the minimum power with constraint beamformer. The maximum likelihood beamformer looks like the minimum power with constraint beamformer except replacing C_x with C_w (the covariance matrix of the received noise). Based on the signal model for ISAR autofocus, it is easily verified that the four optimum beamformers are equivalent [2]. The output power of an optimum beamformer is given by

$$P_o = \left(v^H C_x^{-1} v \right)^{-1}. \tag{3.29}$$

The special form of C_x as given by (3.21) allows its inverse to be written in the form[233]

$$C_x^{-1} = \sigma_w^{-2} I_M - \frac{p_n / \sigma_w^2}{\sigma_w^2 + M p_n} DD^H. \tag{3.30}$$

Then the output power of the optimum beamformer turns into

$$P_o = \left\{ \sigma_w^{-2} M - \frac{p_n / \sigma_w^2}{\sigma_w^2 + M p_n} v^H DD^H v \right\}^{-1}. \tag{3.31}$$

and by inspection this achieves its maximal value at the same point as the conventional beamformer apart from a scaling factor, i.e., when

$$v_{opt2} = D. \tag{3.32}$$

with a maximal value of

$$P_{omax} = p_n + \frac{\sigma_w^2}{M}. \tag{3.33}$$

Figure 3.6 shows the output power P_o of the optimum beamformer as a function of speed. The parameters of simulation are the same as in section 3.3.1. It is indicated that the beamwidth of the optimum beamformer is narrower than that of conventional beamformer, the sidelobe level of optimal beamformer is lower than that of conventional beamformer, and the local maximum is reduced.

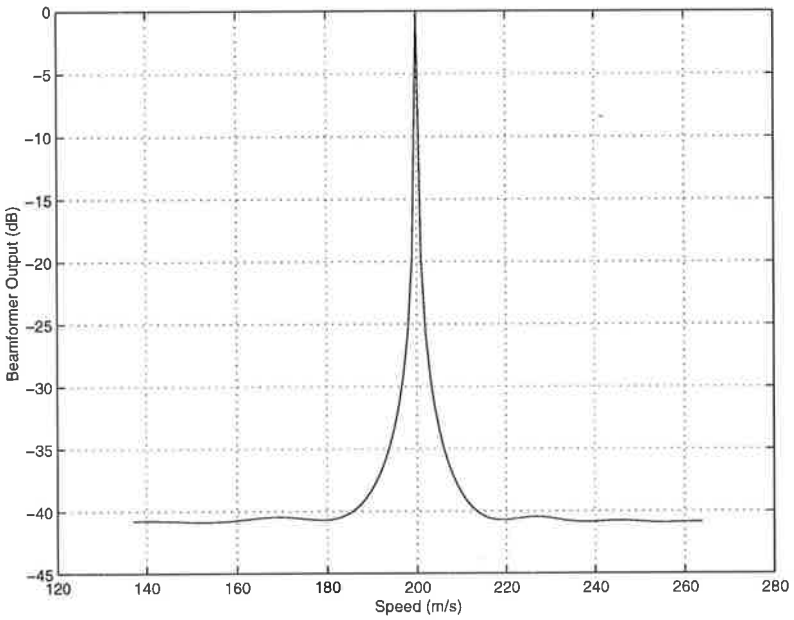

Figure 3.6 Output power P_o of optimum beamformer

The optimum beamforming weights for ISAR autofocus are the v that give

$$\max\left\{\left(v^H C_x^{-1} v\right)^{-1}\right\} \tag{3.34}$$

with constraint $v^H v = M$ which is equivalent to

$$\min\left\{v^H C_x^{-1} v\right\} \tag{3.35}$$

subject to $v^H v = M$. This constrained optimization can be converted into an unconstrained optimization by defining the function

$$\varepsilon = \frac{1}{2} v^H C_x^{-1} v - \mu\left[v^H v - M\right]. \tag{3.36}$$

By setting $\nabla_v \varepsilon = 0$, we have

$$C_x^{-1} v - \mu v = 0 . \tag{3.37}$$

Thus μ and v are identified to be the eigenvalue and eigenvector of C_x^{-1}, respectively. As C_x is Hermitian symmetrical and positive definite, the eigen decomposition of C_x has the form

$$C_x = \sum_{i=1}^{M} \lambda_i u_i u_i^H . \tag{3.38}$$

The inverse of C_x can be expressed as

$$C_x^{-1} = \sum_{i=1}^{M} \frac{1}{\lambda_i} u_i u_i^H . \tag{3.39}$$

Therefore $1/\mu$ and v are found to be the eigenvalue and eigenvector of C_x, respectively. Then (3.34) is changed into

$$\max\left\{\left(v^H C_x^{-1} v\right)^{-1}\right\} = \max\left\{\left(\frac{M}{\lambda_i}\right)^{-1}\right\} = \frac{\lambda_1}{M} \tag{3.40}$$

when the estimated steering vector v is equal to the eigenvector u_1 of C_x corresponding to the maximal eigenvalue, that is,

$$v = u_1 . \tag{3.41}$$

Thus both the conventional and optimum approaches require the solution of an eigenvector problem.

3.4 Subspace Methods for ISAR Autofocus

Based on the ISAR autofocus signal model (3.11), the covariance matrix of the received signal is rewritten as

$$C_x = p_n D D^H + \sigma_w^2 I_M \tag{3.42}$$

where p_n and σ_w^2 are the powers of signal and noise, respectively. D is the complex vector of translational motion and I_M is the identity matrix. It is shown in Appendix A that the largest eigenvalue of C_x is

$$\lambda_1 = p_n M + \sigma_w^2 \tag{3.43}$$

and its corresponding eigenvector is

$$u_1 = \frac{D}{M} \tag{3.44}$$

and all the other eigenvalues are equal to σ_w^2. Therefore the dimensions of signal subspace and noise subspace are equal to 1 and $M-1$, respectively, for ISAR autofocus.

In order to visualize, consider an example where three pulses are transmitted by the radar, that is, $M = 3$. The signal and noise subspaces may be represented as shown in Figure 3.7. The signal subspace is a one-dimensional space (u_1 axis in the diagram) and the noise subspace is the u_2u_3 plane. The array manifold, defined as the locus of the steering vector, is a spherical surface with the constraint $v^H v = 3$ and intersects the signal subspace at point c when the steering vector v points to the complex vector D as shown in Figure 3.7. At the point c the steering vector v has a maximum projection length onto the signal subspace and a minimum projection onto the noise subspace. These properties are the principles of the signal and noise subspace methods described below.

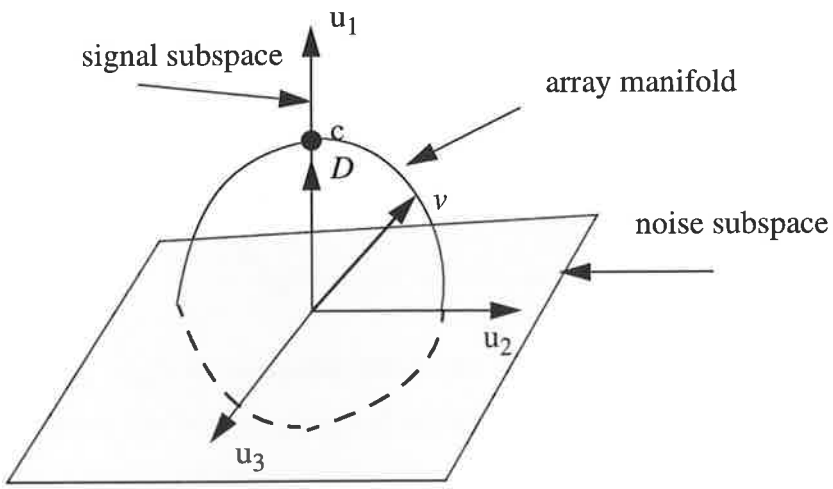

Figure 3.7 Eigen-space decomposition for ISAR autofocus

3.4.1 Signal Subspace Approach

The third new approach for ISAR autofocus is to exploit the signal subspace. The projection of the steering vector v onto the signal subspace is $P_{rs}v$. The projection matrix P_{rs} onto the signal subspace may be expressed as

$$P_{rs} = \frac{DD^H}{M} \tag{3.45}$$

which has eigenvalues of 1 and 0. The signal subspace approach for ISAR autofocus is to maximize the projection of the steering vector on the signal subspace, that is,

$$\max \left\| P_{rs}v \right\|^2 \qquad \forall v \tag{3.46}$$

with constraint $v^H v = M$ where $\| \ \|$ is the Euclidean norm. Noting the $P_{rs}^2 = P_{rs}$, (3.46) is equivalent to

$$\max \{ v^H P_{rs} v \} \tag{3.47}$$

subject to $v^H v = M$. This optimization happens when the steering vector equals the eigenvector corresponding to the maximal eigenvalue of P_{rs}, that is,

$$v = \frac{D}{M}. \tag{3.48}$$

3.4.2 Noise Subspace Approach

The fourth new approach for ISAR autofocus makes use of the noise subspace. The dimension of the noise subspace is $M-1$ and their corresponding eigenvectors are denoted by $u_2, \ldots, u_M$. The projection matrix P_{rn} onto the noise subspace is

$$P_{rn} = (u_2, \ldots, u_M)\ (u_2, \ldots, u_M)^H. \tag{3.49}$$

The projection of the vector v onto the noise subspace is $P_{rn}v$. The noise subspace approach for ISAR autofocus is to minimize the projection of the steering vector on the noise subspace, namely,

$$\min \left\| P_{rn}v \right\|^2 \qquad \forall v \tag{3.50}$$

with constraint $v^H v = M$ which is equivalent to

$$\min \{v^H P_{rn} v\} \tag{3.51}$$

subject to $v^H v = M$. With the relation of $P_{rn} = I - \frac{DD^H}{M}$, this minimum occurs if

$$v = \frac{D}{M}. \tag{3.52}$$

Theoretically the noise subspace approach is equivalent to the signal subspace approach. However in practice numeric computation occasionally results in some differences between them.

3.5 Subaperture Processing

Subaperture or subarray processing techniques have been proposed for spatially smoothing the covariance matrix in array processing when the signal sources are correlated [106] [107]. They have also used for estimating the shape of a towed array [145]. Subaperture processing is used here to improve computational efficiency. Subaperture processing of ISAR autofocus first divides the entire synthesized aperture into many subapertures which are connected through a sampled aperture point (circle point) as shown in Figure 3.8, then conducts the beamforming or subspace processing for each subaperture to estimate the complex signal vector corresponding to each subaperture, and finally restores the complex signal vector for ISAR autofocus by summing the phases of subapertures through the connecting point.

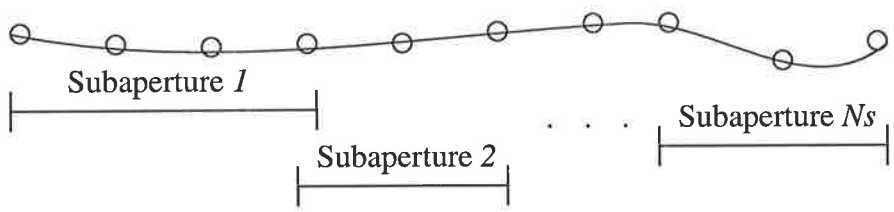

Figure 3.8 Subaperture arrangement

The main advantage of subaperture processing is the reduction of computational load. The number of numerical operations required to perform matrix eigendecomposition is approximately proportional to the cube of the size of the matrix. For example if an M pulse aperture is segmented into N_s subapertures with the same size of M_s pulses, the reduction ratio of computational complexity is $M^3/\left(N_s M_s^3\right)$. The smaller each subaperture, the greater reduction in computation. But subaperture processing is at the expense of a small increase of the CRLB of D when the SNR is small as discussed in the next chapter.

There are many schemes to determine the subapertures. Consider an extreme case where each subaperture has two pulses, that is, $M_s = 2$ and $N_s = M - 1$. For the mth subaperture, the covariance matrix in the nth range cell is expressed as

$$C_x = p_n \begin{bmatrix} 1 & \exp\{j\frac{4\pi}{\lambda}(R_{o(m+1)} - R_{om})\} \\ \exp\{-j\frac{4\pi}{\lambda}(R_{o(m+1)} - R_{om})\} & 1 \end{bmatrix} + \sigma_w^2 I_2 \qquad (3.53)$$

and the eigenvector corresponding to the largest eigenvalue of C_x is

$$u_1 = \begin{bmatrix} 1 \\ \exp\{-j\frac{4\pi}{\lambda}(R_{o(m+1)} - R_{om})\} \end{bmatrix}. \qquad (3.54)$$

However in practice the covariance matrix has to be estimated by range cell averaging, that is,

$$\hat{C}_x = \frac{1}{N}\sum_{n=1}^{N} \begin{bmatrix} x_{nm} \\ x_{n(m+1)} \end{bmatrix} \begin{bmatrix} x_{nm}^* & x_{n(m+1)}^* \end{bmatrix}, \qquad (3.55)$$

the eigenvector corresponding to the largest eigenvalue of $\hat{C}$, derived in Appendix B, is

$$\hat{u}_1 = \begin{bmatrix} 1 \\ p_1 \sum_{n=1}^{N} x_{nm}^* x_{n(m+1)} \end{bmatrix} \qquad (3.56)$$

where p_1 is a scalar as shown in Appendix B. Thus we have an estimation

$$\exp\{-j\frac{4\pi}{\lambda}(\hat{R}_{o(m+1)}-\hat{R}_{om})\} = \left(\sum_{n=1}^{N} x_{nm}{}^{*}x_{n(m+1)}\right) \Big/ \left|\sum_{n=1}^{N} x_{nm}{}^{*}x_{n(m+1)}\right|. \quad (3.57)$$

Finally the elements of the estimated complex signal vector for the entire aperture can be restored by summing the phase difference between adjacent subarrays, namely,

$$\exp\{j\hat{\phi}_{m+1}\} = \exp\{j\hat{\phi}_m\}\exp\{-j\frac{4\pi}{\lambda}(\hat{R}_{o(m+1)}-\hat{R}_{om})\} \quad (3.58)$$

where $\hat{D} = [\exp(j\hat{\phi}_0), \ldots, \exp(j\hat{\phi}_{M-1})]^T$ and $\hat{\phi}_0 = 0$. (3.57) and (3.58) indicate that when each subaperture is composed of two pulses, the eigendecomposition of the covariance matrix can be obviated and replaced with the operations in the data domain to estimate the complex vector of the entire aperture which results in a significant reduction of computation.

3.6 Computer Simulation

Computer simulations were conducted to verify the validity of beamforming and subspace approaches for ISAR autofocus. One-dimensional and two-dimensional ISAR imaging were both simulated. In the case of one-dimensional ISAR imaging, a narrowband signal rather than a wideband signal was used resulting in high resolution only in cross-range. One-dimensional version of the ISAR technique could be applied directly to a narrow coherent radar to enhance the cross-range resolution. For two-dimensional ISAR imaging, a wideband signal was used which produced a two-dimensional high resolution ISAR image in range and cross-range directions.

3.6.1 One-dimensional ISAR Imaging

The developed beamforming and subspace approaches were illustrated by simulation with a simple target consisting of two point scatterers 15 m apart in cross-range, flying in a straight line at constant velocity 200 m/s. The initial range R_{o0} and initial aspect angle θ_0 were 30 km and 0^o, respectively as shown in Figure 3.1. A coherent radar transmitted a narrowband waveform with central frequency 10 GHz and pulse-repetition-frequency (PRF) 400 Hz. The number of the transmitted waveforms M was 1024. The received signal was represented by

$$s_m = \sum_{k=1}^{2} \rho_k \exp\{-j\frac{4\pi}{c} f_0 r_{km}\} + w_m \quad (3.59)$$

where $\rho_1 = \rho_2 = 1$ and w_m was complex Gaussian noise such that the signal-to-noise ratio (SNR) was 20 dB. The covariance matrix was estimated by averaging 10 time samples.

Figure 3.9 shows the cross-range ISAR images: (a) is the unfocused image (i.e. the DFT amplitude of the received signal), (b) is the ideal focused image (i.e. using zero noise and known R_{om} to effect perfect focusing), (c) is the focused image with the conventional beamforming approach, (d) is the focused image with the optimum beamforming approach, (e) is the focused image with the signal subspace approach, (f) is the focused image with the noise subspace approach and (g) is the focused image with the image contrast method recently proposed[16][17]. The cross-range resolution is 0.88 m. (a) is out of focus because the two point scatterers disappear. Compared with (a), the focused qualities of (c), (d), (e) and (f) are highly marked. Moreover (c), (d), (e) and (f) are in good agreement with (b) and (g).

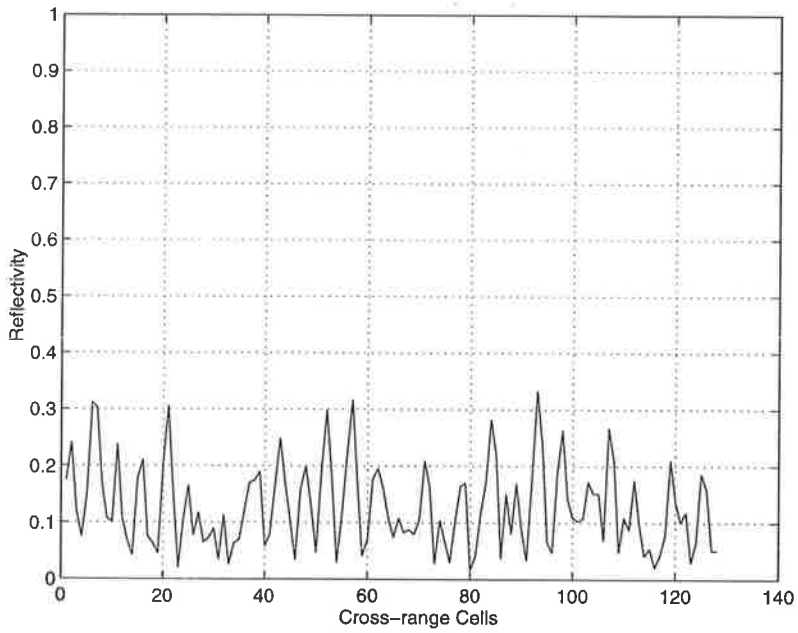

(a) Unfocused image

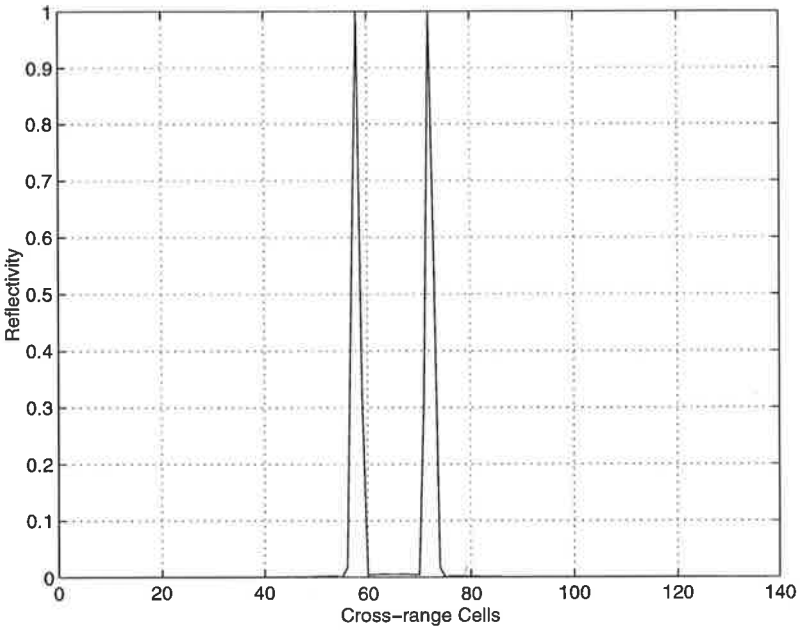

(b) Ideal focused image

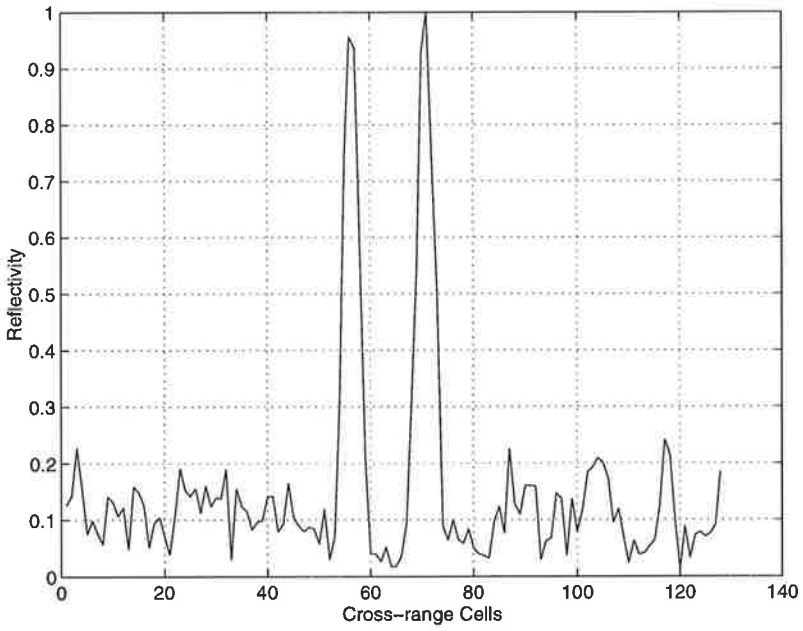

(c) Focused image with the conventional beamforming approach

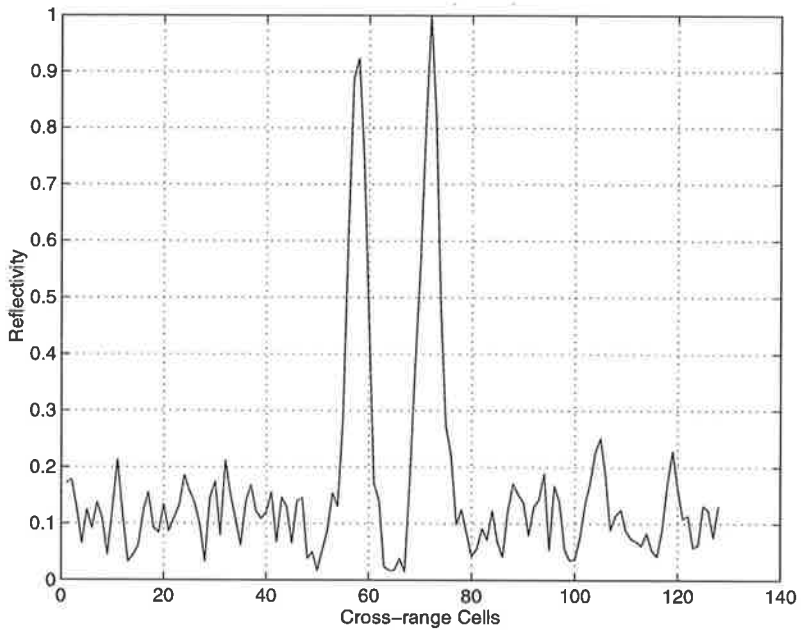

(d) Focused image with the optimum beamforming approach

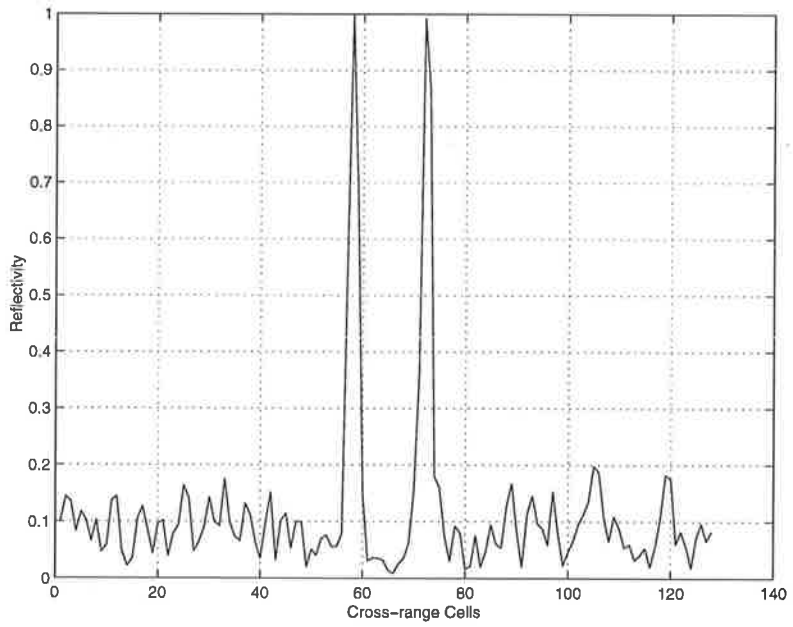

(e) Focused image with the signal subspace approach

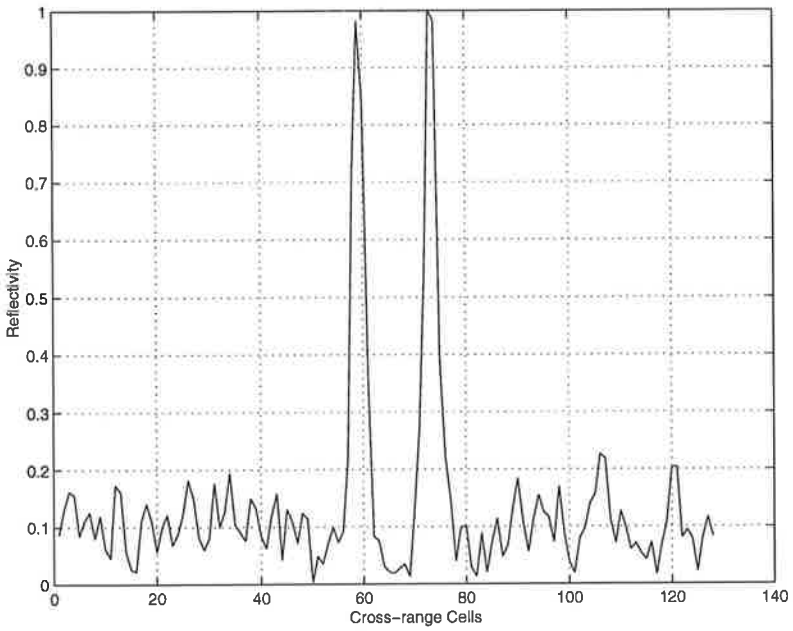

(f) Focused image with the noise subspace approach

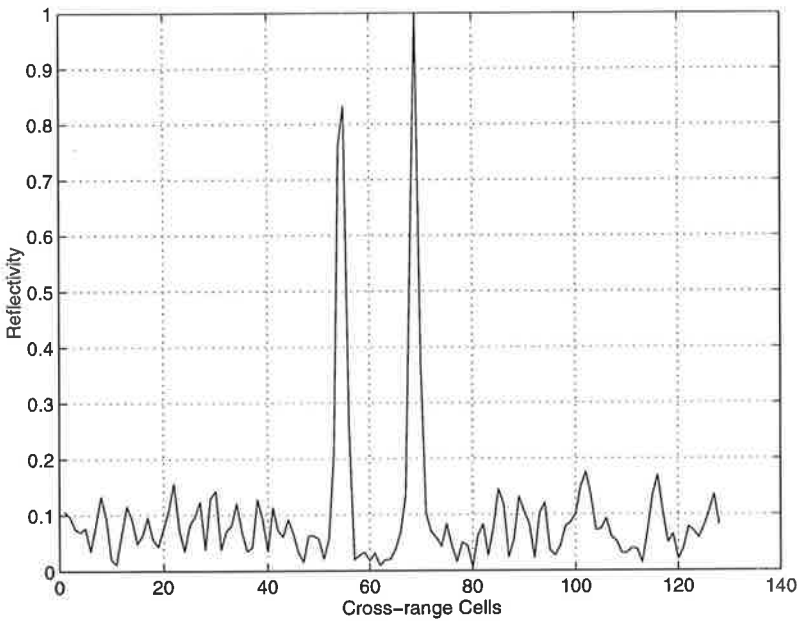

(g) Focused image with the image contrast approach

Figure 3.9 Cross-range ISAR images of simulated data

3.6.2 Two-dimensional ISAR Imaging

As an example of two-dimensional ISAR imaging simulation, the scattering model of an aircraft is shown in Figure 3.10. The return from the aircraft was assumed to be dominated by scattering from its nose, engine intakes and exhausts, wing pods and horizontal stabiliser extremities with metre coordinates $(11, 0)$, $(0, 2)$, $(0, -2)$, $(-3.3, 2)$, $(-3.3, -2)$, $(0, 8)$, $(0, -8)$, $(-9, 3)$, and $(-9, -3)$. The reflectivities of the nine scatterers were equal. The radar transmitted a stepped-frequency waveform with an effective bandwidth of 50 MHz which resulted in 3 m range resolution. The number of stepped frequencies was 16 and the radar wavelength was 3 cm. The initial distance between the radar and the aircraft was 30 km and the initial aspect angle was 0^o as shown in Figure 3.1. The aircraft was flying in a straight line with a speed of 200 m/s. The total change of angle was 0.38^o which provided a 2 m resolution in cross-range.

The received signals were generated by (3.6) with $\text{SNR} = 10\log\left(\sum_{k=1}^{9} \rho_k^2/\sigma_w^2\right) = 20$ dB. They were processed by range compression, range realignment, autofocus and range-Doppler imaging. The covariance matrix was estimated by averaging over all the range cells. Figure 3.11 shows the ISAR images of the simulated aircraft: (a) is the ISAR image without autofocus, (b) is the ISAR image focused by the conventional beamformer approach, (c) is the ISAR image focused by the optimum beamformer approach, (d) is the ISAR image focused by the signal subspace approach and (e) is the ISAR image focused by the noise subspace approach,. The reconstructed ISAR images have correspondences to the scattering model of simulated aircraft as shown in Figure 3.10. The small difference between (b) and (c) can be attributed to imperfection in the optimization associated with size of the search steps.

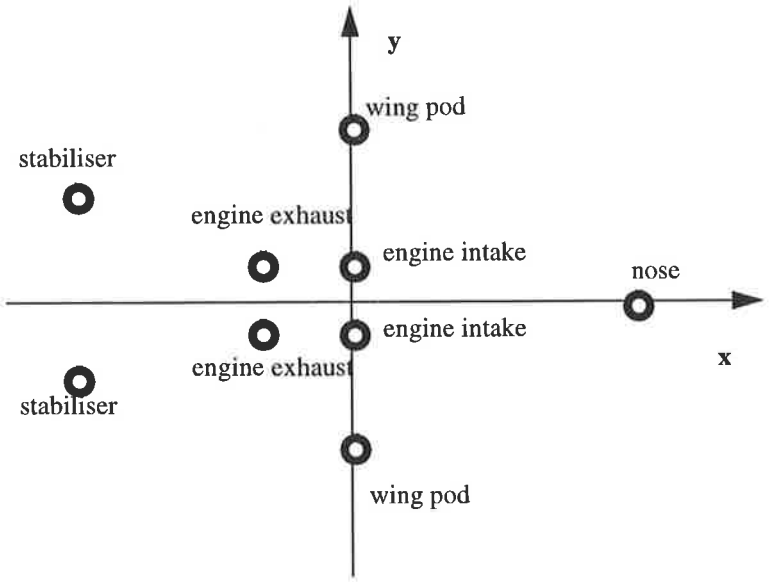

Figure 3.10 Scattering model of simulated aircraft

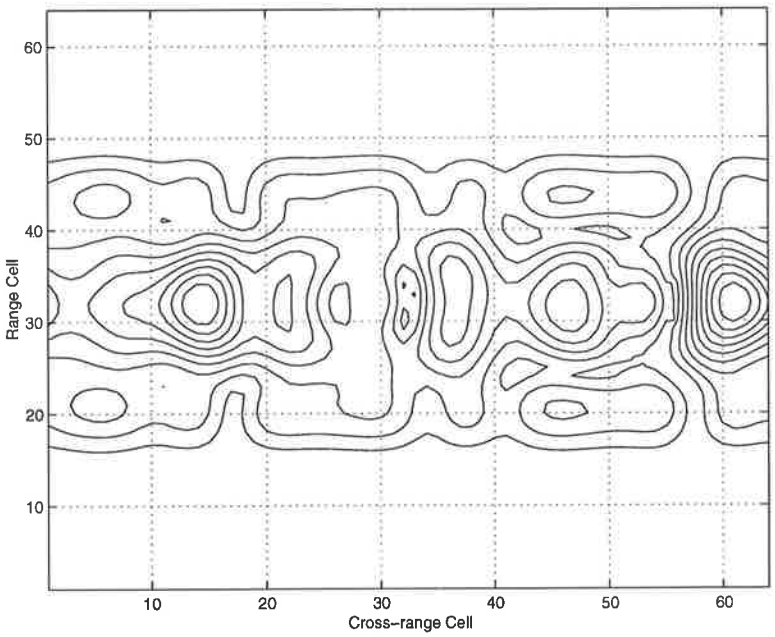

(a) Unfocused image

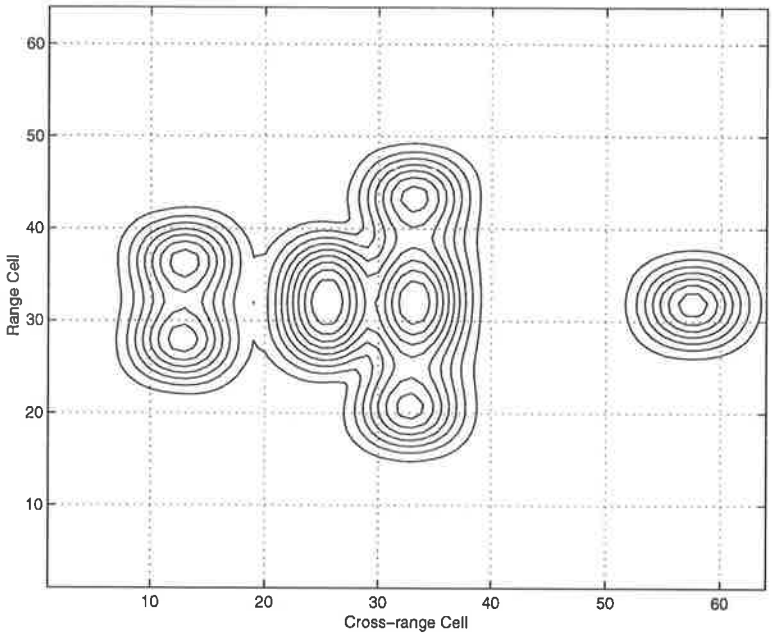

(b) Focused image with the conventional beamforming approach

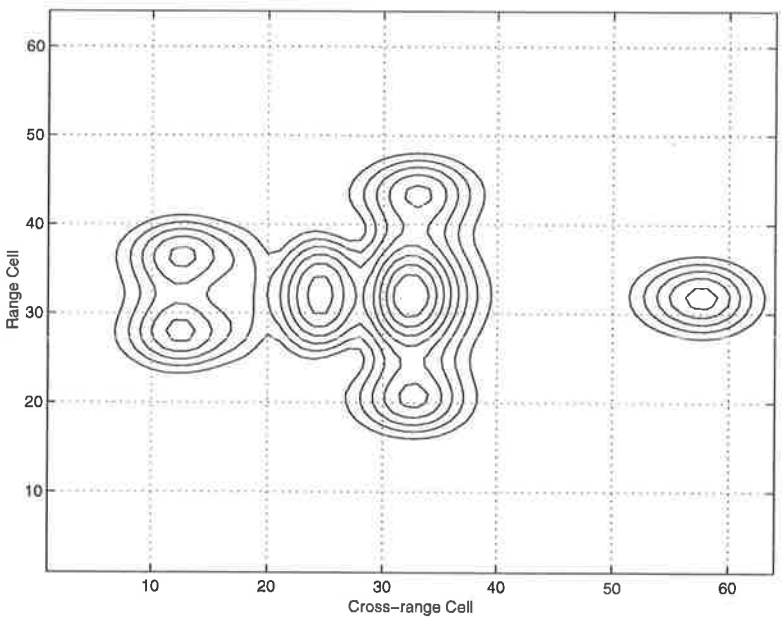

(c) Focused image with the optimum beamforming approach

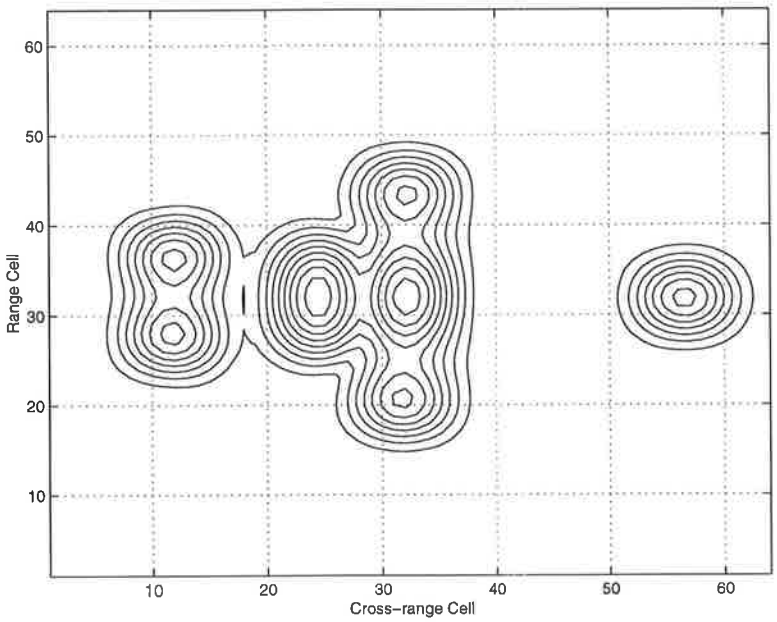

(d) Focused image with the signal subspace approach

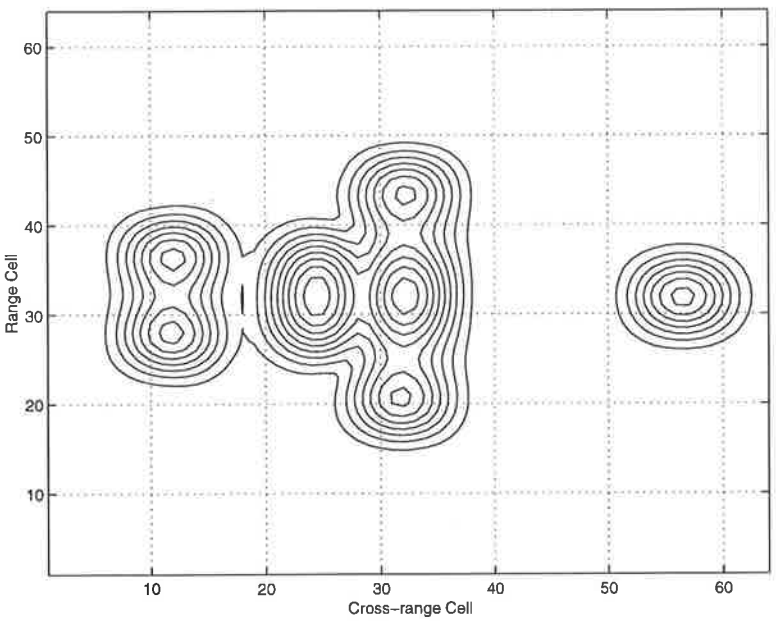

(e) Focused image with the noise subspace approach

Figure 3.11 ISAR images of simulated aircraft

3.7 Real Data Results

3.7.1 One-dimensional ISAR Imaging

The field experiment was carried out with a C-band tracking radar. The object was a bomber which was flying in a straight line with a speed of 280 m/s . The range between radar and object was about 18 km . The radar transmitted 2048 narrowband signals with PRF 600 Hz . The coherent signal returns were collected and recorded with I and Q channels. Figure 3.12 gives the results of processing real data with (a) being the unfocused image, (b) being the focused image with the conventional beamforming approach, (c) being the focused image with the optimum beamforming approach, (d) being the focused image with the signal subspace approach, (e) being the focused image with the noise subspace approach, and (f) being the focused image with the image contrast method [16][17]. The cross-range resolution is about 1m for all methods. It is clear that (b), (c), (d) and (e) are well focused compared with (a) and have an agreement with (f).

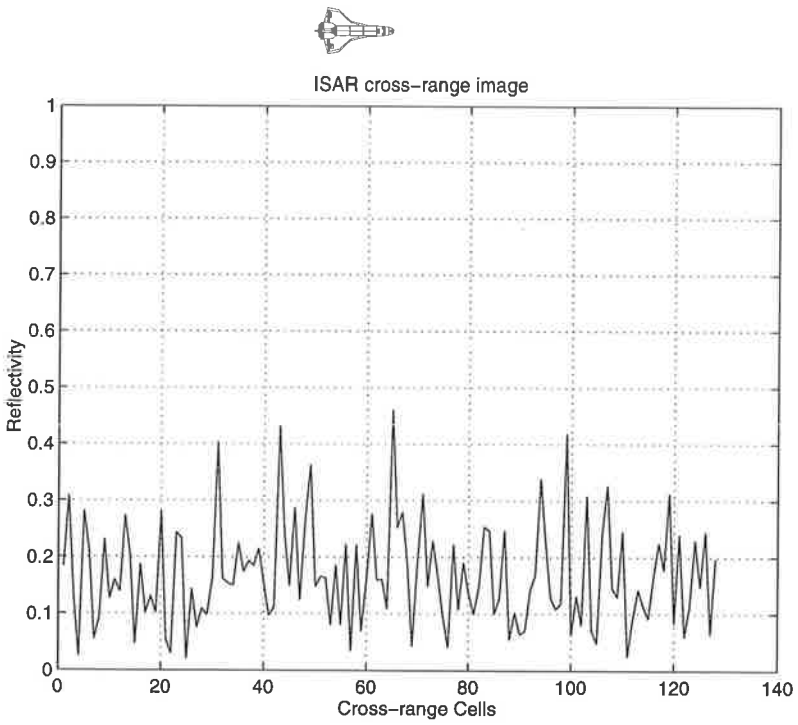

(a) Unfocused image

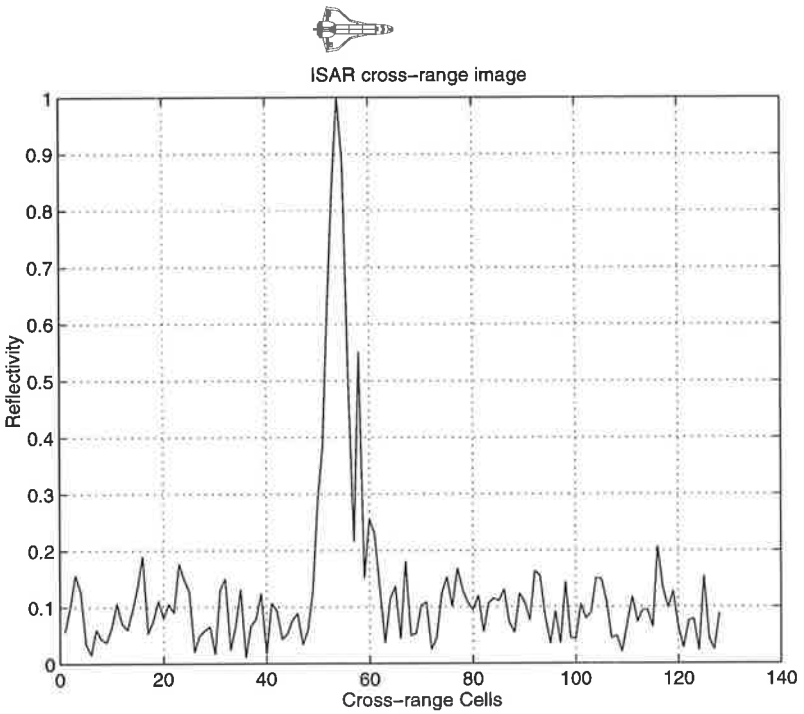

(b) Focused image with the conventional beamforming approach

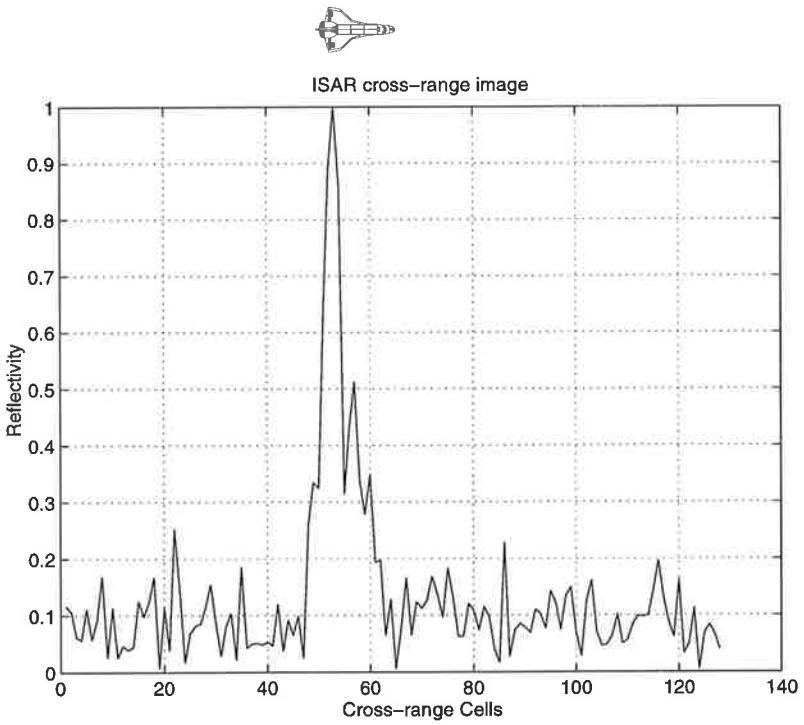

(c) Focused image with the optimum beamforming approach

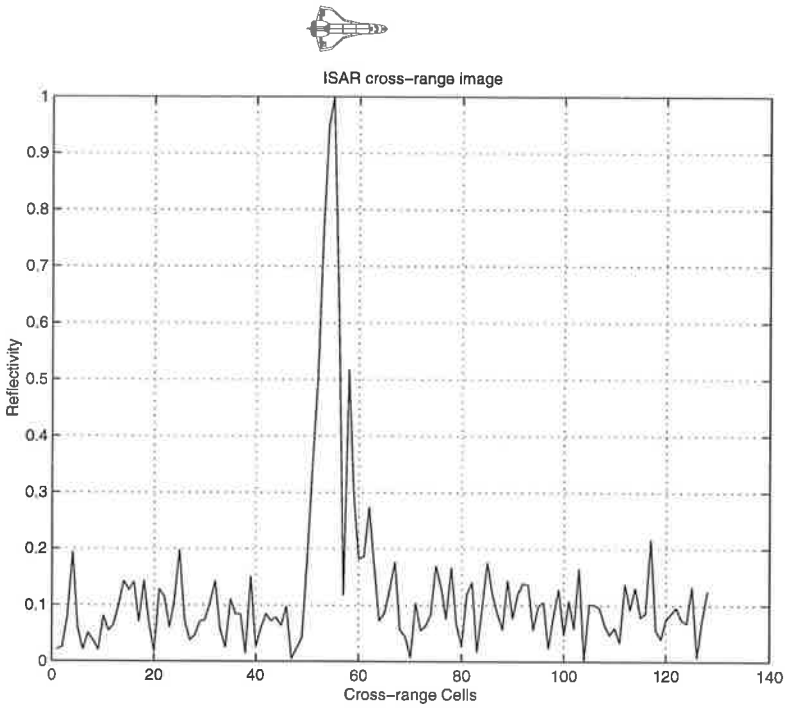

(d) Focused image with the signal subspace approach

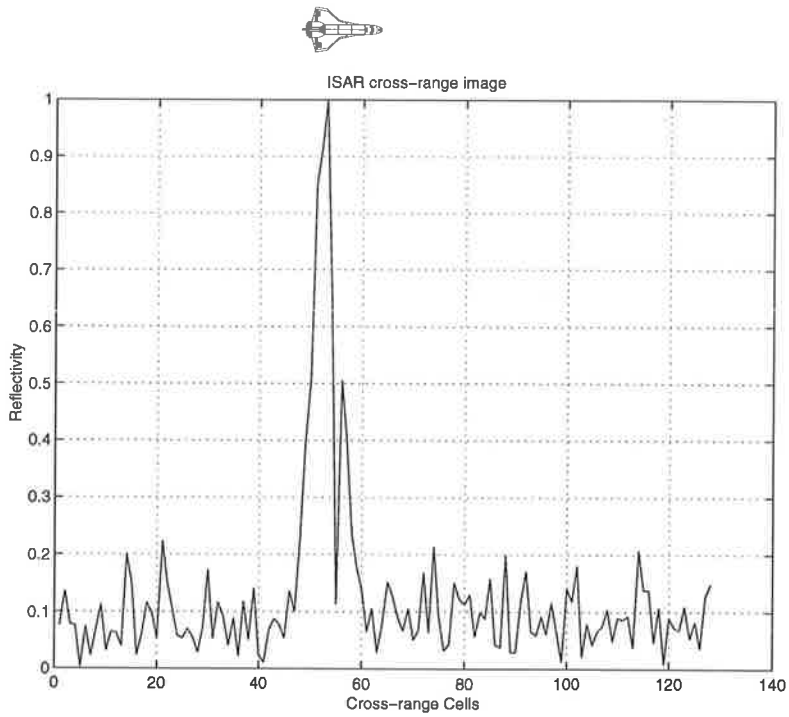

(e) Focused image with the noise subspace approach

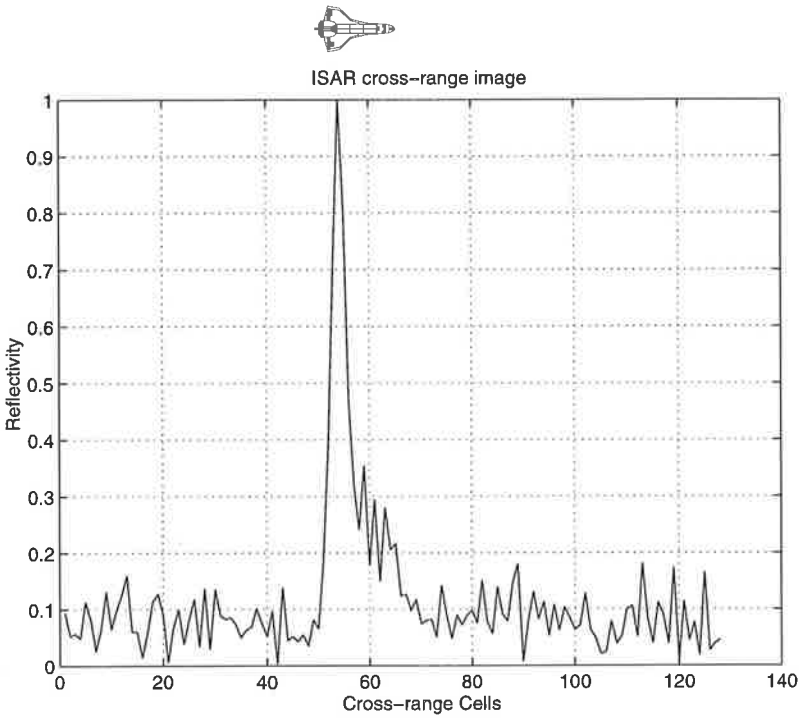

(f) Focused image with the image contrast approach

Figure 3.12 Cross-range ISAR images of real data

3.7.2 Two-dimensional ISAR Imaging

Thanks to Professor B.D.Steinberg of the University of Pennsylvania, we received two-dimensional experimental data of a Boeing-727 flying into the Philadelphia International Airport. The range, speed and altitude of the aircraft were about 2.7 km , 120m/s and a few thousand feet, respectively. The central frequency of radar was 9.6GHz (X-band) (λ = 3.123 cm). Range resolution of 1m was achieved by transmitting a narrow pulse of width 7 ns . Signals in 120 range cells were recorded and the PRF was 400 Hz . The real data were processed with range realignment, autofocus, and range-Doppler imaging. The ISAR images of the Boeing-727 are shown in Figure 3.13 where (a) is the unfocused image, (b) is the focused image with the conventional beamforming approach, (c) is the focused image with the optimum beamforming approach, (d) is the focused image with the signal subspace approach and (e) is the focused image with the noise subspace approach. Compared with the plan view of Boeing-727 as shown in Figure 2.6 (b), the focused images with conventional and optimum beamforming, signal and noise subspace methods are quite impressive.

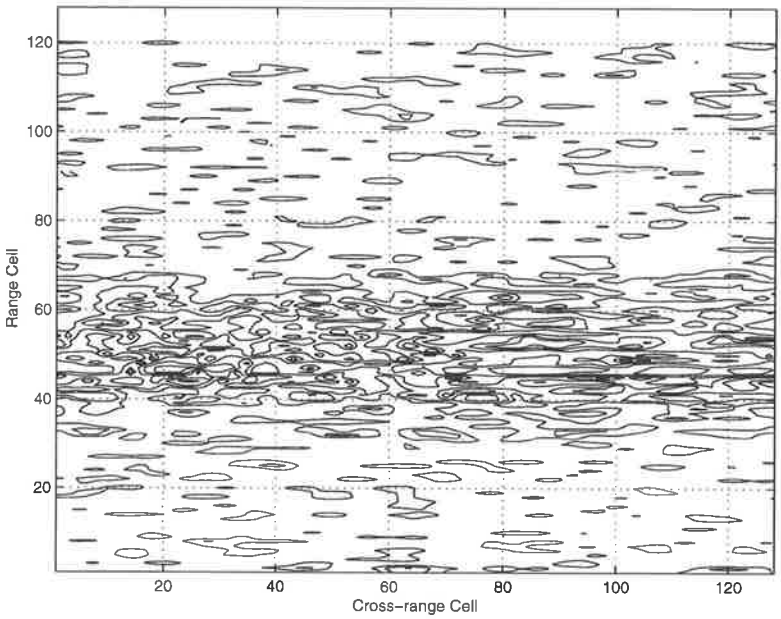

(a) Unfocused image

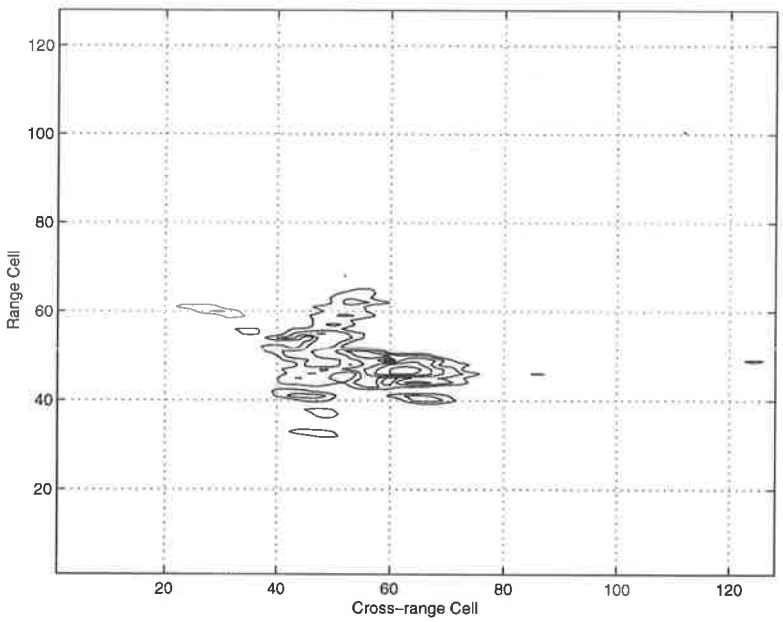

(b) Focused image with the conventional beamforming approach

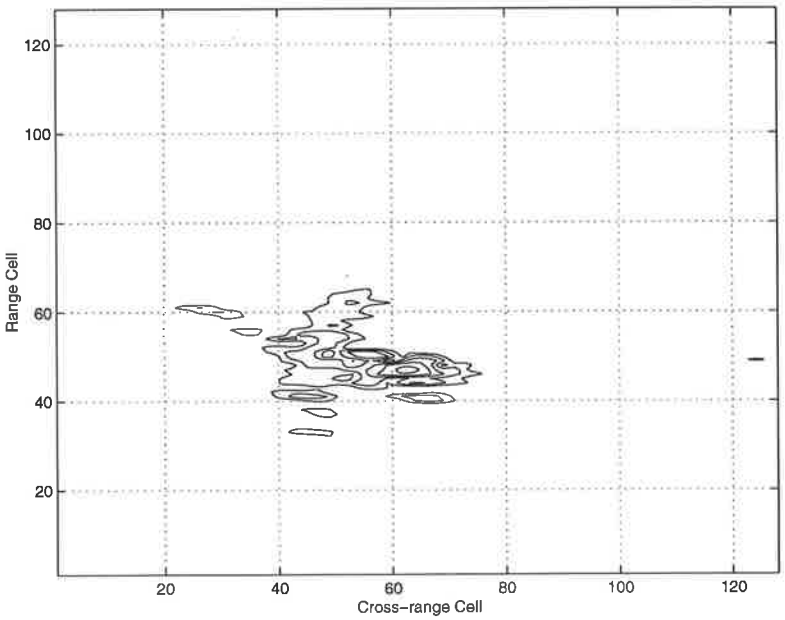

(c) Focused image with the optimum beamforming approach

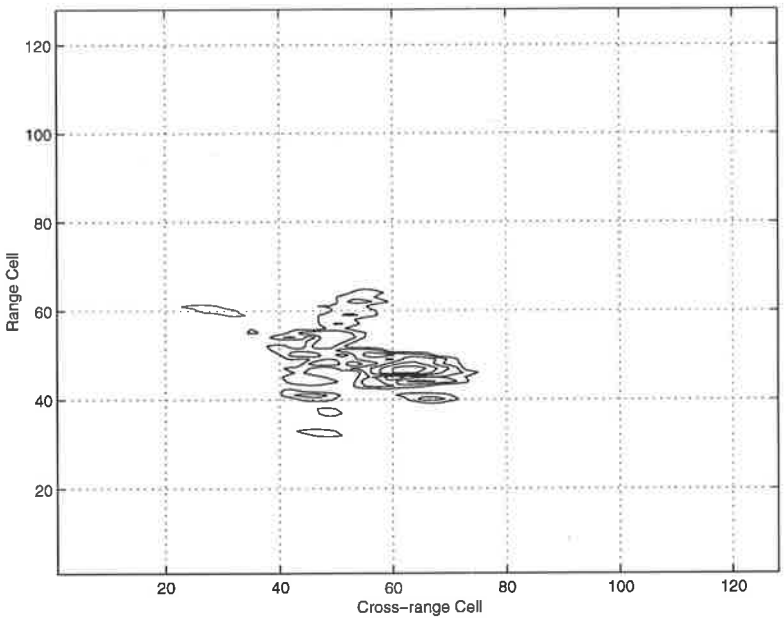

(d) Focused image with the signal subspace approach

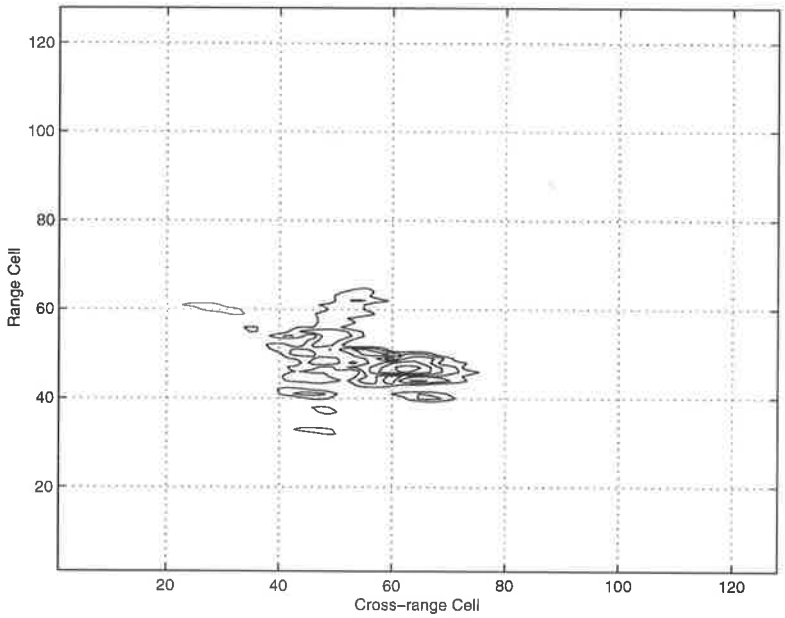

(e) Focused image with the noise subspace approach

Figure 3.13 ISAR images of Boeing-727

Subaperture processing of the signal subspace approach was applied to the real data of the Boeing-727. The ISAR images are shown in Figure 3.14 where (a) $N_s = 2$, $M_s = 16$ and (b) $N_s = 30$, $M_s = 2$. The focusing quality of Figure 3.14 is approximately the same as that of Figure 3.13 (d) (i.e., the signal subspace approach for the entire aperture) because as shown in the next chapter the CRLB of D for ISAR autofocus is almost independent of M if the SNR is high enough. The computations associated with eigendecomposition are listed in Table 3.1 which illustrates that subaperture processing allows a dramatic reduction in computation complexity. The computational loads in Figure 3.14 (a) and (b) are reduced by a factor of 3.637 (124.13/34.13) and 124.13 (124.13/1), respectively, as compared with that in Figure 3.13 (d).

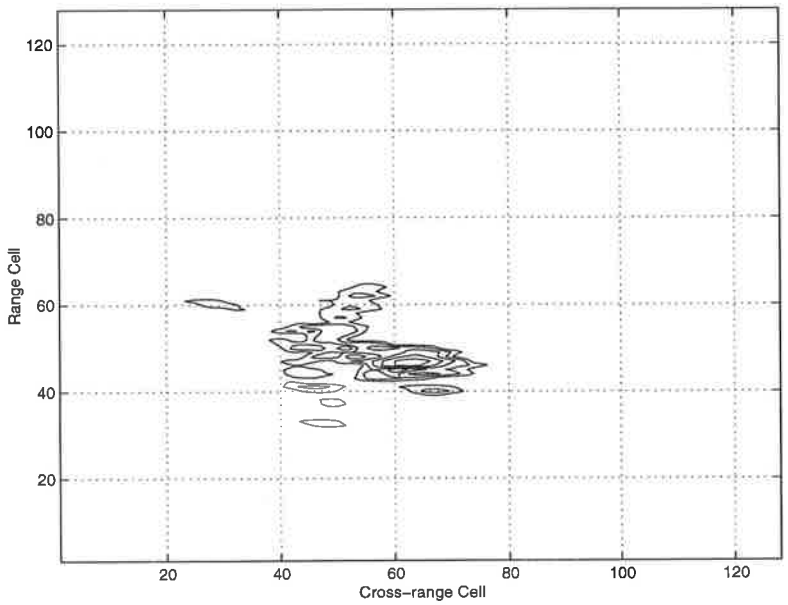

(a) $M_s = 16, N_s = 2$

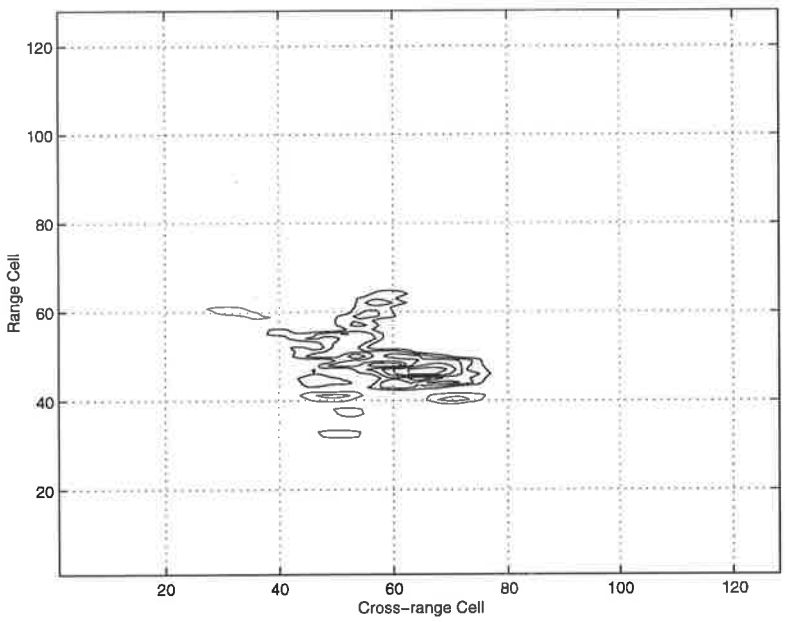

(b) $M_s = 2, N_s = 30$

Figure 3.14 ISAR images of Boeing-727 with subaperture processing

Table 3.1 Computational operations of eigendecomposition

	No subaperture processing in Figure 3.13(d)	Subaperture processing 1 in Figure 3.14 (a)	Subaperture processing 2 in Figure 3.14 (b)
M_s	31	16	2
N_s	1	2	30
$M_s^3 N_s$	29791	8192	240
Normalization	124.13	34.13	1

3.8 Conclusions

The original work reported in this chapter is the application of array processing techniques including conventional beamformer, optimum beamformer, signal subspace and noise subspace to ISAR autofocus. All techniques can be efficiently implemented using eigendecomposition. They are listed below:

1. The signal model of ISAR autofocus is derived based on a point scatterer model which provides a way to obviate the need for phase unwrapping.

2. Conventional and optimum beamformers are used to autofocus ISAR image by adjusting the steering vector to maximize the output power of corresponding beamformer.

3. The signal subspace method is to maximize the projection of the steering vector onto the signal subspace of the covariance matrix. Alternatively the noise subspace method is to minimize the projection of the steering vector onto the noise subspace of the covariance matrix.

4. The subaperture processing is described to reduce the computational complexity. In the extreme case where each subaperture consists of two pulses, the eigendecomposition of covariance matrix may be obviated and replaced by a operation in the data domain which results in a significant reduction in computation.

Computer simulations were conducted and real data were processed for both one-dimensional and two-dimensional ISAR imaging. A simple object consisting of two scatterers was simulated for one-dimensional ISAR imaging. A simulated aircraft model was used for two-dimensional ISAR imaging. One-dimensional ISAR images of a bomber

and two-dimensional ISAR images of Boeing-727 were obtained by processing the real data with the four developed approaches.

The advantages of conventional beamforming, optimum beamforming, signal subspace and noise subspace methods for ISAR autofocus are that the received signals are processed with the covariance matrix rather than signal phase so that the problem of phase unwrapping is obviated. The developed approaches promise to provide a deep insight and potential application to other focusing problems.

Chapter 4 Statistical Analysis of ISAR Autofocus Approaches

4.1 Introduction

The derivations in the previous chapter are based on the assumption that the exact covariance matrices are available. However in practice these must be estimated from a finite number of data samples. In this chapter, we consider ISAR autofocus from an estimation perspective and investigate the statistical performances of the approaches developed in the previous chapter.

The likelihood function is the logarithm of the joint probability density function of the measurement with respect to unknown parameters. The first derivative of the likelihood function determines the position of the peak of the likelihood function, that is, the maximum likelihood (ML) estimation of the unknown parameters. The second derivative of the likelihood function at this peak position determines the limiting accuracy of estimated parameters, i.e., the CRLB [84]. Further the CRLB gives the minimum variance that an unbiased estimator can achieve. Comparison of the errors of estimators with the CRLB enable us to evaluate the accuracy of developed approaches.

Several schemes to estimate the covariance matrix are described in section 4.2. When some strong scatterers exist, the signal subspace approach is simplified into the strong scatterer reference method in section 4.3. Section 4.4 verifies that the signal subspace approach for ISAR autofocus is the ML estimation of complex vector associated with the translational motion of the object. The CRLB of the estimated complex vector related to the translational motion of the object, which is the theoretical bound of ISAR autofocus, is derived in section 4.5. The CRLB of the estimated distance between two scatterers, which

is an indication of the ability of ISAR to resolve spatially separated scatterers, is given in section 4.6. The behaviour of both CRLBs has been analysed as a function of the SNR, number of range cells and number of pulses. Monte-Carlo simulations are conducted in section 4.7; the statistical performances of conventional beamforming, optimum beamforming, signal subspace and noise subspace for calibration are investigated and compared to the CRLBs.

4.2 Covariance Matrix Estimation

In the derivations of section 3.3 and section 3.4, we have used the exact covariance matrix of the vector of received pulses which is defined as

$$C_x = \mathrm{E}\{X_n X_n^H\} \tag{4.1}$$

where E denotes ensemble average. However in practice we only have a single realization (snapshot) and need to derive schemes to sensibly estimate C_x.

By inspection of (3.11) the vector D is independent of range cell index and so the covariance matrix can be estimated by replacing the ensemble average with one over range cells. In the situation of ISAR autofocus, four schemes are proposed to estimate C_x.

1. The ensemble averaging is approximated by averaging over all the range cells, that is,

$$\hat{C}_x = \frac{1}{N}\sum_{i=1}^{N} X_i X_i^H. \tag{4.2}$$

where N is the total number of range cells. This assumes that the estimated covariance is constant for all range cells.

2. The ensemble averaging is approximated by averaging over N_1 to N_2 adjacent range cells, that is,

$$\hat{C}_x = \frac{1}{N_2 - N_1}\sum_{i=N_1}^{N_2} X_i X_i^H. \tag{4.3}$$

The estimated covariance matrix is normally different for each range cell.

3. The ensemble averaging is approximated by averaging over the range cells selected where strong scatterers are located. This results in reduced computational load and SNR enhancement.

4. The entire aperture is divided into many subapertures with the subaperture processing as described in section 3.5. C_x is estimated for each subaperture which has a computational advantage over that for the entire aperture. Then the complex signal vector for the entire aperture is estimated by combining the complex signal vectors estimated for individual subapertures.

The above four schemes to estimate C_x do not guarantee $\hat{C}_x$ to be full rank. When $\hat{C}_x$ is singular, the $\hat{C}_x^{-1}$ will be replaced by the Moore-Penrose generalized inverse or pseudo-inverse of $\hat{C}_x$.

4.3 Relation to Strong Scatterer Reference Method

The strong scatterer reference method depends upon the existence of a prominent scatterer[10]. As pointed out in section 3.2, the approaches developed in the previous chapter do not need this condition. However if some strong scatterers are detected, they are related to the strong scatterer reference method under certain approximation. If a dominant strong scatterer exists in the n_1 th range cell, $\hat{C}_x$ can be approximated as

$$\hat{C}_x \approx X_{n_1} X_{n_1}^H + \hat{\sigma}_1^2 I \tag{4.4}$$

where $\hat{\sigma}_1^2$ is the estimated power of additive noise. In this case, the largest eigenvalue of $\hat{C}_x$ is $\|X_{n_1}\|^2 + \hat{\sigma}_1^2$ where $\|\ \|$ is the Euclidean norm and the corresponding eigenvector of the signal subspace is

$$u_1 = X_{n_1}. \tag{4.5}$$

(4.5) is equivalent to the strong scatterer referencing method[10]. Consequently if a dominate strong scatterer exists, the signal subspace approach simplifies to the strong scatterer reference method.

If K strong scatterers exist in the range cells labelled $n_1, n_2, \ldots n_K$, $\hat{C}_x$ has an approximation

$$\hat{C}_x \equiv \frac{1}{K}\sum_{i=1}^{K} X_{n_i} X_{n_i}^H + \hat{\sigma}_2^2 I. \tag{4.6}$$

In this situation, the signal subspace approach fuses the signals of strong scatterers to do autofocus which is similar to multiple scatterer algorithm (MSA)[12] and recursive MSA (RMSA)[13]. But the signal subspace approach combines the signals of strong scatterers by estimating the covariance matrix averaged over them. MSA and RMSA calculate the average phase of the signals of strong scatterers which needs to unwrap the phase. Therefore the signal subspace method obviates the problem of phase unwrapping.

A strong scatterer was detected in the real data of the Boeing-727 as described in section 3.7.2 by use of the criterion of minimal normalized amplitude variance[10]. The ISAR image autofocused with this strong scatterer is shown in Figure 4.1 which is comparable to Figure 3.13 (b) - (e).

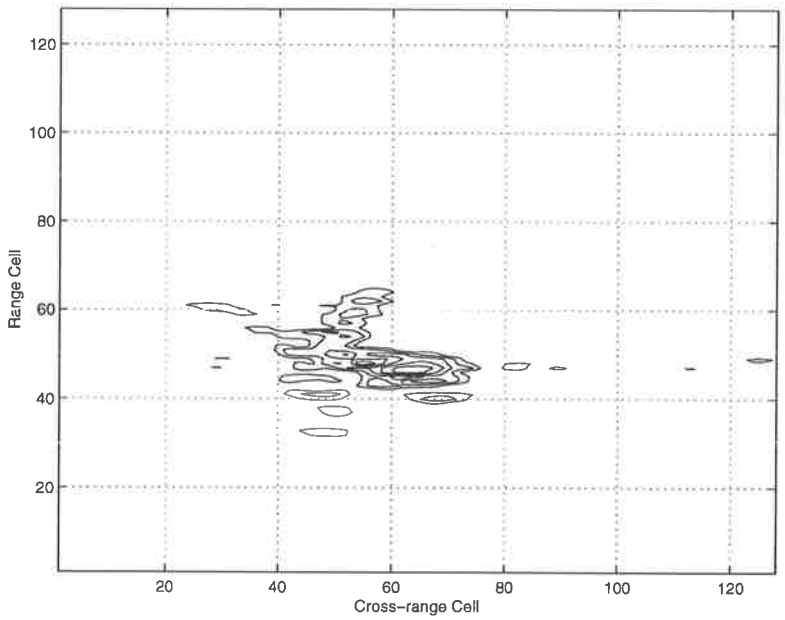

Figure 4.1 ISAR image of Boeing-727 with the strong scatterer reference

4.4 ML Estimation for ISAR Autofocus

ISAR autofocus requires the estimation of the complex vector D corresponding to the translational motion of object and it is shown here that the signal subspace approach is a ML estimator for D. This estimate is formed by choosing that D which maximizes the joint probability density of the set of observations. If the received noise is assumed to be Gaussian distributed, the joint probability density function of a single observation is

$$p(X;D) = \pi^{-M}\{\det(C_x)\}^{-1}\exp\{-X^H C_x^{-1} X\} \tag{4.7}$$

where $\det(\ )$ denotes the determinant of a matrix. For multiple observations, the joint probability density function of multiple independent observations is given by

$$p(X_1, \ldots, X_N;D) = \pi^{-MN}\{\det(C_x)\}^{-N}\exp\{-N\,\mathrm{Tr}\left(C_x^{-1}\hat{C}_x\right)\} \tag{4.8}$$

where $\hat{C}_x = \frac{1}{N}\sum_{n=1}^{N} X_n X_n^H$ is an estimator of the covariance matrix and $\mathrm{Tr}(\ )$ stands for the trace of a matrix. Maximizing the log probability density function with respect to D leads to minimization of

$$l(D) = N\ln(\det(C_x)) + \mathrm{Tr}\left(C_x^{-1}\hat{C}_x\right) \tag{4.9}$$

where $C_x = p_n DD^H + C_w$ and C_w is the covariance matrix of noise. ML estimation generally requires a numerical optimization algorithm[232], however the ML estimator of D has an explicit solution. Minimizing (4.9) results in the following equation[86]

$$\tilde{C}u_1 = \lambda_{max}u_1 \tag{4.10}$$

where $\tilde{C} = C_w^{-\frac{H}{2}}\hat{C}_x C_w^{-\frac{1}{2}}$, λ_{max} is the maximal eigenvalue of $\tilde{C}$ and u_1 is the corresponding eigenvector.

If the receiver noise is spatially uncorrelated and has an equal power, that is, $C_w = \sigma_w^2 I$, (4.10) can be changed into

$$\hat{C}_x u_1 = \lambda'_{max}u_1 \tag{4.11}$$

where $\lambda'_{max} = \lambda_{max}\sigma_w^2$. (4.11) indicates that the eigenvector corresponding to the maximal eigenvalue of $\hat{C}_x$ is the ML estimation of D.

If the receiver noise is spatially correlated with known covariance matrix C_w, the standard prewhitening technique can be used. An example of a situation in which the receiver noise is spatially correlated arises from multiple path propagation. The eigenvector u_1 of $\tilde{C}$ corresponding to maximal eigenvalue is estimated and the generalized eigenvector of $\hat{C}_x$ corresponding to maximal eigenvalue can be calculated by $C_w^{H/2}u_1$ although there are considerable difficulties associated with estimating C_w in practice.

4.5 CRLB of the Estimated Complex Vector

In (3.11), D is the complex vector associated with the translational motion of the object. The CRLB of D indicates the accuracy limitation of ISAR autofocus. The CRLB of D treated as a fixed, non-random but unknown vector is derived below.

The estimation variance of a complex variable is at first defined, then the relation of this variance to the estimation variances of its real and imagery parts is found and finally the estimation variances of the real and imagery parts are computed. Define the variance of the mth element of the complex vector D as

$$\mathrm{Var}\,(\hat{D}_m) \;=\; \mathrm{E}\{\left|\hat{D}_m - D_m\right|^2\}\,. \tag{4.12}$$

It can be shown that [87]

$$\mathrm{Var}\left(\hat{D}_m\right) \geq 4\left(J_D^{-1}\right)_{mm} \tag{4.13}$$

where J_D^{-1} is the inverse of the complex Fisher's information matrix J_D. The elements of J_D are calculated as

$$(J_D)_{mn} \;=\; -\mathrm{E}\left\{\frac{\partial^2}{\partial D_m \partial D_n}\ln p\,(X;D)\right\} \tag{4.14}$$

where $\dfrac{\partial}{\partial D_m}$ is a complex operator defined by

$$\frac{\partial}{\partial D_m} \;=\; \frac{\partial}{\partial u_m} + j\frac{\partial}{\partial w_m} \tag{4.15}$$

where $D_m \;=\; u_m + jw_m$.

However (4.13) is not the best lower bound attainable and it is more appropriate to consider the real and imaginary parts separately. For the real and the imaginary components of D_m, we have

$$\mathrm{Var}\,(\hat{u}_m) \geq \left(J_u^{-1}\right)_{mm}, \tag{4.16}$$

$$\mathrm{Var}\,(\hat{w}_m) \geq \left(J_w^{-1}\right)_{mm}. \tag{4.17}$$

By use of $\mathrm{Var}\left(\hat{D}_m\right) = \mathrm{Var}\,(\hat{u}_m) + \mathrm{Var}\,(\hat{w}_m)$ and $(J_D)_{mm} = (J_u)_{mm} + (J_w)_{mm}$, we have

$$\mathrm{Var}\left(\hat{D}_m\right) \geq \left(J_u^{-1}\right)_{mm} + \left(J_w^{-1}\right)_{mm} \geq 4\left(J_D^{-1}\right)_{mm}. \tag{4.18}$$

Thus a low bound that an estimator can reach easily is $\left(J_u^{-1}\right)_{mm} + \left(J_w^{-1}\right)_{mm}$ rather than $4\left(J_D^{-1}\right)_{mm}$ as was given in [87]. $\left(J_u^{-1}\right)_{mm} + \left(J_w^{-1}\right)_{mm}$ is calculated below.

In general the CRLB may be computed by a numerical method, however a closed-form expression for the CRLB of D can be found and is given below. In the signal model of (3.11), we assume that both e_{n0} and D are unknown where e_{n0} is the signal in the nth range cell. Thus an ambiguity occurs when e_{n0} and D become ke_{n0} and $k^{-1}D$, respectively. If we set constraints $e_0^{\,H} e_0 = N$ where $e_0 = (e_{00}, \ldots, e_{N-1,0})^T$ and $\mathrm{Im}\,(e_{00}) = 0$, the ambiguity will be removed [88].

Let $D = u + jw$ and $e_0 = r + jt$ with constraints $t_0 = 0$ and $e_0^{\,H} e_0 = N$. Based on the derivation in [88], the CRLBs of u and w are given by

$$\left(J_u^{-1}\right)_{mm} = \frac{1}{2N}(P)_{mm} + \beta w_m^2 \tag{4.19}$$

$$\left(J_w^{-1}\right)_{mm} = \frac{1}{2N}(P)_{mm} + \beta u_m^2 \tag{4.20}$$

where the noise covariance matrix $C_w = P + jQ$, u_m the mth element of the vector u, $\beta = (N - p_0) / \left(2Np_0\left[D^H C_w^{-1} D\right]\right)$, $p_0 = |e_{00}|^2$ and $(P)_{mm}$ the mth diagonal element of the matrix P. Thus the CRLB of D_m takes the form

$$\mathrm{CRLB}\,(D_m) = \frac{1}{N}(P)_{mm} + \beta. \tag{4.21}$$

4.6 CRLB of the Estimated Distance Between Two Scatterers

The accuracy of the estimated distance between two scatterers separated in cross-range is one figure of merit of ISAR resolving capability and the CRLB for this is derived below.

In this analysis, the object is composed of two scatterers A and B with the coordinates (x_1, y_1) and (x_2, y_2) as shown in Figure 4.2. When the distance between the radar and the object is much larger than the size of object, the returned signal of the mth pulse can be approximated as

$$z_m = \rho_1 \exp\{-j\frac{4\pi}{\lambda}[r_m + x_1 \sin\theta_m + y_1 \cos\theta_m]\} + \rho_2 \exp\{-j\frac{4\pi}{\lambda}[r_m + x_2 \sin\theta_m + y_2 \cos\theta_m]\} + w_m \quad (4.22)$$

where ρ_1 and ρ_2 are proportional to the reflectivities of A and B, respectively. r_m denotes the distance between the radar and the centre of the two scatterers when the mth pulse is sent. w_m is the additive noise which is the independent identically distributed complex Gaussian noise component with zero mean and variance σ_w^2.

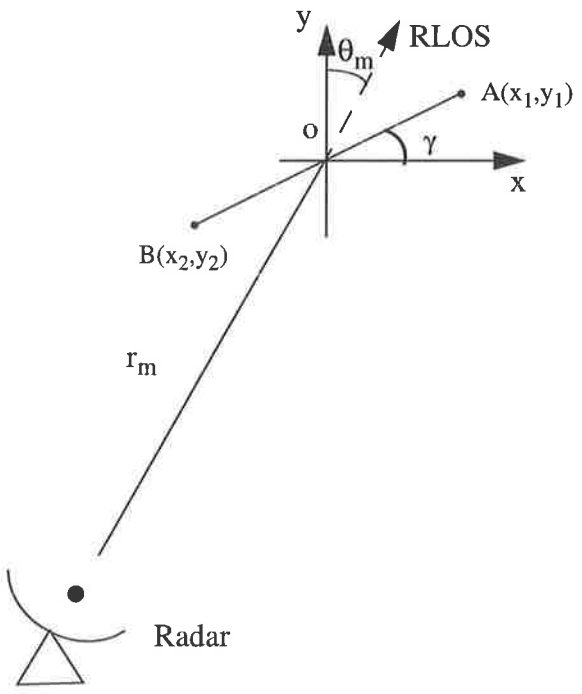

Figure 4.2 ISAR imaging of two scatterers

Assuming, for simplicity, $\rho_1 = \rho_2 = \rho$, (4.22) becomes

$$z_m = 2\rho\cos\{\frac{2\pi}{\lambda}d\sin[\theta_m+\gamma]\}u_m + w_m \tag{4.23}$$

where d is the distance between the two scatterers, γ is the angle between the x axis and a straight line through the point A and the point B, and $u_m = \exp\{-j\frac{2\pi}{\lambda}[2r_m + (x_1+x_2)\sin\theta_m + (y_1+y_2)\cos\theta_m]\}$. The probability density function of complex variable w_m is

$$p(w) = \frac{1}{\pi\sigma_w^2}\exp\left\{-\frac{|w|^2}{\sigma_w^2}\right\}. \tag{4.24}$$

If γ, θ_m and u_m are assumed to be known, the joint probability density function of a single observation is

$$p(z_m;d) = \frac{1}{\pi\sigma_w^2}\exp\left\{-\frac{\left|z_m - 2\rho\cos\{\frac{2\pi}{\lambda}d\sin[\theta_m+\gamma]\}u_m\right|^2}{\sigma_w^2}\right\} \tag{4.25}$$

and the joint probability density function of multiple independent observations is

$$\begin{aligned} p(z_0,\ldots,z_{M-1};d) &= \prod_{m=0}^{M-1} p(z_m;d) \\ &= (\pi\sigma_w^2)^{-M}\exp\left\{-\frac{1}{\sigma_w^2}\sum_{m=0}^{M-1}\left|z_m - 2\rho\cos\{\frac{2\pi d}{\lambda}\sin[\theta_m+\gamma]\}u_m\right|^2\right\} \end{aligned} \tag{4.26}$$

Thus we get the log joint probability density function

$$l(z_0,\ldots,z_{M-1};d) = -M\ln\left(\pi\sigma_w^2\right) - \frac{1}{\sigma_w^2}\sum_{m=0}^{M-1}\left|z_m - 2\rho\cos\{\frac{2\pi d}{\lambda}\sin[\theta_m+\gamma]\}u_m\right|^2. \tag{4.27}$$

The lower bound of estimated variance, CRLB, is defined by[184]

$$\mathrm{CRLB}(d) = \left[-\mathrm{E}\left(\frac{\partial^2 l}{\partial d^2}\right)\right]^{-1}. \tag{4.28}$$

From Appendix C the CRLB of d is given by

$$\text{CRLB}(d) = \frac{\lambda^2}{32\pi^2 \,\text{SNR} \sum_{m=0}^{M-1} \sin[\theta_m + \gamma]^2 \sin\{\frac{2\pi d}{\lambda}\sin[\theta_m + \gamma]\}^2} \tag{4.29}$$

where $\text{SNR} = \rho^2/\sigma_w^2$ denotes the signal-to-noise ratio (SNR). The important result is that this CRLB is independent of u_m and consequently it is not required to be known. It is noted that in the above derivations we have actually formed the CRLB under the assumption that γ, $\{\theta_m\}$ and SNR are all known. In practice this may not be the case; however for comparison of different methods this approach is justified.

4.7 Statistical Performance

In order to inspect the statistical performance of the conventional beamforming, the optimum beamforming, the signal subspace and the noise subspace approaches for ISAR autofocus, Monte-Carlo simulations were conducted. In the simulation, w_m was independent identically distributed complex Gaussian noise components with zero mean and variance σ_w^2. Thus we had $C_w = \sigma_w^2 I_M$. The CRLB of each component corresponding to the translational motion from (4.21) takes the form

$$\text{CRLB}(D_m) = \left(1 - \frac{1}{2M}\right)\frac{\sigma_w^2}{N} + \frac{1}{2M\,\text{SNR}} \tag{4.30}$$

where $\text{SNR} = p_0/\sigma_w^2$. The term σ_w^2/N is related to SNR due to the constraint $e_0^H e_0 = N$ in the derivation of CRLB.

Figure 4.3 gives the CRLBs for various values of N (the number of range cells) with $M = 128$ (the number of pulses) and $\sigma_w^2 = 1$. It shows that the CRLBs of D decrease with the increase of N and SNR. They are approximately proportional to $1/N$ if the SNR is high enough. The CRLB reaches 0 dB, −10 dB and −20 dB when N is equal to 1, 10 and 100, respectively, in the case of high SNR.

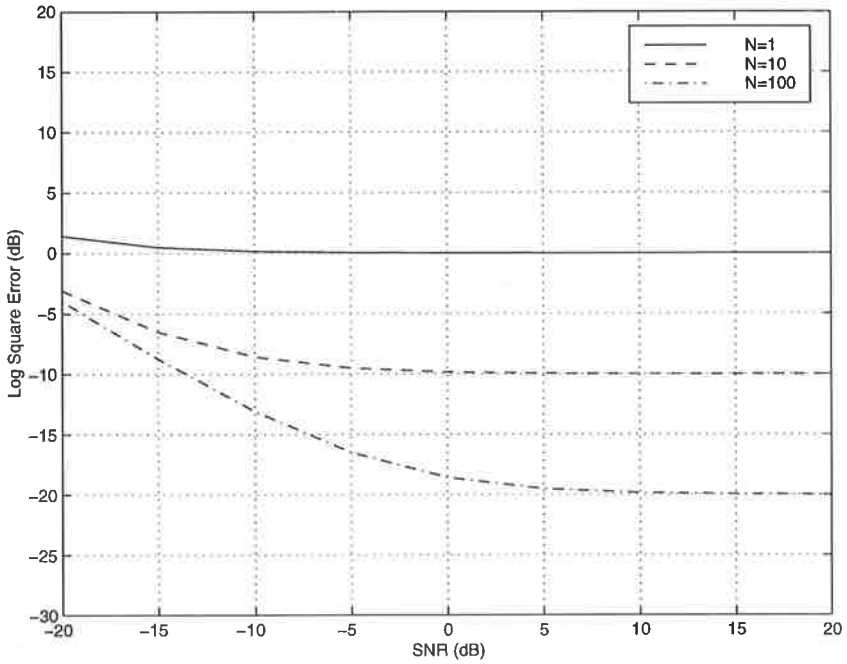

Figure 4.3 The CRLBs versus SNR for three N values

The CRLBs for $N = 10$ and three values of M are shown in Figure 4.4. We see that the difference between them becomes indiscernible in the case of high SNR. In other words the CRLB is almost independent of M if SNR is high enough where the CRLB approaches -10 dB . This means that the subaperture processing is more effective for high SNR.

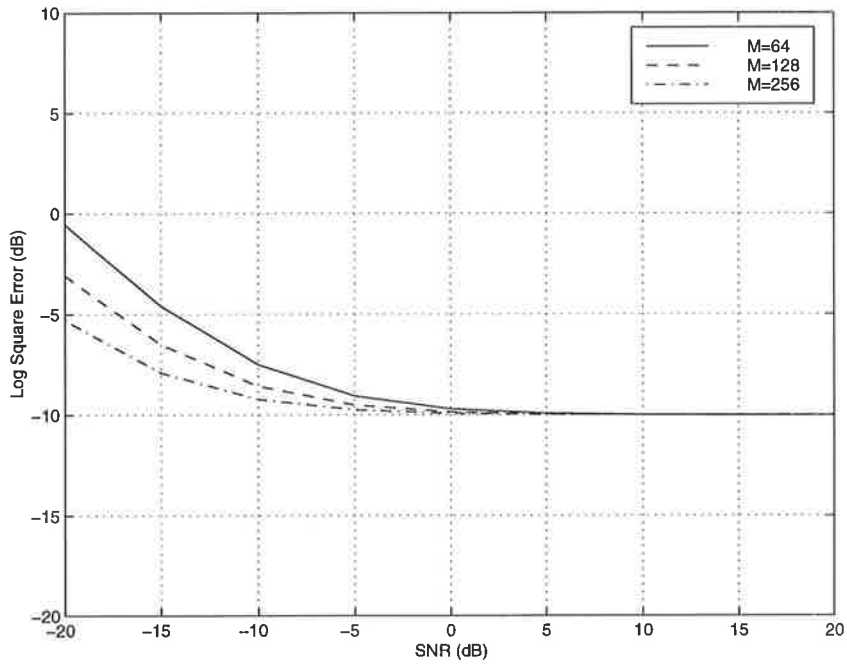

Figure 4.4 The CRLBs versus SNR for three M values

The parameters of ISAR simulation were described in section 3.6.1. The statistics were based on 100 simulations for each estimator at the specified SNR level. The mean square errors of the complex vector estimated by the conventional beamforming approach (P_c), the optimum beamforming approach (P_o), the signal subspace approach (P_s) and the noise subspace approach (P_n) versus SNR are shown in Figure 4.5 and compared with the CRLB for $M = 128$ and $N = 10$. The figure indicates that P_c, P_s and P_n approach the CRLB when $\text{SNR} \geq 0$ dB and P_o reaches the CRLB as $\text{SNR} \geq 5$ dB.

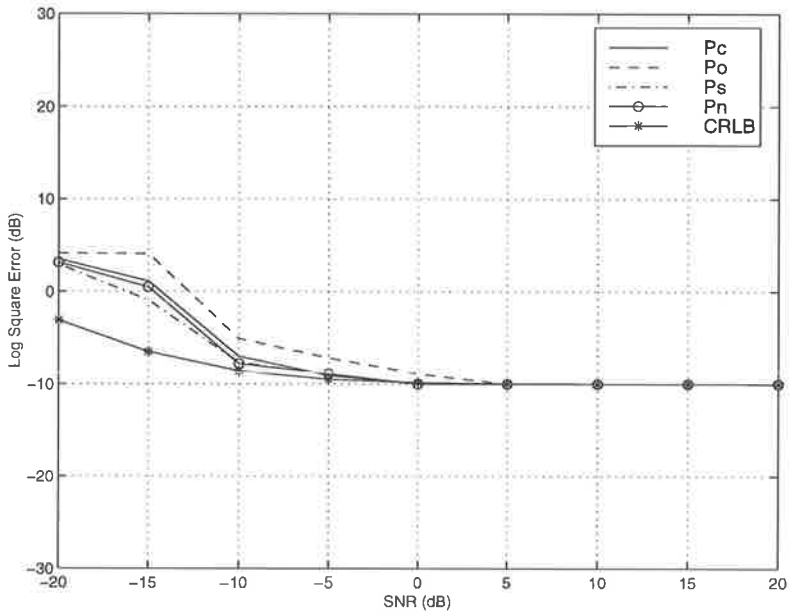

Figure 4.5 Mean square error of the estimated complex vector

Monte-Carlo simulations were also conducted to analyse the accuracies of four ISAR autofocus approaches for estimating the distance between two scatterers. The parameters of simulation were available in section 3.6.1. After ISAR autofocus, ISAR images were produced and the distance between the two scatterer was estimated by detecting the peak position corresponding to the two scatterers. The statistics were based on 100 simulations for each estimator at the specified SNR level. Figure 4.6(a) shows the bias (mean error) of the estimated distance between the two scatterers determined by P_c, P_o, P_s and P_n versus SNR. It indicates that the SNR thresholds of the four approaches are -5 dB. When SNR is higher than -5 dB, the bias of these methods approaches zero. This means that the four approaches are the statistical unbiased estimators in this case. If SNR is below -5 dB, the bias increases.

The mean square errors of the estimated distance between two scatterers determined by the four approaches are given in Figure 4.6(b) and compared with the CRLB. It is illustrated that the experimental variances of the conventional beamforming, the signal subspace and the noise subspace approaches reach the CRLB when $SNR \geq 15$ dB . This means that they are statistically efficient. Although the optimum beamforming approach does not reach the CRLB, the mean square error is close to the CRLB as SNR increases.

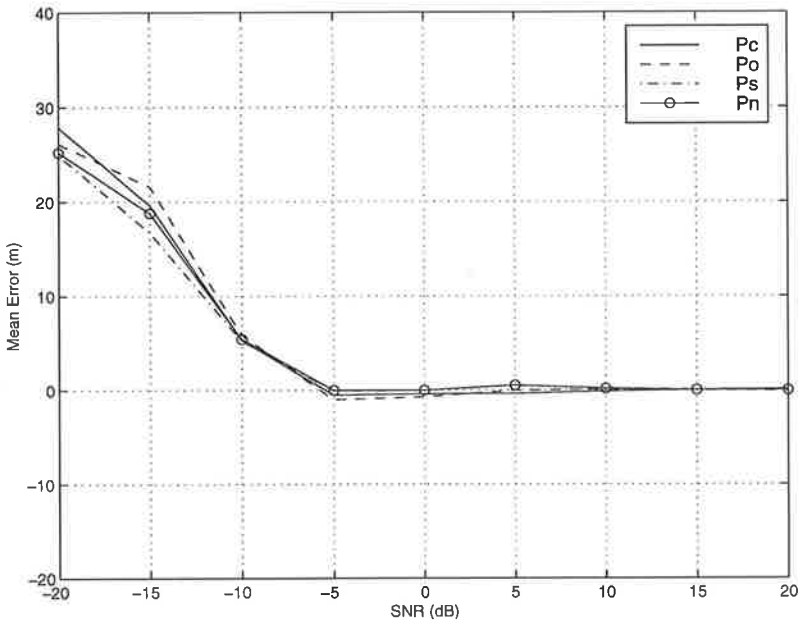

(a) Bias

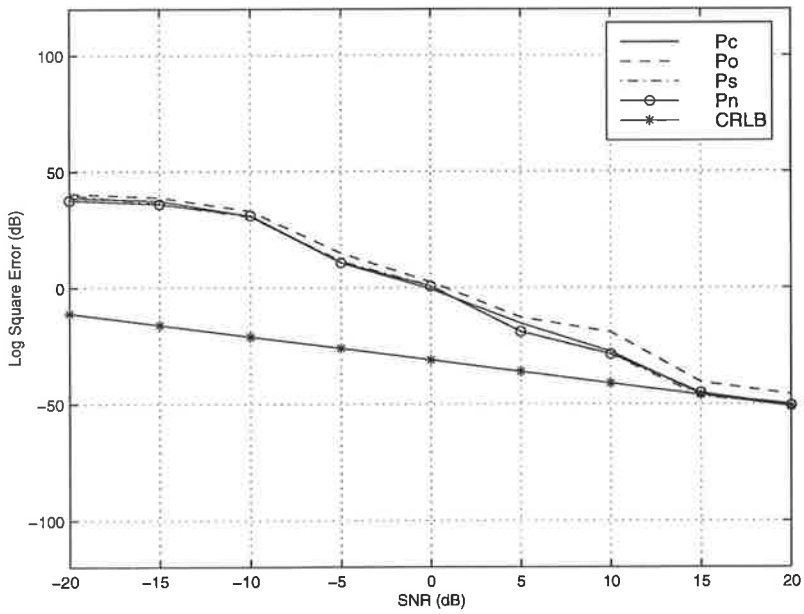

(b) Mean square error

Figure 4.6 Bias and mean square error of the estimated distance between two scatterers

4.8 Conclusions

ISAR autofocus was studied from a statistical point of view and schemes to estimate the covariance matrix were given. If several strong scatterers are detected, the signal subspace approach was shown to be related to the strong scatterer reference method. The signal subspace approach has been identified as the ML estimation of the complex signal vector associated with ISAR autofocus. The theoretical low bounds for the mean square errors of the estimated complex vector related to the translational motion of the object and the estimated distance between two scatterers were derived. The CRLB of the complex vector corresponding to the translational motion of object decreases with the increase of SNR and the number of range cells. However it is approximately independent of the number of transmitted pulses for high SNR which means that the subaperture processing is particularly attractive in this situation. The CRLB of the estimated distance between two scatterers is inversely proportional to SNR. Monte-Carlo simulations have demonstrated that CRLBs appear to be a very tight bound on estimator performance for the approaches developed in the previous chapter.

Chapter 5 3D SAR Imaging Via MPSAR Processing

5.1 Introduction

As described in chapter 2, SAR is able to produce a two-dimensional high resolution image in the range and azimuthal directions. The high range resolution is obtained by transmitting a wide-band signal and the high azimuthal resolution is achieved by synthesizing an azimuthal aperture. InSAR is a technique which uses two SAR imaging flight passes to produce the interferogram and reconstruct the digital elevation models (DEM) by unwrapping the principal phase value of the interferogram. MPSAR (Multiple Pass SAR) imaging is an extension of InSAR. It makes use of more than two SAR imaging flight passes to synthesise an aperture in elevation which results in improved accuracy and resolving power in the elevational direction [89] [90]. The resulting resolution in elevation, combined with the resolving capability of single-pass SAR imagery in range and azimuth, produces a 3D SAR image. This chapter investigates the theory of 3D SAR imaging and develops the approach to 3D SAR image reconstruction via MPSAR processing.

The mathematical model of 3D SAR imaging is first presented in section 5.2. Then an algorithm for 3D SAR imaging via MPSAR processing is developed in section 5.3. Compared with InSAR benefits of MPSAR processing are highlighted in section 5.4. Computer simulation is described in section 5.5 and the results of processing ERS-1 data are shown in section 5.6 which confirm the effectiveness of MPSAR processing.

5.2 Mathematical Model of 3D SAR Imaging

MPSAR imaging makes use of more than two flight passes which are parallel and equi-spaced in elevation as shown in Figure 5.1 where x and z represent the ground range and elevation, respectively. P_i denotes the ith flight path where $i = 1, \ldots, N_p$. For each flight path, the radar transmits a wideband signal and the returns are processed coherently to produce a complex SAR image $G_i(x, y)$ where x and y are the ground range and azimuth coordinates. This SAR image formation step involves conventional processing.

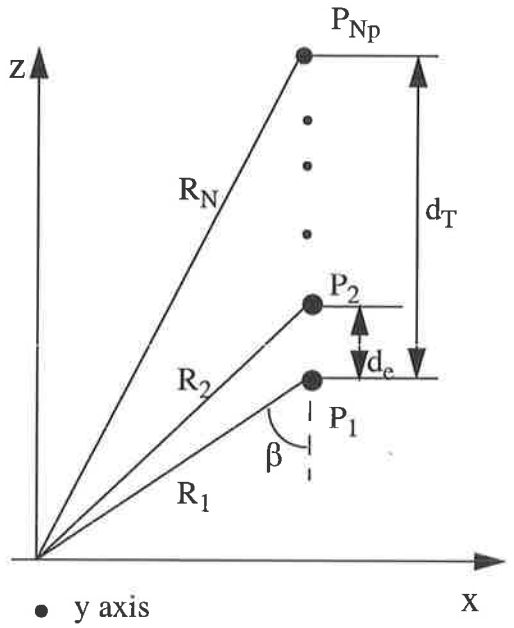

Figure 5.1 Flight path distribution of MPSAR

The set of complex SAR images $G_i(x, y)$ i=1,…, N_p undergoes a post-processing stage to produce a 3D image. This stage involving image registration, phase correction and elevational processing of each pixel in all images is presented below. In other words, if we consider the set of image $G_i(x, y)$ i=1,…, N_p as a single 3D image $G(x, y, i)$, then this processing stage is applied along the i-axis of the image. The resulting 3D image is the range-azimuth-elevation image $\rho(x, y, z)$ of the observed terrain.

Now we develop the mathematical model of 3D SAR imaging and its interpretation will help understanding of the processing steps of 3D SAR imaging presented in the next section. Figure 5.2 shows the geometry of 3D SAR imaging. The ground range, azimuth and elevation coordinates are represented by x, y and z, respectively. Consider a terrain

patch whose centre is taken as the origin. The patch is assumed to be composed of a finite number of point scatterers spread on its surface, each having its own elevation. Slant ranges from the closest point B of approach for each flight path to the patch centre o and scene point A with coordinates (x, y, z) are denoted by R_0 and R, respectively.

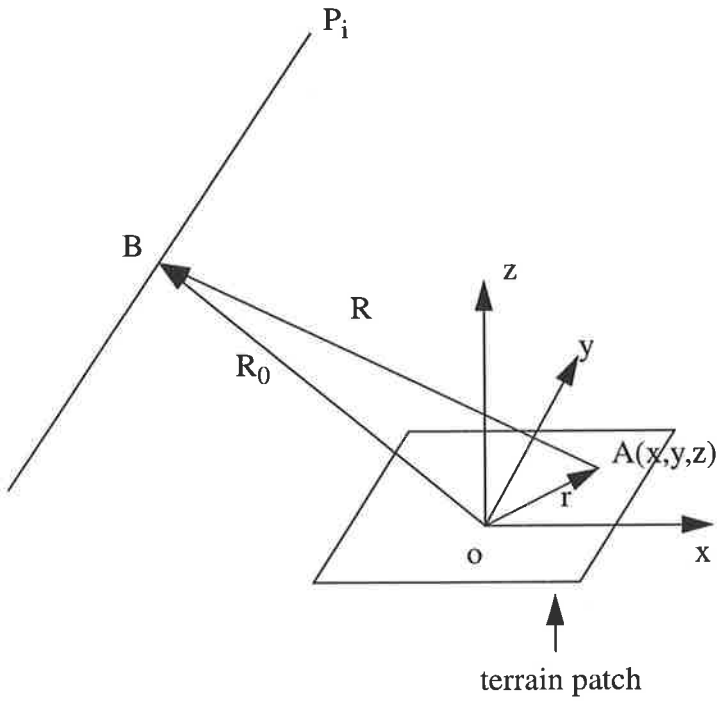

Figure 5.2 3D SAR imaging geometry

For a transmitted signal, $u(t)$, the received signal, $s_r(t, R_0)$, from point scatterer A is

$$s_r(t, R_0) = \rho(x, y, z)\, u\left(t - \frac{2R(x, y, z)}{c}\right) \tag{5.1}$$

where $\rho(x, y, z)$ is the reflectivity of A which is assumed to be independent of frequency and aspect angle. The total received signal from all scatterers of the distributed object is given by

$$s_r(t, R_0) = \int_V \rho(x, y, z)\, u\left(t - \frac{2R(x, y, z)}{c}\right) dx\, dy\, dz \tag{5.2}$$

where the vector $\mathbf{r}$ is from the origin to the differential scattering volume element $dx\, dy\, dz$ as shown in Figure 5.2 and $\rho(x, y, z)$ is the reflectivity density which includes propagation effects and various system gains for convenience. The integration is carried

out over a terrain volume V. If we take the Fourier transform of (5.2) with respect to t, we obtain

$$S(f, R_0) = U(f) \int_V \rho(x, y, z) \exp\left(-j\frac{4\pi f R(x, y, z)}{c}\right) dx\, dy\, dz \tag{5.3}$$

where $U(f)$ is the complex Fourier spectrum of the transmitted signal. The output of a filter $H(f, R_0) = U^*(f) \exp\left(j\frac{4\pi f R_0}{c}\right)$ matched to a reflection of the transmitted wavefront from an ideal scatterer [1] at the origin o is given by

$$S_o(f, R_0) = S(f, R_0) H(f, R_0) = |U(f)|^2 \int_V \rho(x, y, z) \exp\{-j\frac{4\pi f}{c} R(x, y, z) - R_0\}\, dx\, dy\, dz \tag{5.4}$$

where R_0 is assumed to be known. If the range of the terrain is large compared with the size of the terrain patch, that is, $R(x, y, z) \gg r(x, y, z)$, we have the approximation

$$R(x, y, z) \cong R_0 - \frac{\mathbf{r}(x, y, z) \cdot \mathbf{R}_0}{R_0} \tag{5.5}$$

where $\mathbf{r}(x, y, z)$ and $\mathbf{R}_0$ are the corresponding range vectors as shown in Figure 5.2. Define a vector $\boldsymbol{q}$ of the reference point as

$$\boldsymbol{q} = \frac{2f}{c}\frac{\mathbf{R}_0}{R_0}. \tag{5.6}$$

For a specific frequency, $\boldsymbol{q}$ lies on the surface of a sphere as $\mathbf{R}_0$ is varied. For various frequencies, $\boldsymbol{q}$ is mapped into a vector in a 3D data space (q_x, q_y, q_z). Thus we have

$$S_o(\boldsymbol{q}) = |U(f)|^2 \int_V \rho(x, y, z) \exp\{j2\pi \boldsymbol{q} \cdot \mathbf{r}(x, y, z)\}\, dxdydz. \tag{5.7}$$

This implies that except for the factor $|U(f)|^2$ the output of motion compensation is a finite inverse three-dimensional Fourier transform of the terrain reflectivity function $\rho(x, y, z)$. This model is consistent with the result in [33].

The support region of $\boldsymbol{q}$ is shown in the data domain[33]. Each pulse is corresponding to a solid radial line as shown in Figure 5.3 (a). Single flight path results in a shaded section region as shown in Figure 5.3 (a). MPSAR processing produces a volume in a three-

[1] This is the reference point for motion compensation.

dimensional data space V_f which is composed of slices of 2D data recorded for various flight paths as shown in Figure 5.3 (b). Letting $\boldsymbol{q} = (q_x, q_y, q_z)$ and $\mathbf{r} = (x, y, z)$ then $\rho(x, y, z)$ can be estimated by the 3D Fourier transform of $\frac{S_o(q_x, q_y, q_z)}{|U(f)|^2}$ over limited support region V_f, that is,

$$\rho(x, y, z) = \iiint_{q_x q_y q_z} \frac{S_o(q_x, q_y, q_z)}{|U(f)|^2} \exp\{-j2\pi(xq_x + yq_y + zq_z)\}\, dq_z\, dq_y\, dq_x \tag{5.8}$$

as shown in Figure 5.3 (c).

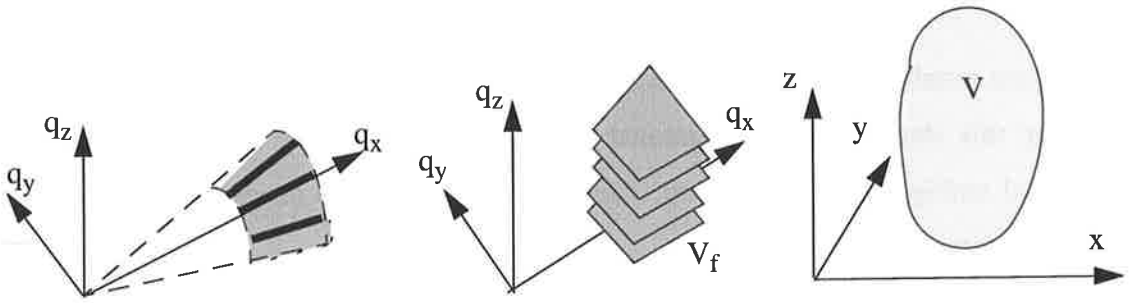

(a) Single flight path data (b) Multiple flight path data (c) Image of object

Figure 5.3 3D data and image space

The equation (5.8) indicates that the 3D reflectivity function $\rho(x, y, z)$ can be estimated by three 1D Fourier transforms. These may be realized by wideband pulse compression in x direction, azimuthal processing in y direction and elevational processing in z direction. If the complex image of each flight path is available, (5.8) can be changed into

$$\rho(x, y, z) = \int_{q_z} G'(x, y, q_z) \exp\{-j2\pi z q_z\}\, dq_z \tag{5.9}$$

where $G'(x, y, q_z) = \iint_{q_x q_y} S_o(q_x, q_y, q_z) / |U(f)|^2 \exp\{-j2\pi(xq_x + yq_y)\}\, dq_y\, dq_x$ represents a SAR complex image of single flight pass after motion compensation. (5.9) shows that with MPSAR processing, $\rho(x, y, z)$, the 3D image, can be estimated by doing a one-dimensional Fourier transform in each pixel cell of the multiple SAR complex image set. In practice, we only have discrete flight passes. Thus we have

$$\rho(x, y, z) = \sum_{i=1}^{N_p} G'(x, y, i) \exp\{-j2\pi z q_i\} \tag{5.10}$$

where $G'(x, y, i)$ denotes the complex SAR image of i the flight path after motion compensation. The spacing of adjacent flight paths d_e determines the maximum elevational distance u_e that can be unambiguously estimated via the relationship

$$u_e = \frac{\lambda R_0}{2d_e}. \tag{5.11}$$

The elevational resolution τ_e depends on the aperture length d_T in the elevational direction by

$$\tau_e = \frac{\lambda R_0}{2d_T}. \tag{5.12}$$

For a given number of flight paths, a small baseline d_e reduces the ambiguity problem. However this degrades the elevational resolution. There is a compromise between elevational ambiguity and resolution. The baseline distribution needs to be designed for specific requirement.

5.3 MPSAR Processing Approach

Each flight pass performs conventional SAR processing including complex I, Q data collection, range compression, quadratic phase correction and azimuthal compression which results in multiple complex SAR images. However rather than forming the absolute value of the complex image at the last step, MPSAR processing uses each SAR image in its complex form. Clearly the N_p complex SAR images $G_i(x, y)$ have different phases for different values of i, which contain the information about the reflectivity distribution along the elevational direction. The main function of MPSAR processing is to extract the reflectivity distribution in the elevation from the N_p complex SAR images. In its simplest form, the elevational imaging involves a straightforward Fourier transform of N_p points along the i-axis of $G'(x, y, i)$ as shown in (5.10).

In the analysis of section 5.2, the motion of the SAR platform is assumed to be known so that motion compensation is conducted precisely. However in practical applications, the flight path is unknown or not known precisely causing individual complex SAR images to be misaligned in the range and azimuth directions. This uncertainty of the flight path

induces an unknown phase factor, and thus each complex SAR image $G_i(x, y)$ needs to be calibrated or corrected in phase prior to elevational imaging, namely,

$$\rho(x, y, z) = \sum_{i=1}^{N_p} G_i(x, y) \exp\{j\phi_i\} \exp\{-j2\pi z q_i\} \tag{5.13}$$

where ϕ_i is the phase for correction caused by the uncertainty of each flight path.

Based on the above analysis, a novel approach to MPSAR processing for 3D SAR imaging was developed. The block diagram is shown Figure 5.4 where after conventional SAR processing of each fight path, two steps are conducted before elevational imaging. One is image registration which aligns the returns resulted from the common terrain in the multiple images into the same image pixel cell. The other is phase correction which multiplies each image by a phase factor to make the phases of the multiple complex images cohere at the reference point of terrain. After image registration and phase correction, a focused beam of the synthetic array is steered at the reference point. Finally the elevational imaging is performed by scanning the focused beams in elevation using a discrete Fourier transform (DFT).

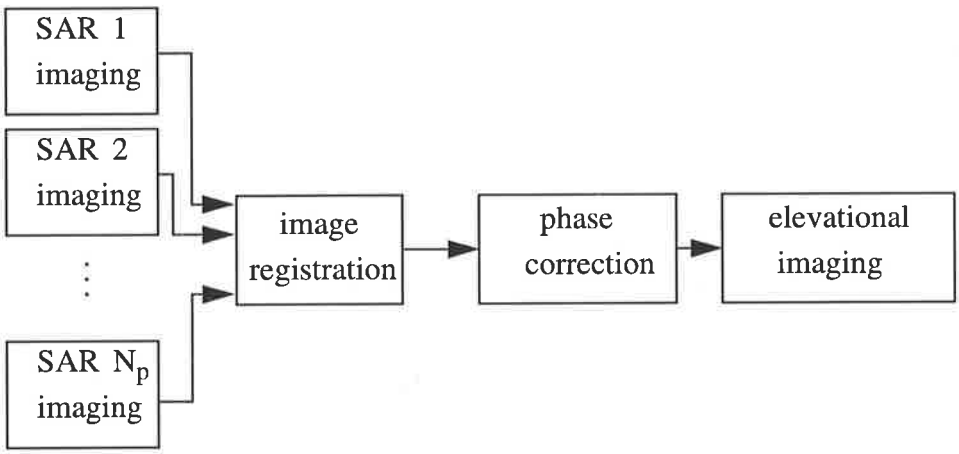

Figure 5.4 Block diagram of MPSAR processing

In summary, MPSAR processing performs the following steps:

1. It carries out conventional SAR imaging for each flight path.

2. It registers multiple complex SAR images for the selected area of interest.

3. It corrects the registered SAR images in phase. The correction of ith image is determined by the position of ith flight path.

4. It performs an N_p-point DFT across various flight paths. This operation is the core of 3D SAR imaging where the DFT acts as an elevational filter with the output of each DFT bin giving the reflectivity whose elevation is within a particular range.

Essentially, three orthogonal axises (range, azimuth and elevation) out of the 3D SAR image field may be visualized by three 2D images in the range-azimuth (top view), range-elevation (front view) and azimuth-elevation (side view) planes. The elevational resolution can be illustrated in the range-elevation and azimuth-elevation images. The range-azimuth image is a speckle-reduced version of a conventional SAR image which will be discussed in section 5.4.

In section 5.2, a matched filter for motion compensation is applied to a patch of image rather than to each pixel in order to reduce the computational complexity of motion compensation. However the size of patch is limited by the phase error tolerance of the SAR system and needs to be determined. When the image registration is accomplished, the multiple SAR images are realigned in range and azimuth directions so that the signal returns of multiple flight paths resulting from the same terrain will located in the same image pixel cell. After phase correction, the focused beam in elevation is formed and points to the reference point o of the terrain patch as shown in Figure 5.2. Using the DFT applies a linear phase across the synthesized elevational aperture to steer the beam away from the reference point. This introduces a phase error due to the linear approximation for R in (5.5). The appropriate size of terrain patch can be determined by limiting the phase error, thus according to Figure 5.2, we have

$$R = \left(R_0^{\,2} + r^2 - 2\mathbf{R}_0 \cdot \mathbf{r} \right)^{\frac{1}{2}}. \tag{5.14}$$

The residual error ΔR in (5.5) is less than $\frac{r^2}{2R_0}$, that is,

$$\Delta R < \frac{r^2}{2R_0}. \tag{5.15}$$

If we restrain ΔR to be less than $\frac{\lambda}{8}$, we have

$$R_0 > \frac{4r^2}{\lambda}. \tag{5.16}$$

Thus the size of terrain patch r_{max} can be determined by

$$r_{max} = \frac{1}{2}(R_0\lambda)^{\frac{1}{2}}. \tag{5.17}$$

With ERS-1 system, we have a satellite altitude of 785km, an incidence angle of 23^o, and a wavelength of 5.67cm, thus $r_{max} = 110$ m.

5.4 Benefits of MPSAR Processing

As a natural extension of InSAR processing, MPSAR processing has following advantages over InSAR processing at the expense of processing more than two flight paths.

5.4.1 No Two-dimensional Phase Unwrapping

The phase in the interferogram of InSAR, which is directly related to the topography, is only measured modulo 2π. In order to reconstruct the DEM unambiguously, it is necessary to add the appropriate number of cycles of phase; this is known as phase unwrapping and many algorithms have been investigated [46] [62] - [76]. Phase unwrapping may be appropriate in a low-noise environment, but in the more realistic high-noise situations a large number of residues appear and thus the phase unwrapping becomes infeasible which limits the application of typical InSAR. In the developed approach for MPSAR processing, the problem of phase unwrapping is avoided. This advantage is at the expense of the above limitation on patch size.

5.4.2 Improved Elevational Resolution

Conventional InSAR processes two flight passes P_1 and P_2 as shown in Figure 5.5 (a). The array aperture function in elevation consists of a pair of impulses spaced by baseline d_e. Consider the response of such an array to a narrow band signal arriving as a plane

wavefront from an elevation θ away from the broadside direction of the array. The normalized instantaneous power output is

$$b_p(\theta) = \left[\cos\left(\frac{\pi d_e \sin\theta}{\lambda}\right)\right]^2. \tag{5.18}$$

For example with $d_e = \frac{\lambda}{2}$ the beam-pattern in elevation is shown in Figure 5.5 (b); the beamwidth is about 50^o.

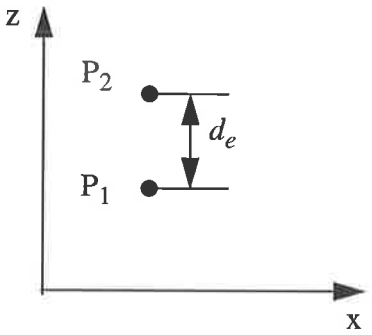

(a) Flight passes of InSAR

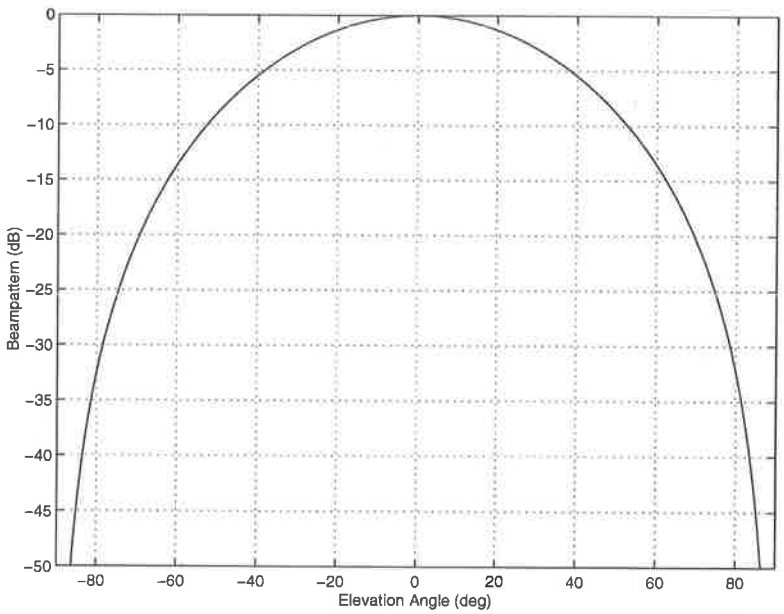

(b) Elevational beampattern of InSAR

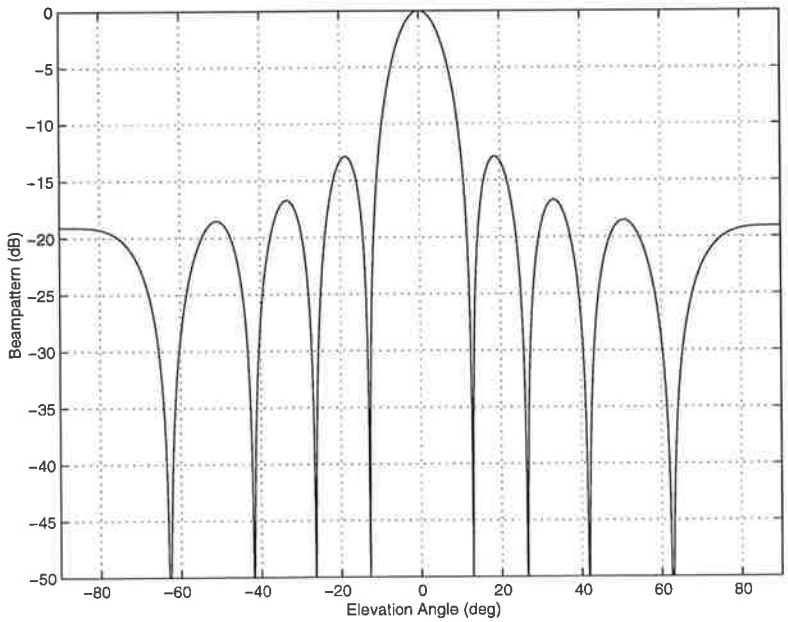

(c) Elevational beampattern of MPSAR

Figure 5.5 Flight passes of InSAR and elevational beampatterns of InSAR and MPSAR

MPSAR processing deploys the array aperture in the elevation direction with more than two flight passes P_i $i = 1, \ldots, N_p$ as shown in Figure 5.1. A simple form of array is one in which the elements are uniformly spaced, that is, $z_i = (i-1)\,d_e$ $i=1,\ldots,N_p$. The resultant beampattern is

$$b_p(\theta) = \frac{1}{N_p{}^2}\left[\frac{\sin\left(\frac{N_p \pi d_e(\sin\theta - \sin\theta_0)}{\lambda}\right)}{\sin\left(\frac{\pi d_e(\sin\theta - \sin\theta_0)}{\lambda}\right)}\right]^2 . \tag{5.19}$$

where θ_0 is a direction of beam steering. If the spacing d_e satisfies $d_e = \frac{\lambda}{2}$, the beam patterns are shown in Figure 5.5 (c) which show the focused beam and resolution in the elevational direction with a beamwidth of 11.11^o for $N_p = 9$ and $\theta_0 = 0^o$. In the practical case of MPSAR processing, the element spacing may be non-uniform and sparse and the positions of the elements may be uncertain. Receiver position errors give rise to increased sidelobes whilst the sparse spacing results in grating lobes [117]. Comparing Figure 5.5 (c) with Figure 5.5 (b), it is seen that MPSAR processing has enhanced resolution power in elevation.

5.4.3 Enhanced Ground-range Resolution

The flight pass may not be vertically one above another as shown in Figure 5.6. Then the aperture synthesized by the multiple flight passes may be decomposed into the elevational component and the ground-range component. The elevational aperture provides resolution in elevation and the ground-range aperture results in improved ground-range resolution.

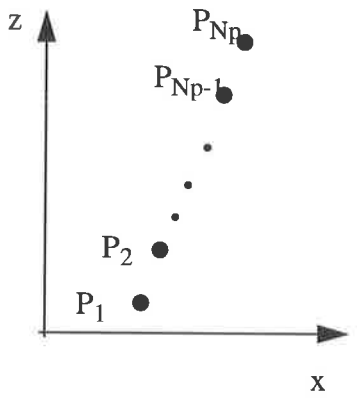

Figure 5.6 Flight passes of MPSAR with ground-range component

The slant-range resolution of a single-pass SAR results in a ground-range resolution $\tau_{g,s}$ which may be expressed as [51]

$$\tau_{g,s} = \frac{\tau_s \cos\gamma_1}{\sin(\beta_1 - \gamma_1)} \tag{5.20}$$

where $\tau_s = c/(2B_w)$ is the slant range resolution, β_1 the beamsteer direction of the synthesized aperture with respect to the broadside direction of the flight path array and γ_1 the slope angle of the terrain as shown in Figure 5.8. Similarly the presence of the aperture component in the ground-range direction leads to the ground-range resolution $\tau_{g,e}$ which is equal to

$$\tau_{g,e} = \frac{\tau_e \cos\gamma_1}{\cos(\beta_1 - \gamma_1)} \tag{5.21}$$

where $\tau_e = (\lambda R_0)/(2d_T)$ with d_T the length of the synthesized aperture for MPSAR processing. $\tau_{g,s}$ and $\tau_{g,e}$ have a physical meaning in the wavenumber domain[51]. They are inversely proportional to the widths of two bands. In order to overcome the problem of decorrelation of SAR images, these two bands need to be overlapped. The enhanced

ground-range resolution τ_g, obtained by combination of the two bands, is finer than $\tau_{g,s}$ and is given by the following relation.

$$\tau_g = \left(\tau_{g,s}^{-1} + \tau_{g,e}^{-1} \right)^{-1} < \tau_{g,s}. \tag{5.22}$$

The improved ratio I_r of ground-range resolution is

$$I_r = \frac{\tau_{g,s}}{\tau_g} = 1 + \frac{\tau_{g,s}}{\tau_{g,e}} = 1 + \frac{d_T}{B_c} \tag{5.23}$$

where $B_c = \dfrac{\lambda R_0 \tan(\beta_1 - \gamma_1)}{2\tau_s}$ is the critical baseline length [47].

For example, a simple case where flight paths are uniformly spaced with a baseline d_e, the synthesized aperture $d_T = (N_p - 1)\, d_e$, and the resultant $I_r = 1 + (N_p - 1)\,(d_e / B_c)$. Figure 5.7 shows I_r versus d_e for several numbers of flight paths. In order to satisfy the overlapping of the bands in the wavenumber domain to keep the coherence of SAR images, d_e should be less than B_c. For specific d_e, I_r increases linearly with N_p. If N_p is fixed, I_r increases linearly with d_e.

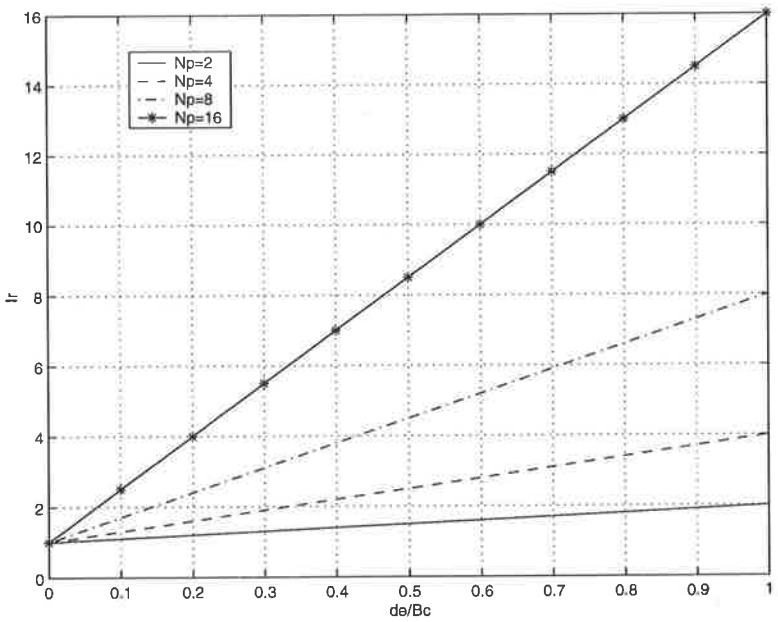

Figure 5.7 Improved ratio of ground-range resolution versus baseline for four N_p values

5.4.4 Reduction in Layover and Shadowing

Typically InSAR suffers from layover and shadowing [92] as shown in Figure 5.8. Layover occurs when two parts (A and B) of terrain with different ground ranges are located at the same slant range. The signals from A and B are superimposed in the interferogram and their elevations can not be estimated by unwrapping the phase of interferogram. MPSAR imaging introduces the elevational resolution and discriminates A and B with different elevational cells. A reduction in layover uncertainty results.

Shadowing happens when part of terrain (C) is invisible to flight pass P_1 and P_2. The corresponding parts of the SAR image consist of noise and the SNR of the interferogram around C is low, making phase unwrapping difficult. With MPSAR processing, the multi-look effect may make C which is invisible to flight pass P_1 and P_2 visible to other flight passes such as P_3. Thus shadowing is reduced.

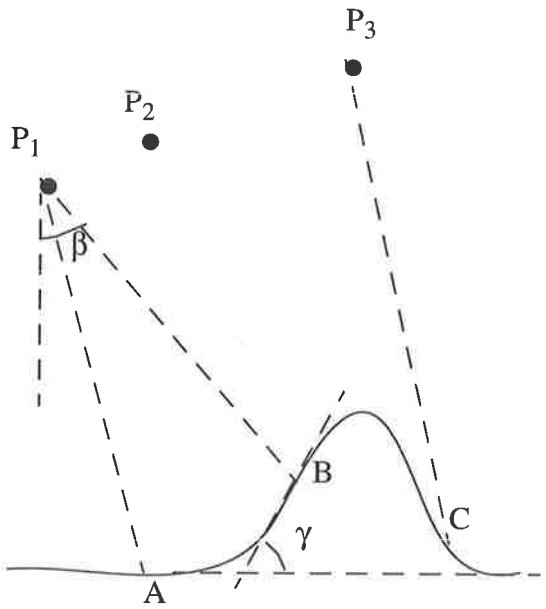

Figure 5.8 Layover and shadowing

5.4.5 Speckle Suppression

When a radar illuminates a rough surface, the return signal consists of waves reflected from many elementary scatterers within a resolution cell. The distances between the elementary scatterers and the receiver vary due to the surface roughness. A strong signal is received if the waves add relatively constructively; a weak signal is received if the waves are out of phase. The effect causes a pixel to pixel variation in intensity which is called

speckle. Unlike a passive incoherent sensor, SAR generates images by coherently processing the returns from successive radar pulses with the path lengths and orientation varying slightly from one pulse to another and consequently their images are highly susceptible to the speckle effect.

Speckle in SAR images complicates the image interpretation, reduces the effectiveness of image segmentation, classification and other information extraction [109]. It has been identified as a multiplicative noise which can not be reduced by simply increasing the power of the radar transmitter. A basic method for SAR speckle suppression is to incoherently average several frames obtained from a portion of the available azimuthal spectral bandwidth. An example of this is multi-look SAR processing [1] which reduces speckle by averaging N_p intensity images and then taking the square root. The ensuing improvement can be explained by considering the probability density of pixel intensity. For a single look, the pixel intensity has a exponential distribution which corresponds a very wide range of variation. By noncoherent averaging N_p intensity images, the pixel intensity will be changed into chi-square distribution which reduces the variance by a factor of N_p.

Multi-look processing only considers the intensity and ignores the phase information. A whitening filter was proposed to suppress speckle by use of fully polarimetric SAR images and provided the maximum achievable reduction in speckle[144]. This algorithm estimated the polarization covariance of the clutter and used this covariance to construct the minimum speckle image. This whitening filter can also be used in MPSAR imaging by replacing the polarization diversity with the spatial diversity. From (5.13), the profile of a 3D SAR image in the reference range-azimuth plane is the coherent summation of multiple SAR images, namely,

$$\rho(x, y, 0) = \sum_{i=1}^{N_p} G_i(x, y) \exp\{j\phi_i\}. \tag{5.24}$$

As presented in chapter 7, the ML estimation of $\exp\{j\phi_i\}$ for phase correction will be the eigenvector corresponding to the maximum eigenvalue of the estimated covariance matrix of the pixel vectors across multiple SAR images. As $\rho(x, y, 0)$ is the principal component of the image in elevation, it has maximum SNR improvement and minimum speckle[110].

5.5 Simulation Results

Computer simulations presented here were carried out based on ERS-1 system parameters where the satellite operated at an altitude of 785km. The radar transmitted a linear-frequency-modulated (LFM) signal with a bandwidth of 15.55MHz and a nominal wavelength of 5.67cm. A point scatterer was located in a flat terrain. 17 flight passes spaced 100m apart vertically as shown in Figure 5.9 were simulated. The distribution of flight passes provided an elevational aperture of 1600m which is similar to that of ERS-1 data processed in the next section.

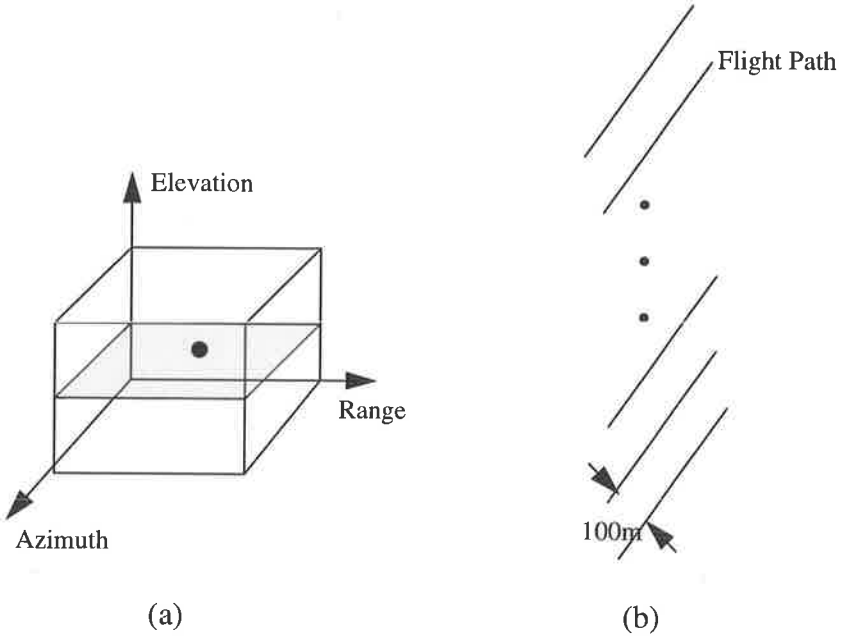

Figure 5.9 Simulation of MPSAR processing: (a) one point scatterer terrain, (b) flight path distribution

At first a matched filter was applied to obtain the SAR complex image for each flight path. Then 17 SAR images were registered, corrected in phase to remove the deviation of flight path, and resolved in the elevational direction for each image pixel with 32 point fast Fourier transform (FFT). Figure 5.10 shows the 3D image of the scatterer illustrating the two-dimensional point-spread-functions (PSF) with (a) in the range-azimuth plane, (b) in the range-elevation plane, and (c) in the azimuth-elevation plane. The 3D image is $32 \times 32 \times 32$ pixels. Each pixel has a size of 9.38m, 13.79m, and 6.90m in the range, azimuthal and elevational directions. The theoretical resolutions in the range, azimuth and elevation are 9.38m, 13.79m and 13.79m, respectively. The maximal unambiguous distance in the elevation is 222.55m.

Resolution and noise are two important performances for an imaging systems since both impact the capability to perform image reconstruction. They are characterized by the PSF of the imaging system. Resolution is characterized by the 3dB width of the main lobe of the PSF while noise is characterized by the height of the sidelobes. The one-dimensional PSFs in range, azimuth and elevation are given in Figure 5.10(d) which show that the MPSAR processing is able to provide the focused resolutions in range, azimuth and elevation, the measured resolutions (3dB width of PSF) in range, azimuthal and elevational directions are consistent with the theoretical resolutions and the peak sidelobes have a level of -24dB, -23dB and -15dB in range, azimuth and elevation directions.

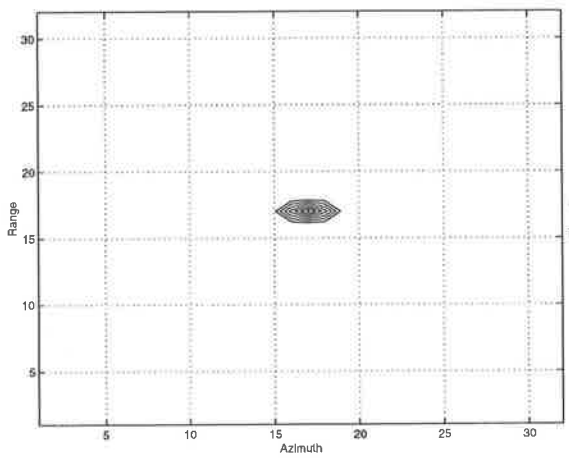

(a) Range-azimuth image

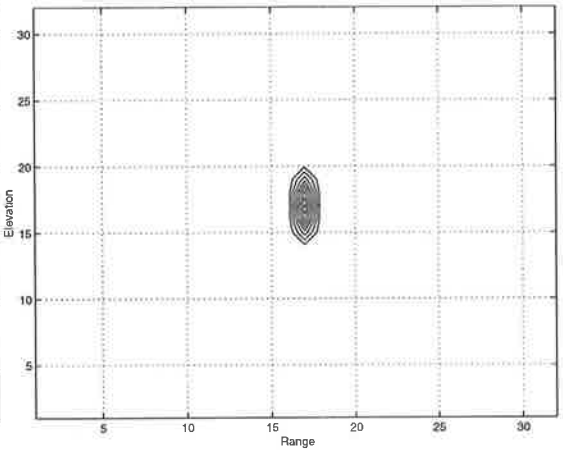

(b) Range-elevation image

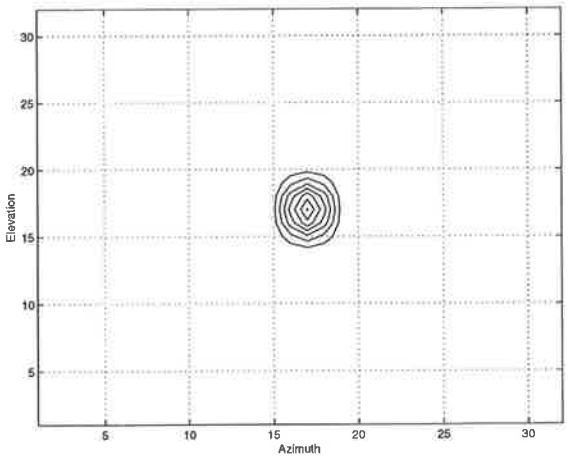

(c) Azimuth-elevation image

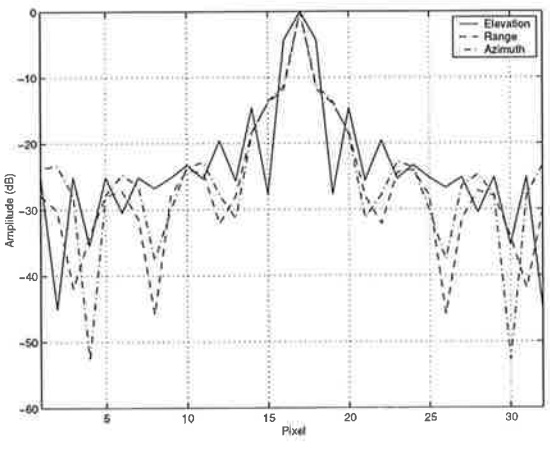

(d) PSFs in range, azimuth and elevation

Figure 5.10 PSFs of 3D SAR image

5.6 ERS-1 Data Results

MPSAR processing was tested using 9 SAR image data sets, acquired by the ERS-1 satellite over a small area in the southwest of the city of Bonn, Germany during the period of 2-29 March, 1992. Parameters of ERS-1 are listed in Table 5.1 [140]. The 9 flight paths were parallel and their elevational positions are shown in Figure 5.11 where the four digit numbers locating in the right above of each flight path are the ERS-1 orbit numbers. The 9 flight paths provided a synthesised aperture length of 1686m. For calibration an array of 19 corner reflectors (1.4 meters) was deployed by the Institute of Navigation, University of Stuttgart, spreading 20km on the terrain as shown in Figure 5.12. The corner reflectors acted as point scatterers which were designed to provide a large radar cross section (RCS) over a wide range of aspect angles and frequencies [93].

Table 5.1 Parameters of ERS-1

Altitude	Central frequency	Bandwidth	Incidence angle	Pulse width
785 km	5.3 GHz	15.55 MHz	23°	37.12 us

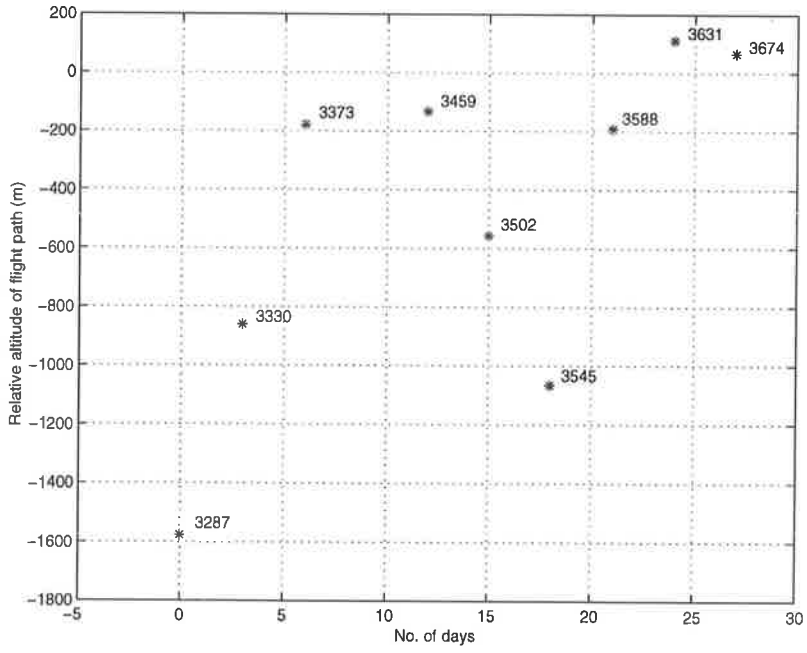

Figure 5.11 Elevational relative positions of ERS-1 flight paths

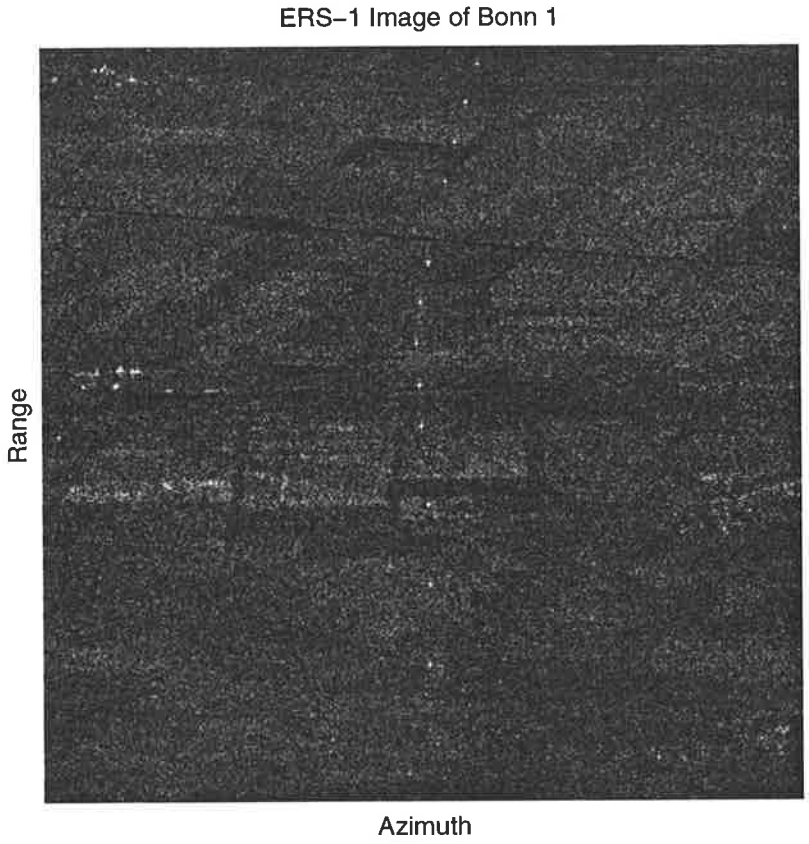

Figure 5.12 ERS-1 SAR image

5.6.1 One Corner Reflector Terrain

First an image patch containing a corner reflector with 32×32 pixels as shown in Figure 5.13 was selected for MPSAR imaging. The 3D image was formed[1] by registering 9 SAR images, correcting them in phase, and beamforming in the elevation with DFT. Figure 5.14 (a), (b) and (c) give the two-dimensional PSFs of 3D SAR image. The one-dimensional PSFs are shown in Figure 5.14 (d). The 3D image is $32 \times 32 \times 16$ pixels. Each pixel has a size of 7.90m, 4.00m, and 6.73m in the range, azimuthal and elevational directions. The resolutions in the range, azimuth, and elevation are 9.38m, 6.00m, and 13.45m, respectively. The focused resolution of the MPSAR processing in the elevation is illustrated in Figure 5.14 (b), (c) and (d). The peak sidelobes in range, azimuth and elevation are -20dB, -18dB and -15dB, respectively. Figure 5.14 (a) shows a reduced speckle of the MPSAR processing compared with a single SAR image in Figure 5.15 (a) and the multi-look SAR image in Figure 5.15 (b). The dynamic ranges and the contour levels in Figure 5.14 and Figure 5.15 are the same.

[1] The registration and correction algorithms are discussed in the following chapters.

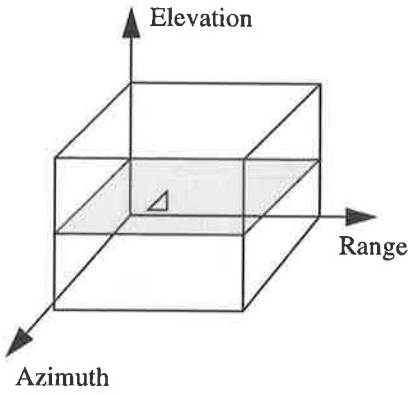

Figure 5.13 One corner reflector terrain

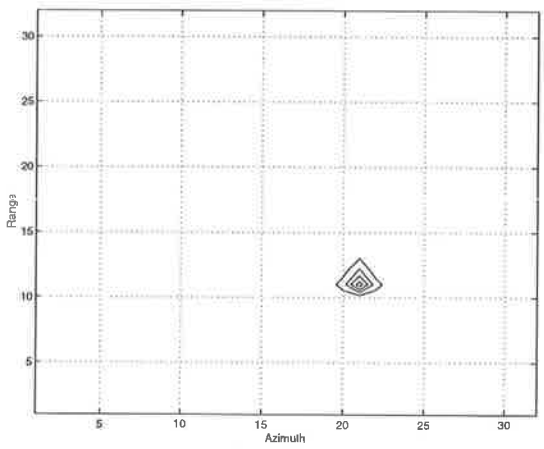

(a) Range-azimuth image

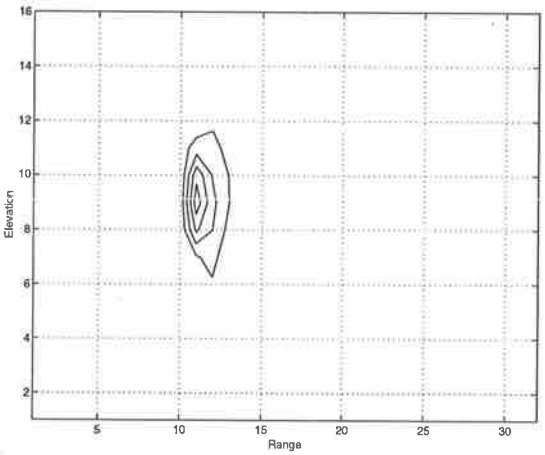

(b) Range-elevation image

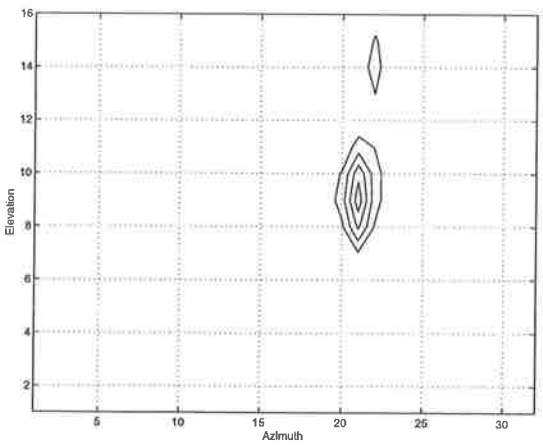

(c) Azimuth-elevation image

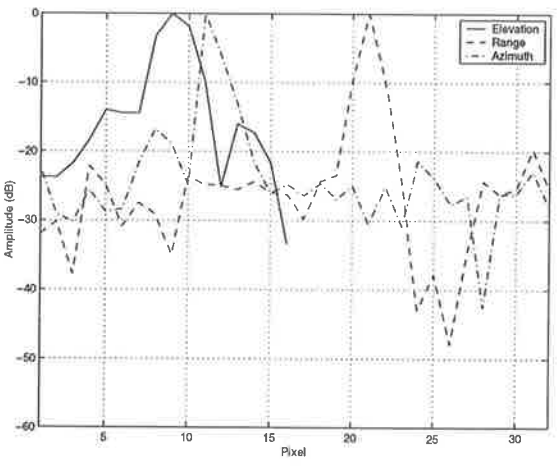

(d) PSFs in range, azimuth and elevation

Figure 5.14 3D SAR image of one corner reflector terrain

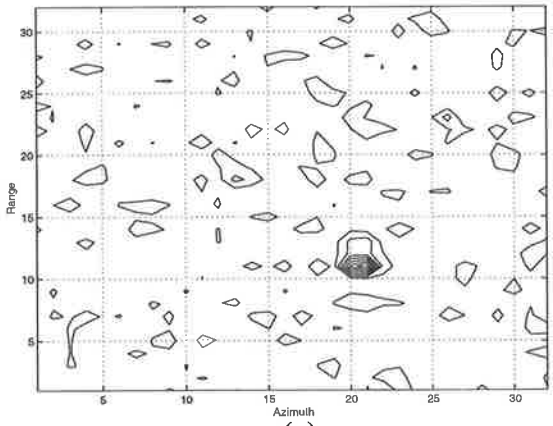

(a)

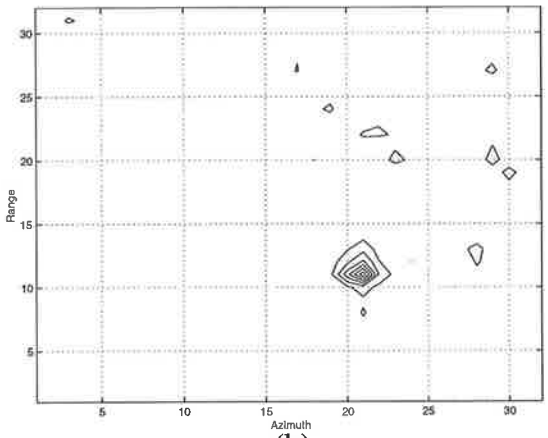

(b)

Figure 5.15 SAR images of single look (a) and multi-look (b) for one corner reflector terrain

5.6.2 Two Corner Reflector Terrain

Next a patch of terrain having two corner reflectors with pixel dimensions 32×32 shown in Figure 5.16 was chosen to do MPSAR imaging. The resulting 3D SAR image is shown in Figure 5.17: (a) the range-azimuth image in which the two corner reflectors are located, (b) and (c) the profiles of the two corner reflectors in the range-elevation plane where different azimuthal slices have been selected to separate the two scatterers, (d) and (e) the profiles of the two corner reflectors in the azimuth-elevation plane where different range slices have been selected to separate the two scatterers. The focused elevation resolution is apparent in the range-elevation and azimuth-elevation images. Enhancement of elevational resolution is presented in chapter 8. The range-azimuth image has a decreased-speckle with comparison with single and multi-look SAR images as shown in Figure 5.18

as the reference range-azimuth image has a maximum SNR improvement and a minimum speckle as discussed in section 5.4.5.

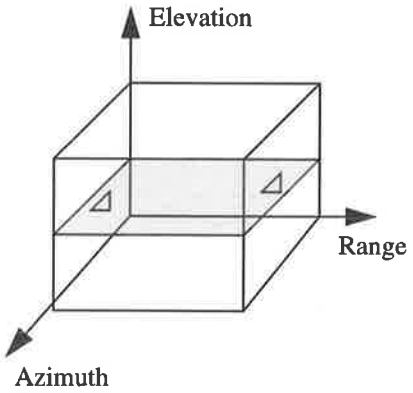

Figure 5.16 Two corner reflector terrain

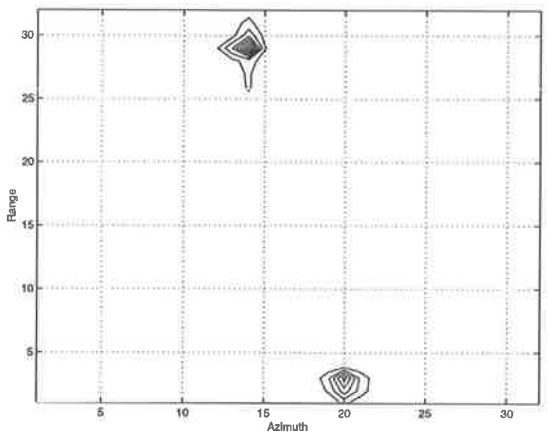

(a) Range-azimuth image across the two scatterers

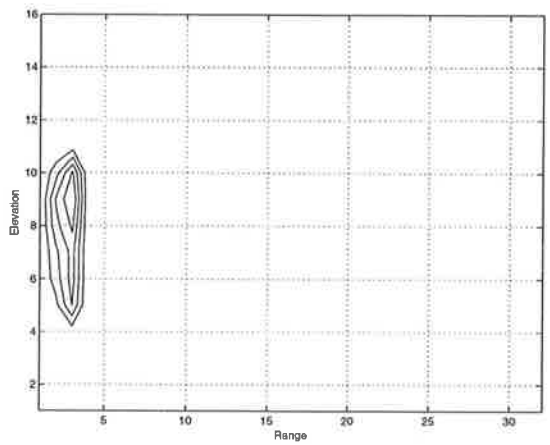

(b) Range-elevation image across the first scatterer

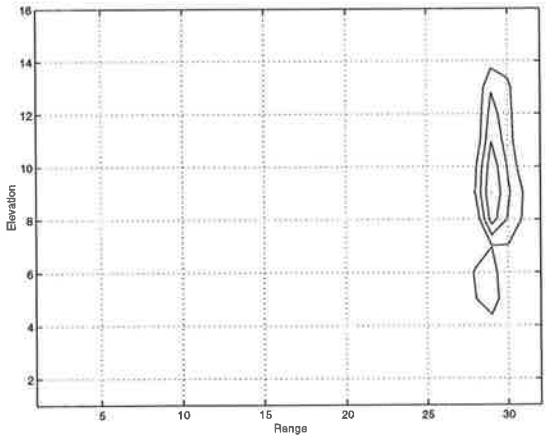

(c) Range-elevation image across the second scatterer

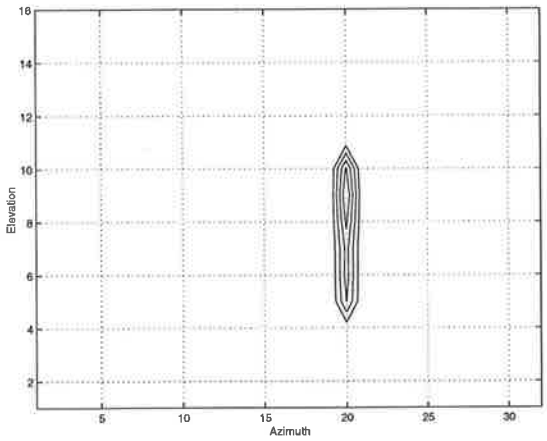

(d) Azimuth-elevation image across the first scatterer

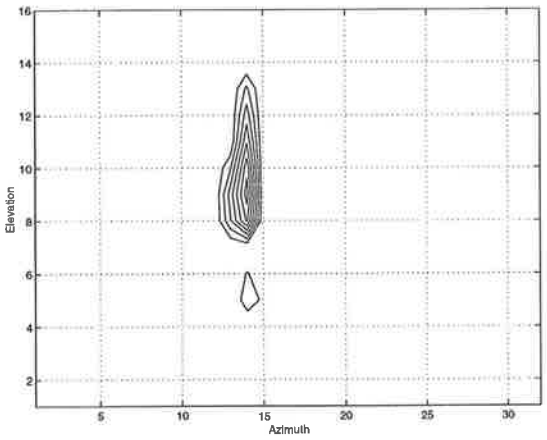

(e) Azimuth-elevation image across the second scatterer

Figure 5.17 3D SAR image of two corner reflector terrain

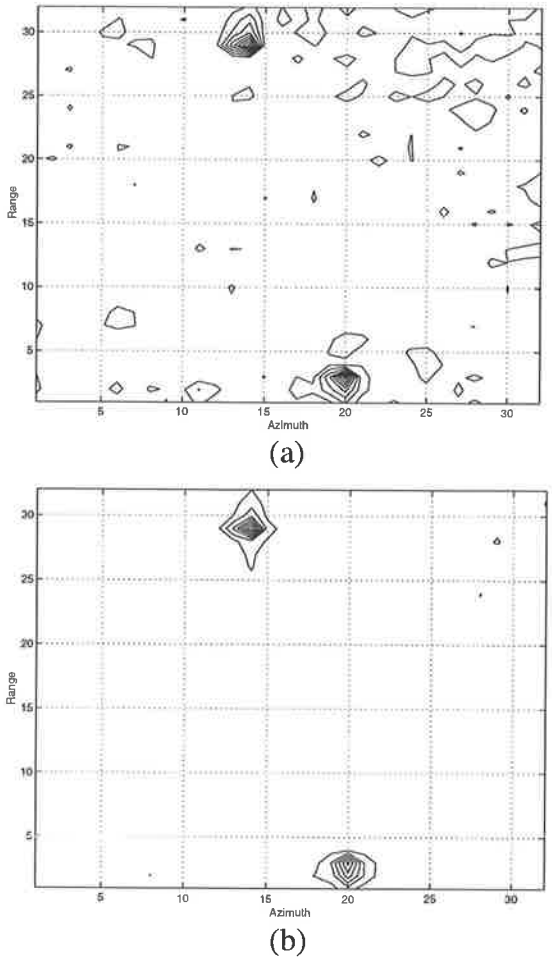

Figure 5.18 SAR images of single look (a) and multilook (b) for two corner reflector terrain

5.7 Conclusions

MPSAR processing is the natural extension of conventional InSAR processing and has good potential for many applications in spaceborne and airborne SAR systems. Contributions of this chapter have been to formulate the 3D SAR imaging as a beamforming problem and to develop the processing steps of MPSAR imaging which include conventional SAR processing, image registration, phase correction and elevational imaging. The benefits of MPSAR imaging over InSAR processing have been analysed. They are to obviate the phase unwrapping, enhance the elevational and ground-range resolutions, and reduce the phenomena of layover, shadow and speckle. MPSAR imaging with 17 flight passes was simulated to illustrate 3D PSFs. The ERS-1 data for one and two

corner reflector terrain were processed. The processing results show the ability to localize in elevation and to reduce speckle in the range-azimuth image.

It is noted that the key steps of MPSAR imaging are image registration, phase correction and elevational imaging which will be further studied in chapters 6, 7 and 8, respectively.

Chapter 6 Image Registration for MPSAR Processing

6.1 Introduction

As discussed in chapter 5, the processing steps of MPSAR imaging are to first co-register multiple complex value SAR images, then to correct the registered images in phase to form the focused beam, and finally to steer the focused beam in elevation. The initial step of co-registering the multiple SAR images is particularly important as image misregistration leads to reduced correlation between the images, and increased phase noise within the interferogram[94]. For example, misregistration of as little as 1/8 of a resolution cell results in a phase noise standard deviation of approximately 23^{o} and 42^{o} for SNR of ∞ dB and 10dB, respectively. Misregistration of one resolution cell produces complete decorrelation, and subsequently an inability to reconstruct the terrain height.

In this chapter, SAR image registration for MPSAR processing is investigated. Concepts are reviewed in section 6.2. Section 6.3 describes a model and a new approach for registering pairs of SAR images by use of complex correlation is proposed in section 6.4. A minimal distance method and an image model matching approach based on this for multiple images are developed in section 6.5. The complex correlation and the image model matching approaches are used to process real ERS-1 data and the results are presented in section 6.6.

6.2 Concepts of Image Registration

Image registration is a fundamental task in image processing for surveillance and remote sensing applications. A series of images acquired in different times, different frequencies, different spatial locations and different polarizations need to be aligned so that differences in them can be detected and removed.

If we define images as two two-dimensional arrays of a given size denoted by A_1 and A_2 where $A_1(x, y)$ and $A_2(x, y)$ represent their amplitudes, then the transformations between images can be expressed as

$$A_2(x, y) = g\{A_1[f(x, y)]\} \tag{6.1}$$

where f is a two-dimensional spatial coordinate transformation or geometric transformation and g is a one-dimensional amplitude transformation or radiometric transformation.

The amplitude of an image pixel is a function of the reflectivity of the corresponding surface area and since different sensors have different responses the radiometric transformation is applicable for the registration of images acquired by different sensors. The radiometric transformation may not be necessary to register images resulting from same sensor because it can be combined with sensor system calibration. In this chapter, the registration of multiple SAR images acquired with same sensor at different times and spatial positions is investigated. The radiometric correction is assumed to have been accomplished by SAR system calibration leaving only the geometric distortions require to be corrected. The corresponding geometric transformations can be classified as rigid, affine, perspective and curved[57].

The geometrical transformation that maps the coordinate system of one image into the other can be either global or local as shown in Figure 6.1. The global one influences the transformation of the image as a whole when one of geometrical parameters changes. In a local transformation such a change influences only part of the image. It is identified in section 6.3 that the geometrical transformation for MPSAR images is a local one and the image registration needs to be conducted locally.

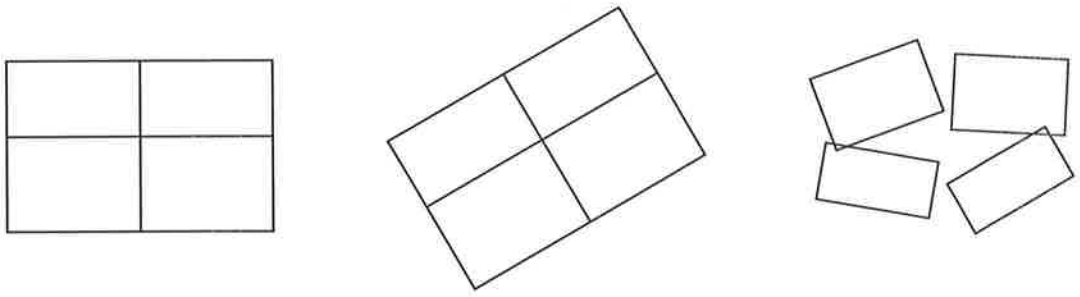

Figure 6.1 Global and local geometrical transformations (a) original (b) global (c) local

Multiple images are registrated if pixels corresponding to same scene point in different images have the same coordinates. Figure 6.2 depicts the registration requirement for three images. The shaded elements represent image cells of same scene point, and the coordinates $(x_i, y_i)\, i = 1, 2, 3$ locate the point in each image. Registration of three images is to make $x_1 = x_2 = x_3$ and $y_1 = y_2 = y_3$.

The registration process can be divided into three phases: enhancement, correlation, and overlay. Enhancement refers to the preprocessing necessary to improve the accuracy of registration; correlation is the process of determining the misregistrations of matched points; and overlay is the geometric transformation process which produces the registered imagery. The crux of the registration process is to determine the spatial misregistrations of matched points.

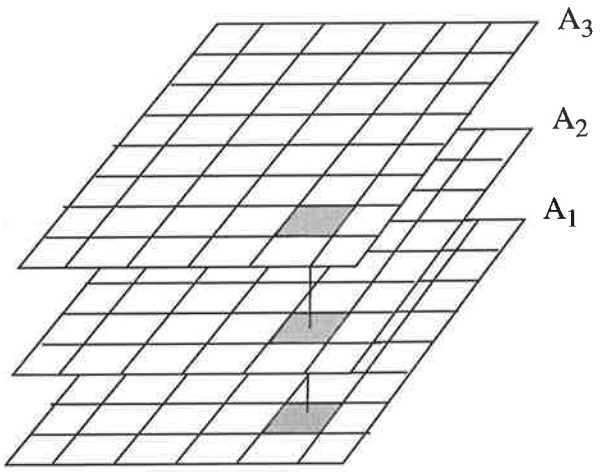

Figure 6.2 Multiple image registration requirement

6.3 Model for MPSAR Images

Although many methods of image registration have appeared, the ideal registration method does not exist. One has to compromise between accuracy, speed and interactivity and to choose the best method for a specific application. In this section, a model for multiple pass SAR images is described[79] which helps to identify the type of geometric distortion of multiple SAR images and to develop appropriate approaches for multiple SAR image registration.

If we only consider the surface backscattering of terrain without allowing for penetration of the microwave energy below the surface, the reflection function can be modelled by

$$\rho(x, y, z) = o(x, y)\,\delta(z - h(x, y)) \tag{6.2}$$

where $o(x, y)$ represents the surface reflectivity density at coordinates (x, y), $h(x, y)$ is the terrain elevation for the same point, and $\delta(x)$ is a Dirac delta function. Substituting (6.2), (5.5) and (5.6) into (5.3), the signal in 3D data space prior to motion compensation can be expressed by

$$S(\boldsymbol{q}) = U(f)\iint_{x\,y} o(x, y)\exp[j2\pi q_z h(x, y)]\exp[j2\pi(xq_x + yq_y)]\exp\left[-j\frac{4\pi R_0}{\lambda}\right]\mathrm{d}x\mathrm{d}y. \tag{6.3}$$

Due to the small variation of azimuthal and elevational angle within a subimage, the support region of the signal in 3D data space for a single flight path as shown in Figure 5.3 (a) can be approximated by a plane[79] which can be expressed as

$$q_z = k_1 q_x + k_2 q_y. \tag{6.4}$$

Thus the returned signal corresponding to this flight path is

$$\begin{aligned} S(q_x, q_y) = U(f)\iint_{x\,y} o(x, y)\exp[j2\pi(k_1 q_x + k_2 q_y)\,h(x, y)] \\ \exp[j2\pi(xq_x + yq_y)]\exp\left[-j\frac{4\pi R_0}{\lambda}\right]\mathrm{d}x\mathrm{d}y \end{aligned} \tag{6.5}$$

The signal support region in the $q_x o q_y$ plane as shown in Figure 6.3 is offset from the origin[79]. The signal translated to the origin is

$$S'(q_x, q_y) = S(q_x + q_0, q_y) = U(f) \iint_{x\,y} o'(x, y) \exp[j2\pi(k_1 q_x + k_2 q_y) h(x, y)] \exp[j2\pi(xq_x + yq_y)] \exp\left[-j\frac{4\pi R_0}{\lambda}\right] dxdy \quad (6.6)$$

where $o'(x, y) = o(x, y) \exp\{j2\pi k_1 q_0 h(x, y)\} \exp\{j2\pi x q_0\}$.

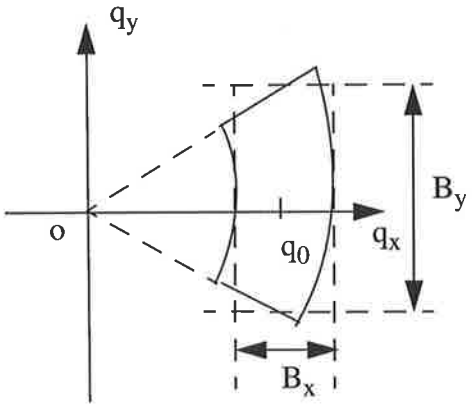

Figure 6.3 Signal support region

The SAR complex image from a single flight path is produced by a two-dimensional Fourier transform of $S'(q_x, q_y)$ in the range and azimuthal directions which is formulated as

$$G(x, y) = \int_{q_x q_y} \int_{x' y'} U(f)\, o'(x', y') \exp[j2\pi(k_1 q_x + k_2 q_y) h(x', y')] \exp[j2\pi(x'q_x + y'q_y)] \exp\left[-j\frac{4\pi R_0}{\lambda}\right] dx'\, dy' \exp[-j2\pi(xq_x + yq_y)]\, dq_x\, dq_y \quad (6.7)$$

If $U(f)$ is assumed to be constant over the support region, $G(x, y)$ can be simplified by changing the order of integration into

$$G(x, y) = \iint_{x' y'} S_a(k_1 h(x', y') + x' - x, k_2 h(x', y') + y' - y)\, o'(x', y') \exp\left[-j\frac{4\pi R_0}{\lambda}\right] dx'dy' \quad (6.8)$$

where $S_a(x, y) = B_x B_y \operatorname{sinc}\left(\frac{xB_x}{2\pi}\right) \operatorname{sinc}\left(\frac{yB_y}{2\pi}\right)$ and $\operatorname{sinc}(x) = (\sin x)/x$. The width of mainlobe of the sinc function is $\frac{4\pi}{B_x}$ by $\frac{4\pi}{B_y}$. The spatial bandwidths B_x and B_y as shown in Figure 6.3 are dependent on the bandwidth of transmitted signals and the change of aspect angle, respectively. If we assume that the terrain elevation $h(x, y)$ varies slowly

enough to be considered constant over the mainlobe width of S_a function, the complex SAR image of a single flight may be interpreted as a convolution summation

$$G(x+\Delta x', y+\Delta y') = Sa(x,y) \otimes o'(x,y) \exp[-j4\pi R_0/\lambda] \quad (6.9)$$

with the shifts $\Delta x' = k_1 h(x,y)$ and $\Delta y' = k_2 h(x,y)$. Equation (6.9) indicates that a reflectivity value for any position in the physical scene will be translated in the SAR image to a new position. The translation is dependent on the flight pass and elevational function $h(x,y)$. Therefore the geometric transformation for multiple image registration is identified to be a local translational transformation.

In order to correct the local translational distortion, image registration for multiple SAR images is generally accomplished in four steps. Firstly, each SAR image is divided into many subimages. The size of a subimage may be determined by the criteria discussed in section 5.3. Secondly, measurements are made of the local misregistrations from one subimage to the other subimages. Thirdly, misregistrations are then used to calculate a warping function, which maps a location in one subimage to the corresponding location in the other. Finally, the subimage is resampled so that it overlays the other precisely.

For each subimage, the local translation can be approximated by the global translation. The complex SAR subimages corresponding to the first and the second flight pass are expressed by

$$G_1(x+\Delta x_1, y+\Delta y_1) = \iint_{x'y'} S_a(x'-x, y'-y)\, o'(x', y') \exp\left[-j\frac{4\pi R_1}{\lambda}\right] dx'\, dy' \quad (6.10)$$

$$G_2(x+\Delta x_2, y+\Delta y_2) = \iint_{x'y'} S_a(x'-x, y'-y)\, o'(x', y') \exp\left[-j\frac{4\pi R_2}{\lambda}\right] dx'\, dy'. \quad (6.11)$$

With reference to Figure 5.1, R_2 is expressed as

$$R_2 = R_1\left[1 + \frac{2d_e}{R_1}\cos\beta + \left(\frac{d_e}{R_1}\right)^2\right]^{\frac{1}{2}}. \quad (6.12)$$

Considering $R_1 \gg d_e$, R_2 may be changed into

$$R_2 = R_1 + d_e\cos\beta. \quad (6.13)$$

The image model for the subimage of the second pass can be approximated by

$$G_2(x,y) \approx G_1(x-\Delta x, y-\Delta y)\exp\left(-j\frac{4\pi d_e \cos\beta}{\lambda}\right) \tag{6.14}$$

where $\Delta x = \Delta x_1 - \Delta x_2$ and $\Delta y = \Delta y_1 - \Delta y_2$.

6.4 Complex Correlation Approach

In this section a distance measure between image pairs is introduced as an indicator of image registration. Image registration is investigated and a complex correlation approach is proposed.

Define a distance measure $\mathcal{D}[G_i(x,y), G_l(x,y)]$ between two images $G_i(x,y)$ and $G_l(x,y)$ satisfying

$$\begin{gathered}
\mathcal{D}[G_i(x,y), G_l(x,y)] > 0 \qquad \forall G_i(x,y) \neq G_l(x,y) \\
\mathcal{D}[G_i(x,y), G_i(x,y)] = 0 \\
\mathcal{D}[G_i(x,y), G_l(x,y)] = \mathcal{D}[G_l(x,y), G_i(x,y)] \\
\mathcal{D}[G_i(x,y), G_l(x,y) + G_k(x,y)] < \mathcal{D}[G_i(x,y), G_l(x,y)] + \mathcal{D}[G_i(x,y), G_k(x,y)]
\end{gathered} \tag{6.15}$$

The conventional amplitude correlation method for image registration makes use of only the amplitude of an image and discards its phase. Based on the criterion of minimal distance between image envelopes, that is,

$$(\Delta x, \Delta y) = \text{Arg min}\ (\mathcal{D}[|G_1(x,y)|, |G_2(x+\Delta x', y+\Delta y')|]), \tag{6.16}$$

the misregistrations Δx and Δy in range and azimuth between two images can be estimated by searching the minimum distance between image pair with respect to $\Delta x'$ and $\Delta y'$. If the distance measure is chosen as

$$\mathcal{D}[|G_1(x,y)|, |G_2(x,y)|] = \sum_x \sum_y (|G_1(x,y)| - |G_2(x,y)|)^2, \tag{6.17}$$

the solution to the minimum in (6.16) is found by the conventional amplitude correlation which estimates Δx and Δy with the peak position of two-dimensional correlation of image amplitude in the range and azimuth directions with the relation of

$$|G_1(x,y)| = |G_2(x-\Delta x, y-\Delta y)|. \tag{6.18}$$

The problem with amplitude correlation measures is the broad and flat nature of the peak regions in the correlation surface. A disadvantage of broad peaks is that registration accuracy is reduced, and small perturbation due to noise has a large effect on accuracy.

This broad peak characteristic of amplitude correlation techniques results from the fact that information of spatial relationships between image pairs is ignored significantly. One approach to solve this problem involves the preferential use of phase information in the images. The relative roles of amplitude and phase were examined in [95] where it was found that the phase information was considerably more important than the amplitude information in preserving the visual intelligibility of the image. Therefore it is reasonable to process both the amplitude and the phase of SAR image for image registration.

By use of the principle of minimal distance between complex SAR images rather than the image envelopes, the misregistrations Δx and Δy can be determined by

$$(\Delta x, \Delta y) = \text{Arg min } (\mathcal{D}[G_1(x,y), G_2(x+\Delta x', y+\Delta y')]) . \tag{6.19}$$

If the distance measure takes the form

$$\mathcal{D}[G_1(x,y), G_2(x,y)] = \sum_x \sum_y |G_1(x,y) - G_2(x,y)|^2, \tag{6.20}$$

the above minimization happens at the peak position of two-dimensional correlation function of the complex image pair. The complex correlation is defined as

$$C_{r3}(\Delta x, \Delta y) = \sum_x \sum_y G_1(x,y)\, G_2^*(x+\Delta x, y+\Delta y) . \tag{6.21}$$

This complex correlation can be computed efficiently in the frequency domain. Thus (6.14) can be rewritten as

$$G_2(x,y) \approx G_1(x-\Delta x, y-\Delta y) \exp(-j\varphi_{21}) \tag{6.22}$$

where $\varphi_{21} = 4\pi d_e \cos\beta/\lambda$. The two-dimensional Fourier transform of (6.22) is

$$S_2(q_x, q_y) = \exp(-j\varphi_{21})\, S_1(q_x, q_y) \exp\{-j2\pi(\Delta x q_x + \Delta y q_y)\} . \tag{6.23}$$

The phase term of two-dimensional Fourier transform of $C_{r3}(\Delta x, \Delta y)$ can be written as

$$\frac{F[C_{r3}(\Delta x, \Delta y)]}{|F[C_{r3}(\Delta x, \Delta y)]|} = \frac{S_2(q_x, q_y) S_1^*(q_x, q_y)}{|S_2(q_x, q_y) S_1^*(q_x, q_y)|} = \exp(-j\varphi_{21}) \exp\{-j2\pi(\Delta x q_x + \Delta y q_y)\} \quad (6.24)$$

Taking a two-dimensional inverse Fourier transform, then

$$F^{-1}\left[\frac{S_2(q_x, q_y) S_1^*(q_x, q_y)}{|S_2(q_x, q_y) S_1^*(q_x, q_y)|}\right] = \exp(-j\varphi_{21}) \delta(x - \Delta x, y - \Delta y) \quad (6.25)$$

where $\delta(x, y)$ is a two-dimensional Dirac delta function. The position of the peak of $F^{-1}\left[\frac{S_2(q_x, q_y) S_1^*(q_x, q_y)}{|S_2(q_x, q_y) S_1^*(q_x, q_y)|}\right]$ in the range and azimuth directions determine the misregistration Δx and Δy.

The image model of complex correlation (6.22) is different from that of the phase correlation method (2.19) and (6.22) is defined in the complex domain rather than in the real domain. Experimental results indicate that the peak of complex correlation is sharper and the sidelobes are smaller as compared with those of conventional amplitude correlation.

6.5 Multiple Image Registration

Typical existing methods of multiple image registration register one pair of images at a time and repeat the operation until all the images are registered. However the registration result is dependent on the order of images and it suffers from image drift error due to the accumulation of errors in the correlation estimation and image variations caused by the decorrelation of SAR images[47]. In order to reduce those errors, the correlation of all images in one step rather than the correlation of image pairs should be used. In this section, a minimal distance approach is firstly proposed, then an image model matching approach is developed to improve computational efficiency.

6.5.1 Minimal Distance Approach

Let Δx_i and Δy_i $i = 1, \ldots, N_p$ be the misregistrations of the ith image $G_i(x, y)$ in the range and azimuthal directions with respect to the terrain coordinates. Multiple image registration depends on a cost function

$$C_1(\Delta x_1, \Delta y_1, \ldots, \Delta x_{N_p}, \Delta y_{N_p}) = \sum_{i=1}^{N_p} \sum_{l=i+1}^{N_p} \mathcal{D}[G_i(x+\Delta x_i, y+\Delta y_i), G_l(x+\Delta x_l, y+\Delta y_l)] \quad (6.26)$$

where $G_i(x+\Delta x_i, y+\Delta y_i)$ is the image of $G_i(x,y)$ with shifts Δx_i and Δy_i in range and azimuthal directions, respectively. The misregistrations of multiple images can be determined by minimizing (6.26), that is,

$$\left(\Delta x_1^0, \Delta y_1^0, \ldots, \Delta x_{N_p}^0, \Delta y_{N_p}^0\right) = \text{Arg } \min\left(C_1(\Delta x_1, \Delta y_1, \ldots, \Delta x_{N_p}, \Delta y_{N_p})\right) \quad (6.27)$$

which is called the minimal distance method.

This minimal distance method considers the correlation of multiple images to be processed rather than the correlation of image pairs. It is less affected by the SAR image decorrelation than the conventional method for image pairs. Moreover, as the method calculates the correlation as a whole instead of computing the multiple correlations between two images it avoids the problem of error accumulation in correlation estimation and the effect of image order. However the computational load is enormous because it requires the optimization of multiple variables. Although it is a good method for multiple image registration, it is impractical especially when the number of images is large.

6.5.2 Image Model Matching Approach

A new algorithm for multiple image registration named image model matching is now developed for practical applications. It is assumed that each image is derived from a reference image $M(x,y)$ by the addition of noise. The cost function of multiple image registration is expressed as

$$C_2(\Delta x_1, \Delta y_1, \ldots, \Delta x_{N_p}, \Delta y_{N_p}) = \sum_{i=1}^{N_p} \mathcal{D}[G_i(x+\Delta x_i, y+\Delta y_i), M(x,y)]. \quad (6.28)$$

Minimizing (6.28) is equivalent to minimizing the distance of each image from the reference image, that is,

$$\min[C_2(\Delta x_1, \Delta y_1, \ldots, \Delta x_{N_p}, \Delta y_{N_p})] = \sum_{i=1}^{N_p} \min\{\mathcal{D}[G_i(x+\Delta x_i, y+\Delta y_i), M(x,y)]\}. \quad (6.29)$$

The misregistrations can be estimated by

$$\left(\Delta x_1^0, \Delta y_1^0, \ldots, \Delta x_{N_p}^0, \Delta y_{N_p}^0\right) = \text{Arg min}\left(C_2\left(\Delta x_1, \Delta y_1, \ldots, \Delta x_{N_p}, \Delta y_{N_p}\right)\right). \quad (6.30)$$

It is noted that the optimization of $2N_p$ variables in (6.27) is simplified into the N_p optimizations of 2 variables in (6.29). Therefore the computational burden of the image model match approach is greatly reduced by compared with the minimal distance approach.

The image model matching method matches each image to the reference image rather than each other image so that the effects of image order and image drift are eliminated and the effect of image variation is reduced. The critical step of image model matching method is how to estimate the reference image. We first measure the $\binom{N_p}{2} = \frac{N_p(N_p-1)}{2}$ distances between all image pairs to determine the misregistrations and distances. The initial reference image $M_1(x, y)$ is formed by summing two registered images with the minimal distance, i.e.,

$$M_1(x, y) = \text{sum}\left[G_k(x + \Delta x_k, y + \Delta y_k), G_l(x + \Delta x_l, y + \Delta y_l)\right] \quad (6.31)$$

where $k, l = \text{Arg min}\left[\mathcal{D}\left(G_i(x + \Delta x_i, y + \Delta y_i), G_m(x + \Delta x_m, y + \Delta y_m)\right)\right], \quad \forall i \neq m,$ $i, m = 1, \ldots, N_p$. When SNR is high, the two images can be summed coherently. If SNR is low, they are added incoherently.

Then the remaining images are reordered as $G_i(x, y)$ $i = 1, 2, \ldots, N_p - 2$ and are matched to $M_1(x, y)$ to determine the misregistrations and distances. The reference image $M_2(x, y)$ is produced by summing $M_1(x, y)$ with one registered image which has a minimal distance with $M_1(x, y)$, namely,

$$M_2(x, y) = \text{sum}\left[M_1(x, y), G_k(x + \Delta x_k, y + \Delta y_k)\right] \quad (6.32)$$

where $k = \text{Arg min}\left[\mathcal{D}\left(G_i(x + \Delta x_i, y + \Delta y_i), M_1(x, y)\right)\right] \forall i = 1, \ldots, N_p - 2$. The above procedure is repeated $N_p - 2$ times until the model $M_{N_p-1}(x, y)$ is produced and images $G_i(x, y)$ $i = 1, \ldots, N_p$ have been registered.

We can further elaborate the image model to increase the accuracy of multiple image registration by iterating the match of the reference image to each image $G_i(x, y)$ until the misregistrations $\Delta x_i, \Delta y_i i = 1, \ldots, N_p$ remain constant.

6.6 Experiment Results

An experimental study was carried out to measure the performances of the complex correlation approach and the image model matching approach using multiple SAR images of the same terrain acquired by ERS-1. The similarity of multiple SAR images was determined by the SNR of the SAR image, the baseline of flight path and the time interval between flights[47]. It increases with an increase of SNR or a decrease of baseline and time interval. The amplitude correlation method, being a standard method, was used as a comparison. The experiment included 162 pairs of SAR subimage data sets obtained from 9 flight paths by choosing subregions with a size of 50×50 pixels containing strong scatterers as illustrated in section 5.6. The translational offset of two images within each pair was known to within a pixel by use of ground control points. For each offset, a window size of 32×32 was selected in the calculation of the registration measure. This allowed for offsets of up to ± 9 pixel positions in each direction.

6.6.1 Complex Correlation Approach

With the aim to determine the robustness of the proposed method to image dissimilarity, the SAR image pairs were grouped according to their similarity. The similarity of each image pair was measured by the correlation coefficient of the two amplitude images evaluated at a known translational offset as defined by (2.16). Registration results were measured by the correct probability of registration for the image pairs within the given image similarity category. Figure 6.4 presents the results of the complex correlation of (6.21) (solid line) and the amplitude correlation of (2.15) (dash line) graphically. It indicates that both provide correct registration when the image similarity is greater than 0.7 for the amplitude correlation and 0.5 for the complex correlation. However, as the similarity of image pairs drops, the complex correlation performs more robustly than the amplitude correlation. The complex correlation continues to provide an accuracy of 80% even if similarity value goes as low as 0.35.

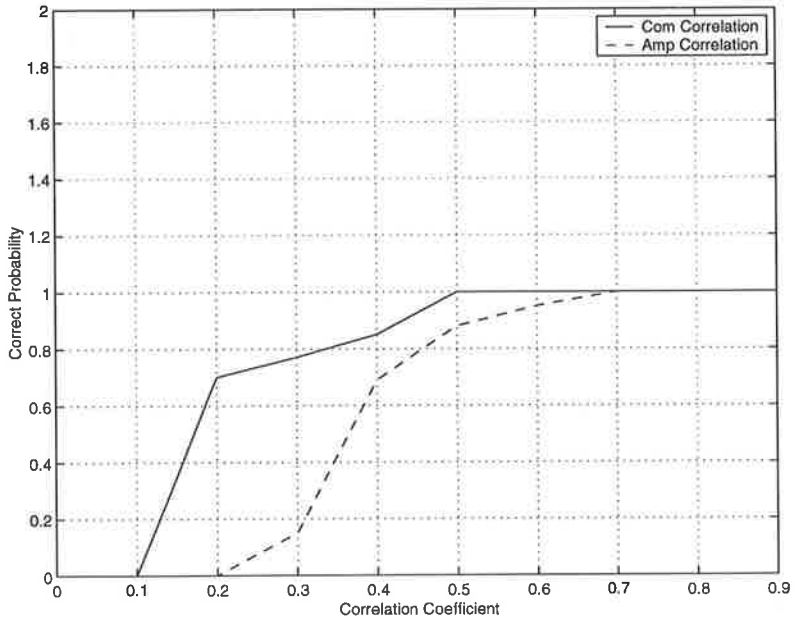

Figure 6.4 Registration accuracy versus image similarity

Figures 6.5 and 6.6 show the amplitudes of correlation functions of the complex and amplitude correlation approaches, respectively in the mesh map (a) and in contour map (b). Figure 6.7 compares the profiles of their amplitudes of correlation functions. They demonstrate that the complex correlation reduces the sidelobe of correlation function significantly and the correlation peak of the complex correlation is a little sharper than that of the amplitude correlation.

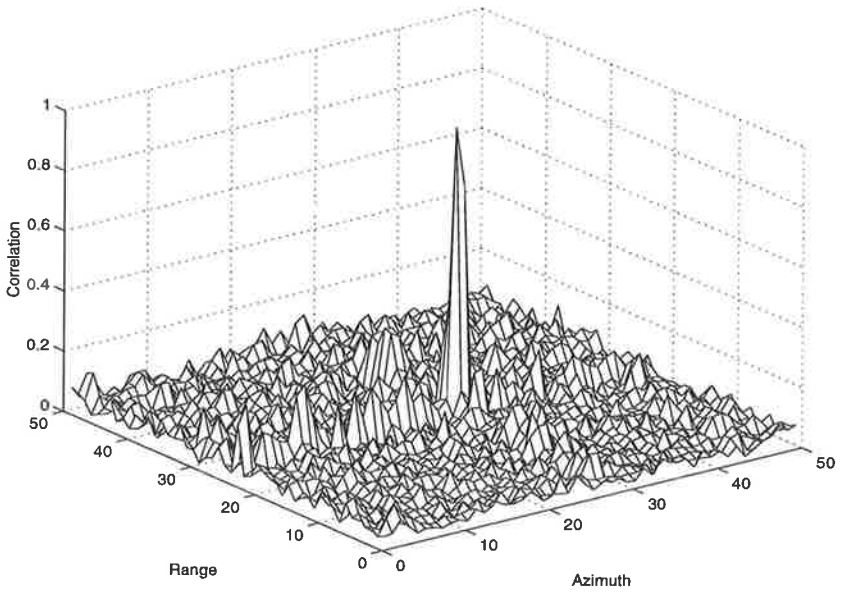

(a) Mesh map

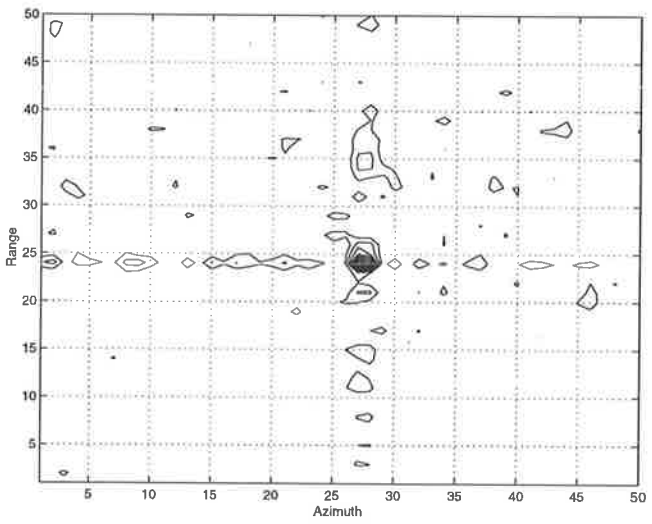

(b) Contour map

Figure 6.5 Amplitude of correlation function of complex correlation

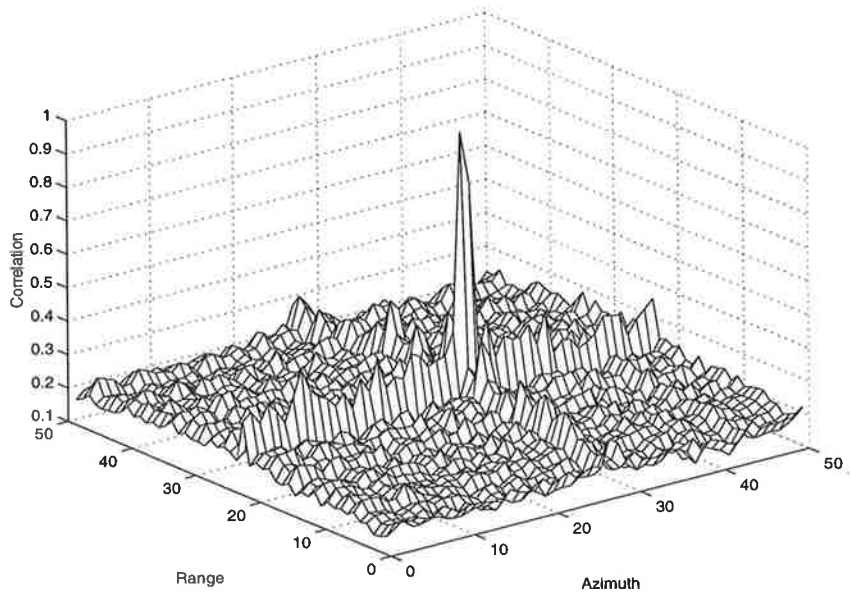

(a) Mesh map

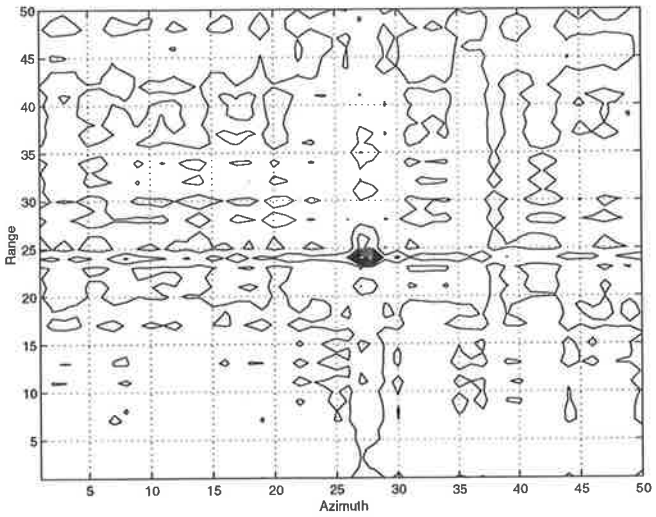

(b) Contour map

Figure 6.6 Amplitude of correlation function of amplitude correlation

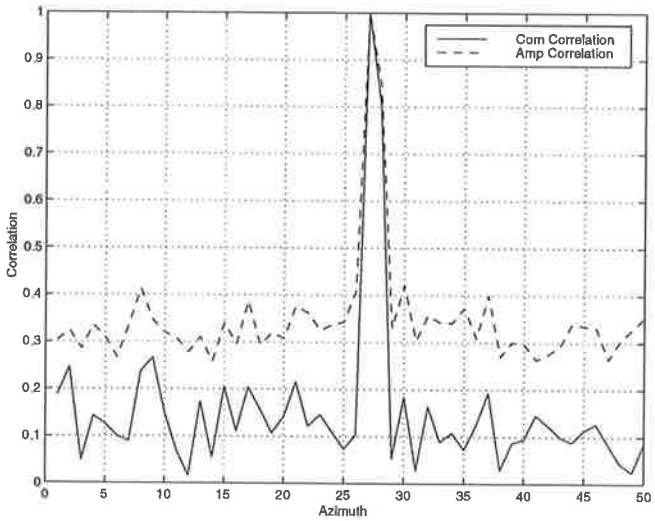

(a) Azimuth profiles

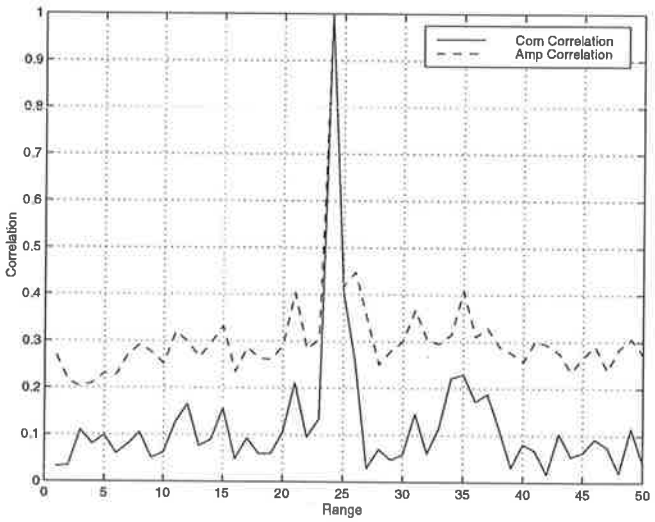

(b) Range profiles

Figure 6.7 Profiles of the amplitudes of complex and amplitude correlation functions

6.6.2 Image Model Matching Approach

The new image model matching approach was used to register the SAR subimage pairs of ERS-1 used in previous section. The distance measure between images of a pair $G_1(x, y)$ and $G_2(x, y)$ was chosen as in (6.20). The image model is updated by the incoherent summation, that is,

$$\text{sum}\,(M(x, y), G(x, y)) = |M(x, y)| + |G(x, y)|. \tag{6.33}$$

Figure 6.8 gives the correct probability of image registration using the image model matching approach (solid line) and the amplitude correlation (dash line). It shows that both provide correct registration if image similarity is greater than 0.6 for the image model matching approach and 0.7 for the amplitude correlation. However the image model matching degrades more slowly as the correlation coefficient decreases. The thresholds of registration accuracy 80% for the image model matching and the amplitude correlation are 0.37 and 0.46, respectively.

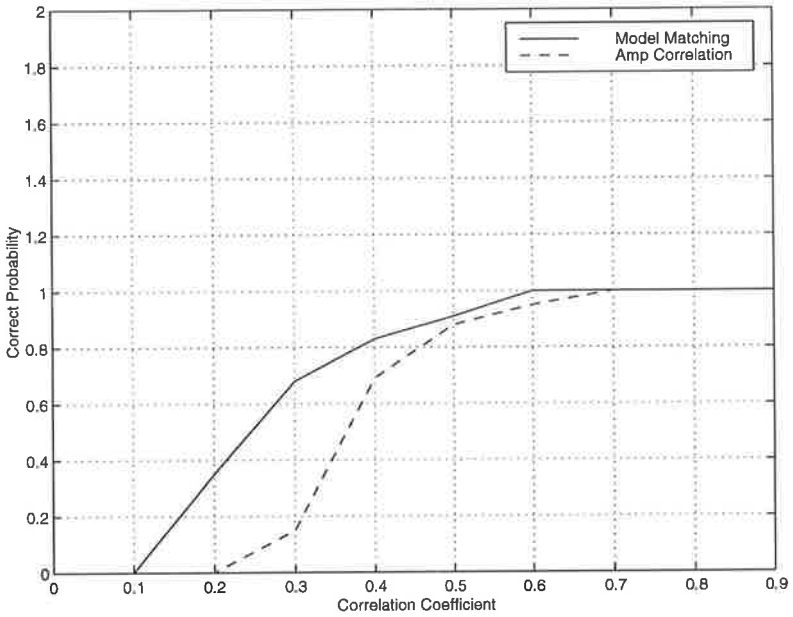

Figure 6.8 Registration accuracy versus image similarity

In Figure 6.9, the dash line denotes the correlation coefficient histogram of image pairs and the solid line is the correlation coefficient histogram between the reference image and each image. It is seen that the reference image has a better correlation with multiple images and so the image model matching approach can increase the accuracy of multiple image registration.

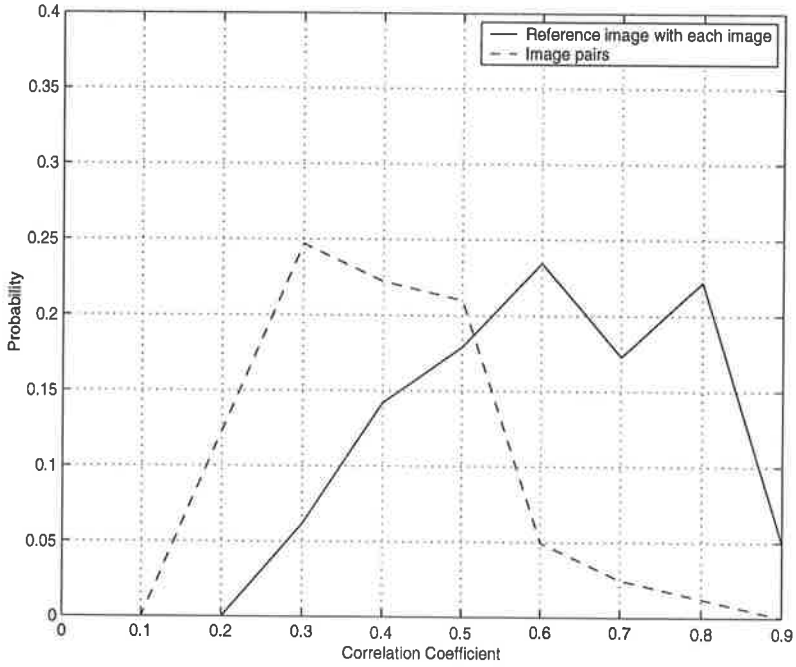

Figure 6.9 Histogram of correlation coefficients

6.6.3 Effect on 3D SAR Images

The effect of image registration on 3D SAR imaging was illustrated by MPSAR processing the ERS-1 data of one corner reflector terrain as described in section 5.6. Figure 6.10 gives the 3D image before image registration. It indicates that the signals resulting from the corner reflector are distributed in several range and azimuth cells. 3D SAR image after image registration is shown in Figure 6.11. It is seen that the signals corresponding to the corner reflector are located in the same range and azimuth cell. However they are still scattered over the elevational direction. The next chapter discusses phase correction to form a focused elevational beam.

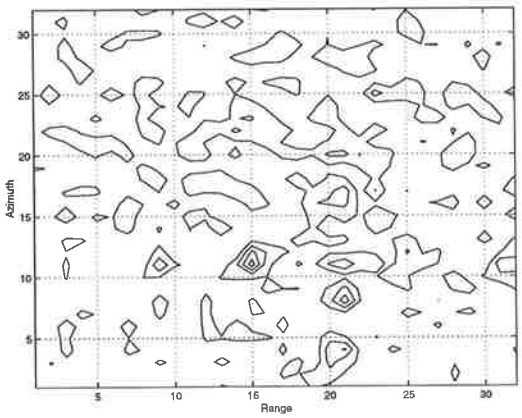

(a) Range-azimuth image

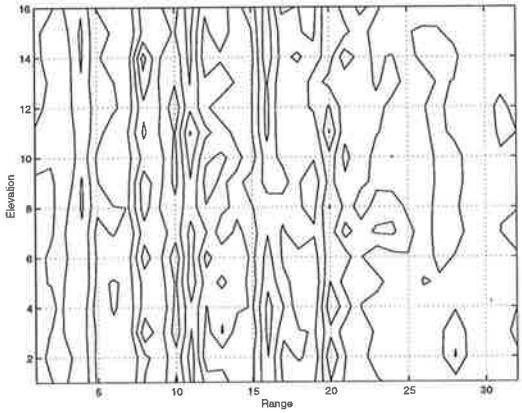

(b) Range-elevation image

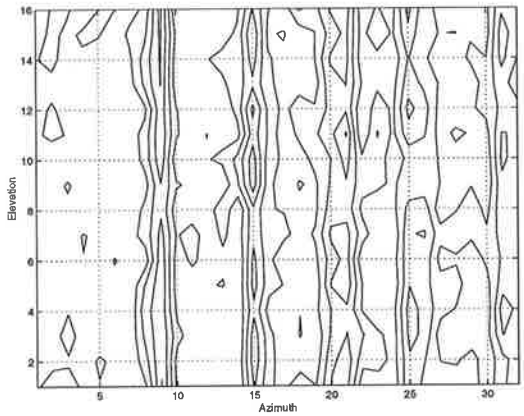

(c) Azimuth-elevation image

Figure 6.10 3D SAR image before image registration

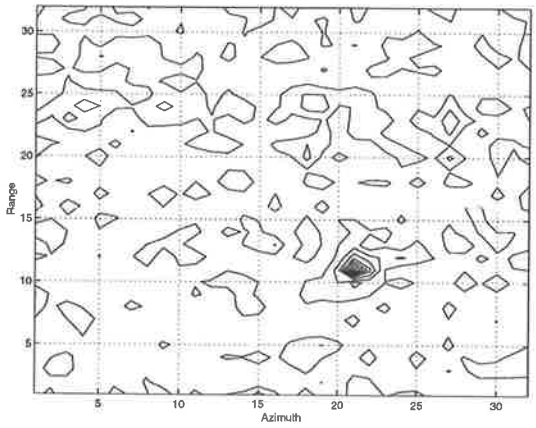

(a) Range-azimuth image

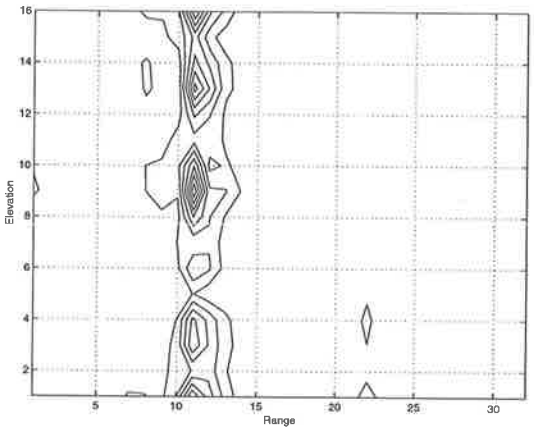

(b) Range-elevation image

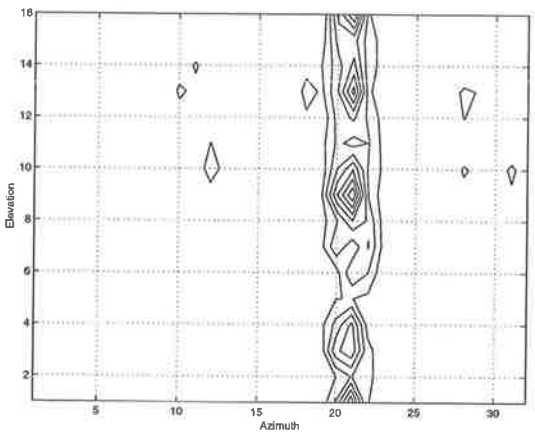

(c) Azimuth-elevation image

Figure 6.11 3D SAR image after image registration with the image model matching

6.7 Conclusions

Image registration is a key step of InSAR and MPSAR processing. The contributions in this chapter are

1. to make use of complex correlation instead of amplitude correlation to improve the accuracy of SAR image registration.

2. to develop the methods for multiple SAR image registration by use of the correlation of multiple images rather than the correlation for image pairs.

The model for multiple pass SAR images is described. The geometric transformation of SAR image registration is identified to be the local translation. The complex correlation approach is developed for the SAR image model. The conventional correlation only uses the amplitudes of images and discards the phases of images resulting in the high sidelobes and the broad peak of the correlation function. The complex correlation utilizes both the amplitude and phase of SAR image to increase the registration accuracy.

The multiple image registration is then studied. The minimal distance approach is the ideal method. It makes use of the correlation of multiple images to reduce image drift error resulting from the accumulation of error in correlation estimation and image variation error caused by the SAR image decorrelation. In order to reduce the computational load of the minimal distance approach, the image model matching is developed.

Finally the complex correlation and the image model matching approaches are used to process the real data of ERS-1. The processing results show that they are both able to increase the registration accuracy for the same image similarity, and to reduce the image coherence requirement for the same registration accuracy compared with the conventional amplitude correlation. The complex correlation can enhance the peak and reduce the sidelobe magnitudes of correlation functions. The image model matching is able to improve the coherence of multiple images by use of the reference image. The effectiveness of image registration is demonstrated by 3D ERS-1 SAR images.

Chapter 7 Phase Correction for MPSAR Processing

7.1 Introduction

The processing steps of MPSAR imaging have been investigated in chapter 5 which include first registration of multiple complex value SAR images, then phase correction of the registered images for beamforming, and finally beamforming in the elevational direction. Image registration of multiple SAR images was studied in previous chapter and the elevational beamforming will be discussed in next chapter. This chapter focuses on the phase correction of complex SAR images. Since phased array techniques are used to form the elevational beams, phase correction can be determined using array calibration principles [120] [121].

The organization of this chapter is as follows. The role of phase correction for SAR images is presented in section 7.2. In section 7.3, three methods of phase correction: eigenvector, terrain centroid tracking, and strong scatterer reference are developed. These approaches to phase correction are verified by processing the real data of ERS-1 in section 7.4 and statistical performances of phase correction are investigated in section 7.5.

7.2 Role of Phase Correction

In the analysis of chapter 5, it is assumed that the multiple flight paths are parallel and equi-spaced in elevation, and thus the beam output formed by summing the registered images enhances a plane wavefront signal incident the flight path array from the broadside direction as shown in Figure 7.1.

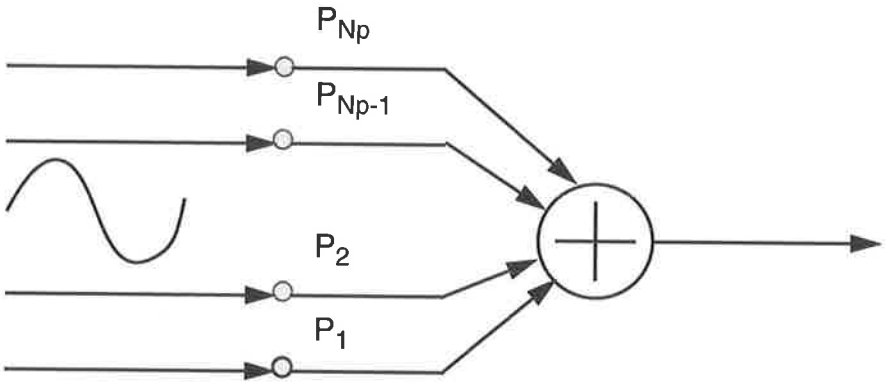

Figure 7.1 Flight path linear array steered at broadside direction

However in practice the flight paths are uncertain and deviate from their nominal position and the propagation medium in ionosphere and troposphere may be inhomogeneous[146]. These defects may destroy the above capability of coherent summation. In order to correct the uncertainty of flight paths and compensate for anomalies in the propagation medium, a phase shift is required to be attached to each flight path as shown in Figure 7.2 to form a focused beam in the elevation.

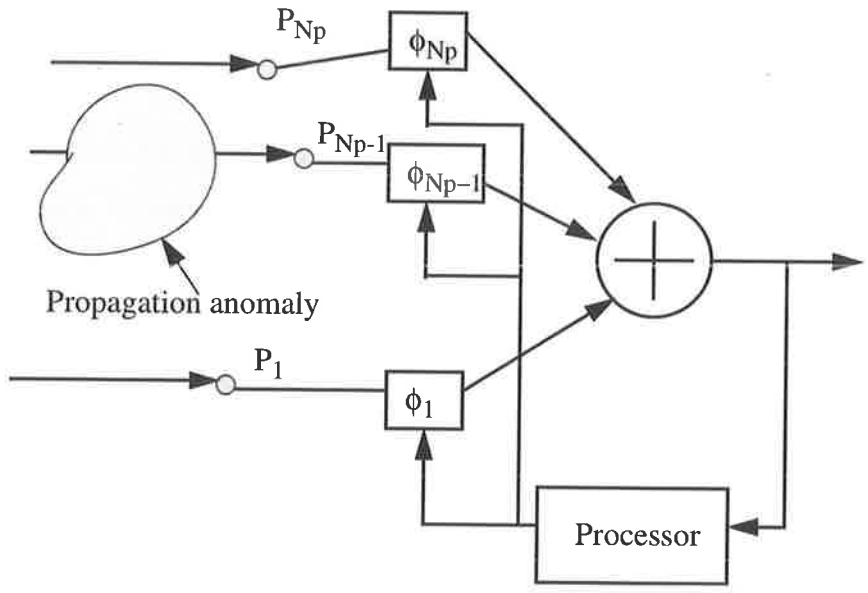

Figure 7.2 Flight path array with self-calibration to compensate for flight path uncertainty and propagation anomalies

Many techniques have been developed to determine the phase factors for array calibration as reviewed in section 2.8.3. A data-driven technique is used for self-calibration where no assisted device is required for calibration measurement. The beamforming and subspace approaches were applied to ISAR autofocus in chapter 3. Due to their theoretical equivalence the signal subspace method is adopted for phase correction in this chapter.

7.3 Phase Correction

MPSAR imaging carries out the phase correction to form a focused elevational beam. However phase correction is dependent upon precise information on flight paths and propagation medium (i.e. distortions need to be known to be the order of $\lambda/8$). In this section, three methods of phase correction are developed based on array self-calibration which do not need the information about flight path and propagation medium.

Based on (6.14), the image model after image registration can be written as

$$G_2(x, y) = G_1(x, y) \exp(-j\varphi_{21}) \tag{7.1}$$

where $G_1(x, y)$ and $G_2(x, y)$ are the subimages of the first and the second flight path, respectively whose size can be determined by the criteria discussed in chapter 5, $\varphi_{21} = 4\pi d_e \cos\beta/\lambda$, d_e the baseline between the first and second flight path, β the incidence angle as shown in Figure 5.1 and λ the radar wavelength. For the complex image corresponding to the ith flight path, (7.1) generalizes to

$$G_i(x, y) = G_{i-1}(x, y) \exp(-j\varphi_{i, i-1}) = G_1(x, y) \exp(-j\phi_i) \tag{7.2}$$

where $\phi_i = \sum_{n=2}^{i} \varphi_{n, n-1}$. Defining a pixel vector $V(x, y) = [G_1(x, y), \ldots, G_{N_p}(x, y)]^T$ and considering the SAR system additive noise, (7.2) has the form for each pixel

$$V(x, y) = G_1(x, y) D_e + W(x, y) \tag{7.3}$$

where $D_e = [1, \exp(-j\phi_2), \ldots, \exp(-j\phi_{N_p})]^T$ and $W(x, y) = [w_1(x, y), \ldots, w_{N_p}(x, y)]^T$. $w_i(x, y)$ is assumed to be independent identically distributed complex Gaussian noise components with zero mean and variance σ_w^2. The task of phase correction is to first

estimate the complex signal vector D_e, and then to compensate the multiple complex SAR images by conjugating with D_e.

It is pointed that the image model (7.3) has an analogy with the signal model (3.11) for ISAR autofocus. Therefore the conventional beamforming, the optimum beamforming, the signal and noise subspace methods developed in chapter 3 for ISAR autofocus can theoretically be applied to phase correction for MPSAR processing. Due to the equivalence of these methods, only the eigenvector method, that is the signal subspace method, is discussed and then its simplified versions such as terrain centroid tracking and strong scatterer reference are described.

7.3.1 Eigenvector Method

The covariance matrix of $V(x, y)$ is

$$C_V(x, y) = \mathrm{E}\{V(x, y)\, V^H(x, y)\} = |G_1(x, y)|^2 D_e D_e^H + C_w \tag{7.4}$$

where $C_w = \sigma_w^2 I$ is the covariance matrix of noise and I the identity matrix. It is verified in Appendix A that the largest eigenvalue of $C_V(x, y)$ is

$$\lambda_1 = |G_1(x, y)|^2 N_p + \sigma_w^2 \tag{7.5}$$

and its corresponding normalized eigenvector is

$$u_1 = \frac{D_e}{N_p} \tag{7.6}$$

and all the other eigenvalues are equal to σ_w^2. (7.6) shows that the eigenvector corresponding to the largest eigenvalue of $C_V(x, y)$, being proportional to D_e, can be used for phase correction.

The eigenvector method also realizes the ML estimation of D_e as follows. The joint probability density function of a single pixel vector is

$$p(V(x, y); D_e) = \pi^{-N_p} \{ \det(C_V(x, y)) \}^{-1} \exp\{-V^H(x, y)\, C_V^{-1}(x, y)\, V(x, y)\}. \tag{7.7}$$

It is assumed that the individual pixel vectors in the subimage are independent and have the same covariance matrix. Thus the joint probability density function of $V = [V(x_1, y_1), \ldots, V(x_{N_x N_y}, y_{N_x N_y})]$, that is the probability density function of all of the pixel vectors in the subimage, is the product of the probability density functions for individual pixel vectors and is given by

$$p(V;D_e) = \pi^{-N_p N_x N_y} \{ \det(C_V(x,y)) \}^{-N_x N_y} \exp\{-N_x N_y \operatorname{Tr}\left(C_V^{-1}(x,y)\, \hat{C}_V \right)\} \tag{7.8}$$

where $\hat{C}_V = \frac{1}{N_x N_y} \sum_{i=1}^{N_x N_y} V(x_i, y_i)\, V^{\mathrm{H}}(x_i, y_i)$ and N_x and N_y are the pixel dimensions of the SAR subimage in range and azimuth, respectively. Maximizing the log probability density function with respect to $\{D_e, |G_1(x,y)|^2\}$ results in the following equation [86]

$$\hat{C}_V D_{eML} = \sigma_w^2 \lambda_{max} D_{eML} \tag{7.9}$$

where λ_{max} is the largest eigenvalue of $\hat{C}_V$ and D_{eML} is the corresponding eigenvector. (7.9) shows that the eigenvector of $\hat{C}_V$ corresponding to the largest eigenvalue is the ML estimator of D_e.

7.3.2 Terrain Centroid Tracking

A new method for phase correction, terrain centroid tracking, is described below which makes use of the subaperture processing of the eigenvector approach to reduce the computational complexity when the number of flight paths is large. The terrain centroid tracking method considers the limiting case where each subaperture consists of two adjacent flight paths. It first forms the interferograms between these adjacent flight paths, then estimates the phase differences of the terrain centroid by averaging the phase within each of the interferograms and finally restores the phase of the terrain centroid for phase correction by accumulating the phase differences. Terrain centroid tracking is derived below.

For the ith subaperture formed by two flight passes P_i and P_{i+1}, the image model of (7.3) becomes

$$\begin{bmatrix} G_i(x,y) \\ G_{i+1}(x,y) \end{bmatrix} = G_i(x,y) \begin{bmatrix} 1 \\ \exp(j\varphi_{i+1,i}) \end{bmatrix} + \begin{bmatrix} w_i(x,y) \\ w_{i+1}(x,y) \end{bmatrix} \tag{7.10}$$

where $\varphi_{i+1,i} = \phi_{i+1} - \phi_i$ is the phase difference and the covariance matrix is estimated as

$$\hat{C}_V = \frac{1}{N_x N_y} \sum_{x=1}^{N_x} \sum_{y=1}^{N_y} \begin{bmatrix} G_i(x,y) \\ G_{i+1}(x,y) \end{bmatrix} \left[G_i^*(x,y) \;\; G_{i+1}^*(x,y) \right]. \tag{7.11}$$

The eigenvector corresponding to the largest eigenvalue of $\hat{C}_V$, derived in Appendix B, is

$$u_1 = \begin{bmatrix} 1 \\ k \sum_{x=1}^{N_x} \sum_{y=1}^{N_y} G^*_i(x,y)\, G_{i+1}(x,y) \end{bmatrix} \tag{7.12}$$

where k is a scalar. Thus the ML estimator of the exponential phase difference can be expressed as

$$\exp(j\hat{\varphi}_{i+1,i}) = \frac{\sum_{x=1}^{N_x} \sum_{y=1}^{N_y} G^*_i(x,y)\, G_{i+1}(x,y)}{\left| \sum_{x=1}^{N_x} \sum_{y=1}^{N_y} G^*_i(x,y)\, G_{i+1}(x,y) \right|} \tag{7.13}$$

which is the average phase of the interferogram formed by adjacent flight paths P_i and P_{i+1}. This phase average is weighted by the amplitude of the interferogram and it is called the phase difference of the terrain centroid. Thus this method tracks the terrain centroid rather than some strong scatterers.

Then the complex exponential phase of the terrain centroid in each flight path for phase correction can be obtained by setting the initial phase to be zero and multiplying $\exp\{j\hat{\varphi}_{i+1,i}\}$ $i = 1, \ldots, N_p - 1$ in flight path series to retain the continuation of phase for the entire aperture.

7.3.3 Strong Scatterer Reference

When K strong scatterers exist in the terrain, the effective SNR is enhanced if the summation in (7.13) is calculated only over the subset of pixels $(x_k, y_k)\, k = 1, \ldots, K$ where strong scatterers are located, i.e.,

$$\exp(j\hat{\varphi}_{i+1,i}) = \frac{\sum_{k=1}^{K} G_i^*(x_k, y_k)\, G_{i+1}(x_k, y_k)}{\left|\sum_{k=1}^{K} G_i^*(x_k, y_k)\, G_{i+1}(x_k, y_k)\right|}. \tag{7.14}$$

If one prominent strong scatterer with coordinate (x_d, y_d) is detected in the terrain, the estimated phase difference is approximated by

$$\exp(j\hat{\varphi}_{i+1,i}) = \frac{G_i^*(x_d, y_d)\, G_{i+1}(x_d, y_d)}{\left|G_i^*(x_d, y_d)\, G_{i+1}(x_d, y_d)\right|}. \tag{7.15}$$

In this case, the phase difference of the terrain centroid is estimated by the phase difference of the dominant strong scatterer which effectively becomes the centroid of the terrain. With initiation $\exp(j\hat{\phi}_1) = G_1(x_d, y_d)/\left|G_1(x_d, y_d)\right|$, then the complex exponential phase of the terrain centroid in each flight path is estimated by

$$\exp(j\hat{\phi}_{i+1}) = \exp(j\hat{\phi}_i)\exp(j\hat{\varphi}_{i+1,i}) = \frac{G_{i+1}(x_d, y_d)}{\left|G_{i+1}(x_d, y_d)\right|} \quad i=1,\ldots,N_p-1. \tag{7.16}$$

In such a case, the phase correction is actually to compensate the complex images by referencing the phase of the strong scatterer which is the popular method for SAR system calibration.

In summary the eigenvector method is the ML estimation for phase correction. The terrain centroid tracking and the strong scatterer reference are the simplified schemes of the eigenvector method. The computational operations of the above three methods are given in Table 7.1 where N_x and N_y are the pixel dimensions of SAR image in the range and azimuth directions, N_p is the number of flight path and a Householder transformation is used for the eigendecomposition of covariance matrix[234]. The number of divisions for the three methods are almost the same, the strong scatterer reference does not need any additions, and its operation of multiplication is less than those of the eigenvector method and the terrain centroid tracking. A numeric example of Table 7.1 for the experiment in this chapter is shown in Table 7.2 where $N_x = 32$, $N_y = 32$ and $N_p = 9$. It is seen that the ratio of multiplications for these three methods is about $N_p + 1 : 2 : 1$ and the ratio of additions between the eigenvector method and the terrain centroid tracking is approximately $N_p : 1$.

Table 7.1 Computational operations of phase correction

	Division	Multiplication	Addition
Eigenvector method	N_p	$N_xN_yN_p+N_xN_yN_p^2+4/3N_p^3$	$N_xN_yN_p^2+4/3N_p^3$
Terrain centroid tracking	N_p-1	$2N_xN_yN_p$-N_xN_y+N_p-1	$N_xN_yN_p$-N_xN_y
Strong scatterer reference	N_p	$N_xN_yN_p$	0

Table 7.2 Numeric example of Table 7.1

	Division	Multiplication	Addition
Eigenvector method	9	93132	83916
Terrain centroid tracking	8	17416	8192
Strong scatterer reference	9	9216	0

7.4 Experiment Results

The three methods proposed for phase correction were used to process the 9 SAR image data sets acquired by the ERS-1 satellite presented in chapter 5. An image patch satisfying the conditions discussed in chapter 5 was selected for MPSAR processing. The 9 SAR images were first registered with the image model matching approach, and then corrected in phase by the three methods developed in this chapter, and finally conventionally beamformed in elevation to produce the 3D SAR images.

The Integrated sidelobe ratio (ISLR)[147] is a useful criterion to measure the focusing quality. It is defined as the ratio of the energy in mainlobe to that in sidelobes, that is,

$$\text{ISLR} = \frac{E_M}{E_T - E_M} \tag{7.17}$$

where E_M denotes the energy in the mainlobe with a 3dB bandwidth and E_T is the total energy. The larger the ISLR, the smaller the sidelobes and the better the resolution capability.

7.4.1 One Corner Reflector Terrain

At first an image patch containing a corner reflector was processed. The reconstructed 3D image was visualized with three 2D profiles, that is, the range-azimuth image, the range-elevation image and the azimuth-elevation image; the resolution of elevation being shown in the range-elevation image and the azimuth-elevation image. Figure 6.11 is the 3D image without phase correction. Figure 7.3, Figure 7.4 and Figure 7.5 are the 3D images where the phase correction is carried out by the strong scatterer reference, the terrain centroid tracking and the eigenvector method, respectively. In these figures (a) is the range-azimuth image, (b) is the range-elevation image and (c) is the azimuth-elevation image.

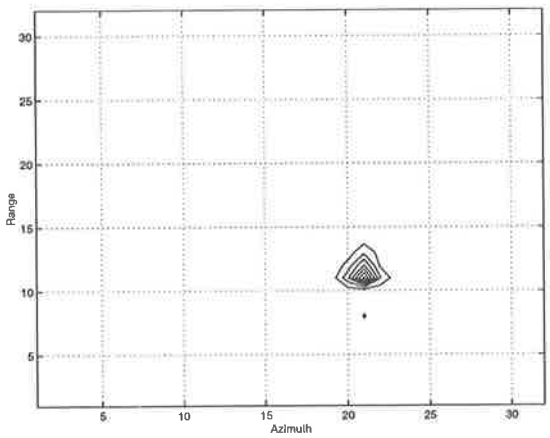

(a) Range-azimuth image

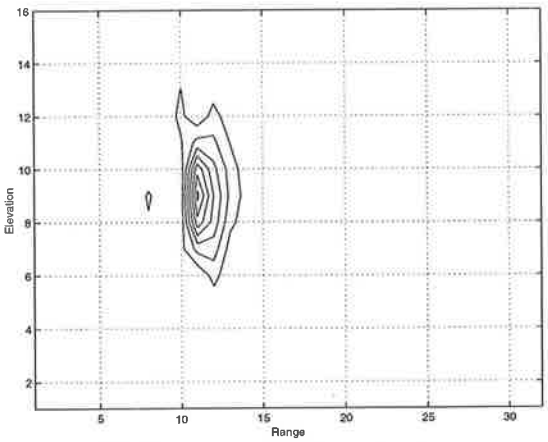

(b) Range-elevation image

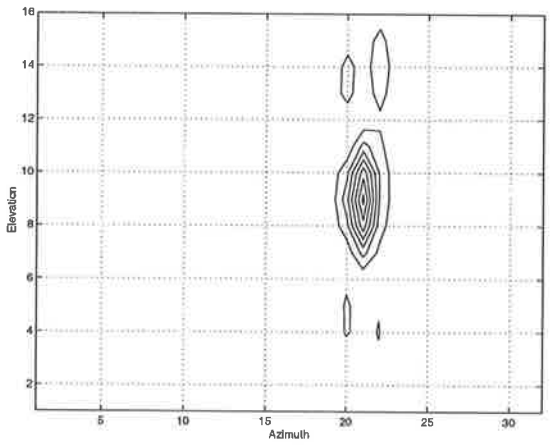

(c) Azimuth-elevation image

Figure 7.3 3D SAR image with the strong scatterer reference

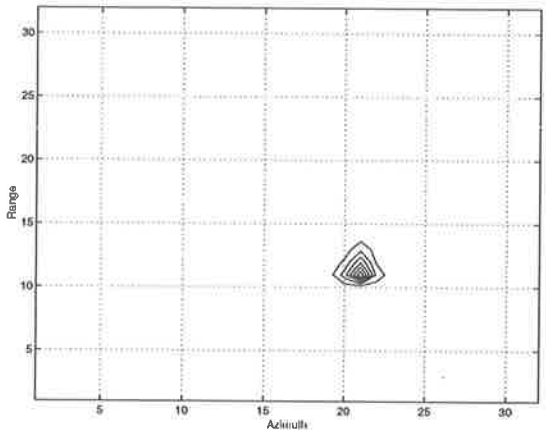

(a) Range-azimuth image

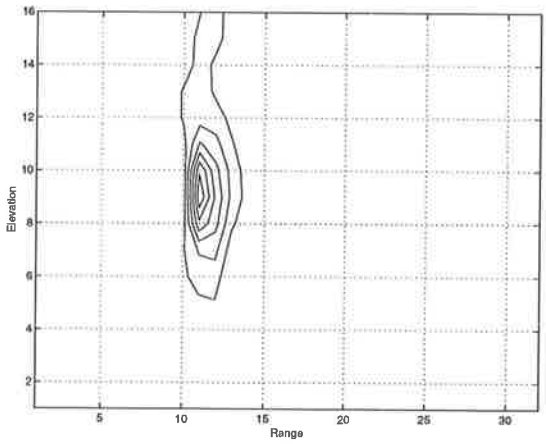

(b) Range-elevation image

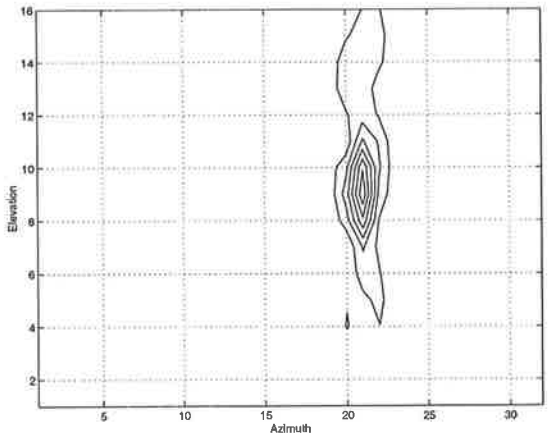

(c) Azimuth-elevation image

Figure 7.4 3D SAR image with the terrain centroid tracking

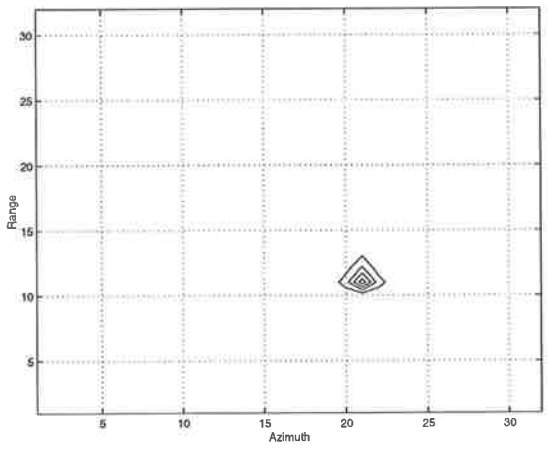

(a) Range-azimuth image

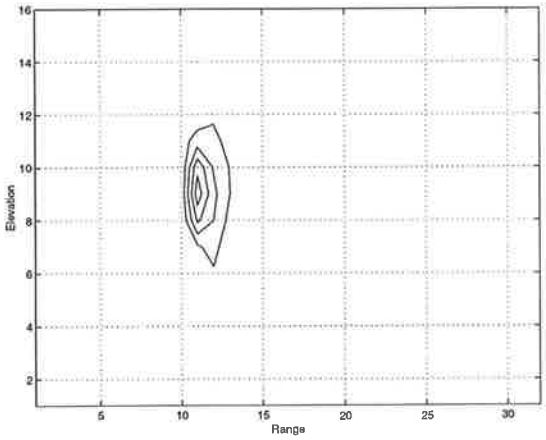

(b) Range-elevation image

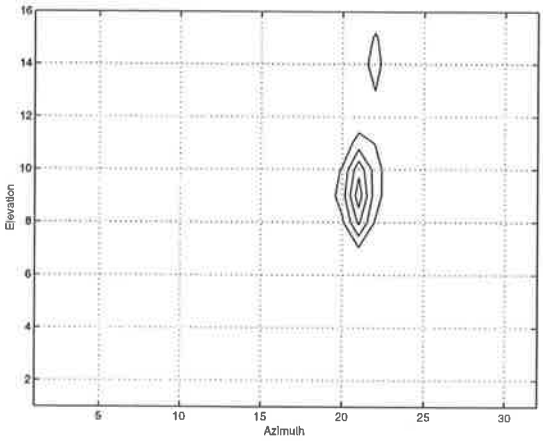

(c) Azimuth-elevation image

Figure 7.5 3D SAR image with the eigenvector method

By comparing with Figure 6.11, the focusing quality in Figures 7.3, 7.4 and 7.5 is clearly better indicating the effectiveness of phase correction. Although these methods are theoretically related, differences do arise due to details in the estimation as discussed in section 7.3. The ISLRs of these SAR images are listed in Table 7.3 which shows that Figure 7.3 is the best and Figure 7.5 is better than Figure 7.4. The loss of SNR caused by estimating the covariance matrix over the non-signal cells makes Figure 7.3 superior to Figure 7.5. The difference between Figure 7.4 and Figure 7.5 is due to the fact that the subaperture processing of the eigenvector method results in a little increase of CRLB of estimated complex vector as discussed in section 4.7.

Table 7.3 ISLRs of 3D SAR images for one corner reflector terrain

ISLR (dB)	No phase correction in Figure 6.11	Strong scatterer reference in Figure 7.3	Terrain centroid tracking in Figure 7.4	Eigenvector method in Figure 7.5
Reflector	0.0473	9.3415	2.0967	3.2679

7.4.2 Two Corner Reflector Terrain

Secondly a subimage containing two corner reflectors at different ranges and azimuths as shown in Figure 5.16 was chosen. Figure 7.6 displays the 3D image without phase correction where (a) is the profiles of the first corner reflector in the range-elevation and

azimuth-elevation planes and (b) is the profiles of the second corner reflector in the range-elevation and azimuth-elevation planes. It is seen that the elevational beam is out of focus without phase correction.

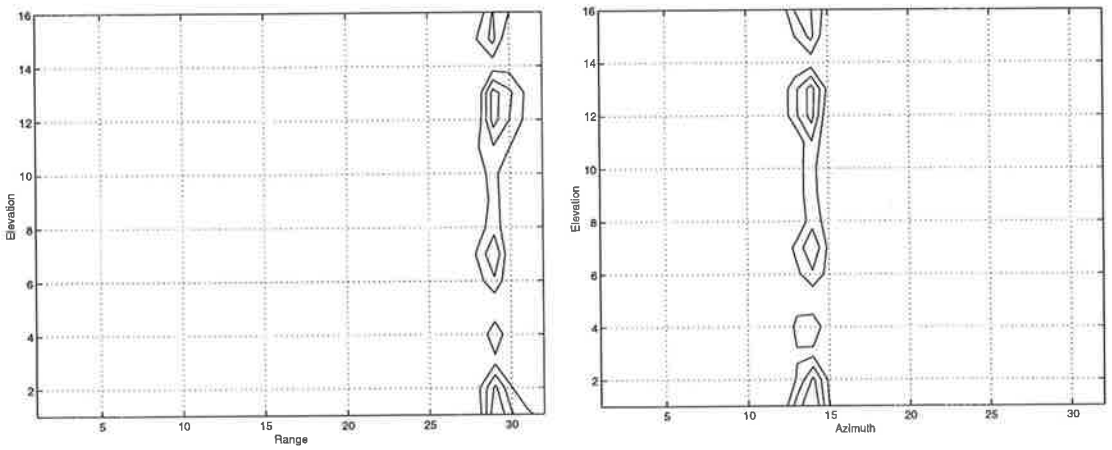

(a) Elevation profiles of the first corner reflector

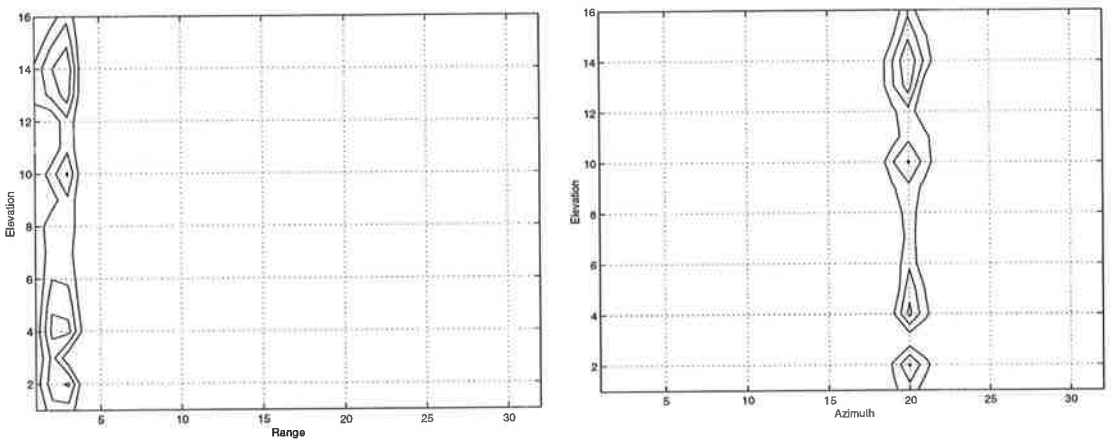

(b) Elevation profiles of the second corner reflector

Figure 7.6 3D SAR image without phase correction

Figure 7.7 and Figure 7.8 give the 3D images where the phase correction is conducted by the strong scatterer reference method with referencing the first and the second corner reflector, respectively. They show that the elevational beam focuses on the corner reflector to be referenced but the other corner reflector is out of focus.

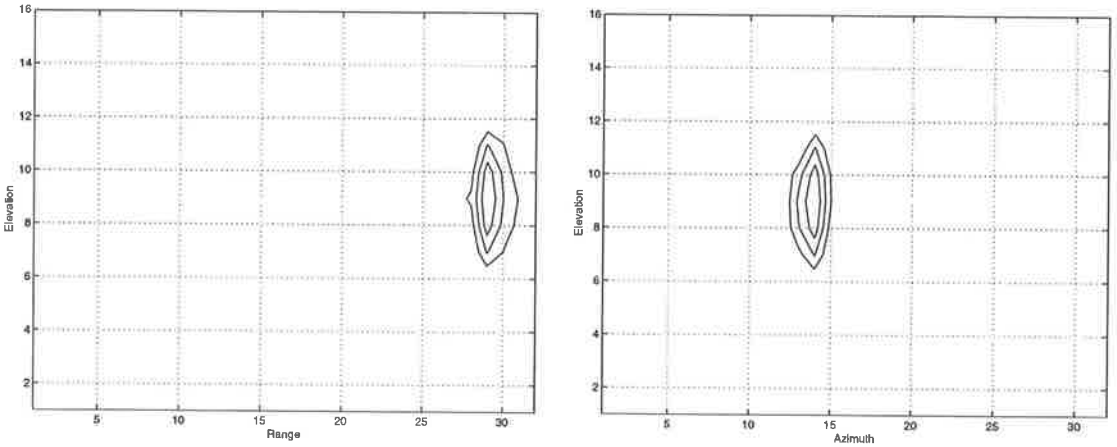

(a) Elevation profiles of the first corner reflector

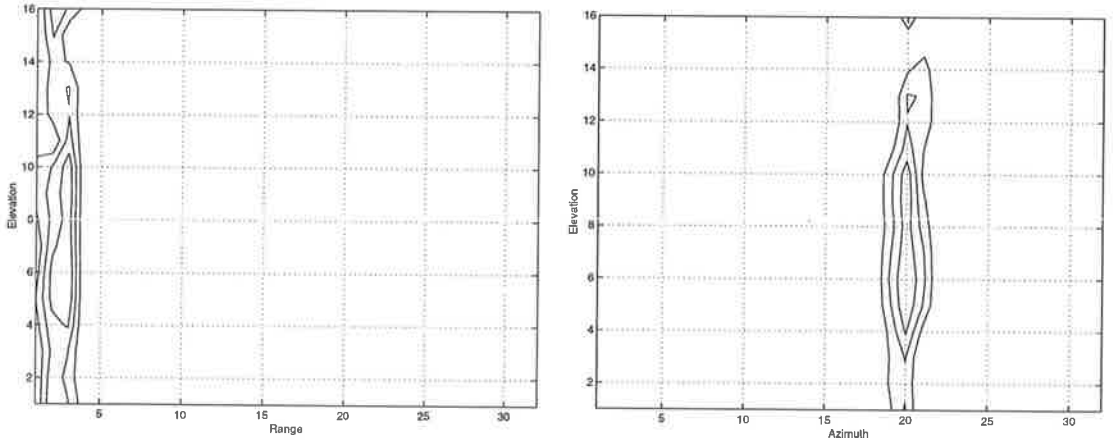

(b) Elevation profiles of the second corner reflector

Figure 7.7 3D SAR image with the first corner reflector reference for phase correction

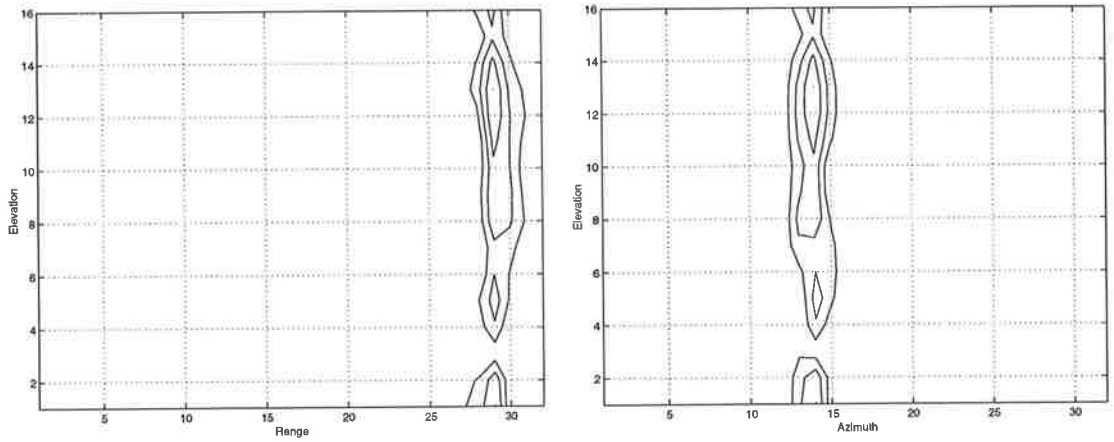

(a) Elevation profiles of the first corner reflector

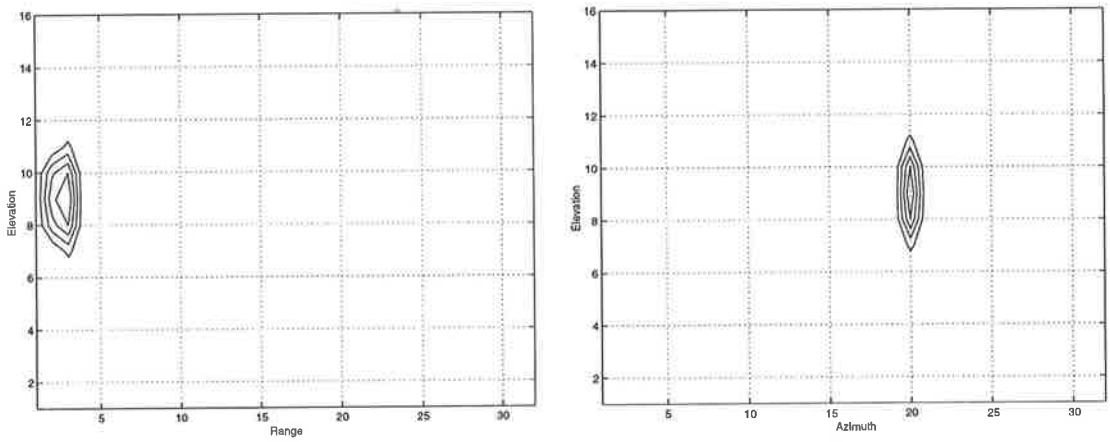

(b) Elevation profiles of the second corner reflector

Figure 7.8 3D SAR image with the second corner reflector reference for phase correction

Figure 7.9 and Figure 7.10 are the 3D images where the phase correction is performed by the terrain centroid tracking and the eigenvector method, respectively. They show that the two corner reflectors are focused simultaneously at the expense of some widening of the beamwidth.

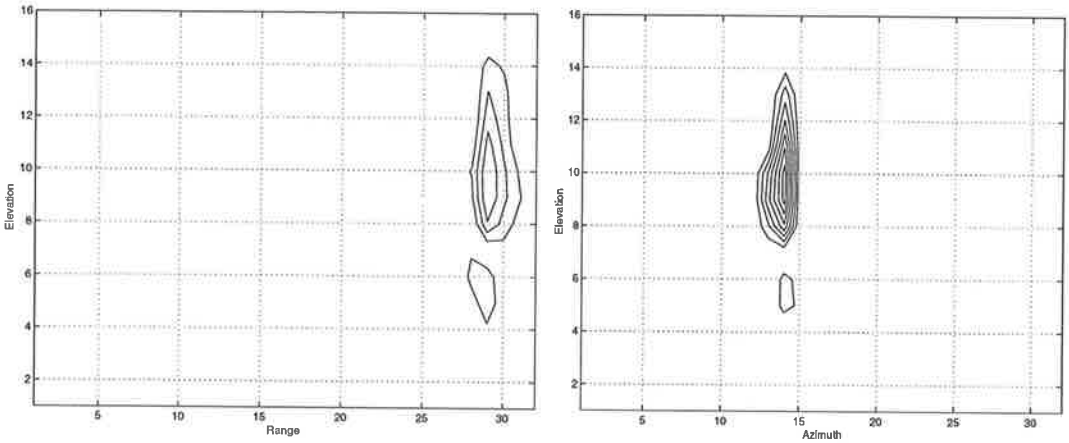

(a) Elevation profiles of the first corner reflector

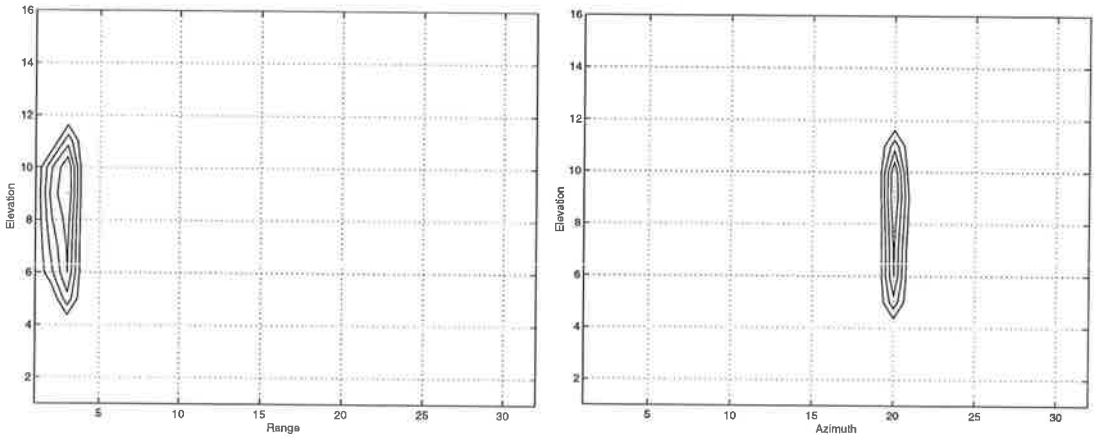

(b) Elevation profiles of the second corner reflector

Figure 7.9 3D SAR image with the terrain centroid tracking for phase correction

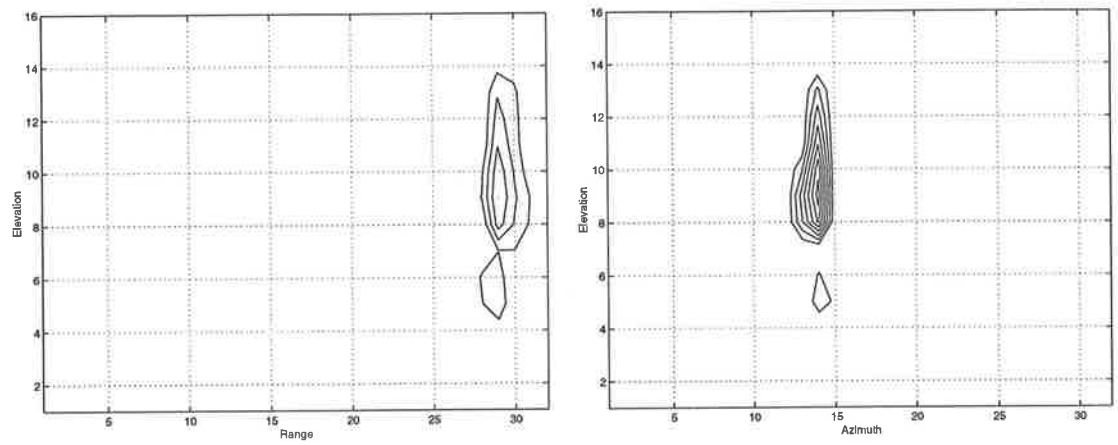

(a) Elevation profiles of the first corner reflector

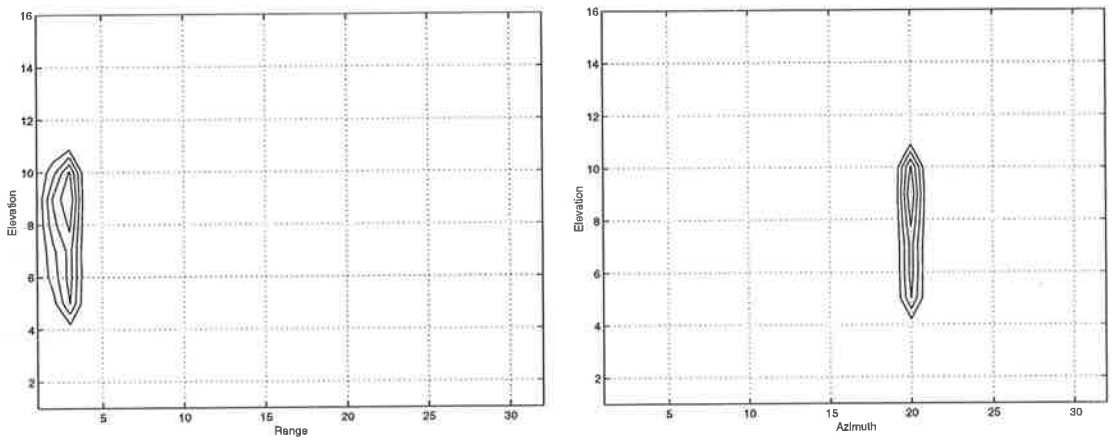

(b) Elevation profiles of the second corner reflector

Figure 7.10 3D SAR image with the eigenvector method for phase correction

The ISLRs of the two corner reflectors in the above 3D images are given in Table 7.4 which show the focusing quality of the three methods for phase correction. The ISLRs are increased by use of the phase correction to form a focused beam. The strong scatterer reference is able to enhance the ISLR of the referenced corner reflector significantly but does not necessarily increase the ISLR of the second reflector. The terrain centroid tracking and the eigenvector method improve the ISLRs of both two corner reflectors properly rather than that of a specific corner reflector.

Table 7.4 ISLRs of 3D SAR images for two corner reflector terrain

ISLR (dB)	No phase correction in Figure 7.6	Strong reflector 1 reference in Figure 7.7	Strong reflector 2 reference in Figure 7.8	Terrain centroid tracking in Figure 7.9	Eigenvector method in Figure 7.10
Reflector 1	1.5296	9.7353	0.8728	2.3814	2.8560
Reflector 2	-1.4972	0.8251	4.0973	1.5679	1.7161

7.5 Statistical Analysis

Statistical tests were conducted to inspect the robustness of phase correction. Consider a terrain containing a strong scatterer, 17 SAR images with equally-spaced flight paths were simulated and white noise was added before MPSAR imaging. The strong scatterer reference method was used for phase correction. Other parameters of the simulation were given in section 5.5. The focusing quality of 3D images was measured by the ISLR of the strong scatterer. This statistics was based on 100 independent realizations for a specific SNR. Figure 7.11 gives the mean ISLR of the scatterer versus SNR of the SAR images. In particular the ISLR is reduced by greater than 3dB with respect to the asymptotic SNR limits when the SNR drops below 5dB.

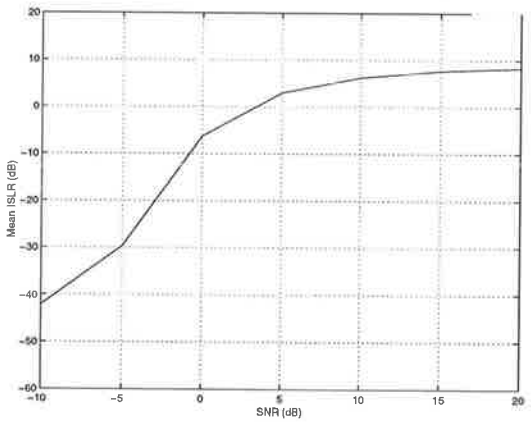

Figure 7.11 Mean ISLR versus SNR

In order to measure the effect of subimage size on the focusing quality of a 3D SAR image, a terrain consisting of two strong scatterers having the same elevational coordinate and different distances in the range-azimuth plane was simulated. 3D SAR image was

formed by phase correction with the reference of one strong scatterer and the focusing quality of the 3D image was measured by the ISLR of the other scatterer. This focusing quality versus the distance between the two scatterers is shown in Figure 7.12. It indicates that a subimage with a size up to 110m can be focused with an ISLR above 3dB which is consistent with the result in section 5.3.

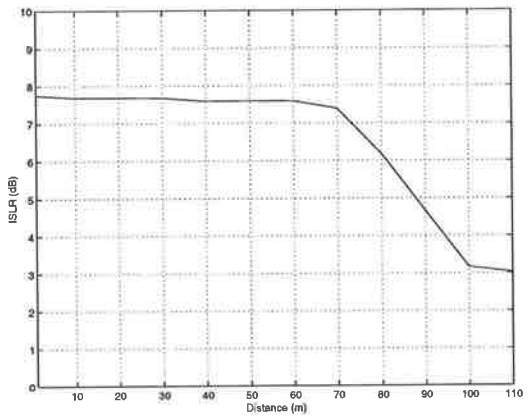

Figure 7.12 ISLR versus subimage size

7.6 Conclusions

Phased array calibration techniques have been employed to effect phase correction to obtain a focused beam in the elevational direction for MPSAR. The original work in this chapter is to apply the methods of array calibration to determine the phase factor for phase correction. Three approaches for phase correction of MPSAR processing are developed.

1. The eigenvector method makes use of the eigenvector corresponding to the largest eigenvalue of the covariance matrix of pixel vector which is the ML estimator for phase correction.

2. The terrain centroid tracking is the subaperture processing of the eigenvector method when each subaperture consists of adjacent two flight paths. It has a reduced computational load (multiplication) by a factor of 5 in Table 7.2 but results in a small increase of estimated variance bound compared with the eigenvector method.

3. If a prominent strong scatterer exists, the strong scatterer reference regards the signal vector of the strong scatterer as the eigenvector corresponding to the largest eigenvalue of estimated covariance matrix. It is straight forward and easy to implement.

The three approaches were verified by processing the ERS-1 data for one and two corner reflector terrains and the statistical performances were analysed. It is concluded that the eigenvector method is versatile for phase correction. However in practical applications it is limited by the accurate estimation of the covariance matrix and the computational load for eigendecomposition when the number of flight paths increases. If a strong scatterer is identified in the terrain, the strong scatterer reference can replace the eigenvector approach effectively to eliminate the SNR loss in estimating the covariance matrix. When no strong scatterer exists in the terrain, the terrain centroid tracking may be used to obviate the estimation of the covariance matrix and the eigendecomposition of the estimated covariance matrix. Selecting a phase correction method suitable for terrain type yields a satisfactory focused elevational resolution with reduced computational complexity.

Chapter 8 Elevational Imaging and Super-resolution for MPSAR Processing

8.1 Introduction

MPSAR imaging as described in chapter 5 involves three steps. First is registration of multiple complex value SAR images, second is phase correction of the registered images, and third is beamforming in the elevational direction. The registration and the phase correction of multiple SAR images have been investigated in chapter 6 and chapter 7, respectively. In this chapter, the elevational imaging with multiple beams in elevation and the enhancement of elevational resolution by super-resolution processing are studied.

This chapter is structured as follows. Frequency domain beamforming in elevation by use of the DFT is described in section 8.2. In section 8.3, the two methods for enhancement of elevational resolution are investigated: the first is a maximal entropy extrapolation for linear enhancement and the second is a subspace method for nonlinear enhancement. The developed approaches for the formation and enhancement of elevational resolution are illustrated by processing the real data of ERS-1 in section 8.4. Statistical performances of elevational imaging and resolution are analysed in section 8.5.

8.2 Elevational Imaging

MPSAR imaging is able to produce a 3D radar image as a function of range, azimuth and elevation. High range resolution is achieved by pulse compression of the wideband transmitted signals. Azimuthal and elevational resolutions rely on the synthesized aperture in azimuth and elevation, respectively. In this section, phased array beamforming

techniques based on frequency domain beamforming are used to obtain the elevational resolution by forming many receiving beams in the elevational direction.

After phase correction, an elevational beam is formed in the broadside direction of the flight path array by coherent addition of the complex images. However signals from other directions are not in phase and will not be reinforced. To form an image in these directions, the complex image of each flight path is required to be shifted in phase to compensate the difference of propagation path in order to sum them coherently. Due to the fact that the variation of azimuthal aspect angle within a subimage is negligible, the difference of propagation path for the ith flight path with respect to the first flight path as shown in Figure 8.1 is

$$\Delta r_{il} = (i-1)\, d_e \sin\theta_l \tag{8.1}$$

where d_e is the baseline between adjacent two flight paths and θ_l the elevational signal direction. Thus the corresponding phase shift is expressed as

$$\eta_{il} = \frac{4\pi}{\lambda}(i-1)\, d_e \sin\theta_l \tag{8.2}$$

due to two-way propagation. The frequency-domain beamforming approach steers the elevational receiving beam by varying η_{il} as shown in Figure 8.1. Two groups of phase shifters are illustrated. The first group ϕ_i conducts the phase correction to compensate for the uncertainty of flight path and propagation anomalies as discussed in chapter 7. The second group η_{il} applies a linear phase across the flight path array to scan the focused beam electronically in the elevational direction.

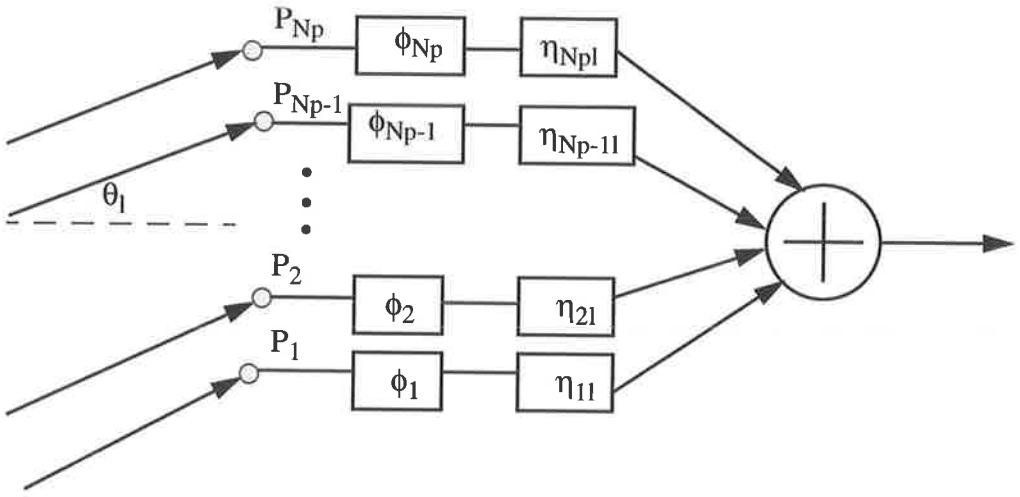

Figure 8.1 Focusing and scanning the elevational beam

For an equi-spaced flight path array, the steering phase factor is $\exp\{-j\frac{4\pi}{\lambda}(i-1)\,d_e \sin\theta_l\}$, thus the output of the elevational beamformer, an estimator of reflectivity $\rho(x, y, z)$, is expressed as

$$\hat{\rho}(x, y, z) = \sum_{i=1}^{N_p} G'(x, y, i) \exp\{-j\frac{4\pi}{\lambda}(i-1)\,d_e \sin\theta_l\} \tag{8.3}$$

where $G'(x, y, i) = G_i(x, y) \exp(j\phi_i)$ and (8.3) can be computed efficiently using an N_p-point DFT.

Use of an N_p point DFT produces multiple receiving beams in directions θ_l given by

$$\sin(\theta_l) = \frac{\lambda}{d_e}\frac{l}{2N_p} \quad |l| < \frac{N_p}{2}. \tag{8.4}$$

Shading weight coefficients b_i $i = 1, \ldots, N_p$ are generally applied to the individual phase corrected images to control the mainlobe width and the sidelobe levels of the elevational beams[99]. In order to increase the number of elevational beams steered, the windowed and phase-corrected images $b_i G'(x, y, i)$ $i = 1, \ldots, N_p$ can be appended with zeros prior to DFT of the extended data[98].

8.3 Super-resolution Processing

Whilst zero-padding of $b_i G'(x, y, i)$ increases the number of steered elevational beams, the elevational resolution remains unchanged because zero-padding does not increase the array aperture and the elevational resolution is determined by the aperture length in elevation which is known as Rayleigh resolution. The Rayleigh resolution can only be enhanced by increasing the effective aperture length, which is impractical for MPSAR processing. Super-resolution processing of MPSAR allows the Rayleigh resolution to be overcome and consequently it is to be preferred as it reduces the number of flight paths required and mitigates the decorrelation of SAR images.

The model of multiple complex sinusoids in (8.3) allows modern spectral estimation techniques to be used to increase the spectral resolution beyond the Rayleigh limit. Super-resolution processing techniques include maximum entropy (ME), auto-regressive (AR), moving average (MA), auto-regressive moving average (ARMA), multiple signal

classification (MUSIC) and estimation of signal parameters via rotational invariance techniques (ESPRIT). In this section two of these methods are used to enhance the elevational resolution. One is the maximum entropy extrapolation of the observed data where the extrapolation procedure is carried out for each pixel cell of multiple registered and phase corrected SAR images in the data domain. The Fourier transform of the extrapolated data produces enhanced elevational resolution. The other is the subspace method which makes use of the orthogonality between the noise subspace and the signal subspace of the covariance matrix of the observed data to provide the super-resolution capability.

The block diagram of elevational super-resolution is shown in Figure 8.2. After image registration and phase correction, the data across multiple SAR images with the same pixel position, that is the output of the flight path array at this pixel, form a pixel series. Instead of DFT processing, high resolution spectral analysis such as maximum entropy extrapolation and subspace methods is applied to each pixel series to enhance the elevational resolution.

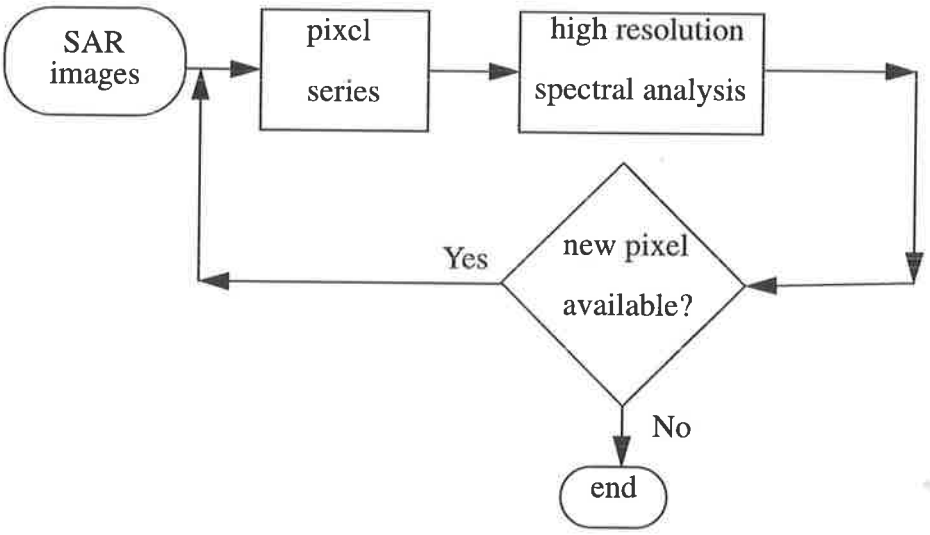

Figure 8.2 Block diagram of elevational super-resolution processing

8.3.1 Linear Super-resolution

The philosophy of maximum entropy spectral estimation is that all extrapolations of the measured data should be consistent with the available data and should make minimal assumptions regarding unavailable data. For a one-dimensional regularly sampled stationary Gaussian process, maximum entropy is equivalent to using the assumption of an

AR process [35] and there are two main ways to estimate the AR spectrum. The first approach is to estimate the prediction coefficients and to calculate the spectrum using the estimated prediction coefficients. The second approach also estimates the prediction coefficients, but then extrapolates the observed data in both directions with the estimated prediction coefficients, and finally applies a Fourier transform to the extrapolated data. Since both approaches use the same prediction coefficients, they should provide essentially the same spectral estimation. However the first approach only estimates the power spectrum and ignores the phase spectrum. The second approach, despite being more computation-intensive, produces both the power and phase spectra and this is sometimes more useful for sonar and radar applications [101] [102]. In this section the second approach is employed. It is called linear super-resolution because it invokes DFT and preserves the phase information.

The block diagram of the proposed linear super-resolution is shown in Figure 8.3. The pixel series $G'(x, y, i)$ at pixel (x, y) is at first used to estimate the prediction coefficients using the Burg algorithm which guarantees numerical stability[103]. This algorithm has a lattice structure with each stage determined by a reflection coefficient. The reflection coefficient $t_k(x, y)$ at stage k is estimated by minimizing the sum of the forward and backward prediction error powers and is given by

$$t_k(x,y) = \frac{-2\sum_{i=k}^{N_p-1} e^f_{k-1}(x,y,i)\, e^{b}_{k-1}{}^{*}(x,y,i-1)}{\sum_{i=k}^{N_p-1}\left(\left|e^f_{k-1}(x,y,i)\right|^2 + \left|e^b_{k-1}(x,y,i-1)\right|^2\right)} \tag{8.5}$$

where the forward and backward prediction errors are calculated by

$$e^f_k(x,y,i) = e^f_{k-1}(x,y,i) + t_k(x,y)\, e^b_{k-1}(x,y,i-1) \quad \text{i=k+1,...,} N_p - 1, \tag{8.6}$$

$$e^b_k(x,y,i) = e^b_{k-1}(x,y,i-1) + t_k^*(x,y)\, e^f_{k-1}(x,y,i) \quad \text{i=k,...,} N_p - 2 \tag{8.7}$$

with initial value

$$e^f_0(x,y,i) = G'(x,y,i) \quad \text{i=1,...,} N_p - 1, \tag{8.8}$$

$$e^b_0(x,y,i) = G'(x,y,i) \quad \text{i=2,...,} N_p - 2. \tag{8.9}$$

The prediction coefficients of the k order transversal filter are determined by the reflection coefficients using the Levinson recursion

$$h_k(x,y,i) = \begin{cases} h_{k-1}(x,y,i) + t_k(x,y)\, h_{k-1}{}^*(x,y,k-i) & \text{i=1,...,}k-1 \\ t_k(x,y) & \text{i=k} \end{cases} \tag{8.10}$$

which is a fast algorithm[103]. The process is repeated Q times until the prediction coefficients $h_Q(x,y,k)$ k=1,..., Q are estimated where Q is the AR model order to be used.

Then the pixel series is extrapolated forward and backward to the length N_pF where F is a factor of extrapolation. The forward extrapolation of data is given by

$$G'(x,y,N_p+i) = \sum_{k=1}^{Q} h_Q(x,y,k)\, G'(x,y,N_p+i-k) \quad \text{i}>0 \tag{8.11}$$

and the backward extrapolation of data is done by

$$G'(x,y,-i) = \sum_{k=1}^{Q} h_Q{}^*(x,y,k)\, G'(x,y,k-i) \quad \text{i}>0. \tag{8.12}$$

Finally the extrapolated pixel series is Fourier transformed to produce the super-resolution.

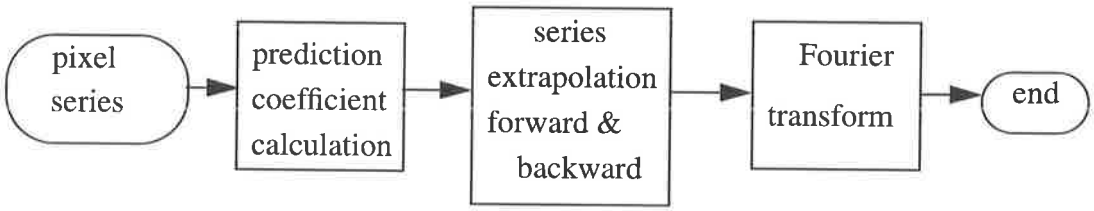

Figure 8.3 Linear super-resolution diagram

The selection of model order is a critical step. If the model order is too low, the spectrum has all the peaks smoothed. On the other hand, if the order is too large, the spectrum may contain spurious peaks. Many criteria such as Akaike Information Criterion (AIC) and Minimum Description Length (MDL) have been proposed to estimate the model order[103]. An effective approach to determine the model order Q of AR for the short data in radar and sonar applications is [101] [102]

$$Q \leq N_p/3. \tag{8.13}$$

and the extrapolation factor F is selected as [101] [102]

$$F = 2 \sim 4. \tag{8.14}$$

8.3.2 Nonlinear Super-resolution

Linear super-resolution extrapolates the elevational aperture with the AR model in the data domain and Fourier transforms the extrapolated data to obtain the super-resolution. However its improvement is limited[102]. The subspace method makes use of the eigendecomposition of the covariance matrix of the observed data. The orthogonality between the noise subspace and the signal subspace of the covariance matrix produces super-resolution. The resolution capability of the subspace method is theoretically unlimited in the absence of noise. But it only provides the location of individual scatterers in elevation and its spectrum has no information about amplitude and phase of reflectivity[104]. Due to this fact it is called nonlinear super-resolution. However once the elevations of the individual scatterers have been obtained the complex amplitude information can be obtained by solving a linear least-square problem.

The block diagram of nonlinear super-resolution is shown in Figure 8.4. The covariance matrix of the pixel series is at first estimated, the eigenstructure of the estimated covariance matrix is analysed to determine the subspaces of signal and noise, and a high resolution spectrum is calculated from the eigenvectors of the noise subspace.

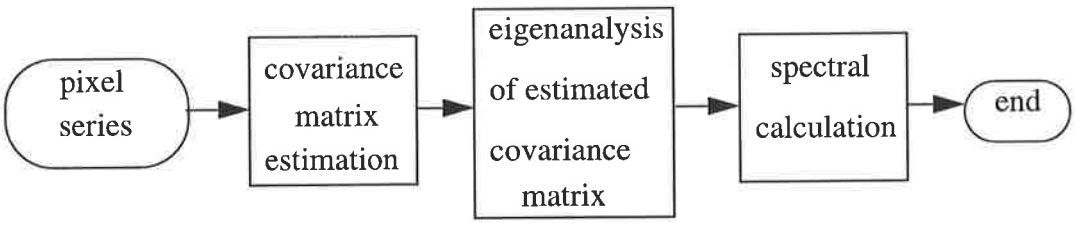

Figure 8.4 Nonlinear super-resolution diagram

From (8.3), the observed model[(1)] is formulated as

(1) Note this can be thought of as the inverse model of (8.3).

$$G'(x, y, i) = \sum_{l=1}^{K} \rho(x, y, z_l) \exp\{j\frac{4\pi}{\lambda}(i-1) d_e \sin\theta_l\} + w_i(x, y) \quad i=1, \ldots, N_p \tag{8.15}$$

where it is assumed that K scatterers exist in the elevation with reflectivity $\rho(x, y, z_l)$ and $w_i(x, y)$ is an additive noise which is assumed to be independently Gaussian distributed. Defining a $K \times 1$ vector $\Sigma_{xy} = [\rho(x, y, z_1), \ldots, \rho(x, y, z_K)]^T$ and $N_p \times 1$ vectors $V'_{xy} = [G'(x, y, 1), \ldots, G'(x, y, N_p)]^T$, $W_{xy} = [w_1(x, y), \ldots, w_{N_p}(x, y)]^T$, we have

$$V'_{xy} = A_{xy}\Sigma_{xy} + W_{xy} \tag{8.16}$$

where $N_p \times K$ matrix $A_{xy} = (a_1, \ldots, a_K)$ and $a_l = \left[1, \ldots, \exp\left(j\frac{4\pi}{\lambda}(N_p - 1) d_e \sin\theta_l\right)\right]^T$. The subspace method makes use of the eigenstructure of the covariance matrix of the observed data. From (8.16), the covariance matrix can be expressed as

$$C_{xy} = \mathrm{E}\left(V'_{xy} V'^{H}_{xy}\right) = A_{xy}\Lambda_{xy}A^{H}_{xy} + C_w \tag{8.17}$$

where E denotes the ensemble average, H the complex conjugate transpose, $\Lambda_{xy} = \mathrm{E}\left(\Sigma_{xy}\Sigma^{H}_{xy}\right)$ and C_w the covariance matrix of the noise. If $w_i(x, y)$ is assumed to be independent noise with mean zero and variance σ_w^2, then (8.17) becomes

$$C_{xy} = A_{xy}\Lambda_{xy}A^{H}_{xy} + \sigma_w^2 I \tag{8.18}$$

where I is the identity matrix. The eigenvalues in descending order and their corresponding eigenvectors of C_{xy} are denoted by $\lambda_1 \geq \lambda_2 \geq \ldots \geq \lambda_{N_p}$ and $e_1, \ldots, e_{N_p}$, respectively. By use of the orthogonality between the noise subspace and the signal subspace, i.e.,

$$\text{span}[e_{K+1}, \ldots, e_{N_p}] \perp \text{span}[a_1, \ldots, a_K], \tag{8.19}$$

the linear combinations of noise subspace vectors with arbitrary weighting b_i such as

$$\sum_{i=K+1}^{N_p} b_i\left(\left|a^H(z)\, e_i\right|^2\right) = a^H(z)\left(\sum_{i=K+1}^{N_p} b_i e_i e_i^H\right)a(z) \tag{8.20}$$

will be zero whenever steering vector $a(z)$ locates in the signal subspace. In practice, estimation errors cause (8.20) not to be zero exactly, but close to zero. This means that the position of each scatterer can be estimated by searching the peak position of the reciprocal of (8.20), i.e.,

$$\hat{\rho}(x, y, z) = \frac{1}{\sum_{i=K+1}^{N_p} b_i\left(\left|a^H(z)\, e_i\right|^2\right)}. \tag{8.21}$$

Two specific algorithms have been proposed. Selecting $b_i = 1$ yields MUSIC [104]

$$\hat{\rho}(x, y, z) = \frac{1}{\sum_{i=K+1}^{N_p} \left|a^H(z)\, e_i\right|^2}. \tag{8.22}$$

Choosing $b_i = 1/\lambda_i$ results in the eigenvector approach [105]

$$\hat{\rho}(x, y, z) = \frac{1}{\sum_{i=K+1}^{N_p} \frac{1}{\lambda_i}\left(\left|a^H(z)\, e_i\right|^2\right)}. \tag{8.23}$$

The peaks in the elevation spectrum indicate the location of the individual scatterers. However the spectral amplitudes of these peaks contain no information with regard to the reflectivity of individual scatterers. Having estimated the locations of the different scatterers, reflectivity estimation remains a separate task and can be obtained via the least square solution [104].

In the above analysis the covariance matrix is assumed to be known. In practice it needs to be estimated by time averaging. This averaging results in a full rank covariance matrix. For MPSAR processing, only one snapshot of each flight path is available at a time implying that the estimate of C_{xy} would be singular and the subspace method would not work properly.

Spatial smoothing can be used to replace the time averaging[106]. The scheme we adopt to do the spatial smoothing over adjacent image pixels is shown in Figure 8.5 where V_{xy} is the pixel vector across multiple SAR images. The covariance matrix of the pixel vector for location (x, y) can be estimated by averaging

$$\hat{C}_{xy} = \frac{1}{5}\left(\tilde{C}_{xy} + \tilde{C}_{x-1,y} + \tilde{C}_{x+1,y} + \tilde{C}_{x,y-1} + \tilde{C}_{x,y+1}\right) \tag{8.24}$$

where $\tilde{C}_{xy} = \frac{1}{2}\left(V_{xy}V^H{}_{xy} + O_{N_p}V_{xy}V^H{}_{xy}O_{N_p}\right)$ and O_{N_p} is an $N_p \times N_p$ exchange matrix which is defined as

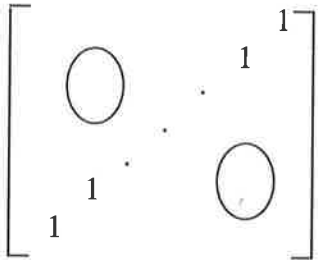

The size of spatial smoothing region determines the rank of the estimated covariance. The spatial smoothing has to pay the penalty of resolution reduction in the range and azimuth directions. The second term in $\tilde{C}_{xy}$ introduced by the exchange matrix helps to reduce this penalty, that is, it increases the resolutions in range and azimuth directions by use of backward spatial smoothing[107].

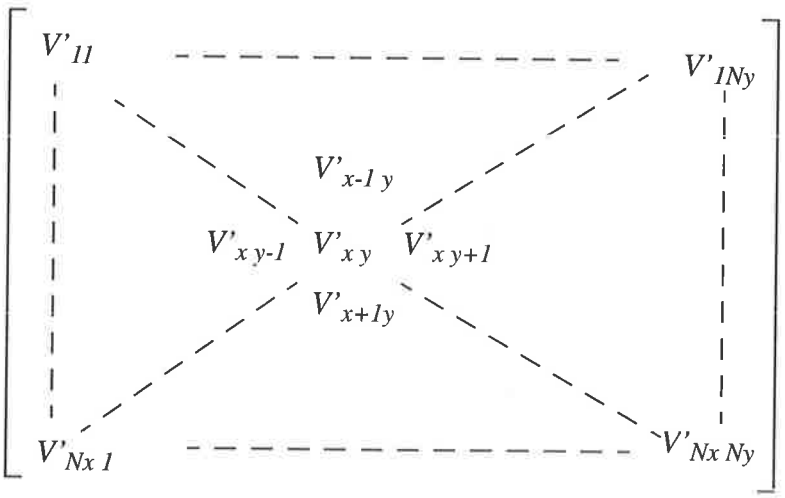

Figure 8.5 Spatial smoothing scheme

A simple idea for separating eigenvectors into the signal and noise subspaces is to examine the eigenvalues of the covariance matrix with (2.33) and (2.34). However in practice it does not work well especially when the signal-to-noise ratio is low. The dimension of the signal subspace can be determined automatically with AIC [108]which is defined as

$$\mathrm{AIC}(K) = (N_p - K)\left[\ln\frac{1}{N_p - K}\sum_{i=K+1}^{N_p}\lambda_i\right] + (N_p - K)^2\sum_{i=K+1}^{N_p}\ln\lambda_i + K(2N_p - K). \quad (8.25)$$

The dimension of the signal subspace is determined by selecting the minimum value of $\mathrm{AIC}(K)$ with respect to K.

8.4 Experiment Results

The methods for elevational imaging and super-resolution processing described above were used to process ERS-1 SAR image data sets. An image patch with 32×32 pixels was selected for MPSAR processing. The 9 SAR images were firstly registered with the image model matching developed in chapter 6, and then corrected in phase by the eigenvector method discussed in chapter 7, and finally imaged in elevation with linear and nonlinear super-resolution techniques. The reconstructed 3D image was visualized with three 2D profiles, that is, the range-azimuth image, the range-elevation image and the azimuth-elevation image. The resolution of elevation is illustrated in the range-elevation and the azimuth-elevation profiles.

The computational operations of the DFT processing, the linear and nonlinear super-resolution processings are given in Table 8.1 where N_x and N_y are the pixel dimensions of SAR image in the range and azimuth directions, N_p is the number of flight path, N_e is the number of extrapolated flight path, Q is the order of AR model, K is the dimension of the signal subspace and a Householder transformation is used for the eigendecomposition of covariance matrix. The DFT processing does not need any division and the number of multiplications and additions required are less than those of the linear and nonlinear super-resolution processing. An example of Table 8.1 for the experiment in this chapter is shown in Table 8.2 where $N_x = 32$, $N_y = 32$, $N_p = 9$, $N_e = 32$, $Q = 3$ and $K = 2$. It is seen that the ratio of multiplication and addition for these three methods is about 1:15:25 and ratio of division between the linear and nonlinear super-resolution is approximately 1:3.

Table 8.1 Computational operations of elevational imaging

	Division	**Multiplication**	**Addition**
DFT processing	0	$N_xN_yN_p^2$	$N_xN_yN_p^2$-$N_xN_yN_p$
Linear super-resolution	N_xN_yQ	$N_xN_y(N_e^2+N_eQ+4N_pQ-2Q^2-3Q)$	$N_xN_y(N_e^2+N_eQ+3N_pQ+N_p-2N_e-3/2Q^2-5/2Q)$
Nonlinear super-resolution	$N_xN_y(N_p+2)$	$N_xN_y(7/3N_p^3+6N_p^2-KNp^2-KN_p)$	$N_xN_y(7/3N_p^3+9N_p^2-KNp^2)$

Table 8.2 Numeric example of Table 8.1

	Division	Multiplication	Addition
DFT processing	0	82944	73728
Linear super-resolution	3072	1229824	1152000
Nonlinear super-resolution	11264	2055168	2322432

8.4.1 One Corner Reflector Terrain

First an image patch containing a corner reflector was processed. The 9-point data of each pixel were weighted by Hamming window, zero-padded to length 16, and transformed by DFT. The resulting 3D image is shown in Figure 8.6. Figure 8.7 is the 3D image without weighting. As illustrated in Figure 8.6 and Figure 8.7, the sidelobes are reduced by means of Hamming weight but the point spread function has a wider mainlobe.

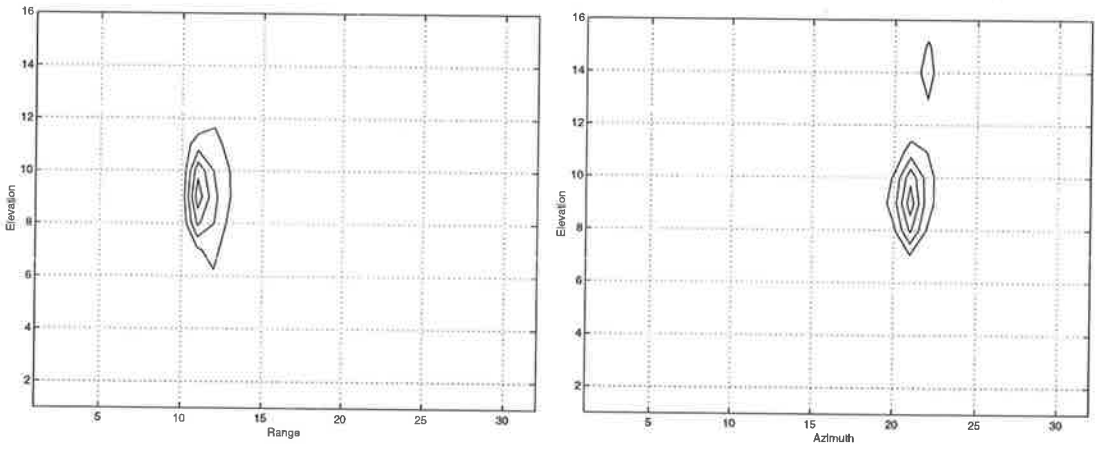

Figure 8.6 3D SAR image with Hamming weight

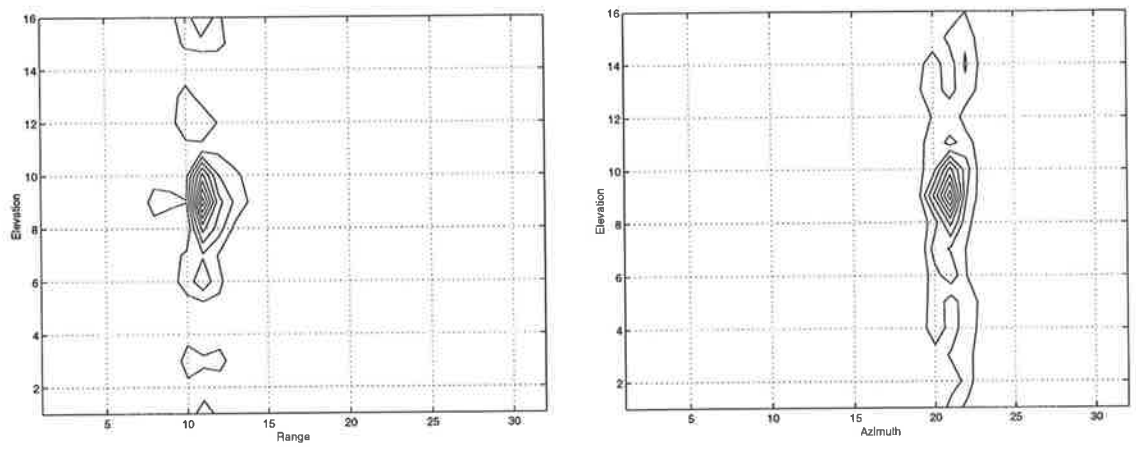

Figure 8.7 3D SAR image without weight

For the linear super-resolution technique, the data were extrapolated forward and backward from 9 to 32. The 32-point data were windowed by Hamming weight and transformed with DFT. The nonlinear super-resolution padded the eigenvectors of the noise subspace from length 9 to 32 with zeros, and then computed the elevational spectrum. The 3D images acquired by the linear and nonlinear super-resolution are shown in Figure 8.8 and Figure 8.9, respectively. For comparison, the conventional processing by windowing 9-point data, zero-padding to length 32 and transforming the 32-point data with DFT is shown in Figure 8.10. The AR model order for linear super-resolution was selected as 3 by use of (8.13). MUSIC was used for the nonlinear super-resolution, and the dimension of signal subspace was chosen as 1 from (8.25). As shown in Figure 8.8, Figure 8.9 and Figure 8.10, the linear and nonlinear super-resolutions are able to enhance elevational resolution compared with the conventional DFT processing. The support region of the corner reflector in the elevation is narrowed approximately by a factor of 3 and 4 compared with the DFT processing when the linear and nonlinear super-resolutions are used, respectively. This means that the nonlinear super-resolution is more powerful than the linear super-resolution. However the computational load of the former is more expensive than that of the latter as shown in Table 8.2 and Figure 8.9 indicates that the spatial smoothing of the nonlinear method results in resolution reduction in the range direction.

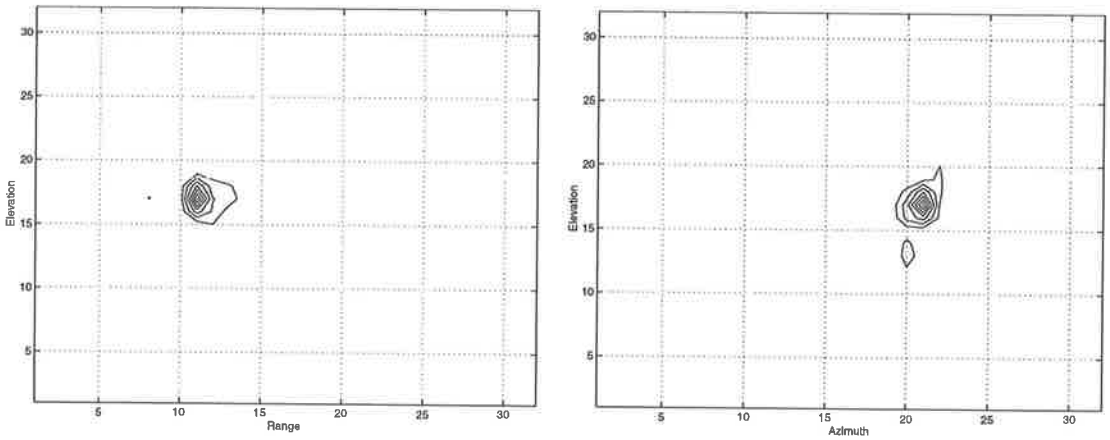

Figure 8.8 3D SAR image with linear super-resolution

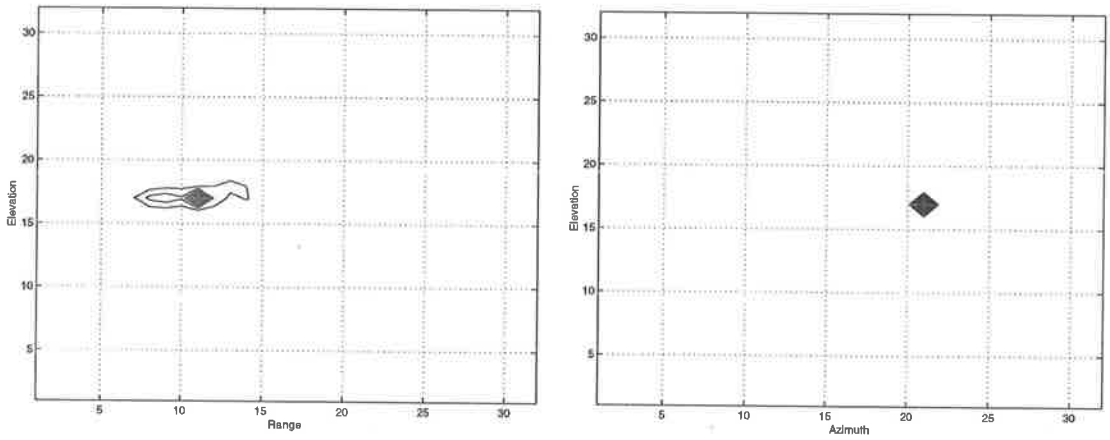

Figure 8.9 3D SAR image with nonlinear super-resolution

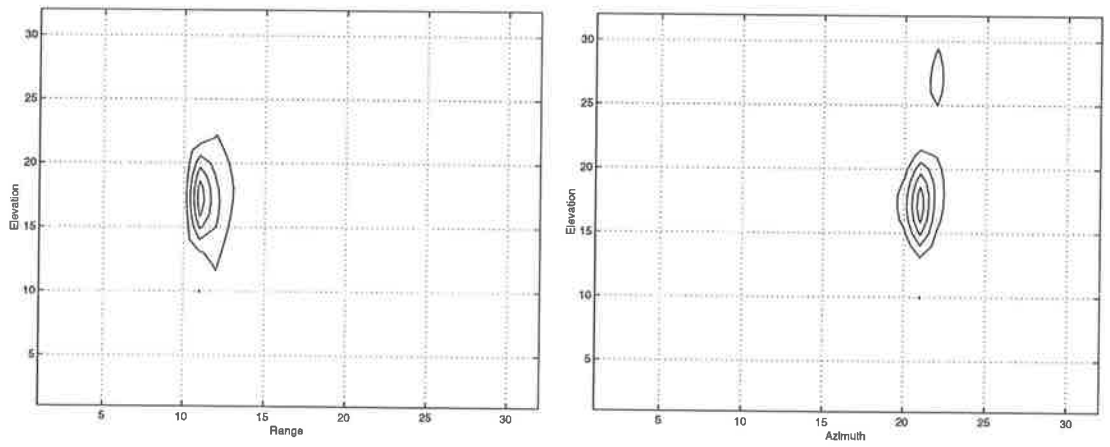

Figure 8.10 3D SAR image with zero-padding and DFT

8.4.2 Two Corner Reflector Terrain

Second a subimage containing two corner reflectors was chosen. Figure 8.11 is the 3D image with Hamming window, zero-padding to length 16 and DFT where (a) shows the profiles of the first corner reflector in the range-elevation and azimuth-elevation planes and (b) shows the profiles of the second corner reflector in the range-elevation and azimuth-elevation planes. The 3D image without windowing is shown in Figure 8.12.

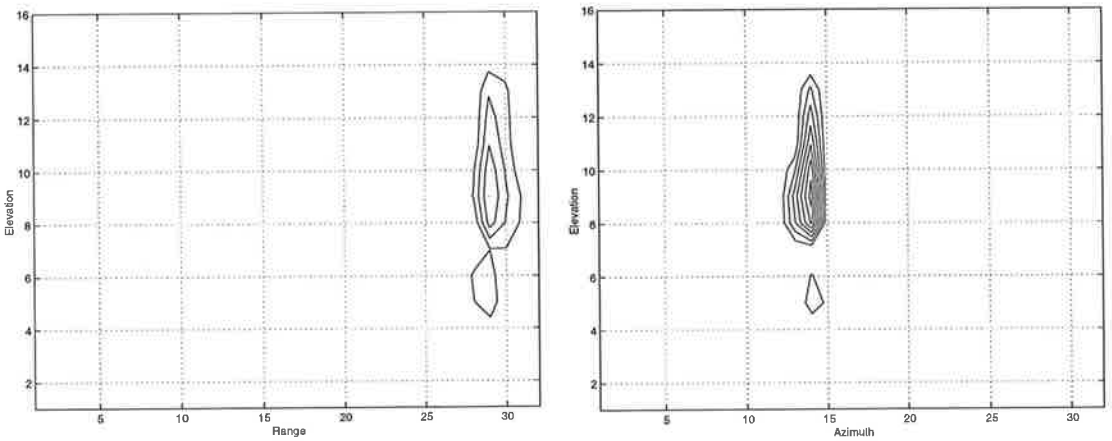

(a) Elevation profiles of the first corner reflector

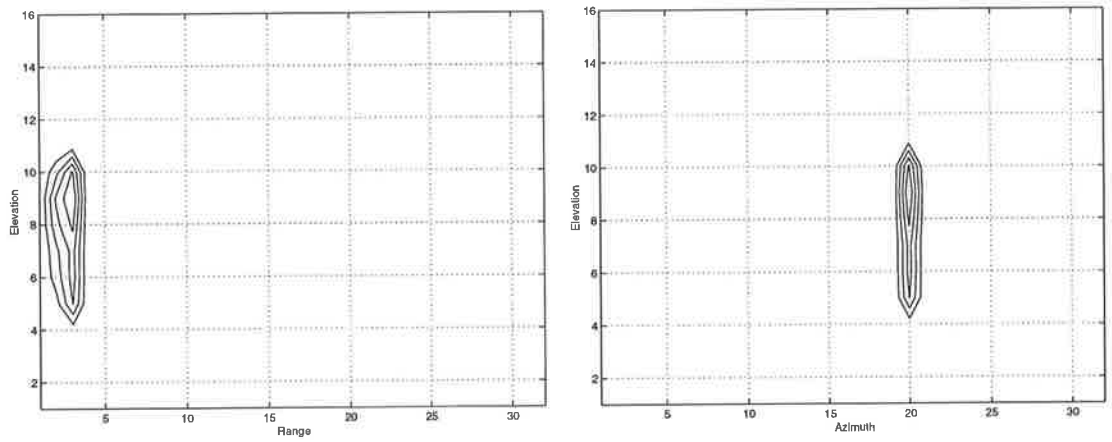

(b) Elevation profiles of the second corner reflector

Figure 8.11 3D SAR image with Hamming weight

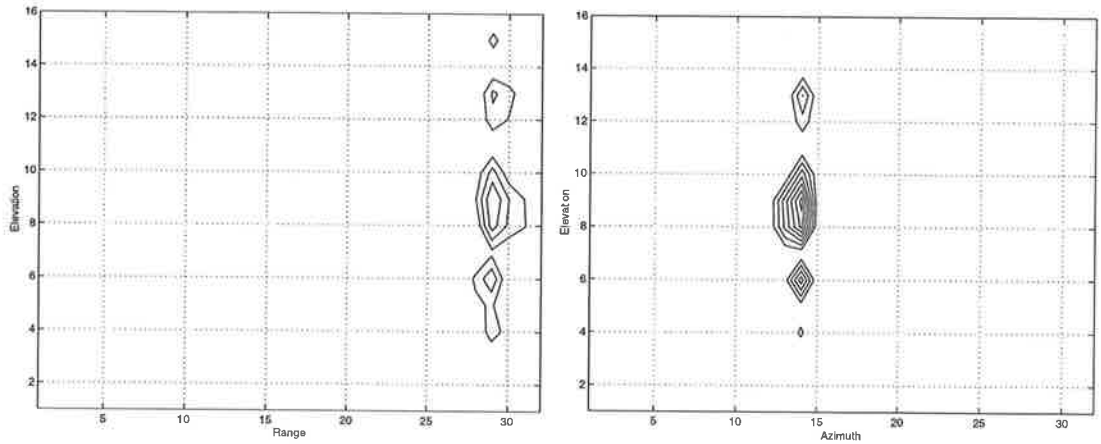

(a) Elevation profiles of the first corner reflector

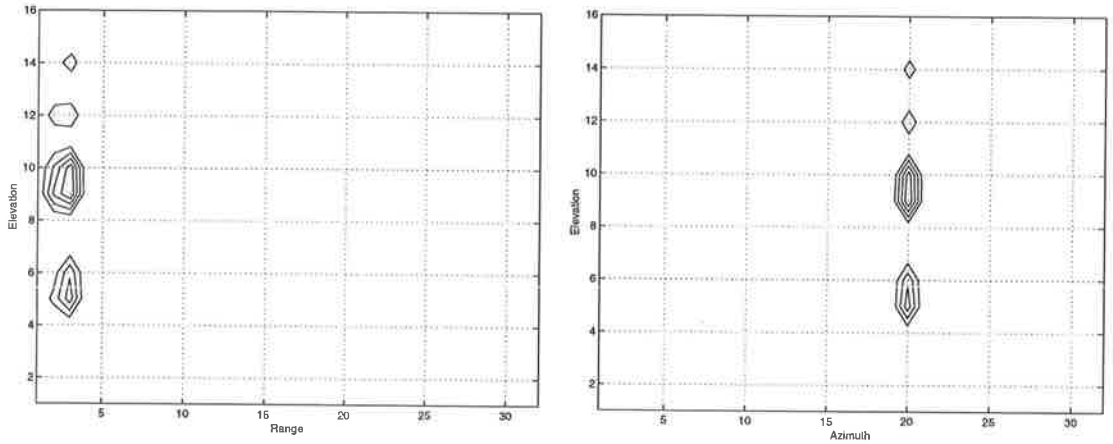

(b) Elevation profiles of the second corner reflector

Figure 8.12 3D SAR image without weight

Figure 8.13 and Figure 8.14 are the super-resolution images produced by the linear and nonlinear methods, respectively. The order of AR model for the data extrapolation was 3 by use of (8.13). MUSIC was used for the subspace method and the dimension of signal space was selected as 2 from (8.25). The image with Hamming window, zero-padding to length 32 and DFT is given in Figure 8.15.

The processing results are consistent with those of one corner reflector terrain and indicate that windowing reduces the sidelobes, zero-padding increases the number of elevational beams but does not enhance the elevational resolution, and the linear and nonlinear super-resolutions techniques enhance the elevational resolution. The resolution improvement factors of the linear and nonlinear methods are 3 and 4, respectively.

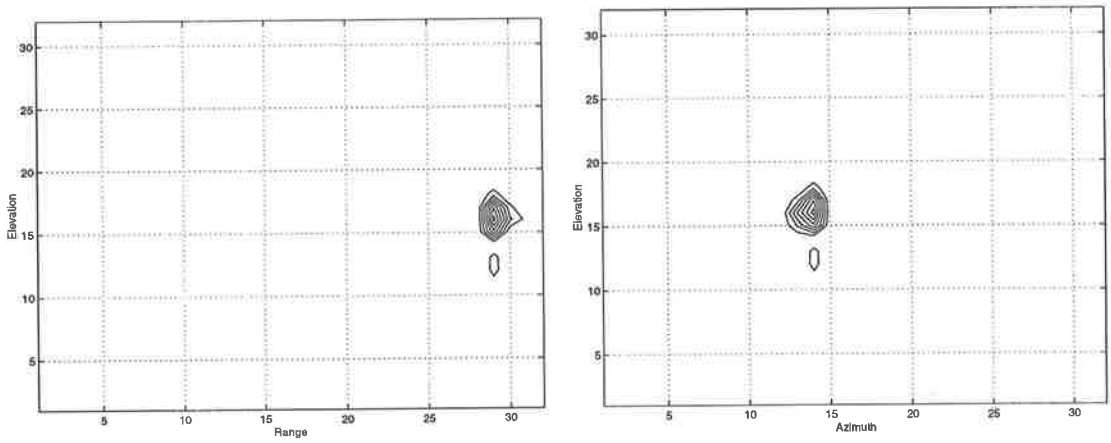

(a) Elevation profiles of the first corner reflector

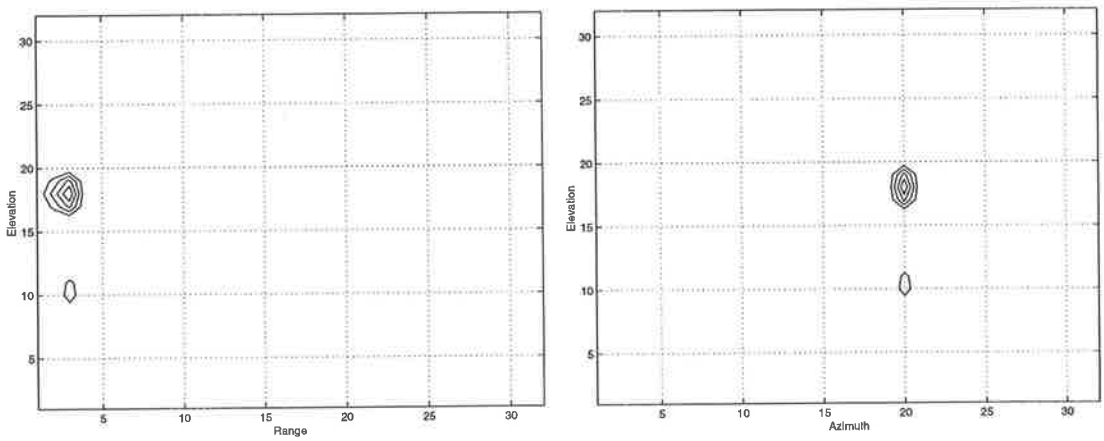

(b) Elevation profiles of the second corner reflector

Figure 8.13 3D SAR image with linear super-resolution

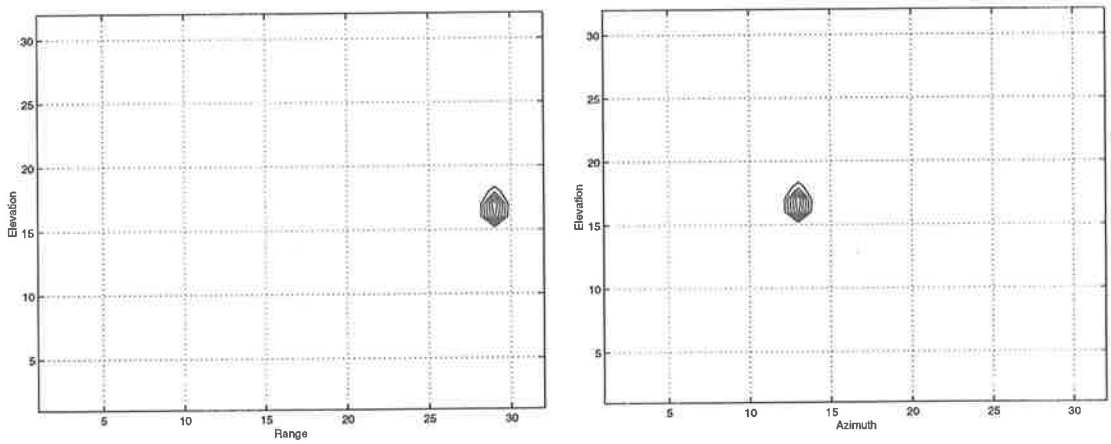

(a) Elevation profiles of the first corner reflector

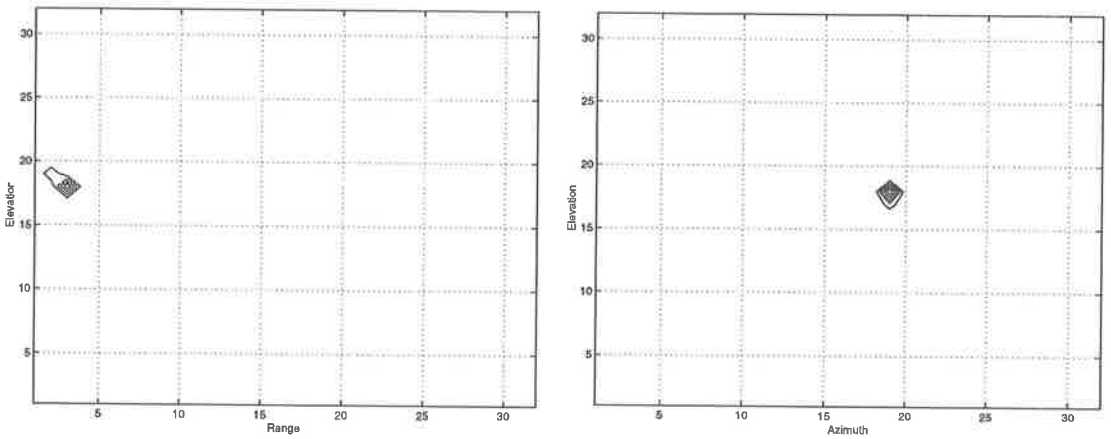

(b) Elevation profiles of the second corner reflector

Figure 8.14 3D SAR image with nonlinear super-resolution

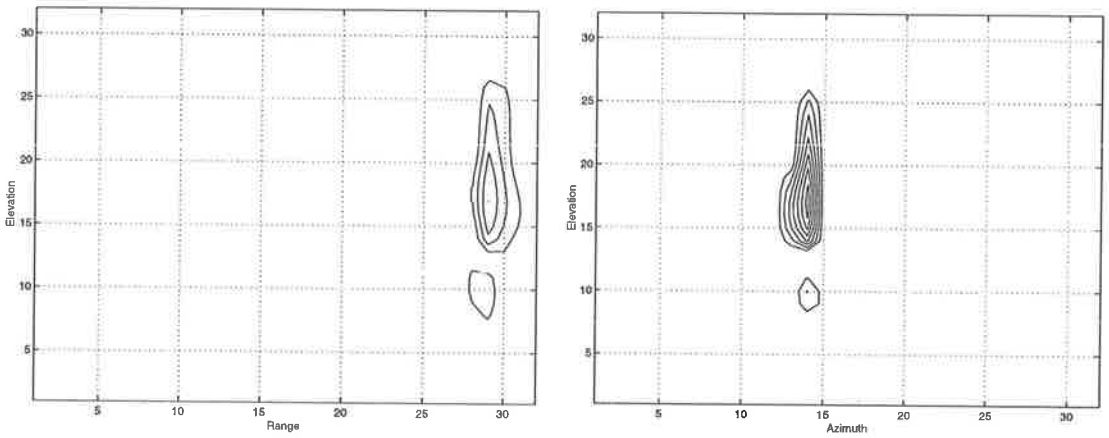

(a) Elevation profiles of the first corner reflector

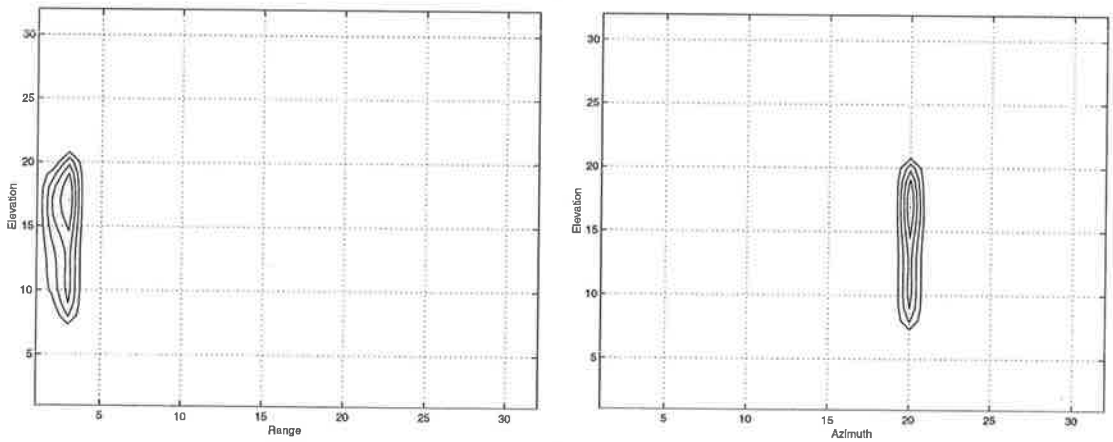

(b) Elevation profiles of the second corner reflector

Figure 8.15 3D SAR image with zero-padding and DFT

8.5 Statistical Analysis

In this section, statistical performances of height estimators are investigated. Monte-Carlo simulations were conducted to calculate the mean and the standard deviation of the height estimator. In the simulations, it was assumed that a strong scatterer located at a height of 12 meter and 17 equally-spaced flight paths were used for MPSAR processing. Other parameters of the simulations are available in section 5.5. Simulated SAR images were added with some white noise before MPSAR imaging. The height of the scatterer was detected by the peak of 3D image intensity in the elevational direction with a search grid of 0.1m. The statistics were inferred from 100 simulations for each set of SNR.

Figure 8.16 shows the mean and standard deviation of the estimated height error of the scatterer versus SNR determined by the DFT elevational imaging. It indicates that the DFT elevational estimator is unbiased and the threshold of SNR for mean and standard deviation is 0dB. Since this is height estimation of a single scatterer it is not necessary to repeat for super-resolution algorithms as they essentially give the same results.

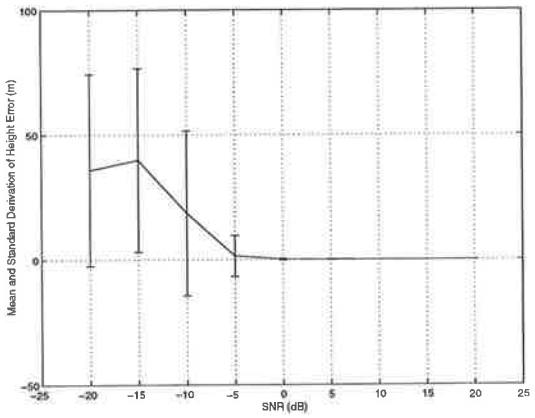

Figure 8.16 Mean and standard deviation of height error

In order to analyse the elevational resolution capability, two strong scatterers having same range and azimuthal coordinates and spacing 48 meter apart in the elevational direction to be easily resolved were simulated. Elevational imaging was conducted by DFT, linear super-resolution and nonlinear super-resolution methods, respectively. The relative height of these two strong scatterers were detected by the peaks of 3D image intensity in the elevational direction. The order of AR model for linear super-resolution was 5 and the dimension of signal subspace for nonlinear super-resolution was selected as 2. The mean and standard deviation of the estimated relative height difference error versus SNR are

shown in Figure 8.17, Figure 8.18 and Figure 8.19, respectively. They show that the three estimators appear to be asymptotically unbiased, and that the DFT is able to resolve the two scatterers precisely when SNR is greater than 15dB, linear super-resolution achieves this if SNR is above 10dB and nonlinear super-resolution is sensitive to noise and has a larger estimation standard deviation than other two methods.

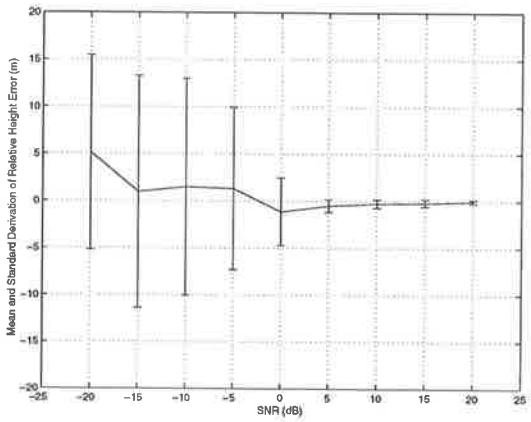

Figure 8.17 Relative height difference error determined by DFT imaging

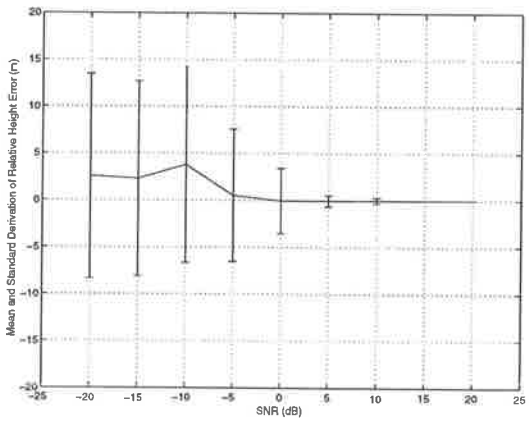

Figure 8.18 Relative height difference error determined by linear super-resolution

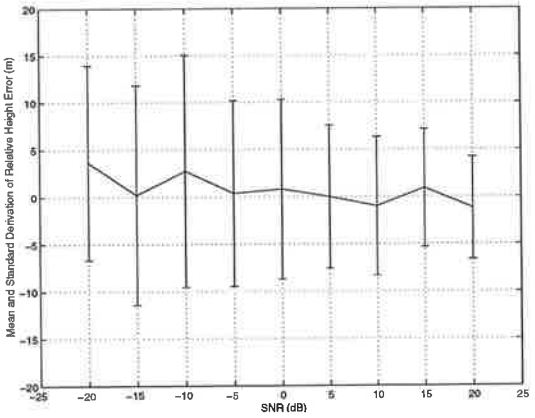

Figure 8.19 Relative height difference error determined by nonlinear super-resolution

8.6 Conclusions

The original work reported in this chapter has been the application of phased array techniques to form multiple receiving beams for elevational imaging and to utilize the methods of modern spectral estimation to enhance the elevational resolution.

At each pixel, a focused elevational beam is formed using images that have been registered and phase corrected. This beam is scanned in elevation electronically by use of DFT which produces multiple beams to do elevational resolution. The linear super-resolution extrapolates the elevational aperture forward and backward in the data domain using an auto-regressive prediction filter. Fourier processing of extrapolated data produces the 3D super-resolution image. The nonlinear super-resolution makes use of the covariance matrix of pixel series. The orthogonality between the noise subspace and the signal subspace of the covariance matrix gives the super-resolution capability.

The DFT, linear and nonlinear super-resolution processings were used to process the ERS-1 data with repeat orbits. The processing results show that the DFT processing produces the 3D SAR images of one and two corner reflector terrain with the Rayleigh resolution in elevation. The linear and nonlinear processings can narrow the beamwidth of elevational beam pattern or the point-spread-function (PSF). The resolution is approximately enhanced by a factor of 3 and 4 when the linear and nonlinear super-resolutions are used, respectively. However the nonlinear super-resolution is sensitive to noise and has a large

estimation variance. The computational complexities of the three methods have been compared for real time implementation.

Chapter 9 Summary

9.1 Overview

In this thesis, array processing techniques have been applied to ISAR autofocus and MPSAR imaging. The work presented in this thesis is overviewed below.

Chapter 2 described the fundamental material about SAR, ISAR, InSAR and array processing. Motion compensation and image formation were identified as the two main steps of ISAR processing. The methods of ISAR image formation and motion compensation were reviewed. ISAR images of Boeing-727 were presented by processing the simulated data from NRL. It was found that autofocus was a key step of ISAR imaging and autofocus should receive particular emphasis in this thesis. Typical InSAR processing included image registration and phase unwrapping. Numerous methods for image registration and phase unwrapping were overviewed. The interferogram of flat terrain was simulated and the interferogram of ERS-1 data was generated. Examples of one and two dimensional phase unwrapping were illustrated. MPSAR, an extension of InSAR, was suggested to be further researched in this thesis. Beamforming, subspace methods and array calibration for array processing were also briefly reviewed.

In chapter 3, ISAR autofocus was conducted by conventional beamforming, optimum beamforming, signal subspace and noise subspace methods. The signal model of ISAR autofocus was established. Adjusting the steering vector to maximize the output powers of conventional and optimum beamformers made the steering vector of beamformer converge to the exact signal vector corresponding to the translational motion of object in the case of the known covariance matrix. Signal and noise subspace methods were applied

to ISAR autofocus which were based on the fact that the noise subspace was orthogonal to the steering vector when this steering vector pointed to the signal vector associated with ISAR autofocus. Subaperture processing was described to improve computational efficiency. One-dimensional and two-dimensional ISAR autofocus by processing the simulated and real data show that the four developed methods are able to produce high quality ISAR images.

In chapter 4, statistical properties of the four methods developed in chapter 3 were examined. The signal subspace method was related to the strong scatterer reference method by approximately estimating the covariance matrix over the range cells where the strong scatterers were located. The signal subspace method was recognized to be ML estimation of the complex vector corresponding to ISAR autofocus. The CRLB of the complex signal vector corresponding to ISAR autofocus and the CRLB of the distance between two scatterers were derived and used to establish a lower bound on the estimator's variance. The statistical performances of conventional beamforming, optimum beamforming, signal subspace and noise subspace methods were analysed and show that they are statistically efficient.

Chapter 5 described the mathematical model for 3D SAR imaging. The processing steps of MPSAR imaging were proposed which included conventional SAR processing, image registration, phase correction and elevational beamforming. MPSAR imaging was found to be an extension of InSAR. Its advantages over InSAR were highlighted. Results of processing simulated and ERS-1 real data show that the developed processing steps for MPSAR imaging are able to produce the focused 3D PSFs.

In chapter 6, a model for MPSAR was described and the complex correlation was proposed for SAR image pair registration based on the this model. The minimal distance and the image model matching approaches were developed for multiple SAR image registration. The complex correlation and the image model matching methods have been used to process ERS-1 image sets. The results illustrate that complex correlation can enhance the peak and reduce sidelobes of the correlation function and the image model matching is able to improve the coherence of multiple images by use of the reference image.

In chapter 7, array calibration techniques were applied to correct the multiple complex SAR images prior to construction of focused beams in the elevation. The eigenvector

method, the terrain centroid tracking and the strong scatterer reference were proposed for phase correction and described in detail. The eigenvector method is the ML estimator of phase correction. The terrain centroid tracking and the strong scatterer reference are the simplified versions of the eigenvector method. The three proposed methods were verified by processing the ERS-1 data, their statistical performances were analysed with respect to SNR and the size of subimage and their computational complexities were discussed. The results show that phase correction is able to produce a focused 3D PSF with a ISLR of 3dB when SNR drops to 5dB or the size of subimage increases to 110m.

Finally, in chapter 8 the elevational imaging was obtained by forming multiple beams. The elevational resolution was enhanced by two methods. One was the maximum entropy extrapolation for linear super-resolution. The other was the subspace method for non-linear super-resolution. The 3D SAR images were produced by processing ERS-1 data with the DFT processing, the linear and nonlinear super-resolution methods. Their statistical performances were analysed and the computational complexities were compared. The results of 3D SAR imaging show that the DFT processing produces the Rayleigh resolution in elevation, the linear and nonlinear super-resolution are able to enhance the elevational resolution approximately by a factor of 3 and 4, respectively.

9.2 Contributions

The key contributions to knowledge of this dissertation are:

1. the derivation of the signal model for ISAR autofocus which avoids the problem of phase unwrapping.

2. the development of ISAR autofocus methods via maximizing the output powers of conventional and optimum beamformers.

3. the development of signal and noise subspace methods for ISAR autofocus by either maximizing the projection of steering vector to the signal subspace or minimizing the projection of steering vector to the noise subspace.

4. the derivation of the ML estimator of ISAR autofocus and the determination of the CRLB for the complex signal vector corresponding to the translational motion of an object and the CRLB of the distance between two scatterers.

5. the development of processing steps for MPSAR imaging which include conventional SAR processing, image registration, phase correction and elevational beamforming.

6. the development of the complex correlation, the minimal distance and the image model matching approaches for multiple SAR image registration.

7. the development of the eigenvector method, the terrain centroid tracking and the strong scatterer reference for phase correction of MPSAR processing.

8. the development of elevational imaging with the DFT and enhancement of elevational resolution with the maximum entropy extrapolation and the subspace methods.

9.3 Future Work

Although this thesis has presented a comprehensive overview of ISAR autofocus and MPSAR imaging, there is still some work to do. We now outline a number of issues which need to be addressed. Possible future work includes:

1. recursive forms of beamforming and subspace methods for ISAR autofocus where the optimum steering vector can be efficiently derived by updating the estimation of the steering vector using the signal vector in each range cell.

2. extension of subspace methods to ISAR autofocus for multiple moving objects.

3. the preprocessing multiple complex SAR images to remove the noise and enhance the coherence between multiple SAR images.

4. elevational imaging based on tomographic principle.

9.4 Conclusions

This thesis has investigated a novel application of array processing methods to calibration for ISAR and MPSAR. It achieves two objectives. One is to apply a rigorously mathematical approach to problems which have traditionally been solved using the conventional methods. The other is to develop a unifying framework where the conventional methods could be interpreted and evaluated from a different point of view.

The techniques were analysed in detail from several aspects such as conventional beamforming, optimum beamforming, signal subspace, noise subspace, image registration, phase correction, elevational imaging and super-resolution. Their statistical performances were examined and their computational complexities were compared. Several important results were found in this thesis by processing the simulated and real data. They have shown how the techniques of array calibration can be used successfully in ISAR and MPSAR and provide valuable insights which have a potential application in modern airborne and spaceborne SAR systems.

Appendix A The Eigen Decomposition of C_x

The covariance matrix C_x of the received signal for ISAR autofocus was derived in chapter 3. The eigen decomposition of C_x is calculated below which was cited in chapters 3 and 7. If C_x is an $M \times M$ matrix, it has an eigen decomposition

$$C_x u_i = \lambda_i u_i \tag{A.1}$$

where λ_i is an eigenvalue and u_i is the corresponding eigenvector. λ_i i=1,..., M are the solutions of characteristic equation

$$\det(C_x - \lambda I) = 0. \tag{A.2}$$

From section 3.2, C_x is expressed as

$$C_x = p_n DD^H + \sigma_w^2 I_M \tag{A.3}$$

Thus C_x is a Hermitian symmetric positive definite matrix. By use of the relation

$$\det\left(kC_x + vv^H\right) = \det(C_x)\left(k + v^H C_x^{-1} v\right), \tag{A.4}$$

we have

$$\begin{aligned} \det(C_x - \lambda I) &= \det\left(p_n DD^H + \left(\sigma_w^2 - \lambda\right) I_M\right) \\ &= p_n \det\left(DD^H + \frac{1}{p_n}\left(\sigma_w^2 - \lambda\right) I_M\right) \\ &= p_n \left(\frac{1}{p_n} + \frac{M}{\sigma_w^2 - \lambda}\right) \det\left[\left(\sigma_w^2 - \lambda\right) I_M\right] \end{aligned} \tag{A.5}$$

Thus (A.2) is changed into

$$\left(\sigma_w^2 - \lambda + Mp_n\right)\left(\sigma_w^2 - \lambda\right)^{M-1} = 0. \tag{A.6}$$

Therefore the eigenvalues of C_x are

$$\lambda_1 = \sigma_w^2 + Mp_n, \tag{A.7}$$

$$\lambda_i = \sigma_w^2 \quad i=2,\ldots,M. \tag{A.8}$$

Substituting λ_1 into (A.1), we get

$$u_1 = \frac{D}{M}. \tag{A.9}$$

Appendix B The Eigenvalues and Eigenvectors of a 2x2 Covariance Matrix

The subaperture processing approach was discussed in chapter 3. If the subaperture is made of two adjacent pulses, subaperture processing of the signal subspace method needs the eigen decomposition of a 2×2 covariance matrix as discussed in chapter 3. The estimated 2×2 matrix $\hat{C}_x$ is expressed as

$$\hat{C}_x = \frac{1}{N}\begin{bmatrix} \sum_{n=1}^{N}|x_{nm}|^2 & \sum_{n=1}^{N}x_{nm}x_{n(m+1)}{}^* \\ \sum_{n=1}^{N}x_{nm}{}^*x_{n(m+1)} & \sum_{n=1}^{N}|x_{n(m+1)}|^2 \end{bmatrix}. \tag{B.1}$$

The characteristic equation of $\hat{C}_x$ is

$$\det(\hat{C}_x - \lambda_i I) = 0 \tag{B.2}$$

where λ_i i=1,2 is an eigenvalue of $\hat{C}_x$. The solutions of characteristic equation are

$$\lambda_{1,2} = \left(\sum_{n=1}^{N}|x_{nm}|^2 + \sum_{n=1}^{N}|x_{n(m+1)}|^2 \pm \left(\left(\sum_{n=1}^{N}|x_{nm}|^2 - \sum_{n=1}^{N}|x_{n(m+1)}|^2 \right)^2 + 4\left|\sum_{n=1}^{N}x_{nm}{}^*x_{n(m+1)}\right|^2 \right)^{\frac{1}{2}} \right) / (2N) \tag{B.3}$$

where $\lambda_1 > \lambda_2$ and the corresponding eigenvectors are

$$u_{1,2} = \begin{bmatrix} 1 \\ k_{1,2} \sum_{n=1}^{N} x_{nm}{}^{*} x_{n(m+1)} \end{bmatrix} \tag{B.4}$$

where $k_{1,2}$ are expressed as

$$k_{1,2} = \left(\begin{bmatrix} \sum_{n=1}^{N} |x_{n(m+1)}|^2 - \sum_{n=1}^{N} |x_{nm}|^2 \pm \\ \left(\sum_{n=1}^{N} |x_{nm}|^2 - \sum_{n=1}^{N} |x_{n(m+1)}|^2 \right)^2 + \\ 4 \left| \sum_{n=1}^{N} x_{nm}{}^{*} x_{n(m+1)} \right|^2 \end{bmatrix}^{\frac{1}{2}} \right) \Big/ \left(2 \left| \sum_{n=1}^{N} x_{nm}{}^{*} x_{n(m+1)} \right|^2 \right). \tag{B.5}$$

Appendix C First and Second Derivatives of $l(z_0, \ldots, z_{M-1}; d)$

In order to calculate the CRLB of the estimated distance between two scatterers, the first and second derivatives of likelihood function $l(z_0, \ldots, z_{M-1}; d)$ respect to the distance d between the two scatterers need to be derived and they are given below.

The first partial derivative of $l(z_0, \ldots, z_{M-1}; d)$ with respect to d is

$$\frac{\partial l}{\partial d} = -\frac{1}{\sigma^2_w} \sum_{m=0}^{M-1} \frac{4\pi\rho}{\lambda} \sin[\theta_m + \gamma] \sin\{\frac{2\pi d}{\lambda} \sin[\theta_m + \gamma]\}$$
$$[u_m z^*_m + u^*_m z_m] + \frac{8\pi\rho^2}{\lambda} \sin[\theta_m + \gamma] \sin\{\frac{4\pi d}{\lambda} \sin[\theta_m + \gamma]\} \quad \text{(C.1)}$$

The second partial derivative of $l(z_0, \ldots, z_{M-1}; d)$ with respect to d has the form

$$\frac{\partial^2 l}{\partial d^2} = -\frac{1}{\sigma^2_w} \sum_{m=0}^{M-1} \frac{8\pi^2\rho}{\lambda} \sin[\theta_m + \gamma]^2 \cos\{\frac{2\pi d}{\lambda} \sin[\theta_m + \gamma]\}$$
$$[u_m z^*_m + u^*_m z_m] + \frac{32\pi^2\rho^2}{\lambda^2} \sin[\theta_m + \gamma]^2 \cos\{\frac{4\pi d}{\lambda} \sin[\theta_m + \gamma]\} \quad \text{(C.2)}$$

The expectation of the second partial derivative is

$$E\left(\frac{\partial^2 l}{\partial d^2}\right) = -\frac{1}{\sigma^2_w} \sum_{m=0}^{M-1} \frac{8\pi^2\rho}{\lambda} \sin[\theta_m + \gamma]^2 \cos\{\frac{2\pi d}{\lambda} \sin[\theta_m + \gamma]\}$$
$$\{u_m E[z^*_m] + u^*_m E[z_m]\} \quad \text{(C.3)}$$
$$+ \frac{32\pi^2\rho^2}{\lambda^2} \sin[\theta_m + \gamma]^2 \cos\{\frac{4\pi d}{\lambda} \sin[\theta_m + \gamma]\}$$

From section 4.6, we have

$$\mathrm{E}[z_m] = 2\rho\cos\{\frac{2\pi}{\lambda}d\sin[\theta_m+\gamma]\}u_m. \tag{C.4}$$

Thus (C.3) becomes

$$\mathrm{E}\left(\frac{\partial^2 l}{\partial d^2}\right) = -\frac{32\pi^2\rho^2}{\sigma_w^2\lambda^2}\sum_{m=0}^{M-1}\sin[\theta_m+\gamma]^2\sin\{\frac{2\pi d}{\lambda}\sin[\theta_m+\gamma]\}^2. \tag{C.5}$$

Bibliography

[1] D. R.Wehner, *High Resolution Radar*, Artech House, 1995.

[2] D. Gray and H. d'Assumpcao, *Beamforming and array processing,* A course held at the Signal Processing Research Institute, the Levels, South Australia, 1998.

[3] M.J.Prickett and C.C.Chen, "Principles of inverse synthetic aperture radar imaging", *IEEE EASCON Conference Record,* 1980, pp.340-345.

[4] D.A.Ausherman, A.Kozma, J.L.Walker, H.M.Jones and E.C.Poggio, "Developments in radar imaging", *IEEE Transactions on Aerospace and Electronic Systems,* Vol.20, No.4, 1984, pp.363-398.

[5] W.M.Brown and R.J.Fredricks, "Range-Doppler imaging with motion through resolution cells", *IEEE Transactions on Aerospace and Electronic Systems,* Vol.5, No.1, 1969, pp.98-102.

[6] C.C.Chen and H.C.Andrews, "Target-motion-induced radar imaging", *IEEE Transactions on Aerospace and Electronic Systems,* Vol.16, No.1, 1980, pp.2-14.

[7] H.Wu and G.Y.Delisle, "Precision tracking algorithms for ISAR imaging", *IEEE Transactions on Aerospace and Electronic Systems,* Vol.32, No.1, 1996, pp.243-254.

[8] S.Simmons, D.Heilbronn and D.Nandagopal, "Kalman range tracking for ISAR motion compensation", *Proceedings of Radarcon,* 1990, pp.689-694.

[9] S.Thomas and S.Arno, "Robust range alignment algorithm via Hough transform in an ISAR imaging system", *IEEE Transactions on Aerospace and Electronic Systems,* Vol.31, No.3, 1995, pp.1173-1177.

[10] B.D.Steinberg, "Microwave imaging of aircraft", *Proceedings of the IEEE,* Vol.76, No.12, 1988, pp.1578-1592.

[11] Z.S.She and Z.D.Zhu, "Detecting the strong scatterers of target with ISAR", *Proceedings of IEEE NAECON,* 1995, pp.992-995.

[12] B.Kang, H.Subbaram and B.D.Steinberg, "Improved adaptive-beamforming target for self-calibrating a distorted phased array", *IEEE Transactions on Antenna and Propagation.* Vol.38, No.2, 1990, pp.186-194.

[13] H.Wu, D.Grenier, G.Y.Delisle and D.G.Fang, "Translational motion compensation in ISAR image processing", *IEEE Transactions on Image Processing,* Vol.14, No.11, 1995, pp.1561-1571.

[14] K.K.Eerland, "Application of inverse synthetic aperture radar on aircraft", *Proceedings of International Conference on Radar,* 1984, pp.618-623.

[15] R.P.Bocker, T.B.Henderson, S.A.Jones, and B.R.Frieden, "A new inverse synthetic aperture radar algorithm for translational motion compensation", *SPIE,* Vol.1569, 1991, pp.298-310.

[16] Z.S.She and Z.D.Zhu, "Two improved methods of motion compensation for 1D cross-range ISAR imaging", *Proceedings of IEEE NAECON,* 1996. pp.227-230.

[17] F.Berizzi and G.Corsini, "Autofocusing of inverse synthetic aperture radar images using contrast optimization", *IEEE Transactions on Aerospace and Electronic Systems,* Vol.32, No.3, 1996, pp.1185-1191.

[18] F.Berizzi and G.Pinelli, "Maximum-likelihood ISAR image autofocusing technique based on instantaneous frequency estimation", *IEE Proceedings, Pt. F,* Vol.144, No.5, 1997, pp.284-292.

[19] D.E.Wahl, P.H.Eichel, D.C.Ghiglia and C.V.Jakowatz, "Phase gradient autofocus - a robust tool for high resolution SAR phase correction", *IEEE Transactions on Aerospace and Electronic Systems,* Vol.30, No.3, 1994, pp.827-834.

[20] Z.D.Zhu, X.H,Qiu and Z.S.She, "ISAR motion compensation using modified doppler centroid approach", *Proceedings of IEEE NAECON,* 1996. pp.359-363.

[21] S.Simmons and R.Evans, "Maximum likelihood autofocusing of radar images", *Proceedings of IEEE International Radar Conference,* 1995, pp.410-415.

[22] A.Jain and I.Patel, "SAR/ISAR imaging of a nonuniformly rotating target", *IEEE Transactions on Aerospace and Electronic Systems,* Vol.28, No.1, 1992, pp.317-320.

[23] G.Wang, Z.Bao, and X.Sun, "Inverse synthetic aperture radar imaging of a nonuniformly rotating target", *Optical Engineering,* Vol.35, No.10, 1996, pp.3007-3011.

[24] V.C.Chen and S.Qian, "Joint time-frequency transform for radar range-Doppler imaging", *IEEE Transactions on Aerospace and Electronic Systems,* Vol.34, No.2, 1998, pp.486-499.

[25] Y.Wang, H. Ling, and V.C.Chen, "ISAR motion compensation via adaptive joint time-frequency technique", *IEEE Transactions on Aerospace and Electronic Systems,* Vol.34, No.2, 1998, pp.670-677.

[26] F.Berizzi and M.Diani, "Target angular motion effects on ISAR imaging", *IEE Proceedings, Pt. F,* Vol.144, No.2, 1997, pp.87-95.

[27] S.Werness, W.Carrara, L.Joyce and D.Franczak, "Moving target imaging algorithm for SAR data", *IEEE Transactions on Aerospace and Electronic Systems,* Vol.26, No.1, 1990, pp.57-67.

[28] G.Y.Delisle and H.Wu, "Moving target imaging and trajectory computation using ISAR", *IEEE Transactions on Aerospace and Electronic Systems,* Vol.30, No.3, 1994, pp.887-899.

[29] Z.S.She and Z.D.Zhu, "Cross-range scaling of inverse synthetic aperture radar", *Proceedings of IEEE NAECON,* 1994, pp.175-180.

[30] Z.S.She and Z.D.Zhu, "An improved approach of cross-range scaling in ISAR", *Proceedings of IEEE NAECON,* 1995, pp.988-991.

[31] G.Nash, *Application of superresolution techniques to ISAR imaging,* Ph.D thesis, the University of South Australia, March, 1994.

[32] T.G.Moore, "A new algorithm for the formation of ISAR images", *IEEE Transactions on Aerospace and Electronic Systems,* Vol.32, No.2, 1996, pp.715-721.

[33] J.L.Walker, "Range-Doppler imaging of rotating objects", *IEEE Transactions on Aerospace and Electronic Systems,* Vol.16, No.1, 1980, pp.23-52.

[34] D.C.Munson, J.D.Obrien and W.K.Jenkin, "A tomographic formulation of spotlight-mode synthetic aperture radar", *Proceedings of the IEEE,* Vol.71, No.5, 1983, pp.917-926.

[35] S.M.Kay and S.L.Marple, "Spectrum analysis - a modern perspective", *Proceedings of the IEEE,* Vol.69, No.11, 1981, pp.1380-1419.

[36] R.F.Van and G.Heidbreder, "Maximum entropy reconstruction of radar images of rotating targets", *Proceedings of International Symposium on Signal Processing and Application,* Brisbane, Australia, 1987, pp.486-490.

[37] R.M.Nuthalapati, "High resolution reconstruction of ISAR images", *IEEE Transactions on Aerospace and Electronic Systems,* Vol.28, No.2, 1992, pp.462-472.

[38] I.J.Gupta, "High resolution radar imaging using 2D linear prediction", *IEEE Transactions on Antenna and Propagation,* Vol.42, No.1, 1994, pp.31-37.

[39] J.W.Odentaal, E.Barnard and C.W.Pistorius, "Two-dimensional superresolution radar imaging using the MUSIC algorithm", *IEEE Transactions on Antenna and Propagation,* Vol.42, No.10, 1994, pp.1386-1391.

[40] Y.Hua, F.Baqai, Y.Zhu and D.Heilbronn, "Imaging of point scatterers from step-frequency ISAR data", *IEEE Transactions on Aerospace and Electronic Systems,* Vol.29, No.1, 1993, pp.195-205.

[41] Z.D.Zhu, Z.R.Ye, X.Q.Wu, J.Yin and Z.S.She, "Superresolution range-Doppler imaging", *IEE Proceedings, Pt. F,* Vol.142, No.1, 1995, pp.25-32.

[42] A.E.E. Boger and R.P. Ingalls, "Venus: Mapping the surface reflectivity by radar interferometry", *Science,* Vol.165, 1969, pp.797-799.

[43] S.H.Zisk, "A new earth-based radar technique for the measurement of lunar topography", *Moon,* Vol.4, 1972, pp.296-300.

[44] L.C.Graham, "Synthetic interferometer radar for topographic mapping", *Proceedings of the IEEE,* Vol.62, No.6, 1974, pp.763-768.

[45] H.A.Zebker and R.M.Goldstein, "Topographic mapping from interferometry synthetic aperture radar observation", *Journal of Geophysical Research,* Vol.91, No.B5, 1986, pp.4993-4999.

[46] R.M.Goldstein, H.A.Zebker and C.L.Werner, "Satellite radar interferometry: Two-dimensional phase unwrapping", *Radio Science,* Vol.23, No.4, 1988, pp.713-720.

[47] H.A.Zebker and J.Villasenor, "Decorrelation in interferometric radar echoes", *IEEE Transactions on Geoscience and Remote Sensing,* Vol.30, No.5, 1992, pp.950-959.

[48] F.K.Li and R.M.Goldstein, "Studies of multibaseline spaceborne interferometric synthetic aperture radars", *IEEE Transactions on Geoscience and Remote Sensing,* Vol.28, No.1, 1990, pp.88-97.

[49] E.Rodriguez and J.M. Martin, "Theory and design of interferometric synthetic aperture radars", *IEE Proceedings, Pt. F,* Vol.139, No.2, 1992,pp.147-159.

[50] C.Prati and F.Rocca, "Improving slant-range resolution with multiple SAR surveys", *IEEE Transactions on Aerospace and Electronic Systems,* Vol.29, No.1, 1993, pp.135-143.

[51] F.Gatelli, A.M.Guarnieri, F.Parizzi, P.Pasquali, C.Prati and F.Rocca, "The wavenumber shift in SAR interferometry", *IEEE Transactions on Geoscience and Remote Sensing,* Vol.32, No.4, 1994, pp.855-865.

[52] P.E.Anuta, "Spatial registration of multispectral and multitemporal digital imagery using fast Fourier transform technique", *IEEE Transactions on Geoscience Electronics,* Vol.8, No.4, 1970, pp.353-368.

[53] D.I.Barnea and H.F.Silverman, "A class of algorithms for fast digital image registration", *IEEE Transactions on Computers,* Vol.21, No.2, 1972, pp.179-186.

[54] W.K.Pratt, "Correlation technique of image registration", *IEEE Transactions on Aerospace and Electronic Systems,* Vol.10, No.3, 1974, pp.353-358.

[55] C.D.Kuglin and D.C.Hines, "The phase correlation image alignment method", *Proceedings of IEEE International Conference of Cybernetic Society,* New York, 1975, pp.163-165.

[56] D.Lee, S.Mitra and T.Krile, "Analysis of sequential complex images using feature extraction and two-dimensional cepstrum techniques", *Journal of the Optical Society of Amercia, A,* Vol.6, No.6, 1989, pp.863-870.

[57] L.G.Brown, "A survey of image registration techniques", *ACM Computing Surveys,* Vol.24, No.4, 1992, pp.325-376.

[58] A.K.Gabriel and R.Goldstein, "Crossed orbit interferometry: theory and experimental results from SIR-B", *International Journal of Remote Sensing,* Vol.9, No.5, 1988, pp.857-872.

[59] Q. Lin, J.F.Vesecky and H.A.Zebker, "New approaches in interferometric SAR data processing", *IEEE Transactions on Geoscience and Remote Sensing,* Vol.30, No.3, 1992, pp.560-567.

[60] G. Fornaro and G Franceschetti, "Image registration in interferometric SAR processing", *IEE Proceedings, Pt.F,* Vol.142, No.6, 1995, pp.313-320.

[61] J. Homer, G.Biddis, I.D.Longstaff and B.Lovell, "Image registration for interferometric SAR via subtraction image methods", *Proceedings of Digital Image Computing: Techniques and Applications,* 1995, pp.461-466.

[62] J.M.Tribolet, "A new phase unwrapping algorithm", *IEEE Transactions on Acoustics, Speech and Signal Processing,* Vol.25, No.2, 1977, pp.170-177.

[63] C.Prati, F.Rocca, A.M.Guarnieri and E.Damonti, "Seismic migration for SAR focusing: interferometrical applications", *IEEE Transactions on Geoscience and Remote Sensing,* Vol.28, No.4, 1990, pp.627-639.

[64] B.R.Hut, "Matrix formulation of the reconstruction of phase values from phase differences", *Journal of the Optical Society of Amercia,* Vol.69, No.3, 1979, pp.393-399.

[65] D.C.Ghiglia, G.A.Mastin and L.A.Romero, "Cellular-automata method for phase unwrapping", *Journal of the Optical Society of Amercia, A,* Vol.4, No.1, 1987, pp.267-280.

[66] H.Takajo and T.Takahashi, "Least-squares phase estimation from the phase difference", *Journal of the Optical Society of Amercia, A,* Vol.5, No.3, 1988, pp.416-425.

[67] H.Takajo and T.Takahashi, "Noniterative method for obtaining the exact solution for the normal equation in least-squares phase estimation from the phase difference", *Journal of the Optical Society of Amercia, A,* Vol.5, No.11, 1988, pp.1818-1827.

[68] D.C.Ghiglia and L.A. Romero, "Direct phase estimation from phase differences using fast elliptic partial differential equation solvers", *Optics Letters,* Vol.14, No.20, 1989, pp.1107-1109.

[69] U. Spagnolini, "2D phase unwrapping and phase aliasing", *Geophsics,* Vol.58, No.9, 1993, pp.1324-1334.

[70] D.C.Ghiglia and L.A.Romero, "Robust two-dimensional weighted and unweighted phase unwrapping that uses fast transforms and iterative methods", *Journal of the Optical Society of Amercia, A,* Vol.11, No.1, 1994, pp.107-117.

[71] M.D.Pritt and J.S.Shipman, "Least-squares two-dimensional phase unwrapping using FFT's", *IEEE Transactions on Geoscience and Remote Sensing,* Vol.32, No.3, 1994, pp.706-708.

[72] U.Spagnolini, "2D phase unwrapping and instantaneous frequency estimation", *IEEE Transactions on Geoscience and Remote Sensing,* Vol.33, No.3, 1995, pp.579-589.

[73] M.D.Pritt, "Phase unwrapping by means of multigrid techniques for interferometric SAR", *IEEE Transactions on Geoscience and Remote Sensing,* Vol.34, No.3, 1996, pp.728-738.

[74] G.Fornaro, G.Franceschetti and R.Lanari, "Interferometric SAR phase unwrapping using green's formulation", *IEEE Transactions on Geoscience and Remote Sensing,* Vol.34, No.3, 1996, pp.720-729.

[75] G.Fornaro, G.Franceschetti, R.Lanari, D.Rossi, and M.Tesauro, "Interferometric SAR phase unwrapping using the finite element method", *IEE Proceedings, Pt.F,* Vol.144, No.5, 1997, pp.266-274.

[76] A. Gollaro, G.Franceschetti, F.Palmieri and M.S.Ferreiro, "Phase unwrapping by means of genetic algorithms", *Journal of the Optical Society of Amercia, A,* Vol.15, No.2, 1998, pp.407-418.

[77] R.O.Harger, *Synthetic Aperture Radar Systems: Theory and Design,* Academic Press Inc., 1970.

[78] J.Curlander and R.McDonough, *Synthetic Aperture Radar: Systems and Signal Processing,* John Wiley and Sons Inc., 1991.

[79] C.V.Jakowatz, D.E.Wahl, P.H.Eichel, D.C.Ghiglia and P.A.Thompson, *Spotlight-Mode Synthetic Aperture Radar: A Signal Processing Approach,* Kluwer Academic Publishers, 1996.

[80] E.F.Knott, J.F.Schaeffer and M.T.Tuley, *Radar Cross Section: Its Prediction, Measurement and Reduction,* Artech House, 1985.

[81] A.W.Rihaczek, *Principles of High-resolution Radar,* Artech House, 1969.

[82] C.V.Jakowatz and D.E.Wahl, "Eigenvector method for maximum-likelihood estimation of phase errors in synthetic-aperture-radar imagery", *Journal of the Optical Society of Amercia, A,* Vol.10, No.12, 1993, pp.2539-2546.

[83] S.U.Pillai, *Array Signal Processing,* Springer-Verlag, 1989.

[84] S.M.Kay, *Fundamentals of Statistical Signal Processing: Estimation Theory,* Prentice-Hall, 1993.

[85] D.Gray, *An Introduction to Subspace Methods for Arrays,* A short course held at the Signal Processing Research Institute, the Levels, South Australia, July, 1998.

[86] D.A.Gray, W.O.Wolfe, and J.L.Riley, "An eigenvector method for estimating the positions of the elements of an array of receivers", *Proceedings of the Australian Symposium on Signal Processing Application,* 1989, pp.391-393.

[87] D.A.Gray and J.L.Riley, "Maximum likelihood estimate and Cramer-Rao bound for a complex signal vector", *Proceedings of the International Symposium on Signal Processing Application*, 1990, pp.352-355.

[88] D.A.Gray, B.G.Quinn and J.L.Riley, "Maximum likelihood estimation of array shape and the Cramer-Rao lower bound", January 1998, to be published.

[89] J.Homer, I.D.Longstaff and G.Callaghan, "High resolution 3D SAR via multi-baseline interferometry", *Proceedings of IGARSS,* 1996, pp.796-798.

[90] J.Homer, I.D.Longstaff and Zhishun She, "Improved digital elevation models via multi-baseline interferometric SAR", *Proceedings of IGARSS,* 1997, pp.1579-1581.

[91] L.Cutrona, "Synthetic aperture radar", in M.Skolnik (ed.), *Radar Handbook,* second edition, McGraw-Hill, 1990.

[92] F.W.Leberl, *Radargrammetric Image Processing,* Artech House, 1990.

[93] G.T.Ruck, D.E.Barrick, W.D.Stuart and C.K.Krichbaum, *Radar Cross Section Handbook,* Plenum Press, 1970.

[94] D.Just and R.Bamler, "Phase statistics of interferogram with application to synthetic aperture radar", *Applied Optics,* Vol.33, No.20, 1994, pp.4361-4368.

[95] A.V.Oppenheim and J.S.Lim, "The importance of phase in signals", *Proceedings of the IEEE,* Vol.69, No.5, 1981, pp.529-541.

[96] M.E.Weber and R.Heisler, "A frequency-domain beamforming algorithm for wideband coherent signal processing", *Journal of the Acoustical Society of Amercia,* Vol.76, No.4, 1984, pp.1132-1144.

[97] B.Maranda, "Efficient digital beamforming in the frequency domain", *Journal of the Acoustical Society of Amercia,* Vol.86, No.5, 1989, pp.1813-1819.

[98] L.R.Rabiner and B.Gold, *Theory and Application of Digital Signal Processing,* Prentice-Hall, 1975.

[99] F.J.Harris, "On the use of windows for harmonic analysis with the discrete fourier transform", *Proceedings of IEEE,* Vol.66, No.1, 1978, pp.51-83.

[100] R.M.Goldstein and H.A.Zebker, "Interferometric radar measurement of ocean surface current", *Nature,* Vol.328, pp.707-709.

[101] D.N.Swingler and R.S.Walker, "Line-array beamforming using linear prediction for aperture interpolation and extrapolation", *IEEE Transactions on Acoustics, Speech, and Signal Processing,* Vol.37, No.1, 1989, pp.16-30.

[102] P.Wu, "A criterion for radar resolution enhancement with Burg algorithm", *IEEE Transactions on Aerospace and Electronic Systems,* Vol.31, No.3, 1995, pp.897-915.

[103] S.M.Kay, *Modern Spectral Estimation*, Prentice-Hall, 1988.

[104] R.O.Schmidt, "Multiple emitter location and signal parameter estimation", *IEEE Transactions on Antenna and Propagation,* Vol.34, No.3, 1986, pp.276-280.

[105] D.H.Johnson and S.R.Degraaf, "Improving the resolution of bearing in passive sonar arrays by eigenvalue analysis", *IEEE Transactions on Acoustics, Speech, and Signal Processing,* Vol.30, No.4, 1982, pp.638-647.

[106] T.J.Shan, M.Wax and T.Kailath, "On spatial smoothing for direction-of-arrival estimation of coherent signals", *IEEE Transactions on Acoustics, Speech, and Signal Processing,* Vol.34, No.4, 1985, pp.806-811.

[107] R.T.Williams, S.Prasad, A.K.Mahalanabis and L.H.Sibnl, "An improved spatial smoothing technique for bearing estimation in a multipath environment", *IEEE Transactions on Acoustics, Speech, and Signal Processing,* Vol.36, No.2, 1988, pp.425-432.

[108] M.Wax and T.Kailath, "Detection of signals by information theoretic criteria", *IEEE Transactions on Acoustics, Speech, and Signal Processing,* Vol.34, No.2, 1985, pp.387-392.

[109] C. Oliver and S. Quegan, *Understanding Synthetic Aperture Radar Images,* Artech House, 1998.

[110] J.S.Lee and K.Hoppel "Principal components transformation of multifrequency polarimetric SAR imagery", *IEEE Transactions on Geoscience and Remote Sensing,* Vol.30, No.4, 1992, pp.686-696.

[111] A.Farina, *Antenna-based Signal Processing Techniques for Radar Systems,* Artech House, 1992.

[112] W.C.Knight, R.G.Pridham and S.M.Kay, "Digital signal processing for sonar", *Proceedings of the IEEE,* Vol.69, No.11, 1981, pp.1451-1506.

[113] J.H.Justice, "Array processing in exploration seismology" in S.Haykin ed., *Array Signal Processing,* Prentice-Hall, Englewood Cliffs, 1985.

[114] A.Macovski, *Medical Imaging Systems,* Prentice-Hall, Englewood Cliffs, 1983.

[115] J.Litva, *Digital Beamforming in Wireless Communications,* Artech House, 1996.

[116] A.R.Thompson, *Interferometry and Synthesis in Radio Astronomy,* John Wiley & Sons, Inc., 1986.

[117] D.H.Johnson and D.E.Dudgeon, *Array Signal Processing Concepts and Techniques,* Prentice-Hall, Englewood Cliffs, 1993.

[118] R.Roy and T.Kailath, "ESPRIT - estimation of signal parameters via rotational invariance techniques", *IEEE Transactions on Acoustics, Speech, and Signal Processing,* Vol.37, No.7, 1989, pp.984-995.

[119] M.Viberg and B.Ottersten, "Sensor array processing based on subspace fitting", *IEEE Transactions on Signal Processing,* Vol.39, No.5, 1991, pp.1110-1121.

[120] Y.Rockah and P.M.Schultheiss, "Array shape calibration using sources in unknown locations - Part I: far-field sources", *IEEE Transactions on Acoustics, Speech, and Signal Processing,* Vol.35, No.6, 1987, pp.724-735.

[121] A.J.Weiss and B.Friedlander, "Array shape calibration using sources in unknown locations - a maximum likelihood approach", *IEEE Transactions on Acoustics, Speech, and Signal Processing,* Vol.37, No.12, 1989, pp.1958-1966.

[122] R.A.Muller and A.Buffington, "Real-time correction of atmospherically degraded telescope images through image sharpening", *Journal of the Optical Society of Amercia,* Vol.64, No.9, 1974, pp.1200-1210.

[123] B.D.Steinberg, "Radar imaging from a distorted array: the radar camera algorithm and experiment", *IEEE Transactions on Antenna and Propagation,* Vol.29, No.5, 1981, pp.740-748.

[124] S.Stergiopoulos, "Implementation of adaptive and synthetic aperture processing schemes in integrated active-passive sonar systems", *Proceedings of the IEEE,* Vol.86, No.2, 1998, pp.358-372.

[125] D.Solomon, *Over-the-horizon radar array calibration,* Ph.D thesis, the University of Adelaide, April, 1998.

[126] K.Gustafsson, F.Mccarthy and A.Paulraj, "Mitigation of wing flexure induced errors for airborne direction-finding applications", *IEEE Transactions on Signal Processing,* Vol.44, No.2, 1996, pp.296-304.

[127] S.W.Flax and M. O'Donnell, "Phase-Aberration correction using signals from point reflectors and diffuse scatterers: basic principles", *IEEE Transactions on Ultrasonics, Ferroelectrics and Frequency Control,* Vol.35, No.6, 1988, pp.758-767.

[128] D.Atkinson, D.Hill, P.Stoyle, P.Summers and S.F.Keevil, "Automatic correction of motion artifacts in magnetic resonance images using an entropy focus criterion", *IEEE Transactions on Medical Imaging,* Vol.16, No.6, 1997, pp.907-910.

[129] V.F.Pisarenko, "The retrieval of harmonics from a covariance function", *Geophysical J. Roy. Astron. Soc.,* Vol.33, 1973, pp.347-366.

[130] M.A.Koerber and D.R.Fuhrmann, "Radar antenna calibration using range-Doppler data", *Proceedings of IEEE 7th SP Workshop on Statistical Signal & Array processing,* 1994, pp.441-444.

[131] A.K.Gabriel, R.M.Goldstein and H.A.Zebker, "Mapping small elevation changes over large areas: differential radar interferometry", *Journal of Geophysical Research,* Vol.94, No.B7, 1989, pp.9183-9191.

[132] H.A.Zebker, P.A.Rosen, R.M.Goldstein, A.Gabriel and C.L.Werner, "On the derivation of coseismic displacement fields using differential radar interferometry: The Landers earthquake", *Journal of Geophysical Research,* Vol.99, No.B10, 1994, pp.19617-19634.

[133] D.Massonet, P.Briole and A.Arnaud, "Deflation of Mount Etna monitored by spaceborne radar interferometry", *Nature,* Vol.375, 1995, pp.567-570.

[134] R.Kwok and M.A.Fahnestock, "Ice sheet motion and topography from radar interferometry", *IEEE Transactions on Geosicience and Remote Sensing,* Vol.34, No.1, 1996, pp.189-200.

[135] W. Xu and I. Cumming, "A region-growing algorithm for InSAR phase unwrapping", *IEEE Transactions on Geosicience and Remote Sensing,* Vol.37, No.1, 1999, pp.124-134.

[136] G.W.Davidson and R. Bamler, "Multiresolution phase unwrapping for SAR interferometry", *IEEE Transactions on Geosicience and Remote Sensing,* Vol.37, No.1, 1999, pp.163-174.

[137] J.Ender, "The airborne experimental multi-channel SAR system AER - II", *Proceedings of European SAR Conference,* 1996, pp.49-52.

[138] J.Ender, "Detection and estimation of moving target signals by multi-channel SAR", *Proceedings of European SAR Conference,* 1996, pp.411-417.

[139] J.Ender, "Signal processing for multi-channel SAR applied to the experimental SAR system AER", *Proceedings of International Conference on Radar,* 1994, pp.220-225.

[140] P.Vass and B. Battrick, *ERS-1 system,* ESA Publications Division, c/o ESTEC, Noordwijk, The Netherlands, 1992.

[141] D.L.Mensa, *High Resolution Radar Cross-section Imaging,* Artech House, 1991.

[142] T.J.Cornwell, "Applications of closure phase to astronomical imaging", *Science,* Vol.245, 1989, pp.263-268.

[143] H.P.Bucker, "Beamforming a towed line array of unknown shape", *Journal of the Acoustical Society of Amercia,* Vol.63, No.5, 1978, pp.1451-1454.

[144] L.M.Novak and M.C.Burl, "Optimal speckle reduction in polarimetric SAR imagery", *IEEE Transactions on Aerospace and Electronic Systems,* Vol.26, No.2, 1990, pp.293-305.

[145] J.J.Smith, Y.H.Leung and A. Cantoni, "The partitioned eigenvector method for towed array shape estimation", *IEEE Transactions on Signal Processing,* Vol.44, No.9, 1996, pp.2273-2283.

[146] H.A.Zebker, P.A.Rosen and S.Hensley, "Atmospheric effects in interferometric synthetic aperture radar surface deformation and topographic maps", *Journal of Geophysical Research,* Vol.102, No.B4, 1997, pp.7547-7563.

[147] C. Boni, M.Richard and S.Barbarossa, "Optimal configuration and weighting of nonuniform arrays according to a maximum ISLR criterion", *Proceedings of International Conference on Acoustics, Speech and Signal Processing,* 1994, pp.V157-160.

[148] W.G.Carrara, R.S.Goodman and R.M.Majewski, *Spotlight Synthetic Aperture radar: Signal Processing Algorithms,* Artech House, 1995.

[149] S.L.Marple, *Digital Spectral Analysis with Applications*, Prentice-Hall, Englewood Cliffs, 1987.

[150] M.Soumekh, *Fourier Array Imaging,* Prentice-Hall, Englewood Cliffs, 1994.

[151] B.D.Steinberg, "Design approach for a high-resolution microwave imaging radio camera", *Journal of the Franklin Institute,* December, 1973, pp.415-431.

[152] B.D.Steinberg, *Principles of Aperture and Array System Design: Including Random and Adaptive Array,* John Wiley & sons, Inc., 1976.

[153] B.D.Steinberg, *Microwave Imaging with Large Antenna Arrays: Radio Camera Principles and Techniques,* John Wiley & sons, Inc., 1984.

[154] B.D.Steinberg and H.M.Subbaram, *Microwave Imaging Techniques,* John Wiley & sons, Inc., 1991.

[155] C.Elachi, *Spaceborne Radar Remote Sensing: Applications and Techniques,* IEEE Press, 1987.

[156] F.T.Ulaby, *Microwave Remote Sensing: Active and Passive, Volume II Radar Remote Sensing and surface Scattering and Emission Theory,* Addision-Wesley Publishing Company, Inc., 1982.

[157] D.J.Daniels, *Surface-penetrating Radar,* IEE, Stevenage, U.K., 1996.

[158] E.Wolf, "Three-dimensional structure determination of semi-transparent objects from holographic data", *Optics Communications,* Vol.1, No.4, 1969, pp.153-156.

[159] J.C.Marron and T.J.Schulz, "Three-dimensional fine-resolution imaging using laser frequency diversity", *Optics Letters,* Vol.17, No.4, 1992, pp.285-287.

[160] Y.Shin and T.Aruga, "Feasibility study of synthetic aperture infrared laser radar techniques for imaging of static and moving objects", Applied Optics, Vol.37, No.24, 1998, pp.5631-5639.

[161] N.H.Farhat and W.R.Guard, "Millimetre wave holographic imaging of concealed weapons", *Proceedings of the IEEE,* Vol.59, No.9, 1971, pp.1383-1384.

[162] N.H.Farhat, "Principles of broad-band coherent imaging", *Journal of the Optical Society of Amercia,* Vol.67, No.8, 1977, pp.1015-1021.

[163] N.H.Farhat, "Prospects for three-dimensional projective and tomographic imaging radar networks", *Radio Science,* Vol.19, No.5, 1984, pp.1347-1355.

[164] H.Li, G.Huang and S.Yen, "Nonuniformly spaced array imaging", *IEEE Transactions on Antenna and Propagation,* Vol.41, No.3, 1993, pp.278-286.

[165] S.Haykin, J.P.Reilly, V.Kezys and E.Vertatschitsch, "Some aspects of array signal processing", *IEE Proceedings, Pt. F,* Vol.139, No.1, 1992, pp.1-24.

[166] A.J.Weiss and B.Friedlander, "Eigenstructure methods for direction finding with sensor gain and phase uncertainties", *Circuits, Systems and Signal Processing,* Vol.9, No.3, 1990, pp.271-300.

[167] D.A.Gray, B.Anderson and P.K.Sim, "Estimation of structured covariances with application to array beamforming", *Circuits, Systems and Signal Processing,* Vol.6, No.4, 1987, pp.421-447.

[168] H.A. d'Assumpcao and G.E.Mountford, "An overview of signal processing for arrays of receivers", *Journal of Electrical and Electronic Engineering, Australia*, Vol.4, No.1, 1984, pp.6-19.

[169] B.D.V.Veen and K.M.Buckley, "Beamforming: A versatile approach to spatial filtering", *IEEE Signal Processing Magazine,* April, 1988. pp.4-24.

[170] H.Krim and M.Viberg, "Two decades of array signal processing research: The parametric approach", *IEEE Signal Processing Magazine,* July, 1996. pp.67-94.

[171] P.Rudnick, "Digital beamforming in the frequency domain", *Journal of the Acoustical Society of Amercia,* Vol.46, No.8, 1969, pp.1089-1090.

[172] B.G.Ferguson, "Sharpness applied to the adaptive beamforming of acoustic data from a towed array of unknown shape", *Journal of the Acoustical Society of Amercia,* Vol.88, No.6, 1990, pp.2695-2701.

[173] B.G.Ferguson, D.A.Gray and J.L.Riley, "Comparison of sharpness and eigenvector methods for towed array shape estimation", *Journal of the Acoustical Society of Amercia,* Vol.91, No.3, 1992, pp.1565-1570.

[174] D.E.Dudgeon, "Fundamentals of digital array processing", *Proceedings of the IEEE,* Vol.65, No.6, 1977, pp.898-904.

[175] D.J.Edelblute, J.M.Fisk and G.L.Kinnison, "Criteria for optimum-signal-detection theory for arrays", *Journal of the Acoustical Society of Amercia,* Vol.41, No.1, 1967, pp.199-205.

[176] H.Cox, "Resolving power and sensitivity to mismatch of optimum array processors", *Journal of the Acoustical Society of Amercia,* Vol.54, No.3, 1973, pp.771-785.

[177] A.Jain and I.Patel, "Dynamic imaging and RCS measurements of aircraft", *IEEE Transactions on Aerospace and Electronic Systems,* Vol.31, No.1, 1995, pp.211-226.

[178] T.Itoh, H.Sueda and Y.Watanabe, "Motion compensation for ISAR via centroid tracking", *IEEE Transactions on Aerospace and Electronic Systems,* Vol.32, No.3, 1996, pp.1191-1197.

[179] R.Voles, "Resolving revolutions: imaging and mapping by modern radar", *IEE Proceedings, Pt. F,* Vol.140, No.1, 1993, pp.1-11.

[180] M.Soumekh, "A system model and inversion for synthetic aperture radar imaging", *IEEE Transactions on Image Processing,* Vol.1, No.1, 1992. pp.64-76.

[181] D.L.Mensa, G.Heidbreder and G.Wade, "Aperture synthesis by object rotation in coherent imaging", *IEEE Transactions on Nuclear Science,* Vol.27, No.2, 1980, pp.989-997.

[182] D.L.Mensa, S.Halevy and G.Wade, "Coherent Doppler tomography for microwave imaging", *Proceedings of the IEEE,* Vol.71, No.2, 1983, pp.254-261.

[183] M.I.Skolnik, *Introduction to Radar Systems,* McGraw-Hill, Inc., 1980.

[184] H.L.Vantrees, *Detection, Estimation and Modulation Theory,* Part I, John Wiley & Sons, Inc., 1968.

[185] W.D.Wirth, "High resolution in azimuth for radar targets moving on a straight line", *IEEE Transactions on Aerospace and Electronic Systems,* Vol.16, No.1, 1980, pp.101-104.

[186] R.K.Raney, "Synthetic aperture imaging radar and moving targets", *IEEE Transactions on Aerospace and Electronic Systems,* Vol.7, No.3, 1971, pp.499-505.

[187] A.D.Cenzo, "A comparison of resolution for spotlight synthetic-aperture radar and computer-aided tomography", *Proceedings of the IEEE,* Vol.74, No.8, 1986, pp.1165-1166.

[188] M.D.Desai and W.K.Jenkins, "Convolution backprojection image reconstruction for spotlight mode synthetic aperture radar", *IEEE Transactions on Image Processing,* Vol.1, No.4, 1992, pp.505-517.

[189] A.Zyweck and R.E.Bogner, "High-resolution radar imagery of the Mirage III aircraft", *IEEE Transactions on Antenna and Propagation,* Vol.42, No.9, 1994, pp.1356-1360.

[190] H.Yang and M.Soumekh, "Blind-velocity SAR/ISAR imaging of a moving target in a stationary background", *IEEE Transactions on Image Processing,* Vol.2, No.1, 1993, pp.80-95.

[191] M.Soumekh, "Reconnaissance with ultra wideband UHF synthetic aperture radar", *Signal Processing Magazine,* Vol.12, No.4, 1995, pp.21-40.

[192] A.W.Rihaczek and S.J.Hershkowitz, *Radar Resolution and Complex-image Analysis,* Artech House, 1996.

[193] E.Yadin, "SAR autofocusing viewed as adaptive beamforming on prominent scatterers", *Proceedings of National Radar Conference,* 1994, pp.138-143.

[194] H.Lee and G. Wade ed., *Imaging Technology,* IEEE Press, 1986.

[195] R. Bamler and P.Hartl, "Synthetic aperture radar interferometry", *Inverse Problems,* Vol.14, 1998, pp.R1-R54.

[196] C.W.Therrien, *Discrete Random Signals and Statistical Signal Processing,* Prentice-Hall, 1992.

[197] R.A.Monzingo and T.W.Miller, *Introduction to Adaptive Arrays,* NY:Wiley-Interscience, 1980.

[198] J.E.Hudson, *Adaptive Array Principles,* London, England: Peter Peregrinas Ltd., 1981.

[199] E.Nicolau and D.Zaharia, *Adaptive Arrays,* Elsevier Science Publishers Co., 1989.

[200] M.Kaveh, "Sensor array processing" in V.K.Madisetti and D.B.Williams (ed.), *Handbook of Digital Signal Processing,* CRC Press, 1998.

[201] S.N.Madsen and H.A.Zebker, "Imaging radar interferometry" in F.M.Henderson and A.J.Lewis (ed.) *Principles and Applications of Imaging Radar, Manual of Remote Sensing,* Vol.2, John Wiley & Sons Inc., 1998.

[202] J.Ender, "Experimental results achieved with the airborne multi-channel SAR system AER-II", *Proceedings of European SAR Conference,* 1998, pp.315-318.

[203] B.Friedlaender and B. Porat, "VSAR - a high resolution radar system for detection of moving target", *IEE Proceedings - Radar, Sonar and Navigation,* Vol.144, No.4, 1997, pp.205-218.

[204] M.Bao, C.Bruning and W.Alpers, "Simulation of ocean waves imaging by an along-track interferometric synthetic aperture radar", *IEEE Transactions on Geoscience and Remote Sensing,* Vol.35, No.3, 1997, pp.618-631.

[205] B.Friedlaender and B. Porat, "VSAR - a high resolution radar system for ocean imaging", *IEEE Transactions on Aerospace and Electronic Systems,* Vol.34, No.3, 1998, pp.755-775.

[206] K.A.Johnson, M.P.Hayes and P.T.Gough, "A method for estimating the sub-wavelength sway of a sonar towfish", *IEEE Journal of Oceanic Engineering,* Vol.20, No.4, 1995, pp.258-267.

[207] D.E.Wahl, "Towed array shape estimation using frequency-wavenumber data", *IEEE Journal of Oceanic Engineering,* Vol.18, No.4, 1993, pp.582-590.

[208] V.C.Chen and W.J.Miceli, "Time-varying spectral analysis for radar imaging of manoeuvring targets", *IEE Proceedings - Radar, Sonar and Navigation,* Vol.145, No.5, 1998, pp.262-268.

[209] L.C.Trintinalia and H.Ling, "Joint time-frequency ISAR using adaptive processing", *IEEE Transactions on Antenna and Propagation,* Vol.45, No.2, 1997, pp.221-227.

[210] C.A.Snarski, "Rank one phase error estimation for range-Doppler imaging", *IEEE Transactions on Aerospace and Electronic Systems,* Vol.32, No.2, 1996, pp.676-688.

[211] W.M.Brown, "Wakler model for radar sensing of rigid target fields", *IEEE Transactions on Aerospace and Electronic Systems,* Vol.16, No.1, 1980, pp.104-106.

[212] K.T.Kim, S.W.Kim and H.T.Kim, "Two-dimensional ISAR imaging using full polarisation and super-resolution processing techniques", *IEE Proceedings - Radar, Sonar and Navigation,* Vol.145, No.4, 1998, pp.240-246.

[213] Z.Liu, R.Wu and J.Li, "Complex ISAR imaging of manoeuvring targets via the Capon estimator", *IEEE Transactions on Signal Processing,* Vol.47, No.5, 1999, pp.1262-1271.

[214] R.L.Mitchell, "Models of extended targets and their coherent radar images", *Proceedings of the IEEE,* Vol.62, No.6, 1974, pp.754-758.

[215] E.N.Leith, "Quasi-holographic techniques in the microwave region", *Proceedings of the IEEE,* Vol.59, No.9, 1971, pp.1305-1318.

[216] E.N.Leith, "Range-azimuth-coupling aberrations in pulse-scanned imaging systems", *Journal of the Optical Society of Amercia,* Vol.63, No.2, 1973, pp.119-126.

[217] H.D.Griffiths, T.A.Rafik, Z.Meng, C.Cowan, H.Shafeeu and D. Anthony, "Interferometric synthetic aperture sonar for high resolution 3-D mapping of sea-bed", *IEE Proceedings - Radar, Sonar and Navigation,* Vol.144, No.2, 1997, pp.96-103.

[218] J.Li, Z.Liu and P.Stoica, "3-D target feature extraction via interferometric SAR", *IEE Proceedings - Radar, Sonar and Navigation,* Vol.144, No.2, 1997, pp.71-80.

[219] J.Li, Z.Bi, Z.Liu and K.Knaell, "Use of curvilinear SAR for three-dimensional target feature extraction", *IEE Proceedings - Radar, Sonar and Navigation,* Vol.144, No.5, 1997, pp.275-283.

[220] M.Soumekh, "Moving target detection in foliage using along track monopulse synthetic aperture radar imaging", *IEEE Transactions on Image Processing,* Vol.6, No.8, 1997, pp.1148-1163.

[221] R.B.Perlow and B.D.Steinberg, "Automatic stereo processing of high resolution radar imagery", *IEEE Transactions on Aerospace and Electronic Systems,* Vol.33, No.3, 1997, pp.802-811.

[222] M.Tu, I.J.Gupta and E.K.Walton, "Application of Maximum likelihood estimation to radar imaging", *IEEE Transactions on Antenna and Propagation,* Vol.45, No.1, 1997, pp.20-27.

[223] M.Soumekh, "Automatic aircraft landing using interferometric inverse synthetic aperture radar imaging", *IEEE Transactions on Image Processing,* Vol.5, No.9, 1996, pp.1335-1345.

[224] M.Soumekh, "Reconnaissance with slant plane circular SAR imaging", *IEEE Transactions on Image Processing,* Vol.5, No.8, 1996, pp.1252-1265.

[225] J.Fortuny, "An efficient 3-D near filed ISAR algorithm", *IEEE Transactions on Aerospace and Electronic Systems,* Vol.34, No.4, 1998, pp.1261-1270.

[226] J.Fortuny and A.J.Sieber, "Three-dimensional synthetic aperture radar imaging of a fir tree: first results", *IEEE Transactions on Geoscience and Remote Sensing,* Vol.37, No.2, 1999, pp.1006-1014.

[227] A.M.Guarnieri and C.Prati, "An interferometric quick-look processor", *IEEE Transactions on Geoscience and Remote Sensing,* Vol.37, No.2, 1999, pp.861-866.

[228] A.Ferretti, C.Prati and F.Rocca, "Multibaseline InSAR DEM reconstruction: the wavelet approach", *IEEE Transactions on Geoscience and Remote Sensing,* Vol.37, No.2, 1999, pp.705-714.

[229] P.W.Vachon, D.Geudtner, A.L.Gray and R.Touzi, "ERS-1 synthetic aperture radar repeat-pass interferometry studies: implications for RADARSAT", *Canadian Journal of Remote Sensing,* Vol.21, No.4, 1995, pp.441-454.

[230] K.K.Knaell and G.P.Cardillo, "Radar tomography for the generation of three-dimensional images", *IEE Proceedings - Radar, Sonar and Navigation,* Vol.142, No.2, 1995, pp.54-60.

[231] M.Costantini, "A novel phase unwrapping method based on network programming", *IEEE Transactions on Geoscience and Remote Sensing,* Vol.36, No.3, 1998, pp.813-821.

[232] J.P.Burg, D.G.Luenberger and D.L.Wenger, "Estimation of structured covariance matrices", *Proceedings of the IEEE,* Vol.70, No.9, 1982, pp.963-974.

[233] R.A.Horn and C.R.Johnson, *Matrix analysis*, Cambridge University Press, 1985.

[234] G.H.Golub and C.F.V.Loan, *Matrix computations*, Johns Hopkins University Press, 1989,